Phase Segmentation and Analysis of Tomographic Rock Images Using Machine Learning Techniques

Dissertation

Doctoral thesis submitted in fulfillment of the requirements
for the degree of Doctor rerum naturalium (Dr.rer.nat.)
at the
Department of Material and Earth Sciences,
Technische Universität Darmstadt

TECHNISCHE
UNIVERSITÄT
DARMSTADT

Submitted by

Swaroop Chauhan, M.Sc.
born on 23.03.1982 in Hyderabad, India

Approved by

Supervisor: Univ.-Prof. Dr. rer. nat. Ingo Sass
Co-supervisor: Univ.-Prof. Dr.-Ing. Michael Kersten

Date of submission: 06. November 2018
Date of Doctoral examination: 06. December 2018
Published Darmstadt 2019

Board of examiners

Head:	**Prof. Dr. Hans-Joachim Kleebe**
Supervisor:	**Prof. Dr. rer. nat. Ingo Sass**
Co-supervisor:	**Prof. Dr. –Ing Michael Kersten**
Examiner:	**Prof. Dr. Eva Schill**
Examiner:	**Prof. Dr. Christoph Schüth**

To
Elena and Arti

Table of Contents

Declaration **X**

Acknowledgments **XI**

Scope of the Study **XII**

Motivation XII

Application XIII

Abstract **XIV**

Kurzfassung **XV**

Preface **XVII**

List of Figures **XXI**

List of Tables **XXIII**

Nomenclature **XXIV**

1. .... Introduction **1**

1.1. Principle of X-ray and Micro Computer Tomography 1

1.1.1. X-rays 1

1.1.2. Micro Computer Tomography 2

1.2. Image Artefacts 3

1.2.1. Beam Hardening and Scattering 3

1.2.2. Edge Enhancement 4

1.2.3. Ring Effect 4

1.2.4. Noise 4

1.2.5. Partial Volume Effect 4

1.3. State of the Art 5

1.3.1. Reactive Transport 5

1.3.2. Combining Experiment and Imaging 6

1.3.3. Multiscale Imaging 6

1.4. A Brief Introduction of Machine Learning in Geosciences 7

1.4.1. Application of Machine Learning in Geothermal Energy 7

1.4.2. Application of Machine Learning Reservoir Modelling 7

1.4.3. Application of Machine Learning in Phase Segmentation 8

1.5. Research Objectives 8

2. .... Processing of Rock Core Microtomography Images: Using Seven Different Machine Learning Algorithms **13**

2.1. Abstract 14

2.2. Introduction 14

2.3. Materials and Methods 16

2.3.1. Rock Sample 16

2.3.2. Image Acquisition and Processing 17

2.4. Image Segmentation Using Unsupervised Clustering 18
2.4.1. K-means 18
2.4.2. Fuzzy C-Means (FCM) 18
2.4.3. Self-Organized Maps (SOM) 19
2.5. Image Segmentation Using Supervised Clustering 20
2.5.1. Artificial Neural Networks 20
2.5.2. Least Square Support Vector Machine 20
2.6. Ensemble Classifiers 21
2.6.1. Bragging 21
2.6.2. Boosting 21
2.7. Results and Discussions 22
2.7.1. Classification and Feature Extraction 22
2.7.2. Image Segmentation 22
2.7.3. Comparison 24
2.7.4. Estimation of Porosity and Pore Size Distribution 24
2.8. Conclusions and Outlook 27

3.....Phase Segmentation of X-Ray Tomography Rock Images Using Machine Learning Techniques: an Accuracy and Performance Study 29

3.1. Abstract 30
3.2. Introduction 30
3.3. Experimental Approach 32
3.4. Image Processing 35
3.5. Machine Learning 35
3.5.1. Unsupervised Learning Techniques 35
3.5.2. Supervised Techniques 36
3.5.3. Ensemble Classifiers Techniques 37
3.6. Feature Selection 38
3.7. Performance 39
3.8. Accuracy 39
3.8.1. Entropy and Purity 41
3.8.2. Mean Square Root Error 42
3.8.3. Receiver Operational Characteristics 43
3.8.4. 10-fold Cross Validation 44
3.9. Results and Discussions 46
3.9.1. Porosity and Pore Size Distribution 46
3.9.2. Performance and Accuracy Analysis 47
3.10. Conclusions 49

4.....CobWeb 1.0 code for automatic tomographic image analysis based on machine learning algorithms 51

4.1. Abstract 52
4.2. Introduction 52

4.3. CobWeb 53
4.3.1. Salient Features 53
4.3.2. Window Panel 54
4.3.3. Overall Framework 55
4.3.4. Control Module 55
4.3.5. Analysis Module 56
4.3.6. Visualization Module 57
4.4. Tomographic Datasets Used for Evaluation of CobWeb 1.0 58
4.4.1. Gas-Hydrate –bearing Sediments 58
4.4.2. Grosmount Carbonate Rock 58
4.4.3. Berea Sandstone Rock 58
4.5. Results and Discussions 60
4.5.1. Image Processing 60
4.5.2. Dual Filtering of Gas Hydrate bearing Sediment 60
4.5.3. Phase Segmentation 61
4.5.4. Grosmont Carbonate and Berea Sandstone 61
4.5.5. Gas-Hydrate (GH) Bearing Sediment Dual-Clustering 61
4.5.6. Representative Elementary Volume 63
4.5.7. Estimation of Relative Porosity and Pore Size Distribution 67
4.6. Conclusions and Outlook 69

5. .... Results and Discussions 71
5.1. Results 71
5.2. Discussions 72

6. .... Outlook 74

7. .... References 77

Appendix 87

Appendix A: MATLAB snippet for removal for Edge Enhancement Effect in gas hydrate datasets 87
1.1 Gas Hydrate Segmentation 87
1.2 Step 1 87
1.3 Step 2 87
1.4 Display image 87
1.5 Concatenate raw data into single array 88
1.6 Perform k-means clustering 88
1.7 Display image 89
1.8 Step three 89
1.9 Index noise pixels 89
1.10 Plot histogram noise 90
1.11 Index EDL pixels 90
1.12 Plot histogram noise 90
1.13 Index liquid pixels 90

1.14 Plot histogram liquid 90
1.15 Index EDH pixels 91
1.16 Plot histogram EDH 91
1.17 Quartz index phases 92
1.18 Quartz 92
1.19 Plot histogram quartz 92
1.20 Gas Hydrate 93
1.21 Plot Histogram Gas Hydrate 93
1.22 Step 4 - rescaling the raw images 94
1.23 With an exception to GH dataset 94
1.24 Replace by average quartz values 95
1.25 Reshape rescaled array 95
1.26 Step 5 96

Appendix B: CobWeb User Manual 99

User Manual 99

List of Tables 102

List of Figures 103

1.....Introduction to CobWeb 1.0 105
1.1. Overview 106
1.2. About the Manual 106

2.....System Requirements 107
2.1. Operating System 107
2.2. Hardware 107
2.2.1. Display 108
2.2.2. User Rights 108
2.2.3. Recommended Setup 108
2.2.4. Third Party Software 109
2.2.5. Remote Access 109

3.....Installation Instruction 110
3.1. MATLAB Runtime License 110
3.2. ParaView 110
3.3. Microsoft® Excel 111
3.4. CobWeb 111

4.....Getting Started 113
4.1. CobWeb 1.0 Interface & Tools 113
4.1.1. Toolbar 113
4.1.2. Inspector 118
4.1.3. Preprocessing Panel 119
4.1.4. Display Window 122
4.1.5. History Panel 122

4.1.6. Control Panel 123
5. .... Demonstration 124
5.1. Loading TIFF Data 124
5.1.1. Loading RAW Data 126
5.2. Image Processing 127
5.2.1. Representative Elementary Volume Selection 128
5.2.2. Image Inspection 129
5.2.3. Image Segmentation — Unsupervised Machine Learning Techniques 130
5.2.4. Image Segmentation — Supervised Machine Learning Technique 132
6. .... Visualisation 135
6.1. Geometrical Properties 135
6.1.1. Relative Porosity 135
6.1.2. Pore Size Distribution 138
6.1.3. Volume Fraction 141
6.2. Validation 145
6.3. Export 147
6.4. Volume Rendering 149
6.4.1. Volume Rendering with CobWeb 1.0 150
6.4.2. Volume Rendering with ParaView 151
7. .... Limitations 157
8. .... Trouble Shooting 158
Curriculum Vitae 161

Declaration

I am aware of and understand Technische Universität of Darmstadt policy on plagiarism and I certify that

i) this is an original report of my research work, has been written by me
ii) has not been submitted for any other degree in my name, to any another university or institution
iii) appropriate credit has been given within this thesis, where references have been made to the work of others

Swaroop.Chauhan

Darmstadt, Date: 31.05.2019

Acknowledgments

Firstly, I would like to express my gratitude toward Prof. Dr. Ingo Sass for his commitment and leadership. His trust in me and his firm belief in the philosophy of machine learning and its implication to the field of geosciences enabled me to push forward despite initial setbacks. Above all, without his financial support through different project and project partner my research work would have been incomplete.

Besides my advisor, I would like to acknowledge Prof. Dr. Michael Kersten, who co-supervised, my doctorate work and his resourceful fellow scientist Dr. Frieder Enzmann who introduced me to the field of digital rock physics; its essence and related challenges. Their critical review, comments and suggestions at different stages of my research work and research publications was essential in the project planning and decision making phases.

My special thanks to Dr.habil. Wolfram Rühaak, his honest, prompt and direct art of communication helped me to adjust, integrate and evolve in the working group. His periodic assessment and regular discussion help me set realistic goals and work towards them. His vast experience as reviewer of different journals helped me in refining my scientific writing skills and tackling the review processes. He tuned my presentation skills in tandem with other colleagues, and taught me the art of presenting complex scientific analysis/results in a lucid and clear manner to non-technical audiences. His technical programming skills were an asset, which I could exploit and benefit for my research work.

I thank Ms. Meike Hinz for suggestions and comments that helped in improving the CobWeb user manual and Ms. Gilian Wilson for the English language correction.

I thank, Mrs. Simone Ross-Kirschbaum for her diligent effort and her friendly nature which made the administrative process at the department and the Technische Universität Darmstadt seem easy and uncomplicated as possible.

Scope of the Study

Motivation

Energy is a vital resource, which has supported the society throughout time. To fulfill the constantly changing energy demand of the world, it is not only essential to identify affordable and reliable energy resources but device mechanism to make it clean by reducing the carbon footprint on the local environment and the changing climate (Bickle 2009; Stern et al. 2016) . Therefore, the fundamental understanding of petrophysics, micromechanics and chemical characteristics of different reservoir rock types is crucial to calibrate numerical models for reliable reservoir prognosis (Joshi 1988; Mukherjee and Economides 1991; Mueller 2007; Cipolla et al. 2009; Brown et al. 2011; Ozkan et al. 2011).

Hence, micro X-ray computer tomography (XCT) can help to better analyze the properties of reservoir rocks. The three-dimensional non-destructive investigation of the pore space of rocks is of great interest in many geoscientific fields. The investigation and modeling of pore spaces and pore networks gives an important insight into the development of permeability and porosity.

For outcrop analog studies, the investigation of pore space geometry and its temporal variation resulting from pressure, temperature, and chemical processes is of particular importance. Such studies are widespread, e.g. in the oil and gas industry but also in the study of geothermal reservoirs. The combined investigation of rock samples from outcrop analogue studies using XCT and a Thermo-Triax cell (TTZ), has been operating for few years at the Department of Geothermal Science and Technology at Institute for Applied Geosciences at the Technical University Darmstadt. This has lead to an improved prognosis of the geothermally relevant rock properties in the reservoir.

One of the major uncertainties in geothermal reservoir characterization is the assignment of flow parameters. Permeability measurements based on analog outcrop surface based can only be postulated to the reservoir at great depths under completely different pressure/temperature conditions. Such values are therefore considered to be less reliable and are often relatively freely modified as part of a calibration (history matching).

One way to extract the information-value (Aussagekraft) of outcrop analog samples is to reconstruct the reservoir conditions (diagenesis and alteration) in the laboratory as an experiment. Where, the rock samples are measured before and after the alteration experiments with XCT. Thereafter, on the basis of XCT measurements, fluid flow simulation through empirical pore network models or lattice Boltzmann simulation (LBE) could be generated to establish a physically based permeability.

The direct combination of both experiments, i.e a direct XCT measurement during a thermo-Triax experiment, is currently not feasible for technical and cost reasons. But, due to the rapid development in measuring and computer techniques, insitu 4D, i.e. spatially and temporally resolved experiments on rock samples in synchrotron facilities are possible. These experiments and technical possibilities and consequent developments provide a considerable potential for a deeper understanding of pore-scale

processes and for upscaling strategies. The current strong demand for high-quality XCT easurements demonstrates the strong interest in this technology and as an additional

Methodology in geoscientific research fields. There is also a growing industrial interest in such research activities.

All these activities in connection with computer-tomographic measurements have the goal of reconstructing and reproducing a spatially (temporally) accurate image of the phase distribution.

Application

Despite the availability of both commercial and open source software, an ideal tool for digital rock physics analysis for accurate automatic image analysis at ambient computational performance is difficult to pin point. More often image segmentation is manually driven where the performance remains limited to two phases. Discrepancies due to artefacts causes inaccuracies in image analysis. To overcome these problems, we have developed CobWeb 1.0 which is automated and explicitly tailored for accurate grayscale (multi-phase) image segmentation using unsupervised and unsupervised machine learning techniques. The user-friendly graphical interface enables image enhancement, segmentation, and evaluates the accuracy of the different segmented classes. Through the graphical user interface a full 3D XCT digital rock dataset can be processed user-friendly. Another option is to perform a quick and easy region-of-interest selection where a representative elementary volume can be extracted and processed. The CobWeb software package is deployed as a series of windows executable binaries which use image processing and machine learning libraries of MATLAB®. Segmentation techniques include K-means, Fuzzy C-means, least square support vector machine (LSSVM), and ensembled classification (bragging and boosting) tools. Additionally, geometrical properties such as relative porosity trends, pore size distribution, and volume fraction of different phases obtained from the segmented data can be calculated and visualized. The resulting data can be exported to ParaView, DSI Studio (.fib), Microsoft® Excel and MATLAB® for further visualisation, animation and numerical simulation. The efficiency of the new workflow is verified using high-resolution synchrotron tomography datasets, as well as lab-based (cone-beam) X-ray micro-tomography datasets.

Abstract

The topic of this thesis is the characterization of different phases and estimation of the geometrical parameters from the digital rock images, which are generated using high resolution X-ray computer tomography (XCT) experiments. High resolution X-ray computer tomography (XCT) is a well-established, long-standing experimental approach used in the rock physics community to study transport of the energy—momentum relationship inside porous- matrix domain. The accuracy and the appropriateness of the continuum based or topology based model prediction relies extensively on the resolution and phase segmentation of the XCT images. The current technology, used in nano tomography and micro tomography is able to generate high resolution image compared to the last decade, but new adaptive and flexible algorithm are urgently needed for accurate image analysis.

Within the framework of this thesis different categories (supervised, unsupervised and ensemble classifiers) of machine learning (ML) techniques in combination with different image filtering techniques were investigated and tested for accurate XCT image segmentation and analysis. This lead to the investigation of seven different ML algorithm K-means, Fuzzy C-means (FCM), Self-Organized Map (SOM), Feed Forward Artificial Neural Networks (FFANN), Least Square Support Vector Machine (LSSVM), Bragging type ensemble classification tree (Bragging) and Boost (Boosting) type ensemble classification tree. Their respective clustering and classification performance and accuracy was compared and cross-validated. Thereafter, a robust workflow was developed to predict geometrical parameters such as porosity, volume fraction of different phases (pore, matrix, mineral) and pore size distribution.

Further, a (standalone) grapical user interface (GUI) "*CobWeb"* was developed. The current version of CobWeb is capable to read and process (reconstructed) XCT files in tiff and raw format. Tools to zoom in, zoom out, cropping, color and scale, assist in the visualization and interpretation of XCT 2D and 3D stack data. Noise filters such as non-local means, anisotropic diffusion, median and contrast adjustments are implemented to increase signal to noise ratio. The user can chose from five segmentation algorithms, namely K-means, Fuzzy C-means (unsupervised), Support Vector Machine (supervised), Bragging and Boosting (enable classifiers) for accurate segmentation and cross-validation. Material properties like relative porosities, pore size distribution, volume fraction (pore, matrix, mineral phases) can be quantified and visualized. The data can be exported into different file formats such as Microsoft® Excel (xlsx), MATLAB® (mat), ParaView (vkt) and DSI studio (fib). The current version is supported for Micosoft® Windows and runs stable on Windows® 7 to Windows® 10.

As ML techniques offer us high quality and accuracy w.r.t XCT segmentation. The future research should focus on comparing numerical simulation based on analytical modelling and molecular level approaches, such as pore network modelling and Lattice-Gas or Boltzmann methods respectively. CobWeb, has further scope of integrate different modules of point cloud data from LIDAR measurements, ultrasound data and acoustic emission data. Volume rendering plugin would be an important step forward good visualization.

Kurzfassung

Thema dieser Forschungsarbeit ist die Charakterisierung verschiedener Phasen und die Abschätzung geometrischer Parameter aus digitalen Gesteinsbildern, die mittels hochauflösender röntgen-computertomographischer (XCT) Experimente erzeugt wurden. Hochauflösende Röntgen-Computertomographie (XCT) ist ein etablierter experimenteller Ansatz, der in der Gesteinsphysik verwendet wird, um den Transport der Energie-Impuls-Beziehung innerhalb der porösen und Matrix-Domäne zu untersuchen. Die Genauigkeit und Bestimmung Angemessenheit der auf kontinuumsbasierenden oder topologiebasierten Modellvorhersagen beruht weitgehend auf der Auflösung und Phasensegmentierung der XCT-Bilder. Der Stand der Technik, der in der Nanotomomographie und der Mikrotomographie verwendet wird, kann im Vergleich zum letzten Jahrzehnt ein hochauflösendes Bild erzeugen. Für eine genaue Bildanalyse ist jedoch ein neuer adaptiver und flexibler Algorithmus zwingend erforderlich.

Im Rahmen dieser Arbeit wurden verschiedene Kategorien (unsupervised, supervised und Ensembleklassifizierer) von maschinellen Lernmethoden (ML) in Kombination mit verschiedenen Bildfiltertechniken untersucht und auf eine genaue XCT-Bildsegmentierung und -analyse getestet. Dies führt zur Untersuchung von sieben verschiedenen ML-Algorithmen: K-means, Fuzzy C-means (FCM), Self-Organized Map (SOM), Feed Forward Artificial Neural Networks (FFANN), Least Square Support Vector Machine (LS-SVM), Braging-Typ Ensemble Classification Tree (Bragging) und Boost Strapping (Boosting) Typ Ensemble Classification Tree. Die jeweilige Clustering- und Klassifizierungsleistung und -genauigkeit wurden verglichen und kreuzvalidiert. Danach wurde ein widerstandfähig Arbeitsablauf entwickelt, um geometrische Parameter wie Porosität, Volumenanteil verschiedener Phasen (Poren-, Matrix-, Mineral-) und Porengrößenverteilung vorhersagen zu können.

Weiterhin wurde die Standalone-Software „CobWeb“ mit grafischer Benutzeroberfläche (grapfical user interface, GUI) entwickelt. Die aktuelle Version von CobWeb ist in der Lage XCT-Dateien in Tiff-und Roh-Format zu lesen und zu verarbeiten (rekonstruiert). Werkzeuge zum Vergrößern, Verkleinern, Beschneiden, Einfärben und Skalieren unterstützen während der Visualisierung und Interpretation von XCT 2D- und 3D-Stack-Daten. Rauschfilter wie nicht-lokale Mittelwerte, anisotrope Diffusions-, Median- und Kontrasteinstellungen werden implementiert, um das Signal-Rausch-Verhältnis zu erhöhen. Der Benutzer kann für eine genaue Segmentierung und Cross-Validierung aus fünf Segementationsalgorithmen wählen: (1) K-Mittel, (2) Fuzzy C-Mittel (unbeaufsichtigt), (3) Support-Vektor-Maschine (überwacht), (4) Bragging und (5) Boosting (aktivieren Klassifikatoren). Die Daten können in verschiedene Dateiformate wie Microsoft® Excel (xlsx), MATLAB® (mat), ParaView (vkt) und DSI Studio (Fib) exportiert werden. Die aktuelle Version wird von Micosoft® Windows unterstützt und läuft unter Windows® 7 und Windows® 10.

ML-Techniken bieten eine hohe Qualität und Genauigkeit bezüglich XCT Segmentierung. Die zukünftige Forschung sollte sich auf den Vergleich der numerischen Simulation auf Grundlage von analytischen Modellierungen und Ansätze auf molekularen Ebenen, wie Pore-Netzwerk-Modellierung und Lattice-Gas oder Boltzmann Methoden konzentrieren. CobWeb hat weitere Möglichkeiten, verschiedene Module von Punktwolken-Daten aus Lidar-Messungen,

Ultraschall-Daten und akustischen Emissionsdaten zu integrieren. Volume Rendering Plugins wäre ein weiterer wichtiger Schritt in Richtung guter Visualisierung.

Preface

This PhD work is funded through APS Antriebs-, Prüf- und Steuertechnik GmbH within the framework of the SUGAR (Submarine Gashydrat Ressorcen) III project, by the German Federal Ministry of Education and Research (BMBF grant no. 03SX381H). It is also, partly supported by the DFG in the framework of the Excellence Initiative, Darmstadt Graduate School off Excellence Energy Science and Engineering (GSC 1070)

The XCT instrument is designed and build at APS Antriebs-, Prüf- und Steuertechnik GmbH, with a primary aim to monitor multiphase processes between Carbon dioxide (CO_2) and Methane (CH_4), which might come in to production by year 2019-20. The scientific studies related to the development of image processing, image segmentation and analysis of the XCT data is been assigned by the department of Geothermal Science and Technology, Institute for Applied Geosciences (IAG), Technical Universität Darmstadt (TUDa). This research work is an outcome of the scientific studies undertaken.

The main objective of this thesis work is a robust, enhanced, near real time workflow for the post processing of the high resolution X-ray computer tomography (XCT) data, which is presented as cumulative dissertation comprising of three research publication attached below as chapters. The associated manuscript gives a general introduction to the topic of image segmentation and its relevance to digital rock physics, along with a comprehensive description of machine learning techniques and its utility for XCT data processing of Methane Hydrates.

Chapter II: **Chauhan, S.**, Rühaak, W., Khan, F., Enzmann, F., Mielke, Philipp., Kersten, M., and Sass, I. (2016): Processing of rock core microtomography images: Using seven different machine learning algorithms, In Computers & Geosciences, Volume 86, 2016, Pages 120-128, ISSN 0098-3004, https://doi.org/10.1016/j.cageo.2015.10.013.

Chapter III: **Chauhan, S.**, Rühaak, W., Anbergen, H., Kabdenov, A., Freise, M., Wille, T., and Sass, I. (2016): Phase segmentation of X-ray computer tomography rock images using machine learning techniques: an accuracy and performance study, Solid Earth, 7, 2016 1125-1139, https://doi.org/10.5194/se-7-1125-2016.

Chapter IV: **Chauhan, S.**, Sell, K., Enzmann, F., Rühaak. W., and Wille, T., Sass, I., and Kersten, M.: CobWeb (2018): CobWeb — a toolbox for automatic tomographic image analysis based on machine learning techniques: application and examples, arXiv:1803.11046v3.

Chapter II: In this study the ability of machine learning (ML) techniques to segmentation and derive geometrical parameters from high resolution XCT data of Andesite rock sample is determined. The three main branches unsupervised (K-means, Fuzzy C-means (FCM), Self Organized Maps (SOM)), supervised (Feed Forward Neural Network (FFANN), Least Square Support Vector Machine (LS-SVM)), ensemble classifiers (Bragging tree, Boosting) and their corresponding algorithm are explored, tuned and adapted for grayscale (phase) segmentation of the Andesite digital rock.

The idea stem from the work Cortina-Jaunchs et al (2001); were, the binary segmentation of the XCT soil images was performed using unsupervised techniques and supervised

segmentation technique FFANN. It was not clear (or clearly described) If the FFANN reclassified─ the previously (classified) segmented image by unsupervised techniques? And, the validation approach used to determine the accuracy?

This lead to a thorough investigation, were the new optimized workflow was implemented specifically tailored for greyscale segmentation. Other segmentation/classification methods, such as LS-SVM, Bragging Tree and Booting were included to determine accuracy based on visual inter comparison and individual computation performance. Then, further the derived relative porosities where validated with laboratory measurements using helium pycnometer. The geometrical pore size distribution (PSD) simulated using GeoDict software for each ML technique cross-validates non-connected pore network in volcanic rock, and the micro porosity caused by geothermal alteration.

I designed the workflow and wrote the program scripts in MATLAB© to perform the pre- and post- processing of the XCT data, generated figures and drafted the manuscript. Wolfram Rühaak supervised the work by periodic input and discussions. He thereafter participated in revising the manuscript by offering comments and correction. Frieder Enzmann conducted XCT measurement and Faisal Khan provided the script for Least Square Support Vector Machine (LS-SVM) segmentation. The geometrical pore size distribution simulation was done using GeoDict software (from MATH2MARKET GmbH) in university of Mainz by Faisal Khan in consultation with Frieder Enzmann. Philipp Mielke did the field work (in New Zealand) and obtained the Andesite sample. He performed the optical microscope analysis and porosity measurement using helium pycnometer. Micheal Kersten and Ingo Sass initiated and supervised the project and the research. All co-authors contributed towards the revision and proof reading of the manuscript.

Chapter III: In this study is a further extension of the work done above. Where, the aim was to quantitatively validate the accuracy and performance of the ML techniques. This benchmark study was essential; where different metrics such as─ entropy, purity, mean square root error, receiver operational characteristic curve and 10 K-fold cross-validation were used to determine the accuracy of unsupervised, supervised and ensemble classifier techniques. This study does not isolate one particular machine learning algorithm which could best suited the complex phase segmentation problem, but provides investigation and discussion on the tuning parameters that can help in selecting the appropriate machine learning techniques for phase segmentation. Despite the gold standard is evaluating segmentation based on human assessors (visual inspection) it is useful to adopt qualitative metrics; as it gives insight in to performance issues. In this study we also implemented PSD scheme based on the work done by Rabbani et al (2014). In this validation study digital rock images of different resolution form 0.74 nm (Berea Sandstone) up to 20 µm are used. Respective relative porosities where cross validated with laboratory measurements using helium pycnometer and benchmark paper of Andrä et al. (2013a,b).

I further extended the workflow and modified the design to accommodate validation routines for ML techniques. I generated the figures, tables and drafted the manuscript. Wolfram Rühaak supervised the work by periodic technical discussions and one-to-one presentation. He thereafter participated in revising the manuscript by offering comments and correction. Hauke Anbergen was responsible for the XCT data exchange for project administration at APS Antriebs-, Prüf- und Steuertechnik GmbH. Alen Kabdenov performed preliminary XCT

measurements of the synthetic sample and assisted in the reconstruction sinograms for the synthetic sample data. Markus Freise and Thorrsten Wille were, responsible for the desig of the XCT instrument. Ingo Sass administered the project and the research at Technische Universität Darmstadt. All co-authors contributed towards the revision and proof reading of the manuscript.

Chapter IV: In this study a graphical user interface (GUI) name CobWeb a standalone execuatble application is developed and its functionalities are tested using gas hydrate synchrotron data set. The CobWeb is based on the ML framework and is well suited for geometrical and representative elementary volume analysis. The user manual to operate CobWeb and analyse XCT data is described in Appendix B. The user interface (UI) is simple yet robust is capable of analyzing and visualizing the data in 2D and 3D. They are several algorithms for noise filtering, smoothing artifact such as edge enhancement, ring effect, specks and noise. The current version of CobWeb is capable to read and process (reconstructed) XCT files in tiff and raw format. Tools to zoom in, zoom out, cropping, color and scale, assist in the visualization and interpretation of XCT 2D and 3D stack data. The data can be exported into different file formats such as Microsoft® Excel (xlsx), MATLAB® (mat), ParaView (vkt) and DSI studio (fib). The current version is supported for Micosoft® Windows and runs stable on Windows® 7 to Windows® 10.

The acquisition of the gas hydrate synchrotron-data was funded by the German Science Foundation (DFG grant Ke 508/20 and Ku 920/18). The gas hydrate experiment was designed conducted by the groups Prof. Dr. Wener Kuhs and Prof. Dr. Michael Kersten at Paul Scherrer Institut synchrotron facility in Switzerland. Sell, K., et al (2016) describes the experimental setup and suggest a workflow for accurate data pre and post processing of the gas hydrate data and its effects on the numerical simulation. Extensive surveyed on noise filtering and different filter combination are suggested to eliminate the edge enhancement effect. Aware of these challenges, we tested the CobWeb capability to filter noise and segment gas, quartz, hydrate in to disjoint phases and geometrical parameters of selected REV.

I designed CobWeb UI and configured the callbacks and its functionality. This was an iterative process which involved extensive survey of different UI and several project meeting/brainstorm discussion with Wolfram Rühaak, Ingo Sass and the user requirement from Antriebs-, Prüf- und Steuertechnik GmbH. The UI and the corresponding callback was created using MATLAB© workbench. Kathleen Sell provided the gas hydrate data and participated in weekly discussion. Freider Enzmann participated in the gas hydrate experiment and (TOMCAT beamline) synchrotron measurements at Paul Scherrer Institut Switzerland. Micheal Kersten and Ingo Sass supervised the research work. All co-authors contributed towards the revision and proof reading of the manuscript.

Furthermore, the research was presented on workshop and conferences in oral and poster sessions, and few among them were published in conference proceeding. All these are listed below in chronological order.

Chauhan, S.**,** Rühaak, W., Anbergen, H., Kabdenov, A., Freise, M., Wille, T., Sass, I. (2016): A new software collection for 3D processing of X-ray CT images. In Proceedings 1st International Conference on Energy Geotechnics ICEGT 2016 CRC Press/Balkema, P.O. Box 11320, 2301 EH Leiden, The Netherlands.

Chauhan S., Rühaak, W., and Sass, Ingo. (2016): X-ray Computer Tomography Data Processing─ An Important Step Towards the Qualitative Assessment of Porous Media. 25. at

Tagung der Fachsektion Hydrogeologie in der DGGV 2016. Karlsruhe Institut für Technologie (KIT), Germany, 14 April 2016.

Chauhan, S., Rühaak, W., Enzmann, F., Khan, F., Mielke, P., Kersten, M., Sass, I. (2015): Processing of Rock Core Microtomography Images: Using Seven Different Machine Learning Algorithms, at 4th Geo-CT Imaging Workshop. Johannes Gutenberg Universität Mainz (JGU), Germany, 15 November 2015.

Chauhan, S., Khan, F., Rühaak, W., Enzmann, F., Mielke, P., Kersten, M., Sass, I. (2014): High Resolution X-ray Tomography of Rock properties and Pore-Network Modeling using Artificial Neural Networks, at 2nd European Geothermal Workshop. Institute for Applied Geosciences, Technical Universität Darmstadt, Darmstadt, Germany, 28 April 2014

Chauhan, S., Rühaak, W., Enzmann, F., Khan, F., Mielke, P., Kersten, M., Sass, I. (2014): Comparison of Micro X-ray Computer Tomography Image Segmentation Methods: Artificial Neural Networks Versus Least Square Support Vector Machine. In: Mathematics of Planet Earth, Lecture Notes in Earth System Sciences, Proceedings of the 15th Annual Conference of the International Association for Mathematical Geosciences. ©Springer-Verlag Berlin Heidelberg 2014. ISSN 2193-8571, ISBN 978-3-642-32407-9, DOI 10.1007/978-3-642-32408-6_34.

Scientific publication and contribution beside the research related to my dissertation.

Parashar, K., Shyam Prasad, M., Chauhan, S.S.S. (2010): Investigations on large scale of cosmic dust from central Indian Ocean. Earth, Moon and Planets 2010, 107:197-217. DOI: 10.1007/s11038-010-9362-3.

Chauhan, S., Höpfner, M., Stiller, G.P., von Clarmann, T., Funke, B., Glatthor, N., Grabowiski, U., Linden, A., Kelmann, S., Milz, M., Steck, T., Fischer, H., Froidevaux, L., Lambert, A., Santee, M.L., Schwartz, M., Read, W.G., Livesey, N.J (2009): MIPAS reduced spectral resolution UTLS-1 mode measurements of temperature, O3, HNO3, N2O, H2O and relative humidity over ice: retrievals and comparison to MLS. Atmos. Meas. Tech., 2, 337-353, https://doi.org/10.5194/amt-2-337-2009, 2009.

Prasad, A, K., Singh S., Chauhan, S.S., Srivastava, M, K, Singh R.P., Singh, R. (2007): Aerosol radiative forcing over the Indo-Gangetic plains during major dust storms. Atmospheric Environment 41, 2007, 6289-6301, doi:10.1016/j.atmosenv.2007.03.060.

Singh, R.P., Prasad, R.K., Chauhan, S.S., and Singh,S.: Impact of growing urbanization and air pollution on the regional climate over India, International Association for Urban Climate Newsletter, Issue No. 14, December 2005, pp. 5-10.

List of Figures

Figure 1. 1: A scheme of the electromagnetic spectrum with indication of wavelengths, frequencies and energie. Courtesy ESA/AEOS media lab, take with permission. 1

Figure 1. 2: Typical tomography setup at a Synchrotron beam-line (a) and for a microCT system with fan beam (b) and cone-beam configurations (c); taken from (Wildenschild and Sheppard 2013) with permission. 3

Figure 1. 3: A schematic description shows the different phases and the order in which the research objectives where accomplished. 10

Figure 2. 1 Schematic illustration of our proposed method 16

Figure 2. 2 (a) Andesite rock sample (b) raw intensity data in the sinograms converted into a 16-bit greyscale image, in which the values range from 0 to 62738, (c) histogram plot of raw image. Distinction between minerals is based on XRD and thin-section analysis ... 17

Figure 2. 3 Top panel shows 2D segmentation obtained using k-means, FCM, and SOM. Bottom panel shows 3D volume rendered plot for k-means 23

Figure 2. 4 Top panel shows 2D segmentation obtained using FFANN, LS-SVM, Bragging tree, Bottom panel shows RUSboost and 3D volume rendered plot for LS-SVM..... 24

Figure 2. 5 Relative difference plot showing the agreement of K-means, FFNN, LS-SVM, and bragging to retrieve fine-grained mineral, mineral, and pore phases 25

Figure 2. 6 Geometrical pore size distribution of an Andesite rock sample obtained from (a) unsupervised clustering and (b) supervised clustering techniques 26

Figure 3. 1 The top panel shows the Andesite and Rotliegend sandstone rocks used for XCT measurements. Middle panel shows the raw images of Andesite (16bit), Rotliegend sandstone (16 bit), synthetic sample (16 bit) and Berea sandstone (16 bit). Mineral composition of Andesite and Rotliegend sandstone was determined from thin sections using polarized microscope. Bottom panel shows, histogram plot of the respective samples. Mineral composition of Berea sandstone is based on Madonna et al. (2012) and Andrä et al. (2013) 33

Figure 3. 2 . Relative porosity values obtained using unsupervised, supervised and ensemble classifier techniques for respective samples 34

Figure 3. 3 Total volume fraction plotted for respective samples 37

Figure 3. 4 The top, middle and last panel show the 2D segmented images and volume rendered plots of respective samples using unsupervised networks (Andesite figure has been modified after Chauhan et al 2016) 40

Figure 3. 5 The pore size distribution of different rock samples using watershed technique. 41

Figure 3. 6 Entropy values of unsupervised techniques plotted for respective samples 43

Figure 3. 7 Mean square root error values of feed forward artificial neural network (FFANN) obtained for respective samples. FFANN was trained using segmented datasets of k-means, Fuzzy C-means with a membership function of 1.10 and 1.85..... 43Figure 3. 8

Receiver operational characteristic curves depicting the accuracy of least square support vector machine multi classification scheme for class four. Few curves which appear in the legend have close proximity to the x-axis and lie behind other curves therefore are invisible 45

Figure 3. 9 Accuracy of ensemble classifiers Boosting and Bragging calculated using 10 K-fold validation for respective samples 46

Figure 3. 10 Mean porosity value obtained using supervised, ensemble classifiers and unsupervised machine learning techniques 50

Figure 4. 1 Market survey of the currently available commercial software (a) and open source software (b) assisting in digital rock physics analysis with features as indicated in legend 53

Figure 4. 2 Snapshots of the CobWeb GUI. XCT stack of Grosmont Carbonate rock is shown as an example for representative elementary volume analysis. The top panel displays the XCT raw sample, the K-means segmented ROI, and the porosity of single slice No. 10. The bottom plot shows pore size distribution of the complete REV stack, the relative porosity and volume fraction, respectively 54

Figure 4. 3. The general workflow of the CobWeb software tool, where the arrow denotes the series in which different modules are compiled and executed. A separate file script is used to generate .dll binaries and executables 56

Figure 4. 4 The most suitable REV's of Berea Sandstone and Grosmont Carbonate rock shown in panel and Gas Hydrate-bearing sediment datasets shown in the panel b59

Figure 4. 5 2D filtered, rescaled, and segmented slices of gas hydrate REV1 dataset .. 63

Figure 4. 6. Schematic representation of the relationship between porosity (φ) and volume (V) of porous media. Bachmat and Bear (1986). 64

Figure 4. 7 Top panel shows surface plot of REVs Berea sandstone and Grosmont carbonate (size 471 x 478 x 480) using visualisation software ParaView. Middle plot shows the relative porosity (%) trend for Berea sandstone and Grosmont carbonate REVs samples. Bottom plot shows the pore size distribution of Berea sandstone and Grosmont carbonate. XCT images were segmented using K-means. In the case of Grosmont, a non-local means filter was used. 65

Figure 4. 8 The top panel shows relative porosity trend analysis of gas hydrates, the middle and bottom panel show the geometrical pore size distribution of the respective REVs. The analysis was performed using CobWeb 1.0 66

Figure 4. 9 Segmented REVs of gas hydrate sample displayed as surface and volume rendered plots. as analyzed using CobWeb 1.0 and exported to VTK format using CobWeb 1.0 ParaView plug-in. Quartz grain phase is represented in green color, gas hydrate in red, and in blue the liquid brine phase. 69

List of Tables

Table 2. 1 Number of pixels in training and test data from X-ray computer tomography used in this study 22

Table 2. 2 Porosity obtained from seven machine learning algorithms 26

Table 2. 3 Computational[b] time for processing ten slices 27

Table 2. 4 Pore size diameter obtained for six machine learning algorithms 27

Table 3. 1 The number of pixels used for training and testing the classification model 38

Table 3. 2 Show the computational time for processing ten slices 48

Nomenclature

Acronyms/Abbreviations

3D Three-dimensional

AD Anisotropic diffusion

ANN Artificial neural networks

BHC Beam hardening corrections

CE Coefficient of efficiency

CT Computer tomography

CCD charged-coupled device

DRP Digital rock physics

exe executable

EH Edge enhancement

EDH Edge enhancement high

EDL Edge enhancement low

FV Feature vector

FANN Feed forward neural network

FCM Fuzzy C-means

GH Gas hydrate

GUI graphical user interface

KeV Kilo electron volt

LSSVM, LS-SVM Least square support vector machine

LBM Lattice Boltzmann

ML Machine learning

MLA Machine learning algorithm

MSE Mean square root

MSRE Mean square relative error

mD mili Darcy

ms mili second

NLM non local means

PNM pore network modelling

PSD Pore size distribution

RAW raw image files

REV Representative elementary volume

RUSboost Boosting, ensemble classifier

ROC Receiver operational characteristics

ROI Region of interest

SOM Self-organized maps

TIFF Tagged imaged file format

XCT X-ray computer tomography

Greek Symbols

μ micro

Roman and Mathematical Symbols

C_j Centroid center

J Objective function

J_{fcm} FCM objective function

K Cluster

m Fuzziness parameter

$m.u_{ij}$ Membership function

n_j Number of items

$P(i,j)$ Probability

$P(F_p)$ Probability of false positive

$P(T_p)$ Probability of true positive

$U = u_{ij}$ Membership criterion

$\cap$ Intersection

|| || Modulus

1. Introduction

1.1. Principle of X-ray and Micro Computer Tomography

1.1.1. X-rays

Röntgenstrahlung, commonly known as *X-ray* was discovered by a German Physicist Wilhelm Conrad Rötgen in 1895. X-rays (soft and hard) are ionized radiation with a wavelength between of 1 to 0.01 nm and energy span 10^{-3} to 10^{-5} eV. They appear between ultraviolet and gamma-ray within the electromagnetic spectrum as shown in Figure 1. 1

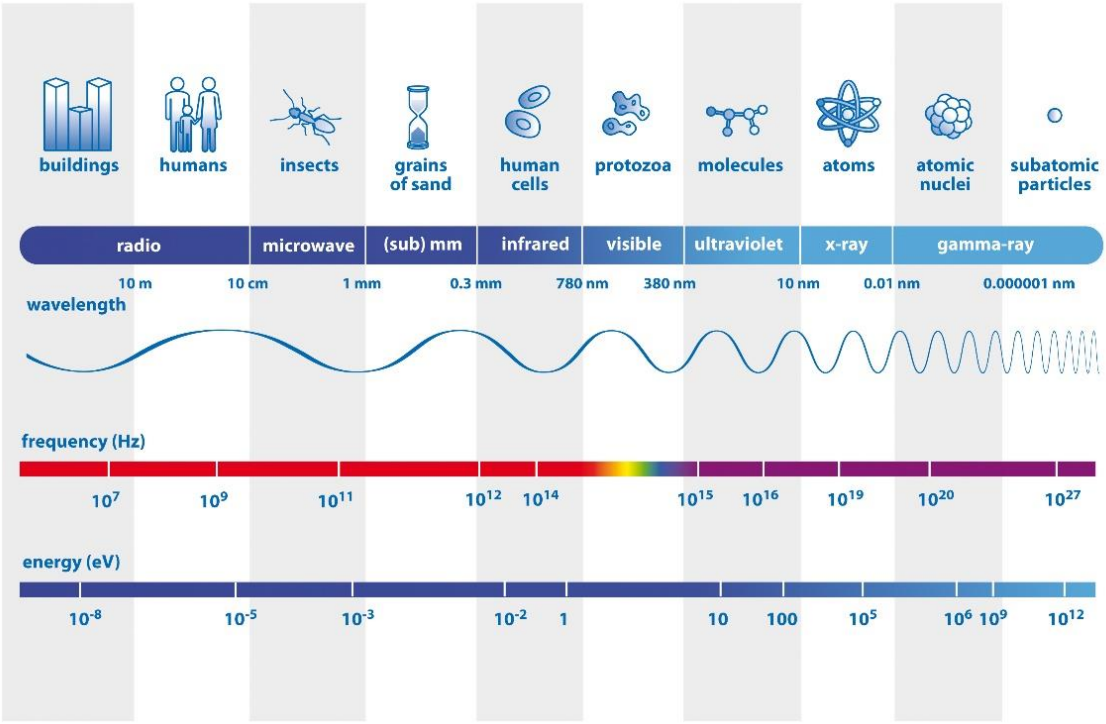

Figure 1. 1: A scheme of the electromagnetic spectrum with indication of wavelengths, frequencies and energie. Courtesy ESA/AEOS media lab, take with permission.

Due to its high energy and small wavelength, X-rays can penetrate materials with different densities. This can be mathematically formulated using Beer-Lambert law.

$$I = I_o e^{-\int \mu(s)\, ds} \qquad (1.1)$$

The Beer' Law in its simplest form, relates, differential changes in light transmission to the differential changes in material absorption. Where,

I is the monochromatic X-ray radiation passing through the material

Io is the incident beam intensity

$\mu(s)$ is the local linear attenuation coefficient along the ray path s

Where, the linear attenuation coefficient is governed by photoelectric effect, Compton scattering, Rayleigh scattering and pair production (Attix 2007). Since, the discovery of X-rays and it characteristics, it is extensively used in wide range of applications in

medical sciences and security systemsIn the year 1970 a new technique was developed know as *computerized transverse axial tomography* (abbreviated as CAT or CT) to overcome loss of information in the z-direction (depth) (Hounsfield 1973; Ambrose 1973; Ommaya et al. 1976). By fixing the sample on a on a platform which is rotated along the spherical axis 2D projecting of the samples optical density are obtained at different angles. These 2D projections, also known as sinogram are stack together to obtain 3D volume of the sample. These 2D/3D projection are converted from spherical coordinates in to cartesian coordinated of different grayscale intensity for visualization of the materials internal structures. This process is known as reconstruction or back-projection and the most commonly used scheme to transform the coordinate is the radon transformation (Cebeiro et al. 2016).

1.1.2. Micro Computer Tomography

In this section, three different kinds of X-ray techniques, namely synchrotron, fan and cone beam setups are briefly discussed and their advantages and artifacts are highlighted. For a comprehensive description and further references, the readers are referred to (Wildenschild and Sheppard 2013) and (Cnudde and Boone 2013). Hereafter, we use the convention XCT to represent micro computer tomography.

In a synchrotron setup shown in Figure 1. 2, a synchrotron source generates an almost parallel polychromatic (white) X-ray beam through bending magnet, wiggler or undulator. After propagating through a long distance, the white X-ray beam is passed through a monocromator to segregate energies of certain bandwidth with quasi-monochromatic wavelength (or pink beam). The quasi-parallel pink beam is attenuated by the object and thereafter, passes through a scintillator screen and is converted in to visible light. Subsequently, different optics are used to magnify this visible light containing object optical properties on to a visible light detector. A trade-off exist between choosing a thin scintillator screen to achieve high resolution by reducing detector efficiency or thick scintillator screen to obtain low resolution and increase detector efficiency (Marone et al. 2009). Phytography in recent years has enable to gain resolution up to 10 nm in the area of X-ray microscopy (Dierolf et al. 2010).

Due to high cost and long waiting list from beam time, lab XCT setup provide an lucrative alternative but at a cost of high acquisition time (7 -24h). The most common lab setup is the cone-beam micro-XCT setup (Feldkamp et al. 1984), shown in Figure. In this setup, the object under investigation is placed and rotated between a divergent pyramidal or cone shape X-ray beam source and a (charged-couple device CCD) detector. The field-of-view (FOV) of the X-ray energy source governs the spatial resolution. The transmission X-ray tube, provides a smaller FOV resulting in a small focal point and, thereby a high spatial resolution up to 1 µm. contrarily, a reflection X-ray tubes provides a larger FOV, resulting in a lower spatial resolution reducing acquisition time. The fan beam XCT setup shown in Figure, is almost similar to cone beam set up, except that, a slit collimator is used to split the beam into fan shaped. The detector optics are same as cone beam setup, difference being, geometrical magnification created by cone beam setup allow large area detectors and hence are preferred for lab setups.

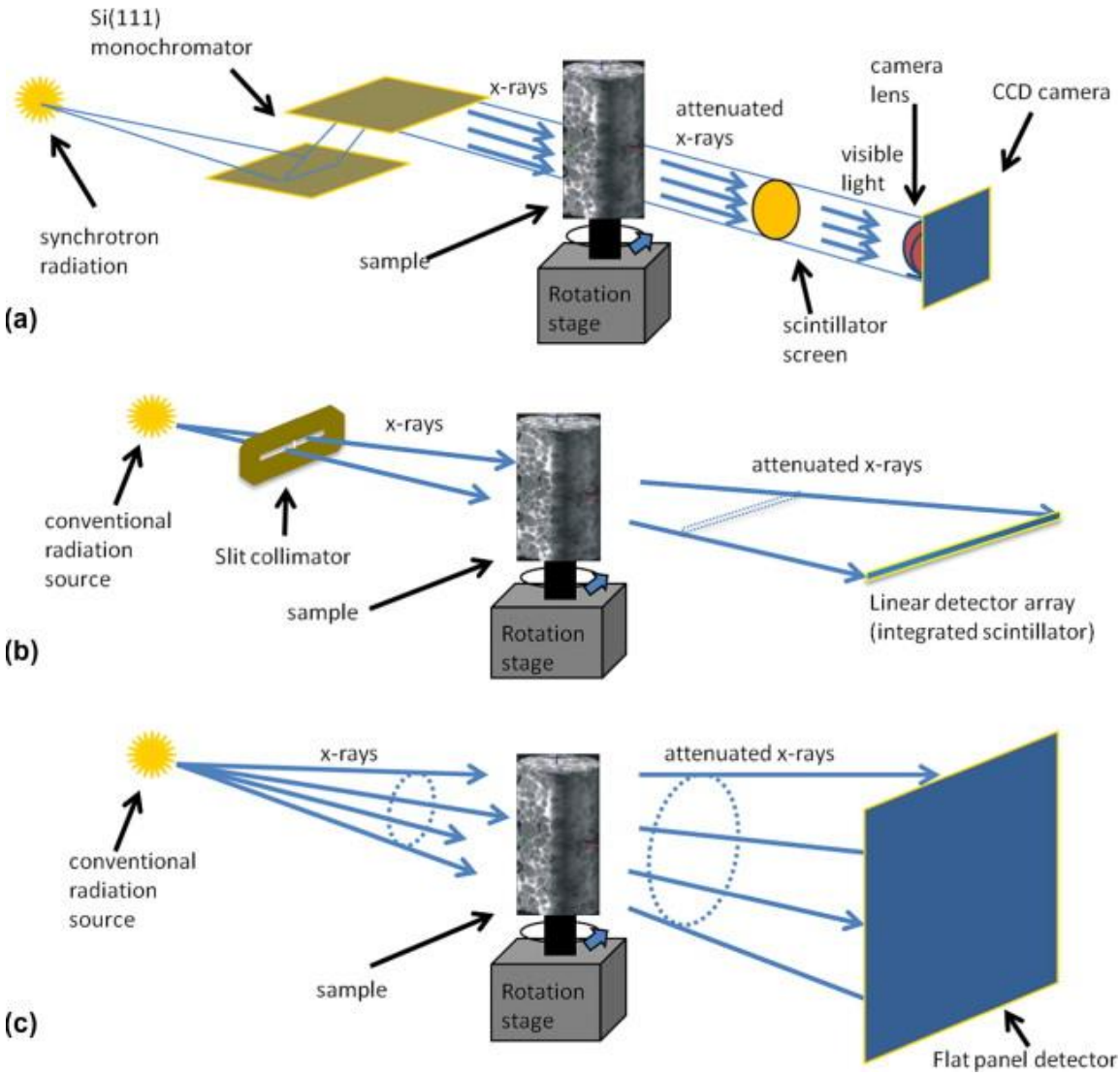

Figure 1. 2: Typical tomography setup at a Synchrotron beam-line (a) and for a micro CT system with fan beam (b) and cone-beam configurations (c); taken from (Wildenschild and Sheppard 2013) with permission.

1.2. Image Artefacts

1.2.1. Beam Hardening and Scattering

The artifacts seen in XCT images are in general caused by imaging physics or the reconstruction mathematics. One of the major artifacts is the beam hardening and scatter artefact. This artefact occurs in lab based XCT setup. As, the lab based X-ray source (transmission or reflection X-ray tube), are unable to produce high energy X-rays particles in comparison to synchrotron radiation. The beam hardening artifacts appear as dark streaks between two highly attenuation materials (metals, minerals) or dark streaks along the edges of a single highly attenuation material. The reason is that, when the polychromatic X-ray beam, strikes a material with high atomic number (ex. Metal or Mineral), the low energy photons (soft X-rays) get absorbed faster compared to the high energy photons (hard X-rays), due to their relative differences in speed. Therefore, the detector detects a beam with very high and low

intensities at the same time. The high intensity beam (hard X-rays) is projected as a scatter and the low intensity beam (soft X-rays) is captured as dark streaks around the scattered

radiation. The beam hardening artifact can be overcome by using special filters to remove soft X-ray, or increase the KeV of the X-ray beam or use dual energy dual energy XCT (Brooks and Chiro 1976; Christ 1984; van de Casteele et al. 2002).

1.2.2. Edge Enhancement

Another major artefact is the Edge Enhancement artifact caused due to high phase contrast. It commonly, seen between materials with completely different attenuation coefficients. For example between organics matter and water, or methane hydrate, quartz crystals and gas film. It appears in the form of bright enhanced edges around the crystals and subsequently followed by a very dark shadow. This contrast is known as phase contrast, it is excellent for visualization but is a nuisance of image segmentation. The edge enhancement artifact is more pronounce in synchrotron XCT imaging compared to lab based XCT setup. The reason is that, the radiation scattered by the sample interferes with the coherent incident monochromatic X-ray beam (pink light). This interference cause a shift in the phase (direction) of the pink beam, producing Fresnel diffraction pattern of high and low crest, which is recorded on a high resolution detector located at a certain distance. This high a low crest (intensity) of the wave front (travelling pink beam) generate a high phase contrast (Snigirev et al. 1995; Nugent 2010). Thus, this phase contrast is also known as Edge Enhancement effect. The phase contract can be minimized by bring the detector closer to the sample or installing elements such as Beryllium windows in the beam path.

1.2.3. Ring Effect

The ring artefact can be recognized as a circular bright and dark ring appearing at the center and expanding till the edges in a 2D image. This is usually caused by defective or saturation of the detector. Usually, recalibration or sometimes replacement of the detector removes this artifact (Sijbers and Postnov 2004).

1.2.4. Noise

Instrumental noise or Poisson noise is caused due to low photon count observed by the detector. Usually appear as streaks for bright and dark scatter around high attenuating objects. Can be removed my combining multiple scans or using iterative approaches during image reconstruction process (Ketcham and Carlson 2001) .

1.2.5. Partial Volume Effect

The partial volume effect is inherent to XCT measurement. As, the rotation of the sample is perpendicular to the detector, the attenuated X-ray protons received by the detector, is, the integrated (averaged) attenuated value of different materials–in-the line-of-sight of the X-ray source. This caused a diffused photon intensity captured by the XCT detector. Resulting in voxel (pixel) values below the detectors resolution (Ketcham and Carlson 2001; Wildenschild and Sheppard 2013; Cnudde and Boone 2013). The partial volume effect help in effective visualization due to grayscale intensity variation but actually is an artifact of the XCT measurement. Due to this effect, the XCT images of densely packed

geomaterials (Rötliegend Sandstone) result in very low grayscale intensities, which overlap with the neighboring pixels. Thus making segmentation a very subjective and clumsy process.

For geomaterials like Rotliegend sandstone which are heterogonous, compact and have very low porosity, thus very low grayscale intensities overlapping each other.

1.3. State of the Art

Each of the following chapter has a dedicated review on Machine Learning (ML), its respective validation techniques and the toolbox currently available. Therefore, the state-of-the-art with respect to ML hasn't been highlighted in this section. To know more about the development in the area of XCT instrumentation, synchrotron and their respective hardware aspects the readers are pointed out to (Ketcham and Carlson 2001; Wildenschild and Sheppard 2013; Cnudde and Boone 2013). (Schlüter et al. 2014), highlights the current and future trends, in the area XCT analysis and pre and post processing.

This section covers the application of XCT in geosciences and their latest trends. Due to the tremendous success of CT in medical sciences and consecutive improvements in the image quality, imaging speed and deposition radiation dose, a new research field immerged in 1980's known as micro computer tomography (Sato et al. 1981; Elliott J. C. and Dover S. D. 1982). Due to its non-destructive capability XCT soon became a potent measurement technique in the geoscience community for visualizing surface as well as internal structures of geological core samples, small scale stress-strain variation on grain size, density, and grain contact angle. Bedding features, sedimentary structures, natural and induced fractures in different types of rock core samples among others.

The basic difference between medical CT and XCT is the rotational movement. In the medical CT the patient remains stationary with respect to X-ray source and detector, whereas, in XCT the sample is rotated and the X-ray source and detector remain stationary. Additionally, the spatial resolution in medical CT reach a maximum of 40 µm whereas, for XCT the spatial resolution can be resolved up to 1-2 µm based on the radiation source and sample size.

1.3.1. Reactive Transport

In past ten years tracing and modelling reactive transport has become a popular playground for CO_2 sequestration and Injection studies among others (Luquot and Gouze 2009; Noiriel et al. 2009; Flukiger and Bernard 2009; Gouze and Luquot 2011). Porosity and Permeability (Poro-Perm) relationship give a good indication of tracing and modelling reactive transport in porous materials. Depending on the type of rock or geomaterial–reactive transport experiments usually cause morphology structural changes in the materials. Generally, dissolution are prevalent in large pores, precipitation in small pores and clogging is caused in pore throats. This generally influences the flow dynamics, which till date cannot be accurately predicted by the classical Kozeny-Carman models. Thereby, demanding a need for more sophisticated models to predict transport flow due to precipitation or dissolution (Wildenschild and Sheppard 2013).

Due, to the sensitivity for reaction transport processed, synchrotron imaging is best suited apparatus for imaging such reactive phenomena's. Thereby, making segmentation and REV analysis even so important, for continuum based (lattice Boltzmann) or topology based (Pore Network Modelling) simulations and prognosis. Thus, the research work conducted in this

thesis with be the cornerstone towards the digital rock physics analysis of reactive transport processes.

1.3.2. Combining Experiment and Imaging

To understand flow and transport processes in deeper subsurface systems such as methane hydrate extraction, oil recovery, geothermal energy extracting and geological sequestration and storage of CO_2; high pressure and elevated temperature (PT) experiments under controlled conditions become extremely desirable (Wildenschild and Sheppard 2013). Modern day XCT manufactures have developed mechanical loading stages which can assemble and disassemble, high PT Hassler cells in combination with acoustic emission and electric sensors which can further be combined with Triaxal experiments. Such an assemblage is sure to avoid disturbance cause due to transport of the sample and simplify image registration issues (Culligan et al. 2004; Porter and Wildenschild 2010). But, a tradeoff exist between the complexity of the (Triaxial) experiments and the stability and equilibrium required to avoid artefact and blur during imaging.

By performing hydraulic fracture simulations under reservoir stresses and observing mechanical failure to rock strength before and after in XCT imaging. Fracture propagation as a function of heterogeneity and roughness of the sample can be determined (Renard et al. 2009).

1.3.3. Multiscale Imaging

In past five years, pore network modelling is undergoing a revival in the form of new open source software packages like OpenPNM (Gostick et al. 2016) and update to the classical maximum ball algorithms (Arand and Hesser 2017). PNM modelling is a topology based approach for predicting transport and flow properties commonly used in rock science and material science communities; which depends extensively on the morphological features. The biggest drawback of PNM is its inaccuracy to quantify 2 phase flow during imbibition processes (Vogel et al. 2005). LBM, on the other hand has become a very popular alternative (Shan and Chen 1993; Gunstensen et al. 1991; Tölke et al. 2002; Khan et al. 2012). Its (LBM) drawback apart from being computational demanding and limited in scale, it is less effective at very low capillary numbers (Wildenschild and Sheppard 2013). Beyond, the technical limitation of the respective approaches to simplify the morphological features; it is the sparseness (information loss) of the XCT data in itself which self-limits the prognosis of these models. As exist a tradeoff between sample size and XCT resolution (partial volume effect).

By experimenting along wide range of resolution, plug to porescale (medical CT to XCT), porescale to submicron scale (XCT to FBSEM) and developing computational tools to integrate the information in a systematic fashion, can help in quantifying the layering/diageneses, morphology and 3D grain structures in the rock samples. Specifically, modelling studies relate to shale and carbonate rocks, which have multi modal pore scale structure (10 cm – 10 nm) (Sok et al. 2010; Gerke et al. 2015).

1.4. A Brief Introduction of Machine Learning in Geosciences

1.4.1. Application of Machine Learning in Geothermal Energy

In general in Europe and in particular in Germany there is keen emphasis to increase the use of renewable energy (Bleicher and Gross 2015; Tissen et al. 2019). One of the affordable solution is the installation of ground source heating pumps (Breede et al. 2013). While for many such pumps the heat conduction is primary from shallow depth (upper 10 meters) of the Earth (Ingo Sass and Dirk Brehm 2016). Other pumps require deep vertical boreholes to draw their heat from the geothermal resource (Schintgen 2015). In principle, these ground connected pumps can be installed everywhere although subjected to regulation and heat can be extracted from the ground (Ingo Sass and Dirk Brehm 2016). Meanwhile, they are of commonly used in heating single household. But, a real impact on a community, state or country scale can only be achieved, with a large-scale deployment. For this a detailed analysis of the thermal properties of the surface layers all over the country has to be done (Schintgen 2015). This is a challenging task as different factors affect the thermal behavior of the ground surface.

The traditional way of conducting such studies using geographical information system (GIS) and map parameters such as thermal conductivity, thermal diffusivity and temperature. Aretz et al. (2016) and Hintze et al. (2018) demonstrated in one such study the hydrothermal potential of the north Upper Rhine Graben, such studies cover when extrapolated over a regional scale can lead to large standard deviation in the geothermal potential values due to the scarcity and sparsity of the data. Machine Learning can assist in such situations where the sparicity of the data can be modelled and predicted using machine learning techniques (Kalogirou et al. 2012).

1.4.2. Application of Machine Learning Reservoir Modelling

Reservoir modelling in a broader sense includes, assimilating geological information and modelling marco- and micro-scales fluid transport regime and developing reliable reservoir simulators. This requires understanding individual reservoir properties such as lithogy, porosity, permeability, mechanical properties like stresses and combining geochemical, petrological and geomechanical information to provide robust models and thereby reliable prognoses (Esmaili and Mohaghegh 2016). Which is not an easy task— left alone the geochemical modelling the complexities related to flow mechanism in natural fractured rocks and its interaction with rock matrix vary drastically for different reservoir types. And, thereafter, the physics of these interaction is simplified to bring down the time consumption of the models (Lee and Sidle 2010).

Mohaghegh and his colleagues develop a new approach where instead of modelling the physics of flow mechanism based on understanding on fracture length, width, height, conductivity etc; advanced data analytics and artificial intelligence-based framework is used to extract information from dataset like production history, geomechanical and geochemical properties to guide the reservoir model (Mohaghegh 2000a, 2000b, 2000c; Mohaghegh 2011; Mohaghegh 2013; Esmaili and Mohaghegh 2016).

1.4.3. Application of Machine Learning in Phase Segmentation

The fundamental understanding of petrophysics, micromechanics and chemical characteristics of different reservoir rock types is crucial to calibrate numerical models for reliable prognosis. This fundamental understanding can be gained through first by visualizing the internal structure and thereafter observing their Interaction. X-ray computer Tomography (XCT) imaging helps us to capture the different phases in the rocks internal structure. Therefore by segmentation, the different rock phase like pore and matrix and extracting the pore space and their pore network, porosity and permeability can be calculated. Which for example can give us an insight about the transport property of the rocks. This segregation of different phases is called phase segmentation.

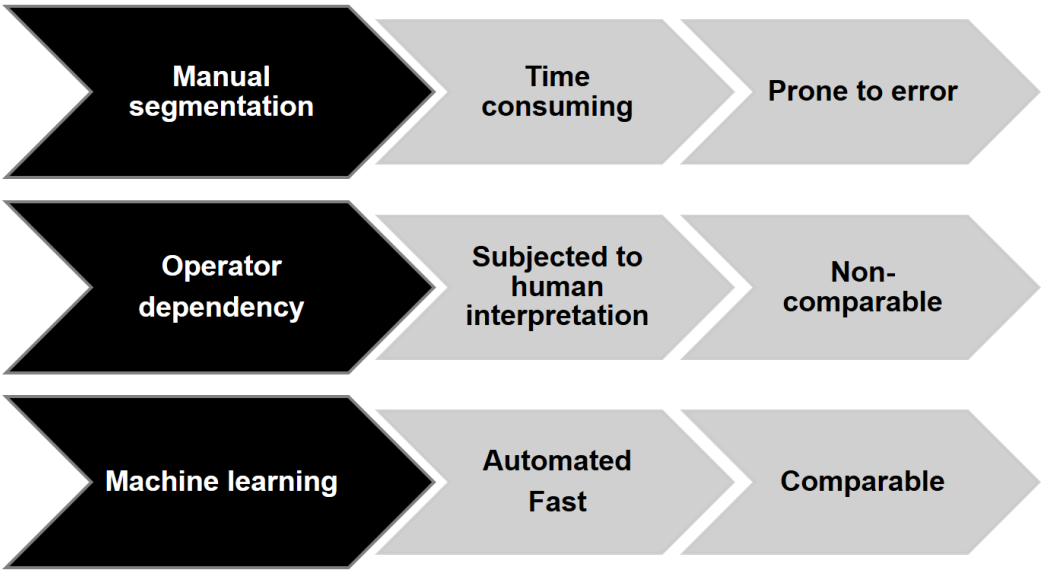

Figure 1. 3: The advantage of machine learning segmentation in comparison to manual segmentation

Phase Segmentation is conventionally done in a manual approach (Buades et al. 2005) .That is, absorbing different images, in a X-ray CT data set, identify different phase and separate them based on their grayscale image intensities (Buades et al. 2005). This is commonly called as histogram approach. The manual segmentation despite it time consumption can be the most accurate segmentation— as it has the gold standard, based on human cognitive capabilities (Amigó et al. 2009; Meilă 2003; Strehl 2002). But this, human or operator dependency can be subjective and therefore is non comparable

The machine learning approach automates the segmentation, making it significantly faster and facilitates inter-comparability and tractability of the results Figure 1. 3

1.5. Research Objectives

The main objective of this study is to provide an autonomous scheme to improve grayscale segmentation of the digital rock images (Iassonov et al. 2009), (Wildenschild and Sheppard 2013), (Schlüter et al. 2014). Therefore, machine learning techniques where investigated to address the well know phase segmentation problem in the digital rock analysis. ML techniques suited the best due to its capability to learn, adapt and classify the datasets of high variances.

This fundamental characteristics of the ML technique simulated the idea to implement it for the autonomous grayscale segmentation of the digital rocks.

The study is dedicated to REV analysis of heterogenous geomaterials, obtained by using high resolution X-ray tomography and synchrotron experiments. Despite the high resolution offered by these experimental techniques, based on composition of the geomaterials (e.g. gas hydrate-sediment), the reconstructed datasets gets infested with artefact such as edge enhancement effect (ED) among others. If ignored or not optimally filtered and segmented, these artefacts cause large scale anomalies in the continuum or topology based digital rock physics models. Manually segmenting and filtering these artifacts is a very cumbersome process. Therefore, three major categories of ML schemes, supervised, unsupervised and ensemble classifiers where explored in combination with image filters to reduce artifact without information loss (morphological features) of the geomaterials. Finally, the dedicated workflow and ML algorithms is encapsulated in a software named '*CobWeb'* and is presented.

Figure 1. 4 shows schematically the framework in which the researched work was executed.

When using ML techniques for segmentation it is necessary to know which ML approach could be best suited for a given geometrical sample.

As, different ML algorithms used different approaches to segment or classify information, for example, unsupervised algorithms classify information into distinct disjoint categories of similar density. Supervised algorithms use training model to familiarize (train) themselves with a small subset of data volume (training dataset) provided as apiori information; commonly, different types of probability functions are used to regularize the models with the apiori information in an iterative process. Thereafter, rest of the information is classified into different segments. Ensemble classifiers also rely on the aprior information but use several training model unlike supervised technique to speed up the training process.

Also, relying just on one ML technique may cause discrepancies between retrieved geometrical parameters (porosity, pore size distribution and volume fraction of respective phases) and lab measurements. Therefore, a framework is presented in chapter 2, which in detail survey different ML schemes and a workflow to perform accurate phase segmentation to address following objectives:

- Inter-comparison of geometrical parameters of volcanic Andesite Rock obtained using ML techniques
- Validation to lab measurements
- Inter-comparison of computational performance of these different ML techniques

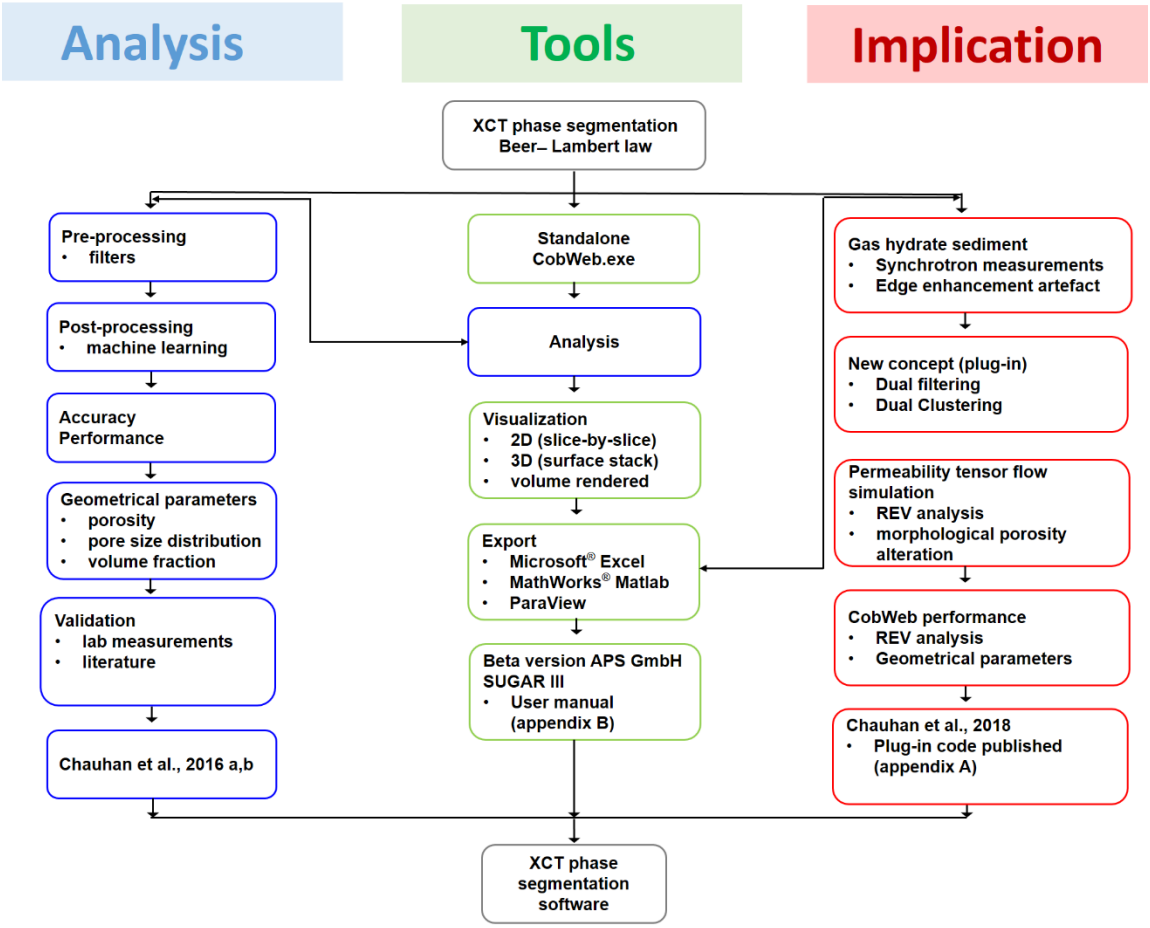

Figure 1. 4: A schematic description shows the different phases and the order in which the research objectives where accomplished.

Accurately segmented REV's are the cornerstone for topology (PNM) or Continuum based (LBM) Simulation. To perform these simulation segmented grayscale images are converted to binary scale images. Therefore, a properly segmented REV stack is necessary to ease the transition process from grayscale to binary scale. Such that, the morphological features such as open pore, closed pores, pore throat connection etc. are retained. Thereby, assisting in simulating transport processes or understanding rock microphysics.

In hindsight, as the human intervention is minimized by the ML techniques–accuracy becomes a key concern. Therefore, the accuracies of these ML algorithms are examined based on metrics such as Entropy, Purity (K-means, FCM SOM), Mean Square Root Error (ANN), Receiver Operational Characteristics (ROC) and 10-fold cross validation (Bragging and Boosting classifiers). The distribution of these metrics value point towards the accuracy of the segmentation classes. Thereby, assisting the user to rely and choose the best segmented category. The chapter 3 highlights these analysis and shows the reliability of the geometrical parameters for synthetic, Sandstone and Volcanic digital rocks images and cross validation with independent lab measurements.

Chapter 4 introduces the Graphical User Interface (GUI) "*CobWeb*". *CobWeb* encapsulated the machine learning algorithms and dedicated workflow described in chapter 2 and chapter 3. It address the following research objectives

- New approach to eliminated edge enhancement artifact in synchrotron based Gas Hydrate dataset
- Architecture and functionality of CobWeb

The last chapter summarizes and discusses the major findings and current limitation of this work and provides an outlook on further improvements planned for *CobWeb* interface.

2. Processing of Rock Core Microtomography Images: Using Seven Different Machine Learning Algorithms

This chapter is based on the manuscript published in an ISI listed Journal Computer and Geosciences. © ELSIVIER Publications

Chauhan, S., Rühaak, W., Khan, F., Enzmann, F., Mielke, Philipp., Kersten, M., and Sass, I. (2016): Processing of rock core microtomography images: Using seven different machine learning algorithms, *In Computers & Geosciences,* Volume 86, 2016, Pages 120-128, ISSN 0098-3004, https://doi.org/10.1016/j.cageo.2015.10.013. © ELSIVIER Publications. Used with permission.

2.1. Abstract

The abilities of machine learning algorithms to process X-ray microtomographic rock images were determined. The study focused on the use of unsupervised, supervised, and ensemble clustering techniques, to segment X-ray computer microtomography rock images and to estimate the pore spaces and pore size diameters in the rocks. The unsupervised k-means technique gave the fastest processing time and the supervised least squares support vector machine technique gave the slowest processing time. Multiphase assemblages of solid phases (minerals and finely grained minerals) and the pore phase were found on visual inspection of the images. In general, the accuracy in terms of porosity values and pore size distribution was found to be strongly affected by the feature vectors selected. Relative porosity average value of 15.92±1.77 % retrieved from all the seven machine learning algorithm is in very good agreement with the experimental results of 17±2%, obtained using gas pycnometer. Of the supervised techniques, the least square support vector machine technique is superior to feed forward artificial neural network because of its ability to identify a generalized pattern. In the ensemble classification techniques boosting technique converged faster compared to bragging technique. The k-means technique outperformed the fuzzy c-means and self-organized maps techniques in terms of accuracy and speed.

2.2. Introduction

Numerous researchers have recently numerically determined petrophysical properties from X-ray microtomographic images. This digital rock physics (DRP) approach using rock images has allowed physical phenomena that cannot yet be measured in the laboratory to be simulated. DRP models can be used to determine realistic distributions of multi-component fluids, such as occur during imbibition and in Haines jump mechanisms (Berg et al. 2013), and to determine effective transport properties, such as the permeability tensor (Khan et al. 2012). These capabilities, coupled with the advanced computational algorithms that are available to interpret images, visualize three-dimensional (3D) images, characterize structures, and determine physical properties from images, have allowed the numerical DRP laboratory approach to be used to study the properties of real heterogeneous geomaterials (Andrä et al. 2013a, 2013b).

Several important processing steps are required to allow a virtual rock-physics laboratory approach to be used. The first step is to perform a computer tomography (CT) scan of the selected rock sample at a high spatial (and eventually also temporal) resolution. Accurate phase segmentation, which can be complicated for a strongly heterogeneous material; eventually to allow an appropriate digital rock model to be built (Fusseis et al. 2014). The segmentation problem is reduced to the need to quantify the binary solid–void phase distribution (i.e., a binarization problem) when modelling fluid transport at the pore scale. However, (Leu et al. 2014) recently performed a sensitivity study in which they showed that even a small bias in the accuracy of the binarization may lead to a significant error in the calculated permeability. Binarization is an essential prerequisite of DRP studies, but there are few accurate and fast binarization algorithms that are not biased by manual (subjective) interventions by the user. Choosing an appropriate scheme to binarize an image is key to characterizing a porous space with a good degree of accuracy and therefore decreasing the magnitudes of the uncertainties involved in determining the geometries of pore networks.

In general, an X-ray CT (XCT) image, or tomogram, consists of a cubic array of reconstructed linear X-ray attenuation coefficient values (also known as pixel values) that have to be quantified by analysing the image. Analysing the image involves four main tasks, namely filtering the image, segmentation, classification, and interpretation or modelling. In segmentation similar pixel values are clustered in to distinct group or classes, using unsupervised learning techniques. Whereas, for classification, using set of predefined features or classes (known as training data) similar pixel values are sorted out from unknown data set (testing data) using supervised learning techniques. These tasks are not independent of each other, but the classification and interpretation tasks determine which of the many available filtering and segmentation routines should be used. The accuracy of the segmentation process clearly determines the reliability of the resulting DRP model. Advanced segmentation routines can be performed when the sinograms are modified (Jovanović et al. 2013) or segmentation can be performed using clustering analysis, which is an unsupervised classification technique, where no manually specified sample regions need to be defined, or discriminant analysis, which is a supervised classification technique (Jain et al. 1999). (Cortina-Januchs et al. 2011) used a novel segmentation and classification technique based on a combination of clustering analysis and an artificial neural network (ANN). Their approach offers advantages when used on large datasets, such as those with high spatial resolutions (e.g., sub-micrometer resolutions). Three different clustering algorithms (k-means, fuzzy c-means (FCM), and self-organized maps (SOM)) were used to segment the pixels in the tomographic images into groups of similar intensities. An ANN classification routine was then used, and this routine was highly modular and flexible and efficiently recognized patterns (e.g., accurately differentiating between solids and voids). Up to 97 % of the pore spaces in the soils that were tested were correctly classified from the images that were acquired.

In this paper we propose a method with some modifications and improvements compared to the ones used by (Cortina-Januchs et al. 2011). The particular improvements made are that the detection (segmentation) of pore space in our method is performed using 3D greyscale intensities, and three discrete machine learning algorithms are now used for the quantitative intercomparison process. It is to be noted that─ all the investigated methods are global, i.e. only gray scale information is processed and neighbourhood information is ignored (e.g. connectivity, regularity or local gradients).

A flowchart of the method is shown in Figure 2. 1. A comparative case study of unsupervised learning classifiers (k-means, FCM, and SOM), supervised learning classifiers (FFANN, least square support vector machines (LS-SVMs)), and ensemble classifiers (boosting and bagging) was performed. In the case of unsupervised classification, initial centroid values, membership function, topology and distance function had to be initially set. Whereas, for the supervised classification, required the user to determine representative areas for each class in order to get a priori knowledge about the class statistics. Our goal was to identify the advanced learning scheme that was best at segmenting the pore space and most accurate at determining the porosity.

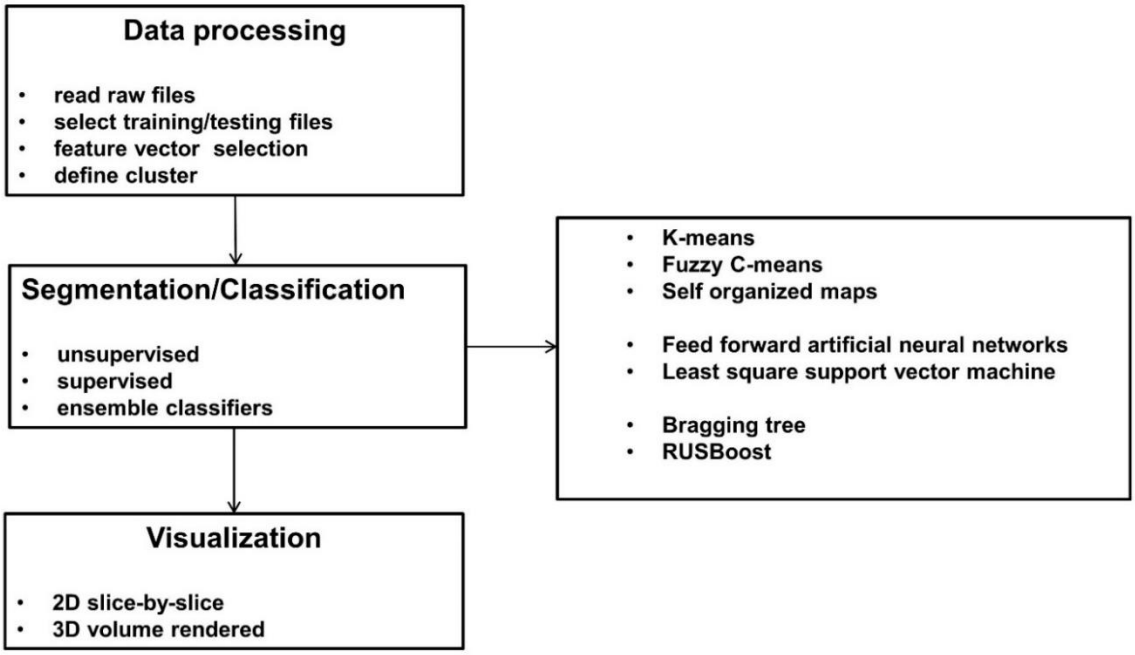

Figure 2. 1 Schematic illustration of our proposed method

2.3. Materials and Methods

2.3.1. Rock Sample

An Andesite rock sample, as shown in Figure 2. 2, was used in the study. The sample was collected from Tongariro National Park, New Zealand. The sample had a porphyritic texture with large plagioclase crystals (up to 3 mm in diameter), pyroxene in a cryptocrystalline matrix, and isolated vesicles up to 6 mm in diameter. X-ray diffraction analysis confirmed that the sample contained 85 % plagioclase and 15 % pyroxene. The sample had an average grain density of 2.75 g cm−3, measured using an AccuPyc II 1340 helium pycnometer (Micromeritics Instrument Corporation, Norcross, GA, USA), and an effective porosity of 17±2 %, measured using a GeoPyc pycnometer (Micromeritics Instrument Corporation).

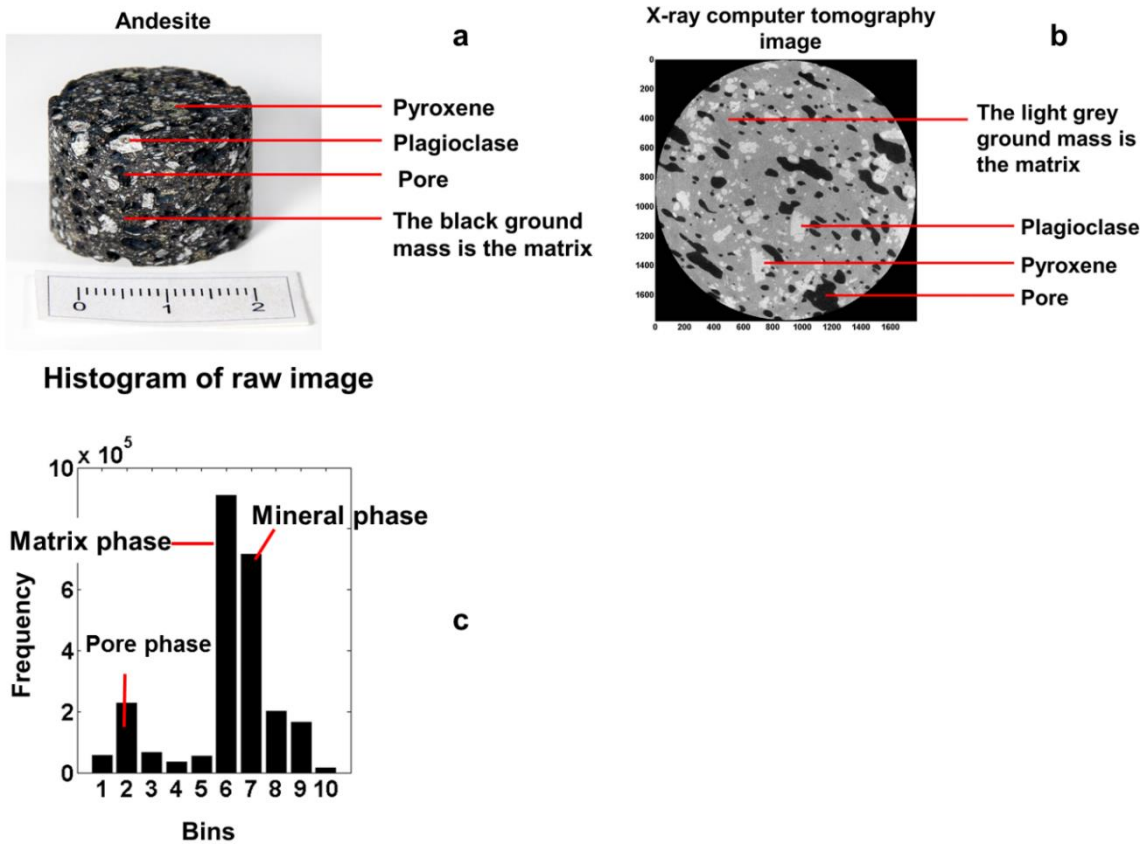

Figure 2. 2 (a) Andesite rock sample (b) raw intensity data in the sinograms converted into a 16-bit greyscale image, in which the values range from 0 to 62738, (c) histogram plot of raw image. Distinction between minerals is based on XRD and thin-section analysis

2.3.2. Image Acquisition and Processing

An image of a cylindrical rock sample with a diameter of 30 mm was acquired using a custom-built XCT scanner based on a CT-Alpha system (ProCon, Sarstedt, Germany) at the Institute for Geosciences laboratory in Mainz, Germany. The XCT scanner consisted of a Feinfocus microfocus X-ray tube (Yxlon, Hamburg, Germany) with a diamond-coated anode target with a focal spot size of a few micrometers. The X-ray data were acquired using a 2048 × 2048 pixel (called '2k') flat panel CCD detector measuring 105 mm × 105 mm (Hamamatsu Photonics, Hamamatsu, Japan).

The XCT scanner was calibrated using a monophasic pure aluminium reference cylinder with a diameter of 30 mm. The Andesite sample was then scanned using a source voltage of 125 kV. The sample was placed 162 mm from the detector panel, giving a final resolution of 13.6 μm per pixel. The sample was rotated in steps of 0.30°, giving 1200 projections to acquire data for the whole 360°, and the exposure time at each step was 0.2 s. Beam hardening correction using hypersurface fitting was performed to make the datasets segmentable (Jovanović et al. 2013). The rock sample projections were then Radon-transformed to give sinograms and then converted into tomograms using the back projection method (Feldkamp et al. 1984). The stacked tomograms produced were 16-bit 3D images, and the voxel resolution was 13.6 μm.

Each 16-bit 3D reconstructed raw image had $2{,}048^3$ voxels. The selected image filtering techniques were tested on all of the raw greyscale images before the segmentation algorithm

was initiated in order to determine whether the image filtering techniques caused the signal- to- noise ratio to change significantly (Fusseis et al. 2014; Leu et al. 2014). The image characteristics, such as noise, blur, background intensity variations, brightness, contrast, and the general pixel value distribution, were not noticeably improved by applying any of the image filtering techniques. This can be attributed to the high quality and high resolution of the raw data.

2.4. Image Segmentation Using Unsupervised Clustering

2.4.1. K-means

The k-means clustering algorithm proposed by (MacQueen 1967) is one of the simplest unsupervised learning algorithms commonly used to address clustering problems. The procedure involves dividing the dataset into clusters (*k*) by initializing *k* centroid centres and then iteratively refining the clusters as described below.

Each datapoint in the dataset is assigned to its closest centroid centre. Each centroid centre C_j is iteratively updated to the mean of the constituent datapoints. The algorithm finally converges when no further change occurs in the assignment of datapoints to the centroids. Convergence is achieved when the objective function, which is the squared root error function, is minimized as shown in the equation

$$J = \sum_{i=1}^{n}\sum_{j=1}^{k}\left\|x^{(i)} - C_j\right\|^2, \qquad (2.1)$$

where $\left\|x^{(i)} - C_j\right\|^2$ is the Euclidean distance between datapoint $x^{(i)}$ and the closest centroid centre C_j.

The performance of the k-means algorithm is strongly dependent on the initial choice of cluster centres. The k-means algorithm will always terminate but will not always identify the global minimum of the objective function. However, the algorithm can be performed a number of times to increase the likelihood than the global minimum of the objective function will be identified.

In our study, the k-means algorithm was configured to perform between three and seven cluster segmentations. These clusters in a one-dimensional feature space are classes, i.e. non-overlapping segments of the histogram. The Euclidean distance function used randomly initialized centroids and an infinite maximum number of iterations.

2.4.2. Fuzzy C-Means (FCM)

The FCM clustering procedure was first proposed by (Dunn 1973) and was later generalized by (Bezdek et al. 1987). The k-means procedure is a hard clustering technique in which each pattern is allocated to a single cluster, and the FCM procedure is an extension of this procedure. Each datapoint in the FCM procedure can be member of multiple clusters, with a membership value between zero and one (Jain 2010; Jain et al. 1999). The FCM clustering procedure involves minimizing the objective function

$$J_{fcm}(Z;U;V) = \sum_{j=1}^{n}\sum_{i=1}^{k}(\mu_{ij})^m \left\|(x_i)^{(j)} - c_k\right\|^2 \qquad (2.2)$$

where $c_k = \sum_{j=1}^{n} u_{ij}x_i$

Where c_k is the k^{th} fuzzy cluster centre, m is the fuzziness parameter (for $m = 1$ fcm simplifies to k-means), $m.u_{ij}$ is the membership function. In our context, if we consider the

entire raw image as a fuzzy set of pixel values, which lie very close to each other - FCMuses membership criterial to “loosely” or “tightly” isolate subsets of pore, mineral and matrix phase. Membership function excels in segregation of intersection subsets of values that lie in between mineral phase and matrix phase.

The first step is the fuzzy partitioning of n datapoints into k clusters using the membership criterion $U = u_{ij}$. The element u_{ij} represents the grade of membership of object x_i^j to cluster c_k. Typically, $u_{ij} \in [0,1]$.

1. The weighted squared root error function (objective function) $\left\|(x_i)^{(j)} - c_k\right\|^2$ is iteratively minimized using U.

U is recomputed in each iterative step and the datapoints are reassigned to the clusters. Optimization is achieved when U is minimized and does not change.

2.4.3. Self-Organized Maps (SOM)

The SOM procedure was proposed by (Kohonen 1990) and is based on an ANN framework. The SOM procedure essentially involves mapping the input data space (or pattern) in a higher dimension space, then using a competitive learning process to seek an optimum classification plane in the transformed space (Cortina-Januchs et al. 2011). The main difference between the k-means and FCM procedures and the SOM procedure is that the SOM procedure arranges the neurons in one of the desired topologies (a grid, hexagon, or random topology) and then uses a distance formula to determine the positions of the neurons in the topology. A winner node will emerge by performing the competitive learning process iteratively. All the neurons in a defined neighbourhood around the winner node are defined as a cluster using the Kohonen rule (Kohonen 1990).

The objective of matching and finding the winner node is determined by the minimum Euclidean distance in the input pattern, which is given by the equations below.

$$\|x(t) - m_c(t)\| = \min_i \|x(t) - m_i(t)\| \qquad (2.2)$$

$$m_i(t+1) = m_i(t) + \alpha(t)[x(t) - m_i(t)] i \in N_c \qquad (2.4)$$

$$m_i(t+1) = m_i(t) i \notin N_c \qquad (2.3)$$

In these equation, t is current learning iteration,

x is the input pattern,

m_c is the winner,

α is time-varying learning rate, and

N_c is the neighbourhood of the winner.

The initial weight vector m_i is filled with random values before the training process is started. Adaptation takes places at each iteration of the learning process, and the difference between the components of the input data x and the weighted vector m_i gradually decreases. The amount of adaptation that occurs is regulated by the learning rate α, which gradually decreases over time. The m_c units that are not changed to match their nearest neighbourhood N_c values during the competitive learning iteration process are classed as the winner m_c units. This strategy allows large clusters to form at the beginning of the procedure, and these clusters

become fragmented through discrimination of the inputs as the learning process (Cortina-Januchs et al. 2011).

In our study, the SOM network structure assumed values of between three and seven. The weighted vectors were randomly initialized. A grid (gridtop) topology was used, and a Manhattan distance weight function was used to determine the nearest neighbourhood distance. The maximum number of iterations was 200.

2.5. Image Segmentation Using Supervised Clustering

2.5.1. Artificial Neural Networks

An ANN can be used to address both clustering and classification problems (Jain et al. 1999). An ANN is an information-processing paradigm that mimics the behaviour of the human brain (Haykin 1995). ANNs are well suited to modelling linear and nonlinear problems. Two possible techniques can be used to solve a non-linear problem using an ANN, a feedback network or a feed-forward network. A FFNN consists of a series of layers. The first layer (the input layer) comprises input nodes. The subsequent layers, known as hidden layers, of which there may be one or more, are each connected to the previous layer. The final layer produces the output of the network. A FFNN can be used for any kind of input-to-output mapping problem. A FFNN with one hidden layer containing sufficient neurons will be able to solve any finite input-to-output mapping problem. FFNNs use the so-called error back-propagation algorithm (Hopfield 1982) to calculate the gradient of the average square error. This algorithm depends on the coefficients of the linear combinations and on the inner parameters of the functions forming the linear combinations (Egmont-Petersen et al. 2002). The algorithm iteratively modifies all of the network parameters until a sufficiently well-fitting input-output function is found for the network. There is no straightforward way of taking model mismatch errors and sensor errors into account or incorporating any a priori knowledge into the FFNN method because the mechanism used has no physical significance. The parameters can therefore only be adjusted on an ad hoc basis.

We used a FFNN to perform a classification task in this study. A FFNN was used to classify the rock image data into the pore phase and different solid phases. The FFNN was tested using each of the segmentation methods mentioned above. The FFNN was set up and the classification process performed using MATLAB© software.

2.5.2. Least Square Support Vector Machine

The LS-SVM method was introduced by (Suykens and Vandewalle 1999). It was developed by introducing the least square term into the cost function of the Vapnik support vector machine (Vapnik and Chervonenkis 1974). This approach significantly decreases the complexity involved in solving a nonlinear problem and the computation time required.

For our study, first, a training data set was created, this data set contained range of pixel values which best represented pore, mineral, matrix and noise regions. These pixel values were further labelled in to different classes, which ranged from one to seven. Care was taken, such that the chosen pixel values did not contain overlapping boundaries between different classes to restrict misclassification. The LS-SVM model was trained using the training data set, the model was tuned using ‘tenfold’ misclassification rate and ‘cross-validation’ function (repeated training and validation) to improve the

generalizationperformance of the classifier - (Suykens and Vandewalle 1999). Once the classifier reached an optimal performance threshold it was tested on rest of the XCT slices.

2.6. Ensemble Classifiers

Ensemble methods have been used in the fields of medical imaging and remote satellite sensing (Chan and Paelinckx 2008; Ochs et al. 2007). The idea behind using ensemble methods is to follow the typical human approach of exploring several options before making a decision. An ensemble of classifiers that are minor variants of the same base classifier is constructed, then the classifiers are trained using the same or different instances of the original data, and the predictions the classifiers make when unknown instances of data are presented to them are assembled. The main reason for combining classifiers in this way is to improve the general applicability of the methods (Dietterich 2000; Galar et al. 2012). The two most frequently used ensemble classification techniques are bragging (Breiman 1996) and boosting (Freund and Schapire 1995).

2.6.1. Bragging

Bragging, which stands for “bootstrap aggregation”, was proposed by (Breiman 1996), and is an ensemble learning method based on the tree algorithm (Kohavi and Quinlan 2002). In the bragging algorithm, a large training dataset is broken down into small sets, then randomly selected samples of the training set are taken, the classifiers are trained, and an unknown dataset is exposed to the classifier ensemble. The trained classifier holds a set of numerical scores. The bragging method leads to a certain amount of misclassification because each classifier is trained using a different sample of the (same) training set. The misclassified instances are collected in the next step, and the classifiers are retrained before the first step is repeated until the misclassification errors are minimized.

2.6.2. Boosting

(Freund and Schapire 1995) introduced the boosting concept, and AdaBoost (Schapire et al. 1998) is the most appropriate algorithm in this family for the problem addressed in our study. The AdaBoost iterative scheme involves using the whole dataset to train the classifiers sequentially, then assigning individual weights to accurate and inaccurate classifiers. The AdaBoost method is then essentially focused on retraining the inaccurate classifiers until the weighted error has been minimized. A prediction based on voting by the individual classifiers weighted by the accuracy of each classifier occurs once the classifiers have been suitably trained. The calculation of the weights has been explained previously by (Schapire et al. 1998).

Table 2. 1 Number of pixels in training and test data from X-ray computer tomography used in this study

Type of classifiers	No. of training pixels	No. of test pixels
K-means	—	31,577,290
Fuzzy c-means	—	31,577,290
Self-organized maps	—	31,577,290
Artificial neural networks	15,788,645	31,577,290
Least square support vector machine [a]	2,077	31,577,290
Bragging and boosting	2,077	31,577,290

[a] using K.U.Leuven MATLAB/C LS-SVMlab toolbox

2.7. Results and Discussions

2.7.1. Classification and Feature Extraction

The intention of the classification process is to categorize every pixel in a digital image, each class of pixel being based on a specific feature. The categorized data could then be used to retrieve useful information. In this study, to compute porosity and assist in pore size distribution.

For segmentation using unsupervised techniques, a set of ten representative images were used to develop feature vector (FV). For, classification using FFANN five images out of ten were used to develop a FV and in the case of LSSVM and ensemble classifiers a set of pixels values which best represented pore, mineral, matrix and noise regions were used as FV. The total number of pixels used to train and test each machine learning algorithm is shown in Table 2. 1.

2.7.2. Image Segmentation

The unsupervised classification methods were used to segment the FV into between three and seven clusters. The 2D segmented images obtained using the k-means, FCM, and SOM methods, and a 3D volume rendering image of the ten slices are shown in Figure 2. 3. Further, using the supervised clustering methods the FV was segmented into three and seven classes. The FFANN was trained using five images (15,788,645 pixels), validated using one image (3,157,729 pixels), and tested using ten images (31,577,290 pixels). The Matlab neural network toolbox provides an objective measure to determine the classification criteria by calculation the mean squared error (MSE) between output and the targets. Lower the MSE value better is the classification, zero corresponds to no misclassification. The best classification rate was found using the FV of the k-means algorithm, which gave a MSE of 0.16, and the worst classification rate was found using the FV of the FCM, which gave a MSE of 0.38. In the case of LS-SVM, trained LS-SVM classifier was used to perform pixel-by-pixel classification on the ten images. The training data contained 2077 pixels (less than 1 % of the total number of pixels in the image), and the remaining 31,577,290 pixels of the same 2D image were used to validate the procedure. The LS-SVM was trained until it reached optimal performance thresholds, then it was tested on the remaining ten images. In the case of ensemble classifiers RUSBoost and Bagtree algorithm have been used (Seiffert et al. 2008; Breiman 1996). The classifiers

were trained using the same FV as that used for the LS-SVM. The learning rate was 0.1 and the algorithms were initiated using a minimum leaf size of five. The 2D segmented images obtained using the FFANN, LS-SVM and ensemble classifiers and a 3D volume rendered image of the ten slices used, are shown in Figure 2. 4.

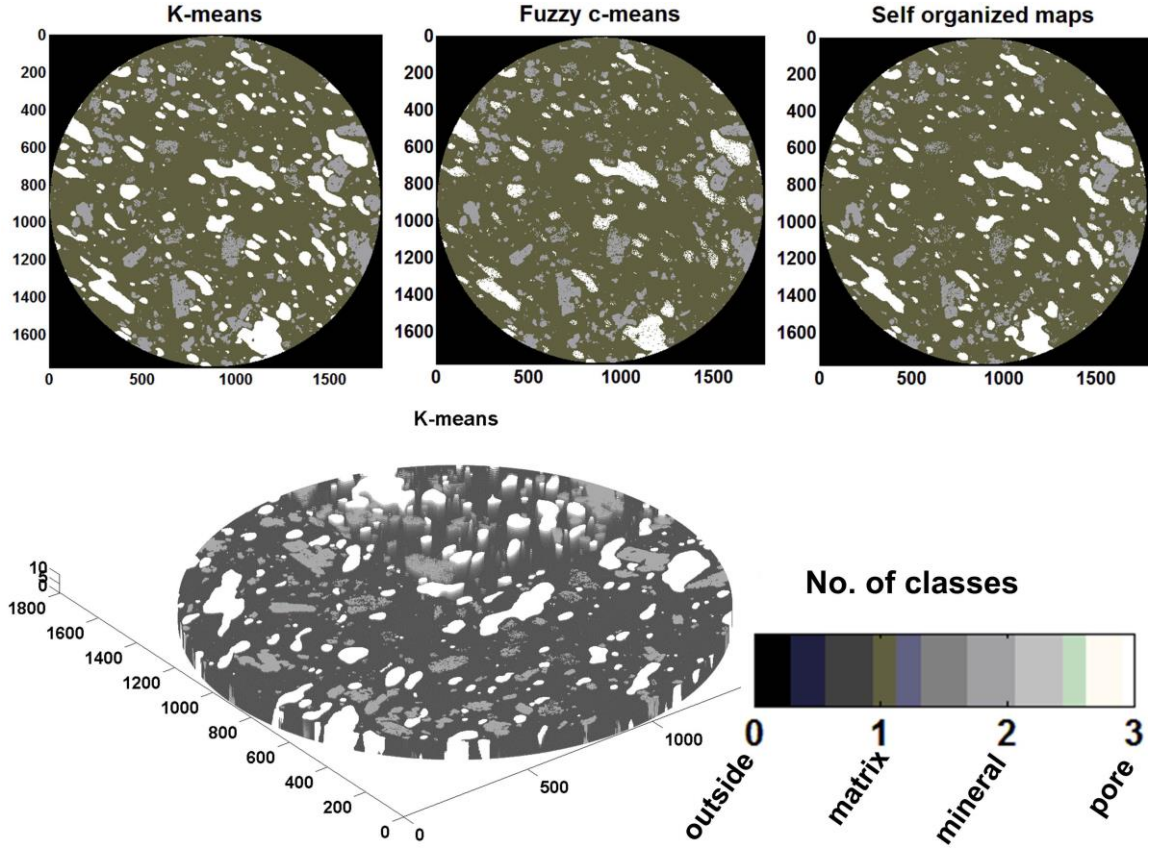

Figure 2. 3 Top panel shows 2D segmentation obtained using k-means, FCM, and SOM. Bottom panel shows 3D volume rendered plot for k-means

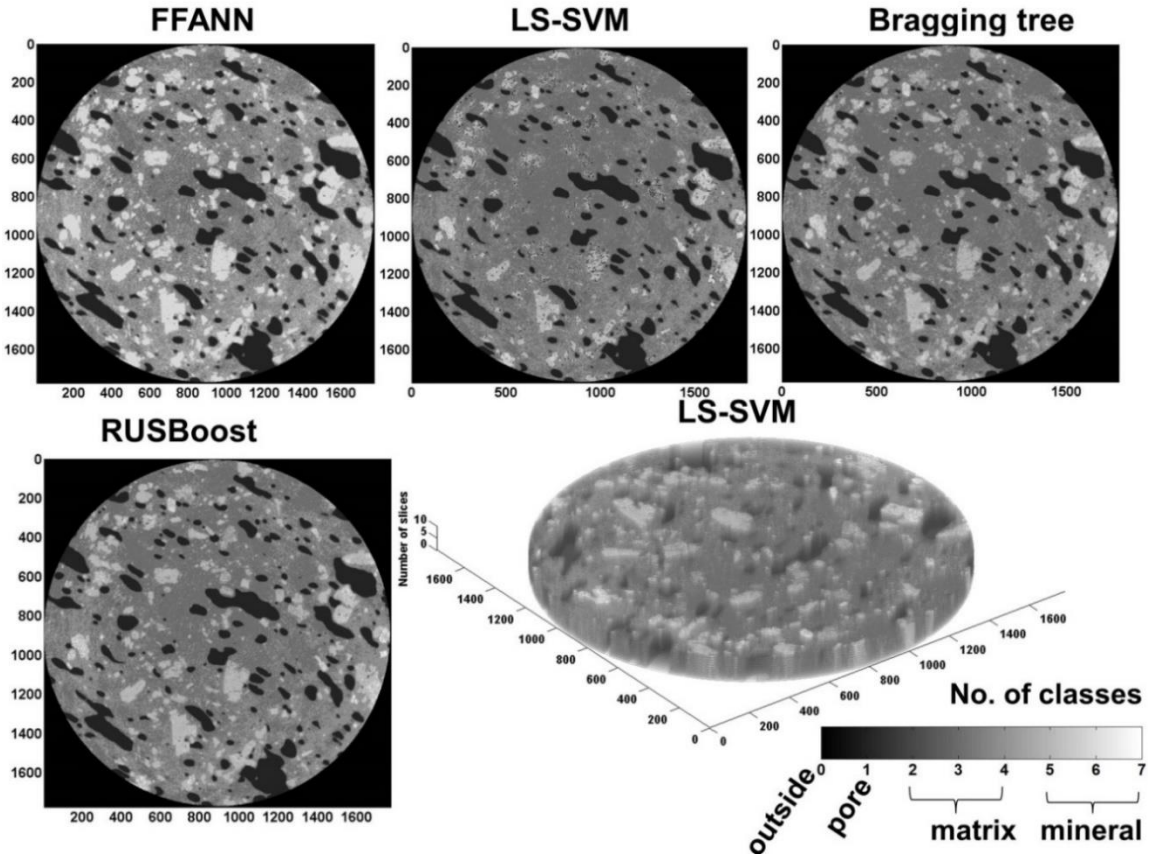

Figure 2. 4 Top panel shows 2D segmentation obtained using FFANN, LS-SVM, Bragging tree, Bottom panel shows RUSboost and 3D volume rendered plot for LS-SVM

2.7.3. Comparison

The performances of the unsupervised, supervised, and ensemble classification methods in terms of how well they classified the pore phase and solid phases (mineral and fine-grained mineral phases) pixels in the XCT images, are shown in the volume fraction plot in Figure 2. 5. FCM with a loosely constrained membership function of 1.60 and 1.85 tends to over-segment pore volume fraction (pore pixels) by 2 % compared to other MLA The matrix and mineral volume fraction vary less than ±4 %. This variability in the matrix and mineral volume fraction could be attributed to the presence of small fragments of cryptocrystalline minerals which cannot be resolved by the XCT, leading to images having variable pixel intensities. These pixels of varying intensities would not have been segmented into the same classes by different machine learning algorithms (MLA).

2.7.4. Estimation of Porosity and Pore Size Distribution

The porosities determined from the stack of ten XCT slices for different clusters and using different MLA are shown in Table 2. 2, and the computational times required by the MLA are shown in Table 2. 3. The porosity is the ratio between the pore phase voxels and entire sample volume multiplied by 100. The porosities determined using the unsupervised clustering methods agreed well with each other for each class. The average porosity obtained using unsupervised MLS is 15.85 ± 2.5 % which is in good agreement

to the effective porosity to gas of 17 ± 2 % measured using GeoPyc pynometer. And, the average porosity obtained using supervised MLS is 15.96 ± 0.8% which is also in

goodagreement with respect to experimental values measured using GeoPyc pynometer. The high standard deviation in the case of unsupervised technique and low standard deviation for unsupervised technique, could be attributed to, the loosely constrained membership function (1.85) of FCM and same set of feature vector used to train LS-SVM and ensemble classifiers respectively. The irregularities in porosities within the seventh class is likely because the MLA reach a 'global' optimum at class six and thereafter for higher number of classes tend to over segement/over-classify the matrix phase- due to variations in the pixel intensities.

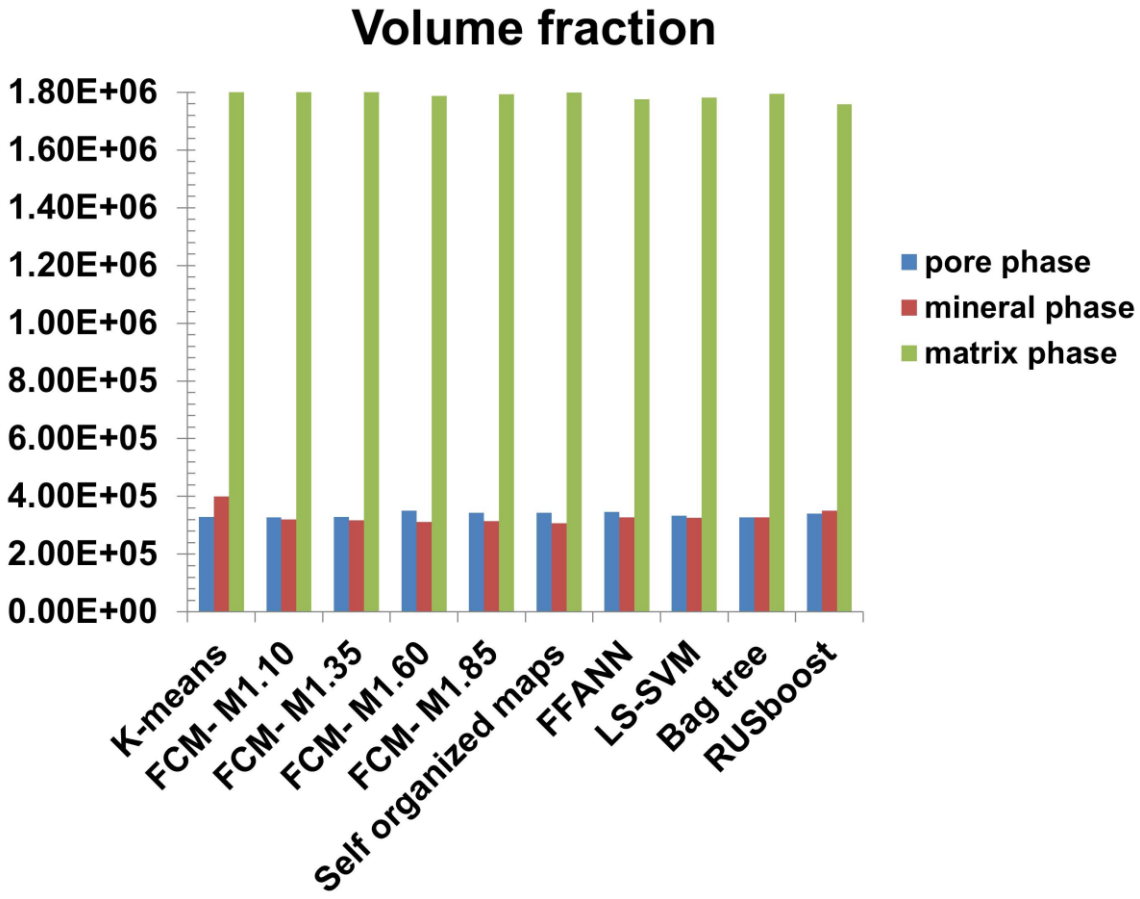

Figure 2. 5 Relative difference plot showing the agreement of K-means, FFNN, LS-SVM, and bragging to retrieve fine-grained mineral, mineral, and pore phases

The PoreDict module of the GeoDict software was used to calculate the geometrical pore size distribution from the 16-bit 3D segmented images. The GeoDict software package (http://www.geodict.com/) predicts physical material properties from tomographic microstructural inputs (Khan et al. 2012). The geometrical pore size distribution was determined by a morphological approach fitting spheres into the pores. This method does not distinguish between pores, closed pores, and blind pores, and it is a purely geometrical cumulative measure of the range of pore sizes in the given porous medium. The cumulative and volume fraction pore percentages determined using the unsupervised, supervised, and ensemble classification methods are shown in Figure 2. 6 (a) and Figure 2. 6 (b). The P10, P50, and P90 values (the pore radii at 10 %, 50 %, and 90 % of the cumulative pore results, respectively) were determined to allow the geometrical pore size distribution to be interpreted in terms of the micro- and macro-pore contributions to the total pore volume. The P10, P50,

and P90 values are shown in Table 2. 4. The high standard deviation in pore size distribution seen in Table 2. 4 is caused by FCM segmentation. As the membership criteria were loosely constrained small pores became more frequent compared to big pores resulting in larger poresize diameter for the diameter range D10. And, FFANN trained with FCM feature vector contributes further to the standard deviation.

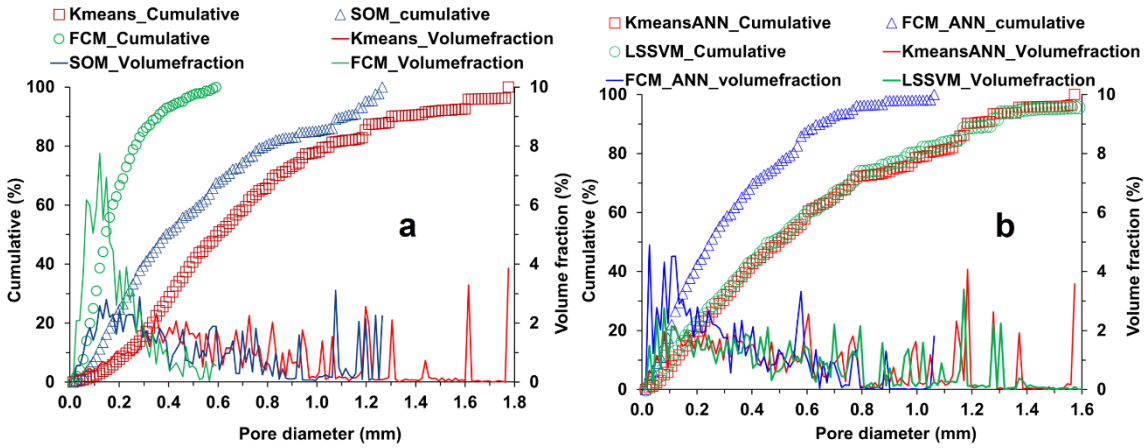

Figure 2. 6 Geometrical pore size distribution of an Andesite rock sample obtained from (a) unsupervised clustering and (b) supervised clustering techniques

Table 2. 2 Porosity obtained from seven machine learning algorithms

Machine learning algorithm	Porosity (%)[a]				
	three	four	five	six	seven
K-means	18.51	17.99	15.56	15.10	10.50
Fuzzy c-means	18.89	17.99	15.56	15.09	10.90
Self-organized maps	18.51	17.99	15.56	15.10	14.55
Feed forward artificial neural networks	18.45	17.93	15.59	15.55	15.14
Least square support vector machine	15.89	15.18	16.01	15.99	15.82
Bragging	15.44	15.41	15.44	15.44	15.41
Boosting	16.05	16.12	16.14	16.09	16.16

[a] **three, four, five, six and seven correspond to number of classes.**

Table 2. 3 Computational[b] time for processing ten slices

Machine learning algorithm	CPU Time (hrs:min:sec)
K-means	00:15:35
Fuzzy c-means	00:20:19
Self-organized maps	01:07:06
Feed forward artificial neural network (k-means)	08:58:18
Feed forward artificial neural network (FCM)	06:36:43
Least square support vector machine	63:29:35
Bragging	05:57:05
Boosting	07:47:05

[b] configuration: Windows Server 2008 R2 Standard, 64-bit Operating System. Two processors Intel(R) Xenon(R). CPU: E5645 2.40 GHz. Installed memory (RAM): 48.0 GB. System type: 64-bit Operating System.

Table 2. 4 Pore size diameter obtained for six machine learning algorithms

Machine learning algorithm	D 10(mm)	D 50(mm)	D 90(mm)
K-means	0.231	0.596	0.130
Fuzzy c-means	0.585	0.145	0.335
Self-organized maps	0.114	0.387	1.108
Feed forward artificial neural networks (k-means)	0.121	0.498	1.182
Feed forward artificial neural networks (FCM)	0.061	0.248	0.647
Least square support vector machine	0.102	0.475	1.267
Bragging	0.103	0.479	1.277
Boosting	0.114	0.549	1.321
Mean ± SD	0.17 ±0.17	0.42 ±0.15	0.90±0.47

2.8. Conclusions and Outlook

A unique insight into the petrophysical properties of an Andesite rock sample was gained by using XCT to scan the rock sample non-destructively, and MLA and mathematical models were then used to segment the pore spaces and solid phases. The abilities of the MLA to segment different phases were compared using qualitative visual inspections and by calculating porosities and plotting volume fraction of pore,mineral and matrix phases against each other. We found that the abilities of the supervised and ensemble classifiers to segment the phases were largely governed by the vector selection features despite the high resolution of the data (giving small noise and volume effects, like beam hardening, ring artefacts and edge effects). We found that different tuning parameters (such as different FCM membership criteria and different SOM topologies and distance functions) need to be tested for the unsupervised techniques. A FCM membership value of 1.85, a SOM topology “gridtop” layout (neurons arranged in a grid format), and a SOM Manhattan distant function (sum of the absolute difference) gave consistent results.

The main advantage of the approach used in this study, compared with the one used by (Cortina-Januchs et al. 2011) is the diversity of the different MLA used. The FFANN classification technique used by (Cortina-Januchs et al. 2011) relies exclusively on using apriori information obtained from unsupervised clustering techniques as feature vectors in the training, validation, and testing the FFANN process. The porosity determined by the FFANN technique therefore closely resembles the a priori values, and a good level of accuracy (up to 97 %) can be anticipated. In our study we used other discrete MLA, such as the LS-SVM, bragging, and boosting, which are driven by feature vectors that are manually selected. These methods are unbiased towards a priori information, unlike the FFANN method used by (Cortina-Januchs et al. 2011). The difference plot for the MLA we used provided a robust cumulative estimate of the performances of the MLA. This study shows that, the porosity values obtained from seven MLA techniques is in good agreement with the experimental results. Further studies on accuracy and misclassification rate which haven't been a part of this study can help in better assessment on the performance of these techniques.

3. Phase Segmentation of X-Ray Tomography Rock Images Using Machine Learning Techniques: an Accuracy and Performance Study

This chapter is based on the manuscript published in an ISI listed open access journal Solid Earth. . © Copernicus Publications

Chauhan, S., Rühaak, W., Anbergen, H., Kabdenov, A., Freise, M., Wille, T., and Sass, I. (2016): Phase segmentation of X-ray computer tomography rock images using machine learning techniques: an accuracy and performance study, Solid Earth, 7, 2016 1125-1139, https://doi.org/10.5194/se-7-1125-2016.Used with permission

3.1. Abstract

Performance and accuracy of machine learning techniques to segment rock grains, matrix and pore voxels, from a 3D volume of X-ray tomographic (XCT) grey-scale rock images was evaluated. The segmentation and classification capability of unsupervised (k-means, fuzzy c-means, self organized maps), supervised (artificial neural networks, least square support vector machines) and ensemble classifiers (bragging and boosting) was tested using XCT images of Andesite volcanic rock, Berea sandstone, Rotliegend sandstone and a synthetic sample. The averaged porosity obtained for Andesite (15.8 ± 2.5 %), Berea sandstone (16.3 ± 2.6 %), Rotliegend sandstone (13.4 ± 7.4 %), synthetic sample (48.3 ± 13.3 %) is in very good agreement to the respective laboratory measurement data and varies by a factor of 0.2. The k-means algorithm is the fastest of all machine learning algorithms, whereas least square support vector machine is the most computationally expensive. Metrics entropy, purity, mean square root error, receiver operational characteristic curve and 10-fold cross validation were used to determine the accuracy of unsupervised, supervised and ensemble classifier techniques respectively. In general, the accuracy was found to be largely affected by the feature vector selection scheme. As it is always a trade-off between performance and accuracy, it is difficult to isolate one particular machine learning algorithm which is best suited for the complex phase segmentation problem. Therefore, our investigation provides parameters that can help selecting the appropriate machine learning techniques for phase segmentation.

3.2. Introduction

Micro X-ray computer tomography (XCT) images of rock sample help in classification of pore-space and assist in modeling of pore-network geometries. Pore-network geometries give an insight about the evolution of permeability and porosity of a rock sample. Image segmentation is the first step toward pore-network modeling. While developing this pore-network model discrimination between porous space and throat has to be resolved to the best possible extent. Currently this discrimination is still subjective (Piller et al. 2009; Boever et al. 2012). A well segmented 2-D or 3-D image of porous geometry provides a good foundation to obtain effective permeability and porosity trends.

Accurate segmentation of different phases from X-ray computer tomography (XCT) rock images is a well know and complex problem in the digital rock physics community (DRP). In General, tomography is a technique that generates a data set (images), called a tomogram, which is a three-dimensional representation of the structure and variation of composition within a rock specimen. Each three-dimensional data point in the tomogram is called a voxel and contains a coefficient value associated with the density of the specimen. X-ray micro computed tomography involves collecting a tomogram using high energy X-rays to achieve very high voxel resolution.

Segmentation is the partitioning of a tomogram (grey-scale image) into disjoint regions that are homogeneous with respect to some characteristic. Porous materials like sedimentary and volcanic rocks contain areas of void, called the pore space, as well as a number of distinct mineral components, each with a comparatively uniform density. These different components are referred to as phases. Segmentation of a porous rock means deciding to which phase each voxel belongs. Tomographic images of such materials consist of a cubic array of reconstructed linear X-ray attenuation coefficient values each corresponding to a voxel of the sample. Ideally, one would wish to have a multi-modal distribution giving unambiguous phase separation of the pore and various mineral phase peaks. For flow properties, in particular, one would like

toobtain a clear distribution separating the pore phase from mineral phase peaks. Unfortunately, the presence of low density pore inclusions (e.g., microporosity, clays) below the image resolution can lead to a spread in the low density signal making it difficult to unambiguously differentiate the pore from the micro porous and solid mineral. As a consequence, significant features can be lost and macroscopic properties of the segmented image can vary greatly with small changes in the segmentation parameters.

They have been extensive studies in various international groups to improve segmentation methods for better quantitative characterization of pore space feature. (Iassonov et al. 2009) in his survey broadly classified segmentation algorithm in two types: (i) Global Thresholding segmentation schemes and (ii) Local Adaptive segmentation scheme.

The fundamental concepts behind of Global Thresholding schemes, is the histogram representation of the intensity and variation of all the gray pixels in a scene. They are many subcategories in the scheme. And the most commonly used are the histogram shape (triangulation) (Zack et al. 1977; Rosin 2001; Sund and Eilertsen 2003) or the signal entropy consideration (Pal and Pal 1989; Pal 1996).

The Local Adaptive segmentation scheme is governed by the fact that segmentation decision is done for each pixel in the scene. By utilization of local information generally provides better segmentation quality and account for some image artifacts. But requires higher computation demand and memory. The most commonly used are L-A kriging (Oh and Lindquist 1999), PMC-Pham which uses indicator kriging, somewhat similar to L-A Kriging, except that the final result is obtained from Fuzzy cluster membership (Pham). PMC-Pham belongs to up supervised segmentation category but due to iteration scheme need more computational power. ED-Yanowitz is a technique based on edge detection and surface procedure proposed by (Yanowitz and Bruckstein 1989). CAC- Sheppard is a hybrid method developed by (Sheppard et al. 2005) which uses a combination of image enhancement, thresholding and convergence active contours. MRF-Berthod is an algorithm for supervised Baysian segmentation developed by (Berthod et al. 1996). The general drawback of CAC – Sheppered and MRF Berthod methods can be attributed to long processing time either caused by insufficient ground truth initialization and long processing time due to simulated annealing technique. (Jovanović et al. 2013) proposed a segmentation scheme which can be performed already at the stage of sinograms. (Cortina-Januchs et al. 2011) used segmentation/classification technique based on a combination of clustering and artificial neural network (ANN) to segment binary soil images. Whereas, (Khan et al. 2016) used supervised technique Least Square Support Vector machine (LS-SVM) for segmentation of XCT rock images. Therefore, with the continuously, improving CT technologies and computational resources machine learning (ML) techniques can be an effective tool for segment and classify for phase segmentation of XCT rock images. Based on the heterogeneity of the sample the user can employ different ML techniques to obtain the best segmented image(s) which can be further used for simulating physical processes.

In our (Chauhan et al. 2016b) a workflow was developed to segment XCT images using unsupervised, supervised and ensemble classifiers ML techniques. The focus of this study is to assess the performance and accuracy of the above mentioned ML techniques to segment rock grain, matrix and pore phases in heterogeneous rock samples such as Andesite, Berea sandstone, Rotliegend sandstone and synthetic sample containing micro porosities.

3.3. Experimental Approach

For this study Andesite (Tongariro National Park, New Zealand), Berea sandstone (Andrä et al. 2013a), Rotliegend sandstone (Rotliegend, Germany) and Synthetic sample Musli (provided by APS Antriebs, Prüf und Steuertechnik Gmbh Göttingen Rösdorf Germany) were used. Figure 3. 1 shows the rock samples and respective histogram plots obtained from the XCT raw files. Effective porosity of Andesite (17 ± 2 %) and Rotliegend sandstone (14 ± 2 %) was measure using a GeoPyc pycnometer (Micromeritics Instrument Corporation Norcross, GA, USA). Thin section analysis using polarized microscope revealed Andesite has a porphyritic texture with large plagioclase crystals (up to 3 mm in diameter), pyroxene in a cryptocrystalline matrix, and isolated vesicles up to 6 mm in diameter (Chauhan et al. 2016b). Whereas, Rotliegend Sandstone had different grain size (between 0.5 to 5 mm) of fine sand and gravel, with monocrystalline quartz 26 %, poly-crystalline quartz up to 35 % , Feldspate 8 %, sedimentary volcanic lithoclast grains 9 % along with 13 % cement (Aretz et al. 2016). (Andrä et al. 2013a) confirms that the porosity of the Berea sandstone (total porosity 19.97 %; TM Petroleum Cores Ohio USA) was performed using Helium Pycnometer 1330 (Micrometrics Instrument Corp. Belgium) and a mercury porosimetry using Pascal 140+440 Mercury Porosimeter (Thermo Electron Corporation, Germany). (Madonna et al. 2012) scanning electron microscope revealed Berea Sandstone has Ankerite, Quartz, Zircon, K-spar and Clay. The Synthetic sample contained large pores, micro pores and mineral grain.

Andesite volcanic rock and Rotliegend sandstone where imaged using custom-built XCT scanner based on CT-Alpha system (ProCon, Sarstedt Germany) at the institute for Geoscience laboratory in Mainz Germany. The samples were scanned by applying X-ray energy of 110 keV and using a prefilter of 0.3 copper. During the reconstruction of the projections noise filter was not used. The projections were Radon-transformed in sinograms, thereafter converted through back-projection into tomograms. These stacked tomograms resulted in a 16-bit 3D imagery, with a resulting voxel resolution of 13 µm and 21 µm for Andesite and Sandstone respectively. Andesite required no beam hardening correction (BHC), whereas BHC for Sandstone was done based on regression analysis using 2D paraboloid fitting. Finally, the tomograms are saved in raw format.

The Berea sandstone dataset was obtained from GitHub FTP server (https://github.com/cageo/Krzikalla-2012). (Andrä et al. 2013a) performed XCT scans at tomographic microscopy and coherent radiology experiment (TOMCAT) (Stampanoni et al. 2006) eamline at Swiss Light Source (Paul Scherrer Institute, Villigen, Switzerland). The beam energy was tuned for best contrast at 26 keV with an exposure time of 500 ms to retrieve a magnification of factor 10 (Andrä et al. 2013a). The projections were magnified by microscope optics and digitized by high resolution CCD camera (PCO.2000), to obtain images of dimension 1024 x 1024 x 1024 with voxel resolution of 0.74 µm. Tomographic images were reconstructed from the sinograms by applying Fourier transform (Marone et al. 2009), and saved in desired file formats (Andrä et al. 2013a).

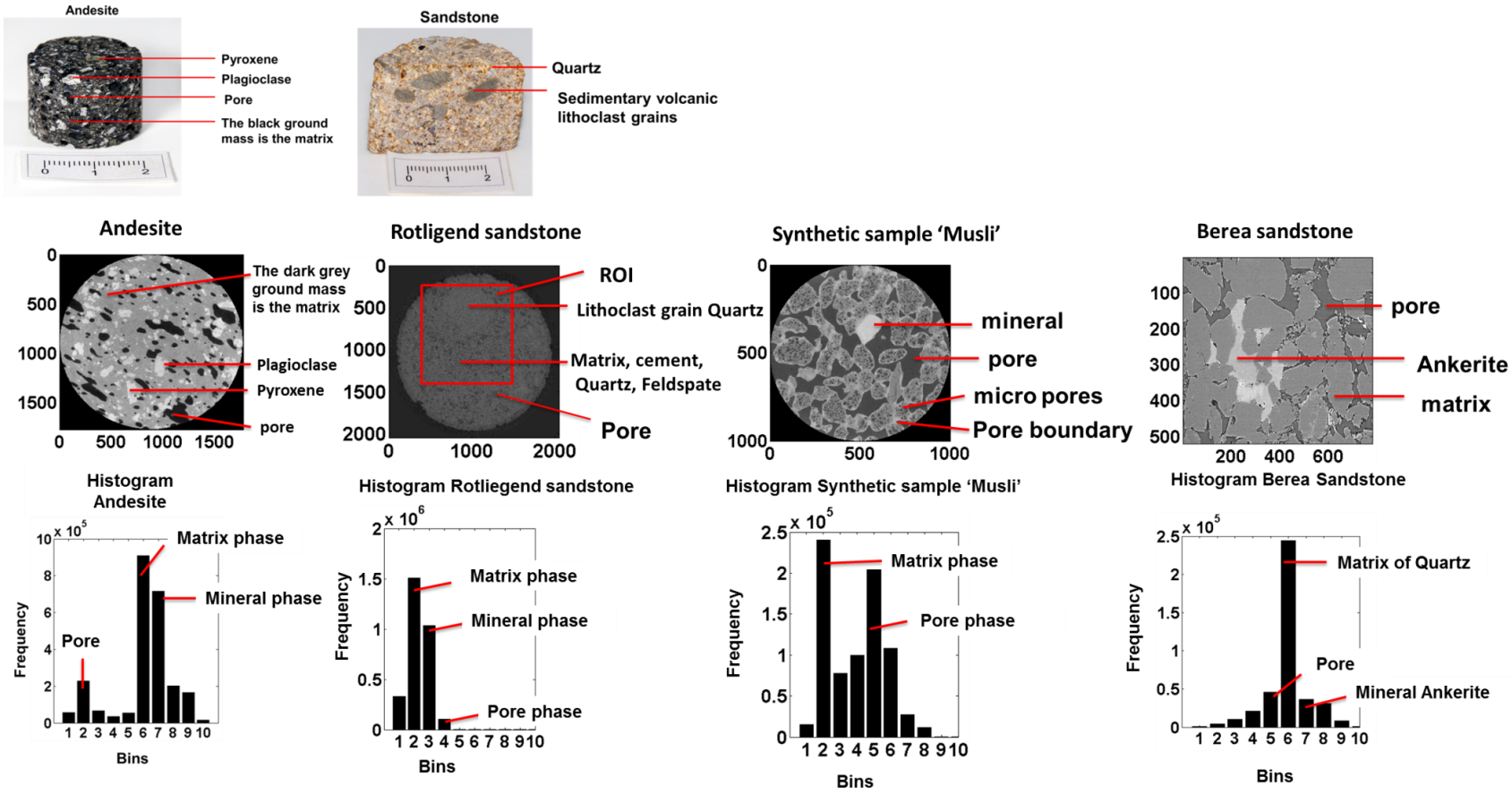

Figure 3. 1 The top panel shows the Andesite and Rotliegend sandstone rocks used for XCT measurements. Middle panel shows the raw images of Andesite (16bit), Rotliegend sandstone (16 bit), synthetic sample (16 bit) and Berea sandstone (16 bit). Mineral composition of Andesite and Rotliegend sandstone was determined from thin sections using polarized microscope. Bottom panel shows, histogram plot of the respective samples. Mineral composition of Berea sandstone is based on Madonna et al. (2012) and Andrä et al. (2013)

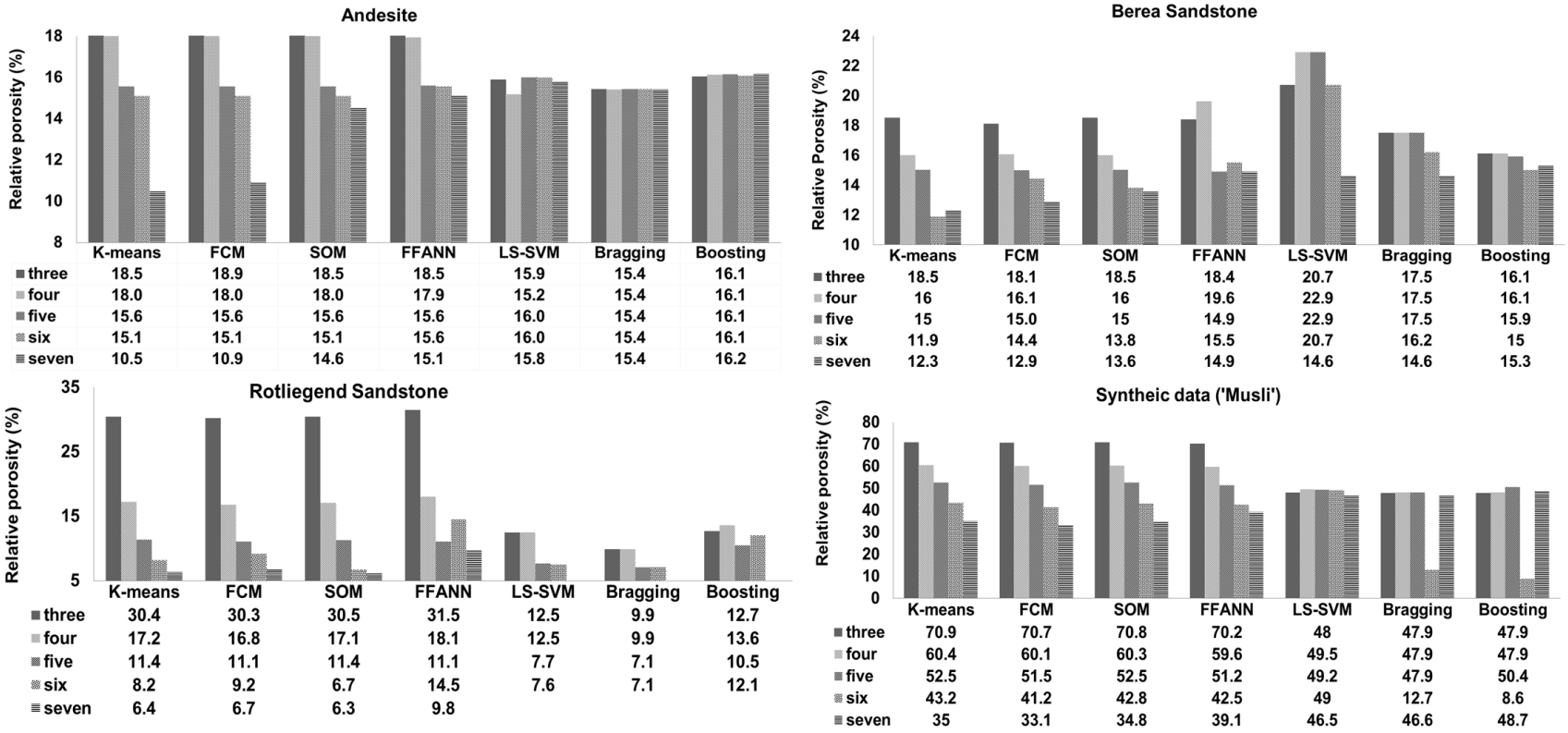

Figure 3. 2 . Relative porosity values obtained using unsupervised, supervised and ensemble classifier techniques for respective samples

3.4. Image Processing

Each of the 16-bit and 8-bit 3D reconstructed raw images resulted in 20483 and 10243 voxels. The image filtering techniques such as blur, background intensity variation and contrast were tested on all the raw images before the segmentation and classification algorithms were initialized. In the case of Rotliegend Sandstone (21 μm) as the XCT images were noisy, contrast filter was used to enhance the image. Whereas, for other XCT images (Berea, Andesite and Musli) as the resolution and contrast were sufficiently high (7.5 μm to 13 μm) using filters did not show any noticeable change. The following sections describe the post processing algorithm and how these were implemented in our image processing schemes.

3.5. Machine Learning

The main focus of this study is to demonstrate the computational performance and accuracy of the different machine learning (ML) algorithm to segment/classify different phases in XCT rock samples - meaning, to map pixels of similar values in to respective classes. ML algorithms rely on features; features are a set of instances which contains descriptive information based on which the ML algorithm trains it classification model and further identifies these features in an unknown dataset and group them in to respective classes. Which in our case are the associated feature values of noise, rock grain, matrix and pore voxels. ML algorithms in general fall in to categories of unsupervised, supervised and ensemble classifiers.

3.5.1. Unsupervised Learning Techniques

In the unsupervised technique k-means (MacQueen 1967), fuzzy c-means (FCM) (Dunn 1973) and self-organized maps (SOM) (Kohonen 1990) were used for segmentation pore, mineral and matrix phases. k-means is one of the simplest unsupervised ML algorithms commonly used to address clustering problem. The k-means algorithm through an iterative scheme calculates the Euclidean distance between the data point (pixel value) to its nearest centroid (cluster). The algorithm converges when the mean squared root error of Euclidean distance reaches minimum, that is, when no further pixel is left to be assigned to the nearest centroid (cluster). The performance of the k-means algorithm is strongly governed by the initial choice of the cluster centres. The k-means has the tendency to terminate without identifying the global minimum of the objective function (Chauhan et al. 2016b). Therefore, it is recommended to run the algorithm several times to increase the likelihood that the global minimum of the objective function will be identified.

Unlike k-means, in the FCM iterative scheme each data point can be a member of multiple clusters by varying the membership function (Jain 2010; Jain et al. 1999). The FCM clustering procedure involves minimizing the objective function

$$J_{fcm}\,(Z;U;V) = \sum_{j=1}^{n}\sum_{i=1}^{k}(\mu_{ij})^{m}\ \left\|x_i^{(i)} - c_k\right\|^2 \tag{3.1}$$

where $c_k = \sum_{j=1}^{n} u_{ij}x_i$

Where c_k is the k^{th} fuzzy cluster centre, m is the fuzziness parameter (for $m = 1$ FCM simplifies to k-means), $m.u_{ij}$ is the membership function. In our context, if we consider the entire raw image as a fuzzy set of data points (pixel values), which lie very close to

each other - FCM uses membership criterial to “loosely” or “tightly” isolate subsets of rockgrains, matrix and pore phase. Membership function influences the segregation of intersection subsets of values that lie in between rock grains/matrix phases for densely packed pixels (Rotliegend sandstone) and pore throat/matrix phases for micro pores dataset (Synthetic sample Musli). FCM can be a better choice in comparison to k-means; but it has a tendency to converge to the local minima of the objective function. Therefore, it is vital to test range of membership values in combination with several centroids (classes) for accurate analysis (Cannon et al. 1986).

For detailed description of SOM the reader is recommended to (Kohonen 1990) and (Chauhan et al. 2016b). SOM procedure uses a competitive learning process based on an artificial neural network framework (ANN). In our context, a raw CT image is considered as input pattern, which has to be classified. SOM first arranges nodes (called as neurons) in one of the desired topologies (grid, hexagon, or random topology; as specified by the user) and assign random weight (values). These nodes are trained using the pixel value of the CT image(s), iteratively using Kohonen rule (Kohonen 1990). During this competitive learning process the difference between the nodal weight and the neighbouring pixel(s) is calculated. The iterative process stops when the difference reaches to a minimum. The amount of adaptation of the nodal weight to its neighbouring values can be influenced and monitored using learning rate parameter α. The nodes that do not change to it surrounding value are classed as winner nodes. These winner nodes are nothing but different classes in the segmented image.

The unsupervised algorithms were configured to perform segmentation of three to seven classes. These classes in one-dimensional feature space are the non-overlapping segments of pixel bins in a histogram. Filter based feature vector selection (Euclidian and Manhattan distance function) were used to initialize centroids for k-means, FCM and SOM. In the case of FCM different degree of membership values [1.10 to 1.85] were tested to ‘loosely’ or ‘tightly’ segregate pixel values between rock grains and matrix phase. Grid topology was chosen in the case of SOM.

3.5.2. Supervised Techniques

In the supervised category feed forward artificial neural Network (FFANN) (Jain et al. 1999) and least square support vector machine (LS-SVM) (Suykens and Vandewalle 1999) were used to classify rock grains, matrix and pore phases (Chauhan et al. 2016b). In general, the supervised algorithms rely on a classification model which has to be trained using example set of data that represent each class.

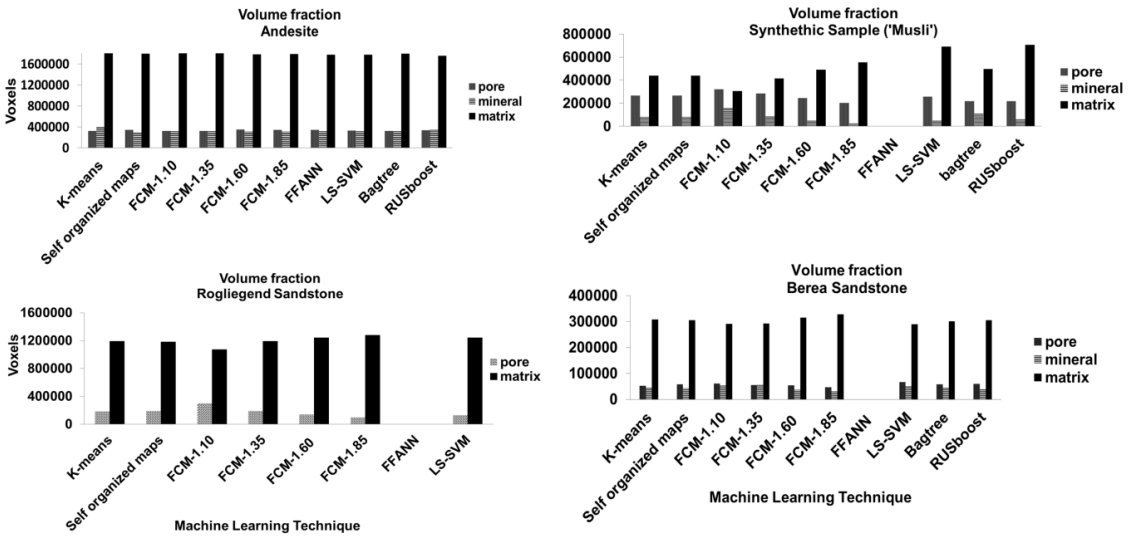

Figure 3. 3 Total volume fraction plotted for respective samples

ANN is an information processing paradigm that mimics the behaviour of the human brain (Haykin 1995). FFANN is based on the ANN framework and uses so called error back propagation algorithm (Hopfield 1982). FFANN can be used for any input-output mapping problem but is best suited for modelling linear and nonlinear problems. In our case The XCT dataset was partitioned in to training and testing dataset. Thereafter, FFANN was setup with input layer, one hidden layer and output layer. The hidden layer was assigned 10 nodes, and the nodes of input and output layer varied depending on training and testing slices. The k-means, FCM segmented dataset were used as feature vector to train the classification model using Levenberg-Marquardt backpropagation method (Levenberg 1944; Marquardt 1963). The classification model was tuned using ten-fold cross validation function (repeated trained and testing) and the misclassification rate was determined using mean squared root error (MSE). Once the classification model reached optimal accuracy it was tested on rest of XCT raw slices.

For LS-SVM a training data set was created, which contained range of pixel values which best represented pore, mineral, matrix and noise regions, these pixel ranges where further labelled in to different classes, which ranged from one to seven. For FFANN and LS-SVM the models were tuned using ten-fold cross-validation function (repeated training and testing) and misclassification rate was determined using mean square root error (MSE) in the case of FFANN. Once the classification model reached an optimal performance threshold it was tested on rest of the XCT slices.

3.5.3. Ensemble Classifiers Techniques

In the ensemble classifier technique RUSBoost and Bragtree algorithms are used (Seiffert et al. 2008; Breiman 1996) to classify pore, rock grains and matrix phases (Chauhan et al. 2016b). In general ensemble classifiers are a ‘bootstrap aggregation’ of different weak classifiers. In general, weak classifiers are algorithms which perform classification with substantially high error rate ─ (< 0.5) but slightly better than random guessing. The main advantage to bootstrap such weak learner is to gain speed. The main difference between Bragging and RUSBoost is the way they train their weak classifiers. Bragtree is an iterative scheme, classifiers are trained with randomly chosen samples from the training data set,

in the second step the misclassified instances are collected and its classifiers are retrained until the misclassification error is minimized. Whereas, RUSBoost sequentially trains its classifiers using the whole training set, essentially focusing on retraining inaccurate classifiers with the large data set until its misclassification error is minimized. The ensemble classifiers where trained using the same feature vector (FV) which was used for LS-SVM. During the training process the ensemble models (of type RUSBoot and Bragtree) were parameterized using (weak) classifier of type 'Decision Tree' with a leaf size of five and trained up to thousand training cycles. The learning rate which is a parameter from [0.0 1.0] controls overfitting ranges was set to 0.1. Smaller values of learning rate require large numbers of weak learners to maintain a constant training error. Empirical evidence suggest that small values of learning rate favors better test error, as the constraint the given number of weak learners to maintain a constant training error.

3.6. Feature Selection

In practical rock CT segmentation/classification task apriori information representing different phases (pore, matrix, rock, cracks, trapped pores ect.) in the XCT image is given to ML algorithms for segmentation or training the classification model. The dataset used as apriori information contains pixel values representing different phases in the XCT image as is termed as feature vectors (FV). For unsupervised k-means, FCM, SOM ten slices from a XCT images were used to develop the FV. For FFANN five images out of ten were used to train the network; for LS-SVM and ensemble based classifiers different subset of pixels representing the pore, mineral, matrix and noise regions were used as feature vectors. The total number of pixel used to train and test each ML algorithm is shown in Table 3. 1

Table 3. 1 The number of pixels used for training and testing the classification model

	Andesite		Rotliegend Sandstone	
Type of classifiers	No. of training pixels	No. of testing pixels	No. of training pixels	No. of testing pixels
k-means		31,577,290		13,681,600
fuzzy c-means		31,577,290		13,681,600
self organized maps		31,577,290		13,681,600
artificial neural networks	15,788,645	31,577,290	6,840,800	13,681,600
least square support vector machine	2077	31,577,290	1511	41,943,040
Bragging and Boosting	2077	31,577,290	1511	41,943,040
	Synthetics sample (Musli)		Berea sandstone	
Type of classifiers	No. of training pixels	No. of testing pixels	No. of training pixels	No. of testing pixels
k-means		10,000,000		40,56,000

fuzzy c-means		10,000,000		40,56,000
self organized maps		10,000,000		40,56,000
artificial neural networks	5,000,000	10,000,000	20,28,000	40,56,000
least square support vector machine	1655	10,000,000	1366	40,56,000
bragging and boosting	1655	10,000,000	1366	40,56,000

3.7. Performance

Computational performance was measured in terms of the segmentation and classification speed of the ML algorithms. Test were performed on Windows Server 2008 R2 Standard 64-bit Operating System, with two six-core processor Intel Xenon, CPU (E645, 2.40 GHz) and installed memory (RAM) of 48.0 GB.

3.8. Accuracy

There is a wide set of evaluation metrics available to compare the quality of clustering and classification algorithms. For unsupervised clustering techniques accuracy can be evaluated by intrinsic i.e how close are the elements to each other within a cluster and how apart to elements of other clusters (Amigó et al. 2009). Extrinsic metrics on the other hand, is a comparison between the output of the clustering system and *gold standard* usually built using human assessors (Amigó et al. 2009). (Strehl 2002); (Meilă 2003) and (Amigó et al. 2009) proposed several types of cluster evaluation metrics tested on different mathematical constraints. However, the appropriate metrics for cluster evaluation is non-trivial and is still a subject of discussion. In this work, we use extrinsic evaluation metrics 'Purity' and 'Entropy' which are most commonly used for clustering problems. The idea is to identify ideal class(es), representing the 'best' porosity values and to compare the clustering algorithm.

Any supervised classification is incomplete until the assessment of its accuracy has been performed. The supervised classification models are trained with apriori information which is almost a subset of classes under investigation. (Stehman and Czaplewski 2003) pointed out the accuracy assessment of a supervised classification problem can be assessed in three different steps: (1) the design of the model, (2) the response of the designed model to obtain the true classification rate (minimum error rate) and (3) the analysis of the classified data.

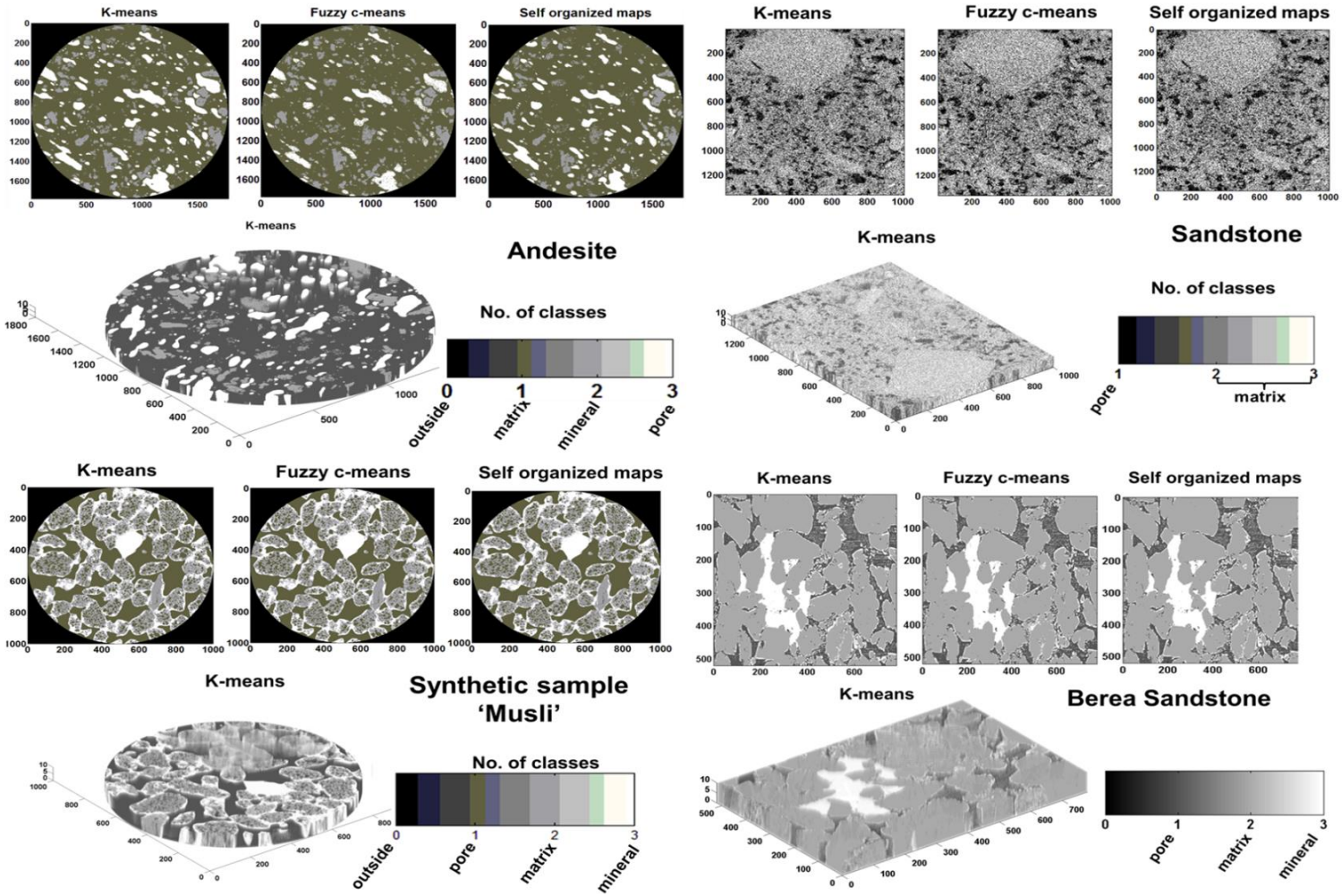

Figure 3. 4 The top, middle and last panel show the 2D segmented images and volume rendered plots of respective samples using unsupervised networks (Andesite figure has been modified after Chauhan et al 2016)

The most common methods used for the analysis of the classified data are confusion matrix or κ – error statistics introduced by (Fleiss et al. 1969). For our accuracy assessment study we have used step 2. the response of the designed model to obtain the true classification rate. The metrics such as mean square root error (MSE), receiver operational characteristics and 10-K fold cross validation for AANN, LS-VM and ensemble classifiers respectively.

Subsections below illustrate all the metrics used unsupervised, supervised and ensemble classifiers.

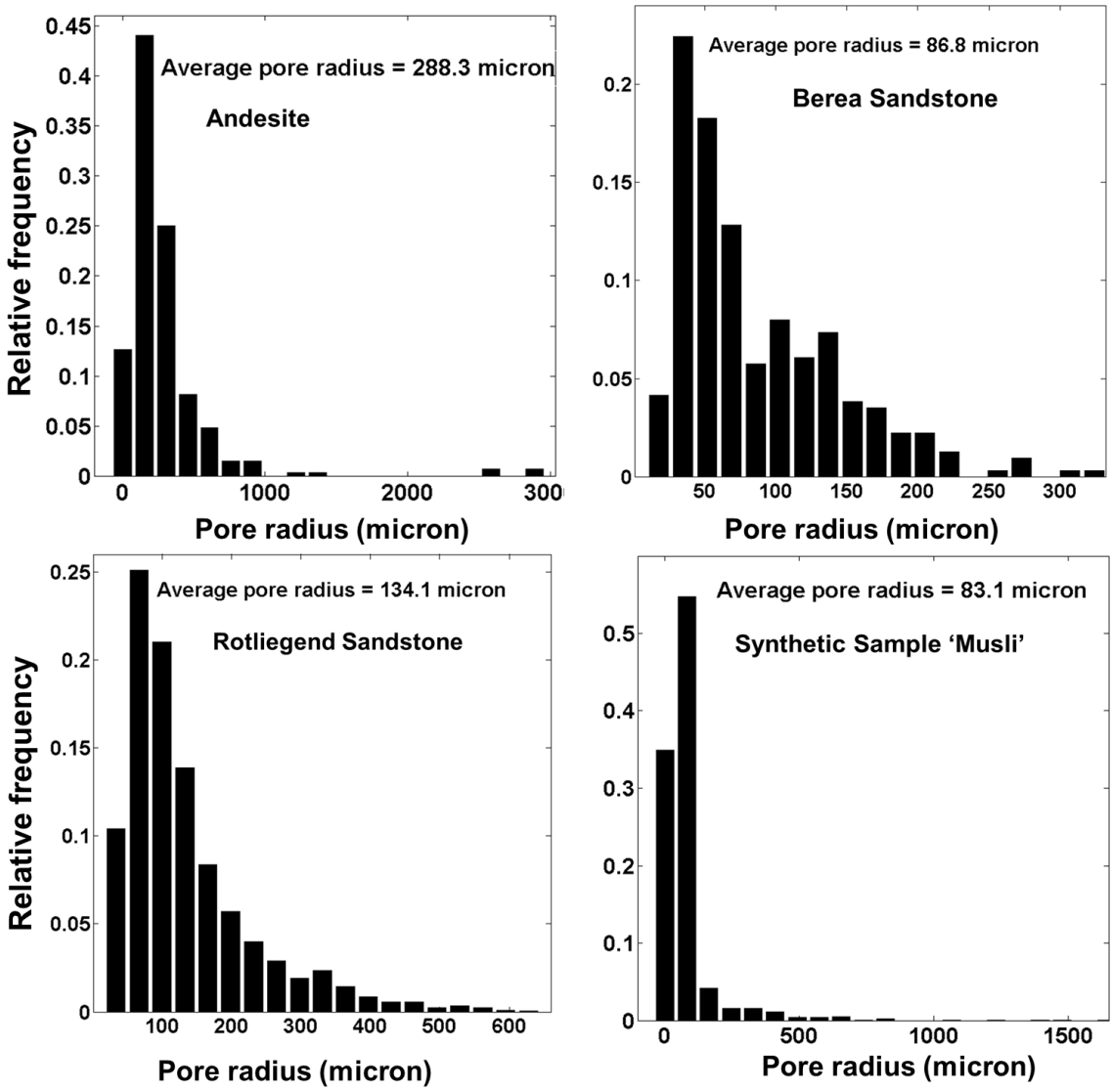

Figure 3. 5 The pore size distribution of different rock samples using watershed technique

3.8.1. Entropy and Purity

The Entropy of a class reflects how the members of the *k* pixels are distributed within each class; the global quality measure is by averaging the entropy of all classes.

$$\text{Entropy} = -\sum_j \frac{n_j}{n} \sum_i P(i,j) \times \log_2 P(i,j) \qquad (3.2)$$

Where $P(i,j)$ is the probability of find an item from the category *i* in the class *j*, where n_j is the number of items in class *j* and *n* the total number of items in the distribution.

Purity focuses on the frequency of most common category in to each class. If *C* is the set of pixels to be evaluated and *L* the set of classes.

Purity = $\sum_i \frac{|C_i|}{N} \max_j Precision\ (C_i L_j)$ (3.3)

Where the precision of pixels C_i for a given classes L_i is defined as:

$Precision\ (C_i L_j) = \frac{|C_i \cap L_j|}{|C_i|}$ (3.4)

3.8.2. Mean Square Root Error

The most commonly used error metrics to assess the accuracy of the FFANN the mean squared error (MSE), the mean squared relative error (MSRE), the coefficient of efficiency (CE), and the coefficient of determination (R^2), shown in the equations below.

MSE = $\sum_{i=1}^{n} \frac{(Q_i - \tilde{Q}_i)^2}{Q_i^2}$ (3.5)

MSRE = $\frac{\sum_{i=1}^{n} \frac{(Q_i - \tilde{Q}_i)^2}{Q_i^2}}{n}$ (3.6)

CE = $1 - \frac{\sum_{i=n}^{n} (Q_i - \tilde{Q}_i)^2}{\sum_{i=n}^{n} (Q_i - \bar{Q}_i)^2}$ (3.7)

$R^2 = \left[\frac{\sum_{i=1}^{n} (Q_i - \bar{Q}_i)(\tilde{Q}_i - \acute{Q}_i)}{\sqrt{\sum_{i=1}^{n} (Q_i - \bar{Q}_i)^2 \sum_{i=1}^{n} (\tilde{Q}_i - \acute{Q}_i)^2}} \right]^2$ (3.8)

Where $\tilde{Q}_i$ are the classified images by FFANN. Q_i are the images used for training the FFANN (K-means and FCM images) $\bar{Q}_i$ is the mean of the images used for training FFANN and $\acute{Q}_i$ is the mean of the classified images To evaluate accuracy of our FFANN model we looked at the MSRE values. Lower the MSRE value higher is the accuracy of the prediction.

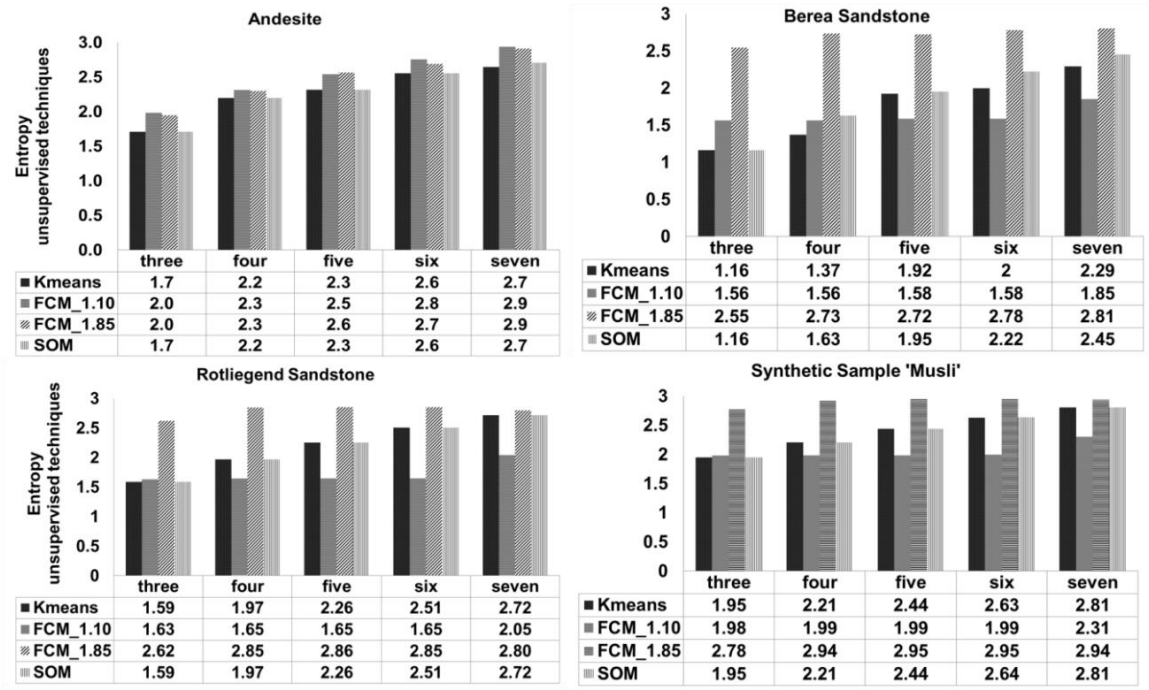

Figure 3. 6 Entropy values of unsupervised techniques plotted for respective samples

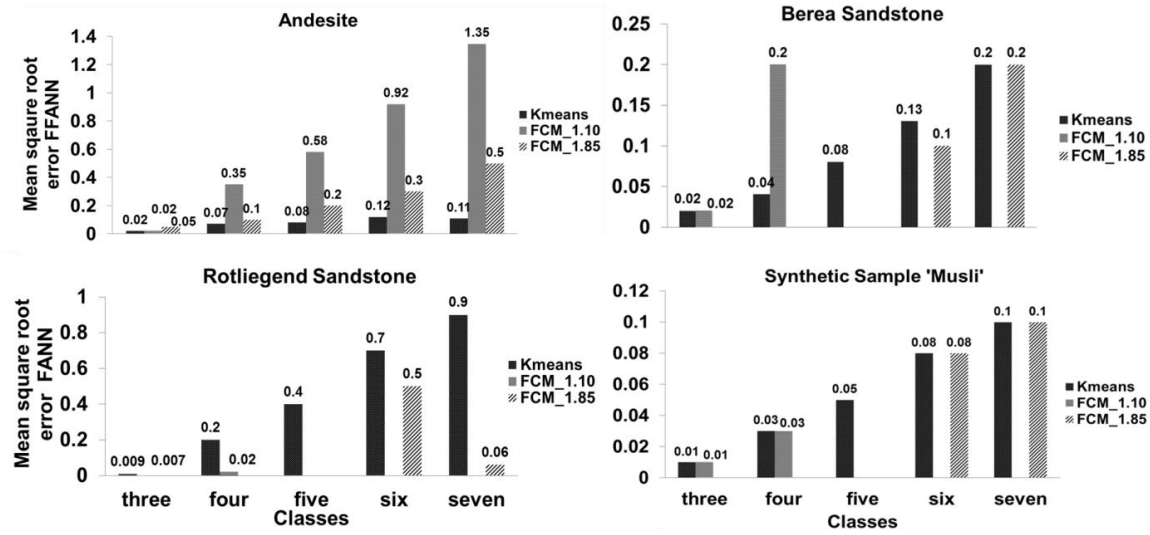

Figure 3. 7 Mean square root error values of feed forward artificial neural network (FFANN) obtained for respective samples. FFANN was trained using segmented datasets of k-means, Fuzzy C-means with a membership function of 1.10 and 1.85

3.8.3. **Receiver Operational Characteristics**

Receiver Operational Characteristics (ROC) curves have long been used in the signal detection theory (Bradley 1997). It is a good way of cross-validation of classifiers accuracy (probability of classifiers correct response *P(C))*.

Accuracy (1 - Error) = $\frac{T_p+T_n}{C_p+C_n} = P(C)$ (3.9)

Sensitivity (1 - β) = $\frac{T_p}{C_p} = P(T_p)$ (3.10)

Specificity (1 - α) = $\frac{T_n}{C_n} = P(n)$ (3.11)

Where, $T_p \; and \; T_n$ are the true positive and true negative examples and $C_p \; and \; C_n$ are total number of true positive and true negative examples.

Probability of false positive is $P(F_p)$ = α

Probability of true positive is $P(T_p)$ = (1 - β)

The accuracy is determined by calculation area under the curve (AUC), and the simplest was to do that is by using trapezoidal approximation

AUC = $\sum_i \left\{(1 - \beta_i \cdot \Delta\alpha) + \frac{1}{2}(\Delta(1 - \beta).\ \Delta\alpha)\right\}$ (3.12)

In our case the AUC was determined using the trapezoidal approximation for each exponential curve and the values was fraction was multiplied by hundred to obtain value in percent.

3.8.4. 10-fold Cross Validation

The idea for cross-validation was first proposed by (Larson 1931). Cross-Validation is a statistical method of evaluating and comparing learning algorithms by dividing data into two segments: one used to learn or train a model and the other used to validate the model. The problem with evaluating such a model is that it may demonstrate adequate prediction capability on the training data, but might fail to predict future unseen data. cross-validation is a procedure for estimating the generalization performance in this context.

Later, (Kohavi 1995) and (Dietterich 1998) investigated several approaches to estimate accuracy of classifier using different combinations of K-fold cross-validation techniques. And recommended 10-fold cross-validation one of the best cross validation technique, as it mitigate biases despite variances in the size of training and testing data sets.

On the onset of 10 K-fold cross-validation, the data set is initially stratified and partitioned in to 10 equally (or nearly equally) segments or folds. Subsequently 10 iterations of training and validation are performed such that, within each iteration a different fold of the data is held-out for validation, while the rest folds are used for learning.

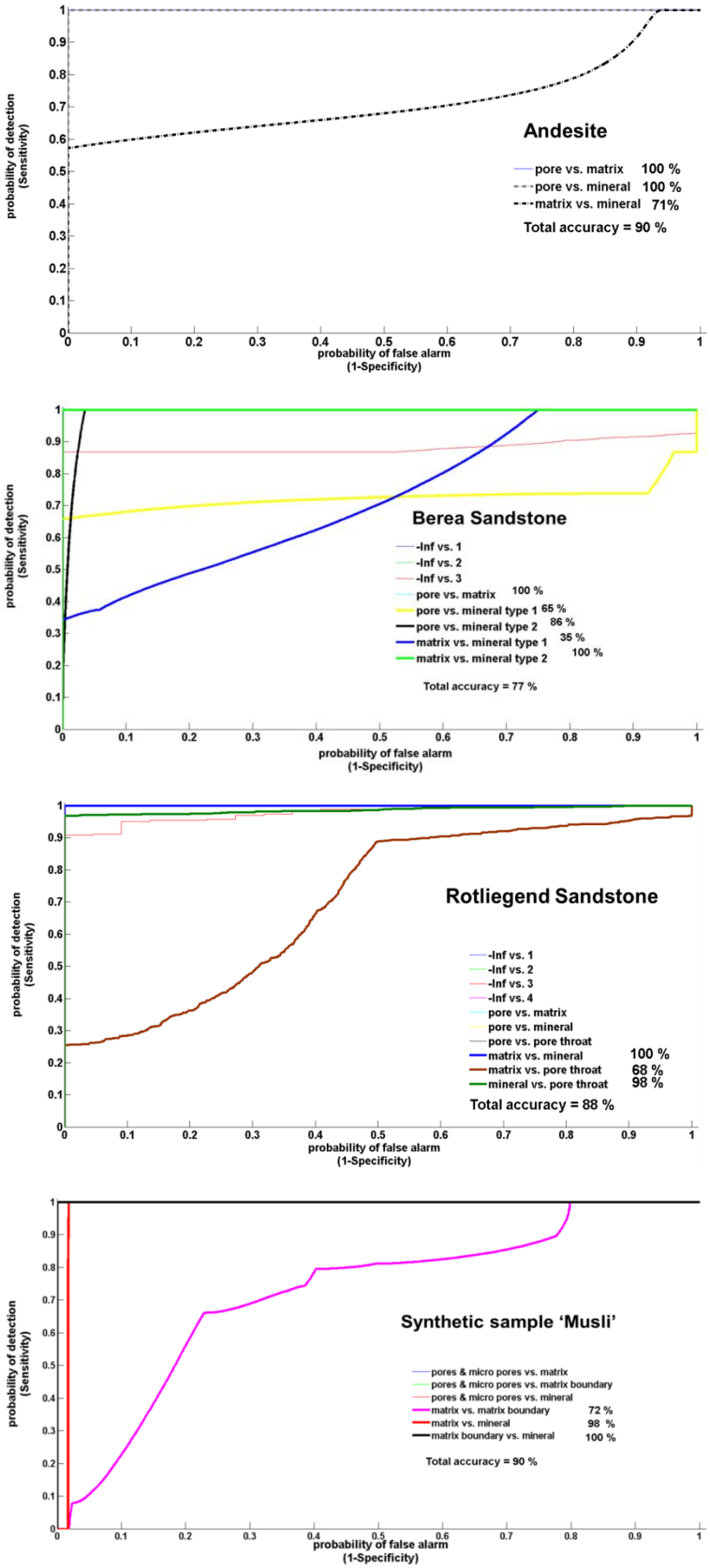

Figure 3. 8 Receiver operational characteristic curves depicting the accuracy of least square support vector machine multi classification scheme for class four. Few curves which appear in the legend have close proximity to the x-axis and lie behind other curves therefore are invisible

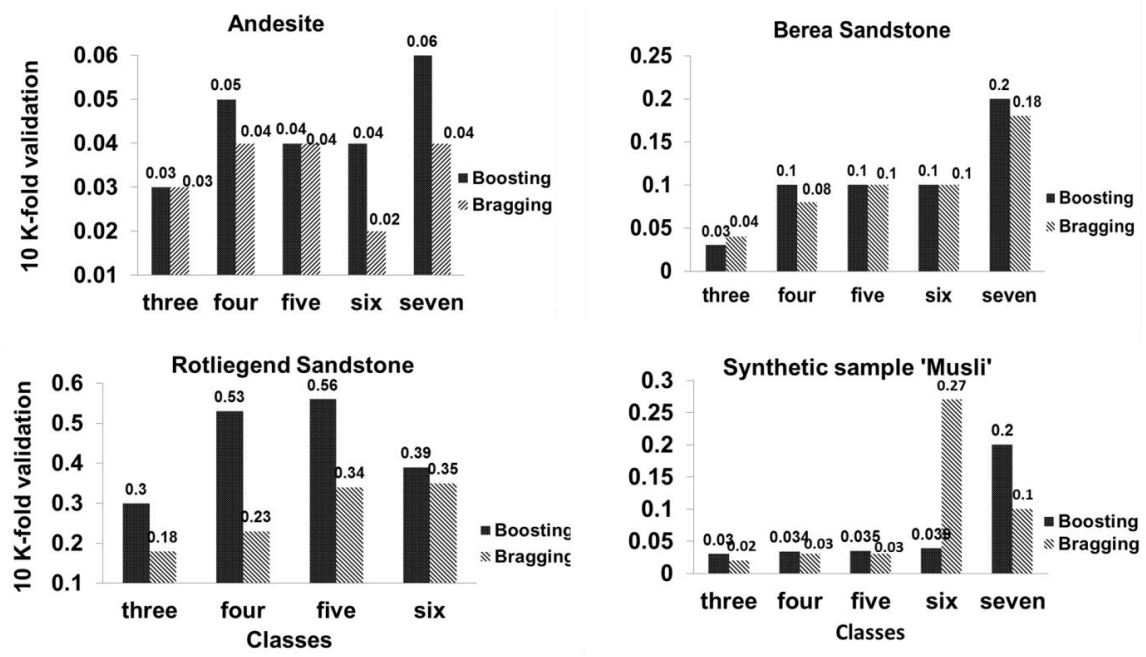

Figure 3. 9 Accuracy of ensemble classifiers Boosting and Bragging calculated using 10 K-fold validation for respective samples

3.9. Results and Discussions

3.9.1. Porosity and Pore Size Distribution

The porosities which were determined from the stack of ten XCT slices for three to seven classes using different ML techniques are shown in the Figure 3. 2. The estimated porosity is the ratio between the pore phase voxels and entire sample volume multiplied by 100. In general, the porosity using unsupervised ML techniques agree well for all the four samples within ±1.2 % for each class. For Andesite, Berea, sandstone, Rotliegend sandstone and Musli, the averaged estimated porosity sum over all classes is 15.8 ± 2.5 %, 16.3 ± 2.6 %, 13.4 ± 7.4 % and 48.3 ± 13.3 % respectively. This is in good agreement to the experimental porosity values obtained for Andesite, Rotliegend sandstone using GeoPycpynometer and Berea Sandstone as reported in Ändra et al. (2013). The large standard deviation in the case of sandstone and Musli is caused by FCM segmentation scheme. When the membership function is tightly constrained [1.10, 1.35] the segregation between pore phase voxels and pore throat voxels is underestimated contributing to the increase in porosity. Conversely, when membership function loosely constrained [1.60, 1.85] pore throat and micro pores are segmented as matrix phases resulting in decrease in porosity and increase in matrix phase, which is clearly visible in the volume fraction plot of Sandstone and Musli in Figure 3. 3. The low standard deviation in the estimated porosity values of Andesite is due to the absence of micro porosity and interconnected pores. The pore, mineral and matrix phases are distinct from each other therefore the ML techniques have less difficult in segmentation and classification. Figure 3. 4 shows the segmented images using unsupervised technique and respective volume rendered images.

Pore size distribution (PSD) of Andesite, Sandstones and Musli was computed using the method suggested by Rabbani et al. (2014). The segmented grey scale images where first

converted to binary images using thresholding technique. Morphological and filtering operations were performed based on the complexity of the segmented images. Distance

transform to convert the bright area into catchment basin and later watershed transformation was performed to segment the pore boundaries. Figure 3. 5 shows the PSD and average pore radius of Andesite, Berea sandstone, Rotliegend sandstone and Musli from k-means segmented images.

3.9.2. Performance and Accuracy Analysis

Performance in the form of computational time is tabulated in Table 3. 2. The k-means algorithm is the fastest among all the ML techniques because segmentation of phases into different classes is based on nearest neighbourhood distances measurements; unlike other ML techniques (exception FCM), where the classification is governed by classification models.

In case of supervised techniques the computational speed is correlated to the size of the feature vector used for training the classification model and post processing of the unknown dataset. One reasons is that supervised techniques are based on a 'single' classification model; training and cross validation of the model with a large amount of feature vectors consumes time. This can be correlated to the high computational time of the Andesite sample using FFANN, were five slices were used to train the classification model compared to other samples where the classification model was trained using only one slice. For LS-SVM – as feature vector pixels are less than 1 % of the total pixel values for the all the samples – the training of the classification model took 1 to 10 minutes. The high computational time was consumed in post processing, large unknown dataset using the trained model. In the case of ensemble classifiers the post processing of an unknown dataset took longer compared to the training of the respective (bootstrapped weak) classification schemes. As the Rotliegend sandstone is densely packed with very low porosity, it resulted in low contrast and badly resolved XCT dataset. As a consequence, the individual (weak) classification models required more computational time to reach to a consolidated nearly accurate well classified result. Therefore, the processing time of Rotliegend sandstone images by ensemble classifiers was higher compares to other XCT samples.

Our clustering problem is to determine the most appropriate class for each pixel. That is, we wish to identify which of the unsupervised ML technique satisfies properties of "cluster homogeneity" (i.e. not mixing items belonging to different categories) and "cluster completeness" (i.e. how good items belonging to same categories are group together) defined by (Amigó et al. 2009). Therefore, the metrics entropy and purity were chosen to evaluate the accuracy of unsupervised ML techniques. The entropy values were calculated using Eq. 2. on the 3D stack of ten slices for each class and are shown in Figure 3. 6. In general class three and four have the lowest entropy values compared to other classes. This shows that if cluster homogeneity and cluster completeness gets violated this may lead to misclassification. Among the three unsupervised ML techniques, k-means has the lowest entropy values therefore it can be assumed that k-means performs the best segmentation compared to SOM and FCM.

For FFANN the accuracy was interpreted using Eq.6 and Eq. 8 and the MSE error shown in Figure 3. 7. FFANN was trained using k-means and FCM and was tested on raw XCT

images of the respective samples. The testing dataset (3D stack of raw images) was scaled between three to seven class values before the start of the testing cycle. In the case of Berea, Rotliegend and Synthetic sample, when the membership function was tightly constrained to 1.10, FCM was able to segment, pore, matrix and mineral grain phases into maximum of three and four classes. Similarly, on moderate (1.60) and looseconstrained (1.85) membership function FCM yield maximum of five, six and seven classes respectively. This explains the variance in the number of dataset used for validation of FFANN. The lower the MSE value, the better is the accuracy; the accuracy decreases with over classification (for class five to six). Different settings such as, increase of the number of training slices up to five and increasing the number of neuron from ten to thirty did not shown any significant improvement in the accuracy. Among all the XCT samples, the worst accuracy was found for Rotliegend sandstone. Based on our analysis, we suggest that FFANN may not be the best suited ML technique for clustering analysis.

In the case of LS-SVM, the low variance seen in the porosity values up to class six, is the indication that LS-SVM is one among the most suitable ML technique for phase segmentation analysis of XCT images. As the hand-picked feature vector dataset of class four had an appropriate mix of all the phases and desired amount of noise, it gave the best trade-off between quality and speed. Hence we show the accuracy of LS-SVM for classification of class four using ROC curve (Metz 1978) in Figure 3. 8. The slope of the ROC curve gives the accuracy of classification which was computed using Eq. 12. The accuracy ranges between 77 % for Berea sandstone, 88 % for Rotliegend sandstone and 90 % for Andesite and Synthetic sample Musli. Up to 100 % accuracy in achieved in discriminating the pore phase with respect to mineral and matrix phases.

Ensemble classifiers also show low variance in the porosity values as LS-SVM because of the same feature vectors used. The accuracy of the ensemble classifiers were tested using 10 K fold validation technique (Quinlan 1996) is shown in Figure 3. 9. Both Bragging and Boosting classifiers where trained using the training data set. The training dataset comprises of the pixel values representing pore, mineral, matrix, noise phases and feature vectors. The initial growth of the leaf size was started with five and the corresponding weak classifiers were trained up to thousand iterations (Breiman 1996). The accuracy was determined by 10K fold cross validation techniques. The best accuracy was achieved for Andesite and Musli XCT (with an exception for class six) images and the worst for Rotliegend sandstone going up to 0.56.

Table 3. 2 Show the computational time for processing ten slices

Machine learning Techniques	CPU: Time (hrs:min:sec)			
	Andesite	Rotliegend sandstone	Synthetic sample Musli	Berea sandstone
K-means	00:15:35	00:12:04	00:10:59	00:05:33
FCM	00:29:19	00:56:03	00:42:21	00:41:05
SOM	01:07:06	1:41:47	01:11:23	00:33:32

FFANN (training using K-means)	08:58:18	00:11:50	00:10:40	00:11:12
LS-SVM[a]	63:29:35	03:22:58	03:02:15	01:45:17
Bragging	05:57:05	07:32:22	12:19:40	03:51:13
Boosting	07:47:05	09:52:56	06:14:58	03:20:42:

a open source public library provided by K.U. Leuven university –ESAT department- SCD-SISTA division was used.

http://www.esat.kuleuven.be/sista/lssvmlab/

3.10. Conclusions

In this study the performance and accuracies of ML techniques were validated and relative porosity and pore size distribution of Andesite (altered minerals), Berea sandstone, Rotliegend sandstone (inter connected pores) and Musli (micro porosity) rock samples were computed. The total averaged porosity values obtained using unsupervised, supervised and ensemble classifiers are shown in Figure 3. 10 and are in good agreement with the experimental values obtained using GeoPycpynometer and data reported in (Andrä et al. 2013a). The high standard deviations up to 13 % seen in the case of Synthetic sample Musli can be attributed to the misclassification caused by ensemble classifiers at class six. The feature vector set contained seventy three pixels representing noise was labelled as class six shown in Figure 3.2. As and when, the training/testing was performed using feature vector up to class six the ensemble classifiers showed high misclassification. Later, stabilized to perform accurate classification when feature vector up to class seven (class seven represented three hundred and ninety three pixel values of cracks and specks in the image) were used. It is difficult to speculate why this happens.

Our analysis shows unsupervised ML techniques perform well with filter based feature extraction techniques. In terms of computational time, k-means outperforms all the other ML techniques. Fuzzy c-means can distinguish well between pore and pore-throat boundaries, given that the membership function is loosely constrained between 1.60 - 1.85. It was found that different tuning parameters (such as different FCM membership criteria and different SOM topologies and distance functions) need to be tested for the unsupervised techniques. A SOM topology “gridtop” layout (neurons arranged in a grid format) and a SOM Manhattan distant function (sum of the absolute difference) gave consistent results and FCM membership function between [1.35 - 1.85] gave consistent results. Low entropy values of k-means indicates that k-means is more accurate compared to fuzzy c-means and self-organized maps.

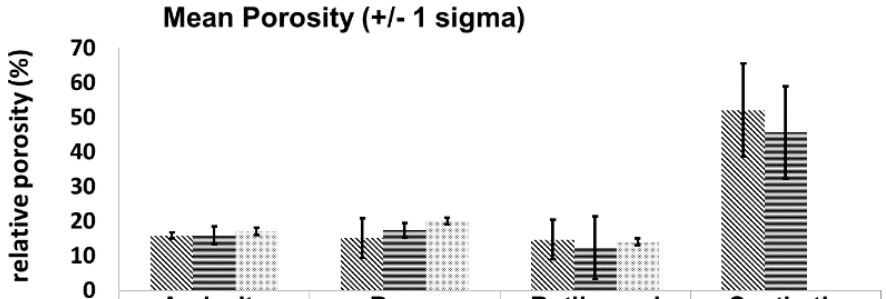

	Andesite	Berea	Rotliegend	Synthetic
Supervised + Ensemble classfiers	16	15	15	52
Unsupervised	16	17	12	46
Laboratory measurements	17	20	14	

Figure 3. 10 Mean porosity value obtained using supervised, ensemble classifiers and unsupervised machine learning techniques

In the case of supervised techniques the computational time was significantly improved by reducing the training dataset of feed forward artificial neural networks (FFANN) and by careful selection of feature vector dataset for least square support vector machine (LS-SVM). Based on our analysis we conclude that FFANN may not be best suited for clustering analysis; due to difficulty in scaling the training dataset (XCT raw files), the interpretation of clustering labels and accuracy becomes extremely difficult. Additionally, the accuracy in terms of mean square root error of the validation cycle (training and repeated testing) is largely regularized by fine and coarse scaling of the testing dataset, which may not always correspond to the image classification. As a consequence, there were cases where despite low accuracy (high MSE error) the classification performed by FFANN was good. On the contrary LS-SVM showed to be one of the best and accurate supervised ML technique for phase segmentation problem. However, it strongly relies on the craft with which the feature vector dataset is constructed. The user has the flexibly to decide which phases or feature are most relevant for phase segmentation. The authors suggest using the histogram plot of the raw image or k-means (or any other unsupervised ML technique) as an orientation for feature vector selection. It is further recommended that the first and second class labels (ex. class three and class four) should contain predominantly phases such as pore, matrix, mineral and noise pixels. Consequently, other interesting feature pixels can be included. A suitable balance has to be found, such that the classifier is not excessively trained on one particular feature and get stuck in local minima. Thereafter, the receiver operation characteristic (ROC) curve validation technique is best suited for accuracy assessment of LS-SVM.

Ensemble classifier can be the second best alternative to tackle phase segmentation problems as it also relies on the feature vector dataset to train the classification model; therefore, the user has more control over the classification scheme. However, the weak learners involved in the ensemble classification scheme remain as black-box to a large extent; therefore, appropriate tuning of the individual weak learners to optimise computational speed and accuracy may be cumbersome. To have a better control over the ensemble classification scheme, and for future work we suggest an ensemble classifier with k-means, FCM and LS-SVM as weak learners.

4. CobWeb 1.0 code for automatic tomographic image analysis based on machine learning algorithms

This chapter is largely based on the manuscript published as electronic preprints (e-prints) arXiv repository and is under moderation. It is distributed using Creative Common Public License 4.0

Chauhan, S., Sell, K., Enzmann, F., Rühaak. W., and Wille, T., Sass, I., and Kersten, M.: CobWeb (2018): CobWeb — a toolbox for automatic tomographic image analysis based on machine learning techniques: application and examples

4.1. Abstract

In this study, we introduce CobWeb 1.0 which is a graphical user interface tailored explicitly for the accurate image segmentation and representative elementary volume analysis of digital rock images derived from high resolution tomography. The CobWeb code is a work package deployed as a series of windows executable binaries which use image processing and machine learning libraries of MATLAB®. The user-friendly interface enables image segmentation and cross-validation employing K-means, Fuzzy C-means, least square support vector machine, and ensemble classification (bragging and boosting) segmentation techniques. A quick region of interest analysis including relative porosity trends, pore size distribution, and volume fraction of different phases can be performed on different geomaterials. Data can be exported to ParaView, DSI Studio (.fib), Microsoft® Excel and MATLAB® for further visualization and statistical analysis. The efficiency of the new tool was verified using gas hydrate-bearing sediment samples and Berea sandstone, both from synchrotron tomography datasets, as well as Gorsmont carbonate rock X-ray micro-tomographic dataset. Despite its high sub-micrometer resolution, the gas hydrate dataset was suffering from edge enhancement artefacts. These artefacts were primarily normalized by the dual filtering approach using both non-local means and anisotropic diffusion filtering. The desired automatic segmentation of the phases (brine, sand, and gas hydrate) was thus successfully achieved using the dual clustering approach.

4.2. Introduction

Despite the availability of both commercial and open source software for digital rock physics (DRP) analysis as compiled in Figure 4. 1, an ideal tool for accurate automatic image analysis at ambient computational performance is difficult to pin point. The best practice so far among researchers is to alternate between different available software tools and to synthesize the different datasets using home-brew workflows. Porosity and in particular permeability can vary dramatically with small changes in segmentation, as significant features can be lost when thresholding greyscale tomography images to binary images, even if using the most advanced data acquiring techniques like synchrotron tomography (Leu et al. 2014). Our new CobWeb 1.0 visualization and image analysis toolkit addresses some of the challenges of selecting representative elementary volume (REV) for X-ray computed tomography (XCT) datasets reported earlier. It is customized to perform image analysis and accurate greyscale phase segmentation of reconstructed high resolution XCT and synchrotron tomographic datasets. As the only one currently available, it is based on machine learning techniques of excellent performance for segmentation analysis as detailed previously (Chauhan et al. 2016b; Chauhan et al. 2016a). This software tool package was developed on a MATLAB® workbench and can be used as a Microsoft Windows standalone executable (.exe) files or as a MATLAB® plugin. In this paper, we demonstrate exemplarily 3D tomographic REV analysis of Berea Sandstone, Grosmont Carbonate Rock, and gas hydrate-bearing sediment datasets. For the latter geomaterial, (Sell et al. 2016) highlighted problems with the edge enhancement (ED) effect and recommended image morphological strategies to compensate for this artefact. In this paper, we suggest a strategy to eliminate ED artefacts using the same dataset using the machine learning approach. The respective MATLAB code is provided in the Appendix. The salient features of CobWeb 1.0 and its overall framework are described in Section 2. Section 3 highlight the image segmentation techniques used in Section 4 for REV, relative porosities and pore size distribution analysis.

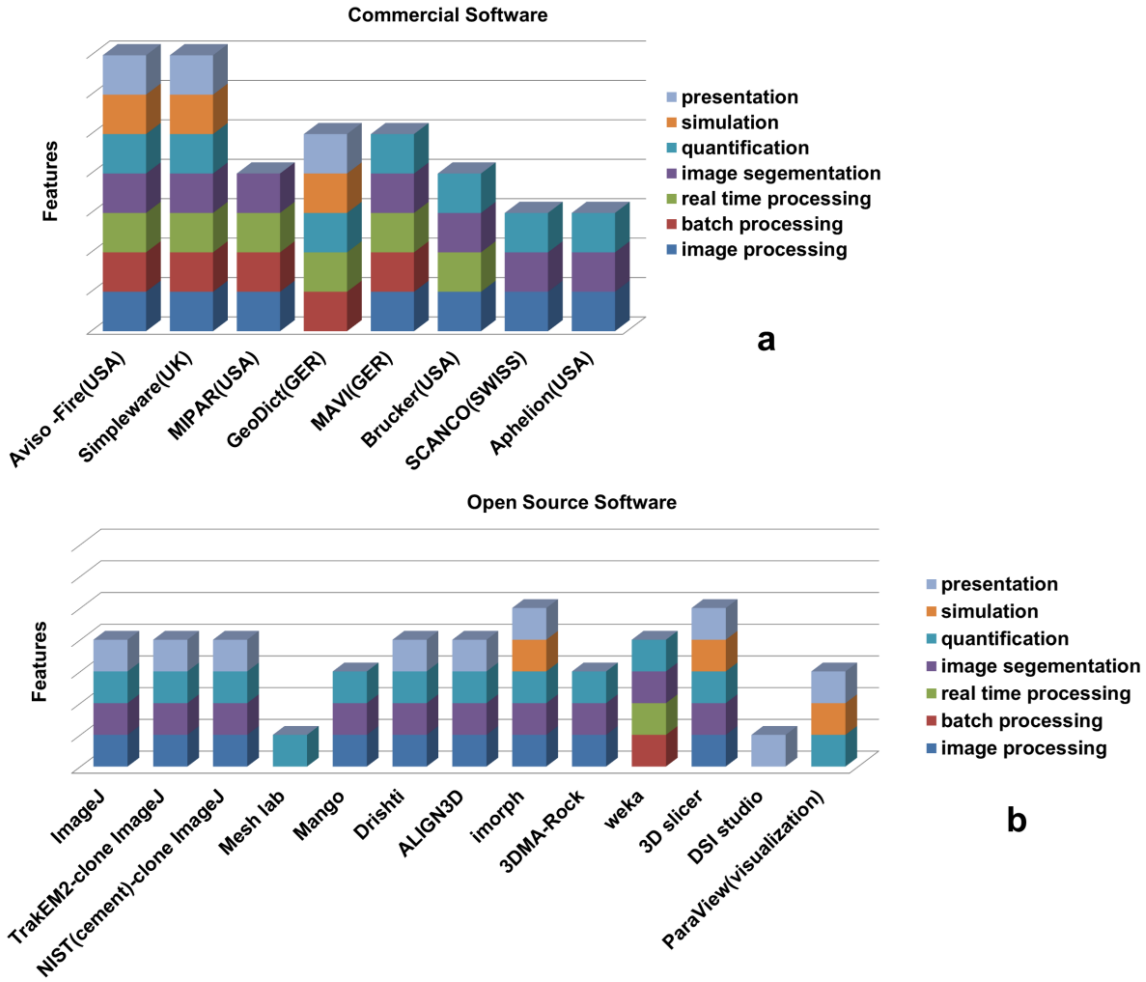

Figure 4. 1 Market survey of the currently available commercial software (a) and open source software (b) assisting in digital rock physics analysis with features as indicated in legend

4.3. CobWeb

4.3.1. Salient Features

The word *Cobweb* means “a tangled three-dimensional spider web”, i.e. something resembling a cobweb in delicacy or intricacy (Oxford Dictionaries). According to Marriam-Webster, it may also mean something that entangles obscures or confuses, as is the philosophy of machine learning - elegant, sophisticated yet stochastic and confusing. This inspired us to name our software tool as CobWeb. The first version 1.0 enables to read and process (reconstructed) XCT files in both tiff and raw formats. The graphical user interface (GUI) is embedded with vizual inspection tools to zoom in/out, cropping, color, and scale, assist in the visualization and interpretation of 2D and 3D stack data. Noise filters such as non-local means, anisotropic diffusion, median and contrast adjustments are implemented to increase signal-to-noise ratio. The user can choose from a series of five different segmentation algorithms, namely K-means, Fuzzy C-means (unsupervised), least square support vector machine (supervised), bragging and boosting (enable classifiers) for accurate automatic segmentation and cross-validation. Relevant material properties like relative porosities, pore size distribution, volume fraction (pore, matrix, mineral phases) can be quantified and visualized as graphics output. The data can be exported into different file formats such as Microsoft® Excel (.xlsx), MATLAB® (.mat),

ParaView (.vkt) and DSI studio (.fib). The current version is supported for Micosoft® Windows PC operating systems (Windows 7 and 10).

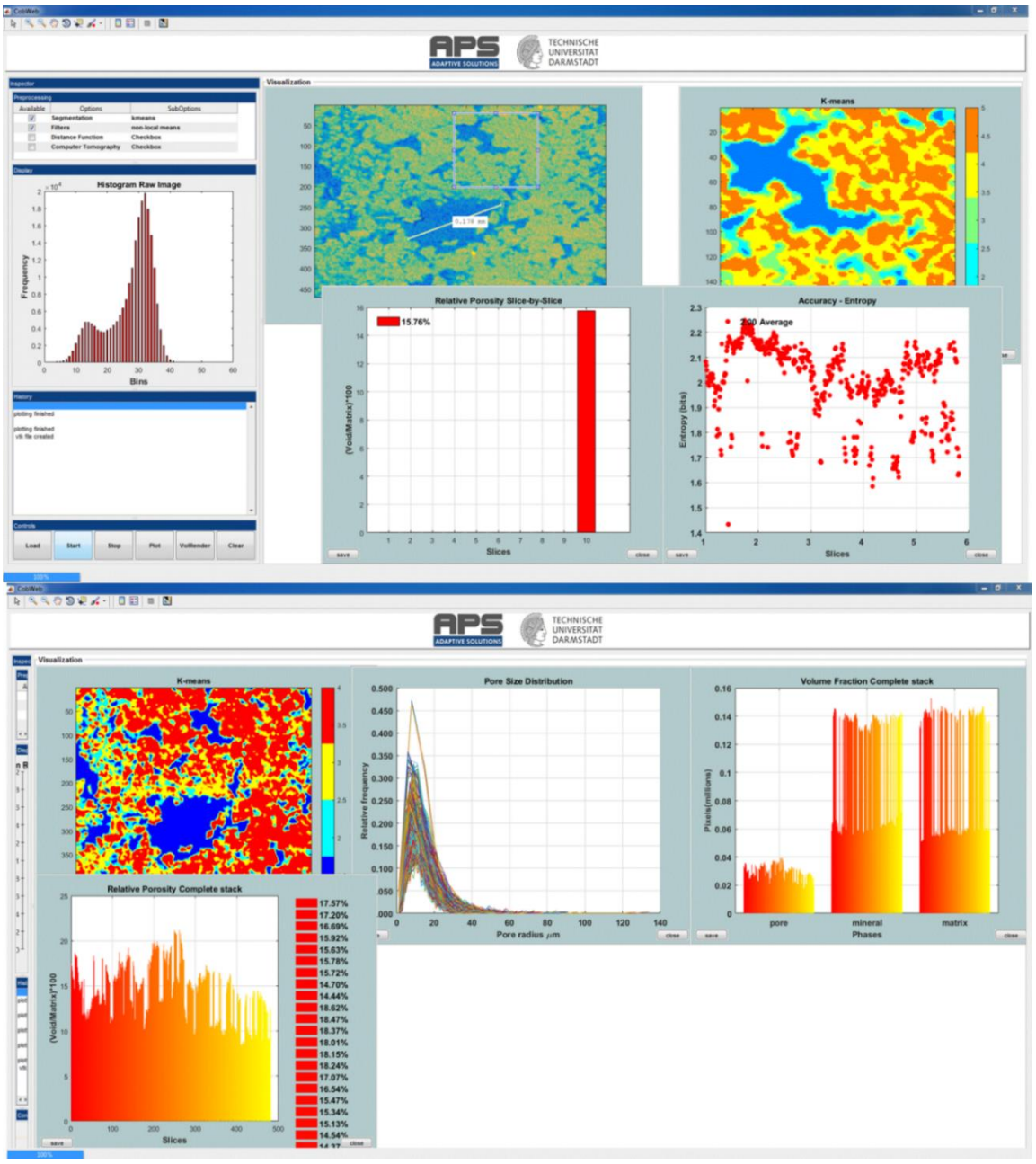

Figure 4. 2 Snapshots of the CobWeb GUI. XCT stack of Grosmont Carbonate rock is shown as an example for representative elementary volume analysis. The top panel displays the XCT raw sample, the K-means segmented ROI, and the porosity of single slice No. 10. The bottom plot shows pore size distribution of the complete REV stack, the relative porosity and volume fraction, respectively

4.3.2. Window Panel

The main GUI window panel divides into three main parts (Figure 4. 2), the tool menu strip, the inspector panel, and the visualization panel. The tool strip contains menus for zoom in and out, pan, rotate, point selection, color bar, legend bar, and measurement scale functionalities. The inspector panel is divided into subpanels where the user can configure the initial process

settings such as segmentation schemes (supervised, unsupervised, ensemble classifiers), filters (contrast, non-local means, anisotropic filter, fspecial), and distance functions (link distance, Manhattan distance, box distance) to assist segmentation and geometrical parameter selection for image analysis (REV, porosity, PSD, volume fraction). The display subpanel records and displays the 2D video of the XCT stack and the histogram of the raw image(s). The history subpanel is a uilistbox that displays errors, processing time/status, processing instruction, files generated/exported and executed callbacks. The control subpanel is an assemblage of uibuttons to initialize the XCT data analysis process and the progress bar. The visualization panel is where the results are displayed in several resized windows, which can be moved, saved and deleted. The window panels displayed in visualization module are embedded with uimenu and submenu to export, plot and calculate different variables like porosity, PSD, volume fraction, entropy, or receiver operational characteristics. To get the desired user functionalities, MATLAB® internal uilibaries where inadequate. Therefore, numerous specific adaptions were adopted from Yair Altman's undocumented Matlab website and the Matlab File Exchange community. Specifically, the GUI Layout Toolbox from David Sampson has been used to configure the CobWeb GUI layout; the uitable, which uses the MATLAB java-component was designed using uitable customization reoprt provided by (Altman 2014).

4.3.3. Overall Framework

An overview of the different modules of the CobWeb toolkit are compiled in Figure 4. 3**,** and the arrow displayed indicates the series in which they are executed. The advantage of using MATLAB® is the access to the structure and respective variables, which are used for further investigations. As a stand-alone, the GUI can be executed on different PC and HPC clusters without any license issues. The CobWeb 1.0 framework can be broadly divided into three modules.

4.3.4. Control Module

In the control module, the menu CobWeb creates the main figure panel, assembles the size/position of the panel, subpanel windows, initializes the control buttons and generates a main structure. Ideally, any button can be activated after the GUI is displayed, but an exception will be displayed in the history window, highlighting the next step. That is to load data, where the Load function checks the file properties, loads the data in .tiff and .raw format, creates and displays 2D video of the selected stack, save the video file in the current folder, and updates the respective variables to the main structure. The Stop function ends the execution. However, when the processing is inside a loop, the Stop function breaks the loop after the i-th iteration.

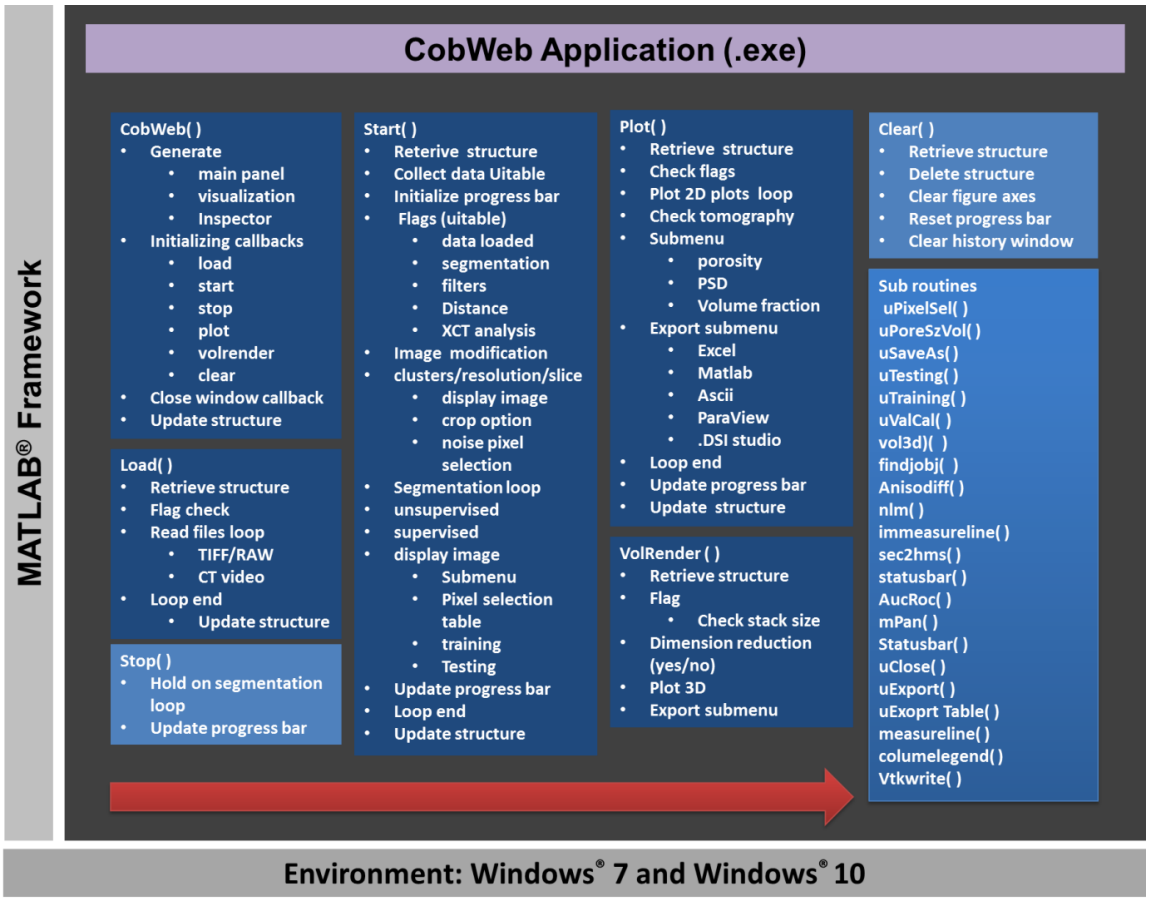

Figure 4. 3. The general workflow of the CobWeb software tool, where the arrow denotes the series in which different modules are compiled and executed. A separate file script is used to generate .dll binaries and executables

4.3.5. Analysis Module

The *Start* function inhabits the analysis category and is a densely nested function, where the bullet points and the indented bullet points represent the outer and the inner nested loops, respectively (Figure 4. 3). Initially, the data is gathered and a sanity check is performed to evaluate whether all the options are correctly selected. If the conditions are not satisfying, an exception alert pops up in the *History* panel highlighting the error and offers an alternative process. The second loop is the image modification loop, where initially the user input is required. This input comprises a desired cluster number, the given image resolution, and the slice number. Afterwards, the chosen slice is displayed in 2D format, and in a separated window. Following, an option of ROI selection is proposed to be accepted or denied. If the user accepts, the REV will be cropped and updated to the main structure and the cropped ROI is display in a separate window as a slice.

Based on the option selected in the *uitable*, the respective unsupervised and supervised loop is initialized. If LSSVM or bragging and bosting is chosen as segmentation scheme, a right click *uimenu* is initialized with options of pixels selection, training, and testing. On pressing the *Pixel Section* option, the subroutine *uPixelSel( )* initiates a *uitable* window representing the columns *Clusters*, *Features*, *X-Coordinate*, and *Y-Coordinate*, and requiring user inputs in the respective columns. The user can explore interesting features (pores, minerals, matrix, noise/specks) in the 2D image windows and collect the data

using zoom in, zoom out, and data cursor tools. Once the respective features X,Ycoordinates are feed in the uitable, the data has to be arranged and exported for training and testing. This is fulfilled by pressing the export button which initiates the subrountine uExportTable( ). The export subroutine collects a total of 36 (6 x 6) pixel values in the perimeter of X,Y coordinates of the respective features given in the uitable. Thereafter, with the training and testing options, respective models (LSSVM, Ensemble Classifiers) are trained using the pixel values of the representative slice. The classification is then performed on the 3D stack, and the main structure is updated. In the case of unsupervised techniques based on the option selected for image filtering, segmentation, distance function, the complete stack is processed. For FCM, the user is given an option to choose the membership criteria (Chauhan et al. 2016b) between the range one to two (decimal values).

The progress can be monitored by the progress bar, the color of the control buttons (red to grey) and the *History* window, which gives the related information on processing time, segmentation scheme, and filter options executed.

4.3.6. Visualization Module

The visualization module consists of the plot function and volume rendering function. The plot function is a densely nested function, where the bullet points and the indented bullet points in the

Figure 4. 3 represents the outer and the inner nested loops, respectively. The execution of the Plot() callback access the main structure, identifies the representative slice number, and plots the segmented 2D image in a new window. The displayed window is embedded with right click menu and submenus, namely:

- Porosity → Porosity, Pore Size Distribution
- Validate → Entropy, Receiver Operation Characteristics, 10-fold Cross Validation
- Export Stack → Paraview Format

When choosing the desired options mentioned above, their respective subroutines (uPoreSzVol, uCalVal, uExport) are started and the desired results are plotted as shown in Figure 4. 2. The user has the option to choose a single slice or the complete stack. The visualized parameter distributions display in a separate window and can further be exported using right-click menu into Excel, ASCII, or MATLAB formats.

The Export Stacks option bundles the complete stack in ParaView code format (.vkt files) using the subroutine function Vtkwrite. When the VolRender button is activated, the subroutine checks for the size of the stack and offer an option to perform volume reduction of the greyscale values. If ignored, depending on the computer RAM capacity, it may take relatively long time to plot a high quality volume rendered figure of the 3D stack. If accepted, the pixel information is 10-fold reduced, which fastens the plotting process but the image quality is hampered. Therefore, CobWeb 1.0 offers the option to export the stack and visualize the stack using ParaView or DSI studio.

4.4. Tomographic Datasets Used for Evaluation of CobWeb 1.0

4.4.1. Gas-Hydrate –bearing Sediments

The in-situ synchrotron-based tomography experiment and post-processing of synchrotron data conducted to resolve the microstructure of gas hydrate-bearing (GH) sediments is given in detail by (Chaouachi et al. 2015), (Falenty et al. 2015) and (Sell et al. 2016). In brief, thetomographic scans were acquired with a monochromatic X-ray beam energy of 21.9 KeV at Swiss Light Source synchrotron facility (Paul-Scherrer-Institute, Villigen, Switzerland) using the TOMCAT beamline (Tomographic Microscope and Coherent Radiology Experiment; Stampanoni et al, 2006). Each tomogram was reconstructed from sinograms by using the gridded Fourier transformation algorithm (Marone and Stampanoni 2012). Adjacent, a three-dimensional stack was derived resulting in an image size of 2560 x 2560 x 2160 voxels with a voxel resolution of 0.74 µm and 0.38 µm at 10-fold and 20-fold optical magnification, respectively.

4.4.2. Grosmount Carbonate Rock

The datasets of the Grosmont carbonate rock were obtained from the *GitHub* FTP server (http://github.com/cageo/Krzikalla-2012) provided for the benchmark project reported by (Andrä et al. 2013a, 2013b). They acquired the Grosmont carbonate rock for their benchmark test from Grosmont formation Alberta, Canada. The Grosmont formation was deposited during upper Devonian and is divided into four facies members, LG UG-1, UG-2, and UG-3 from the bottom up. The sample was taken from UG-2 facies and is mostly composed of dolomite and karst breccia (Machel and Hunter 1994; Buschkuehle et al. 2007). Laboratory measurements of porosity and permeability reported in (Andrä et al. 2013b) are around 0.21 (21 %) and 150 mD ─ 470 mD, respectively. The Grosmont carbonate dataset was measured at the high-resolution X-ray computer tomographic facility of the University of Texas with an Xradia MicroXCT-400 instrument (ZEISS, Jena, Germany). The measurement was performed using 4x objective lenses, 70 kV polychromatic X-ray beam energy and a 25 mm CCD detector. The tomographic images were reconstructed from the sinograms using proprietary software and corrected for the beam hardening effect as typical for lab-based polychromatic cone-beam X-ray instruments (Jovanović et al. 2013). The retrieved image volume was cropped to a dimension of 1024 x 1024 x 1024 with voxel resolution of 2.02 µm.

4.4.3. Berea Sandstone Rock

The Berea sandstone dataset was also obtained from the *GitHub* FTP server provided for the benchmark project reported by (Andrä et al. 2013a, 2013b). The Berea sandstone sample plug was acquired from Berea Sandstone TM Petroleum Cores (Ohio USA). Porosity values of around φ = 0.20 (20 %) were obtained using a Helium pycnometer 1330 (Micromeritics Instrument Corp., Germany) and a Pascal 140+1440 Mercury porosimeter (Thermo Electron Corporation, Germany) as described by (Giesche 2006). The permeability reported in the same benchmark test (Andrä et al. 2013b) ranges between 200 mD and 500 mD. (Machel and Hunter 1994) reported for this sample a mineral composition of Ankerite, Zircon, K-feldspar, Quartz, and Clay using a polarized optical microscope and a scanning electron microscope. The synchrotron tomographic scans of Berea sandstone were acquired also at the SLS TOMCAT beamline (Stampanoni et al. 2006). The beam

energy was monochromatized to 26 keV for an optimal contrast with an exposure time of 500 ms. This resulted in a 3D tomographic stack of dimension 1024 x 1024 x 1024 and voxel resolution of 0.74 µm.

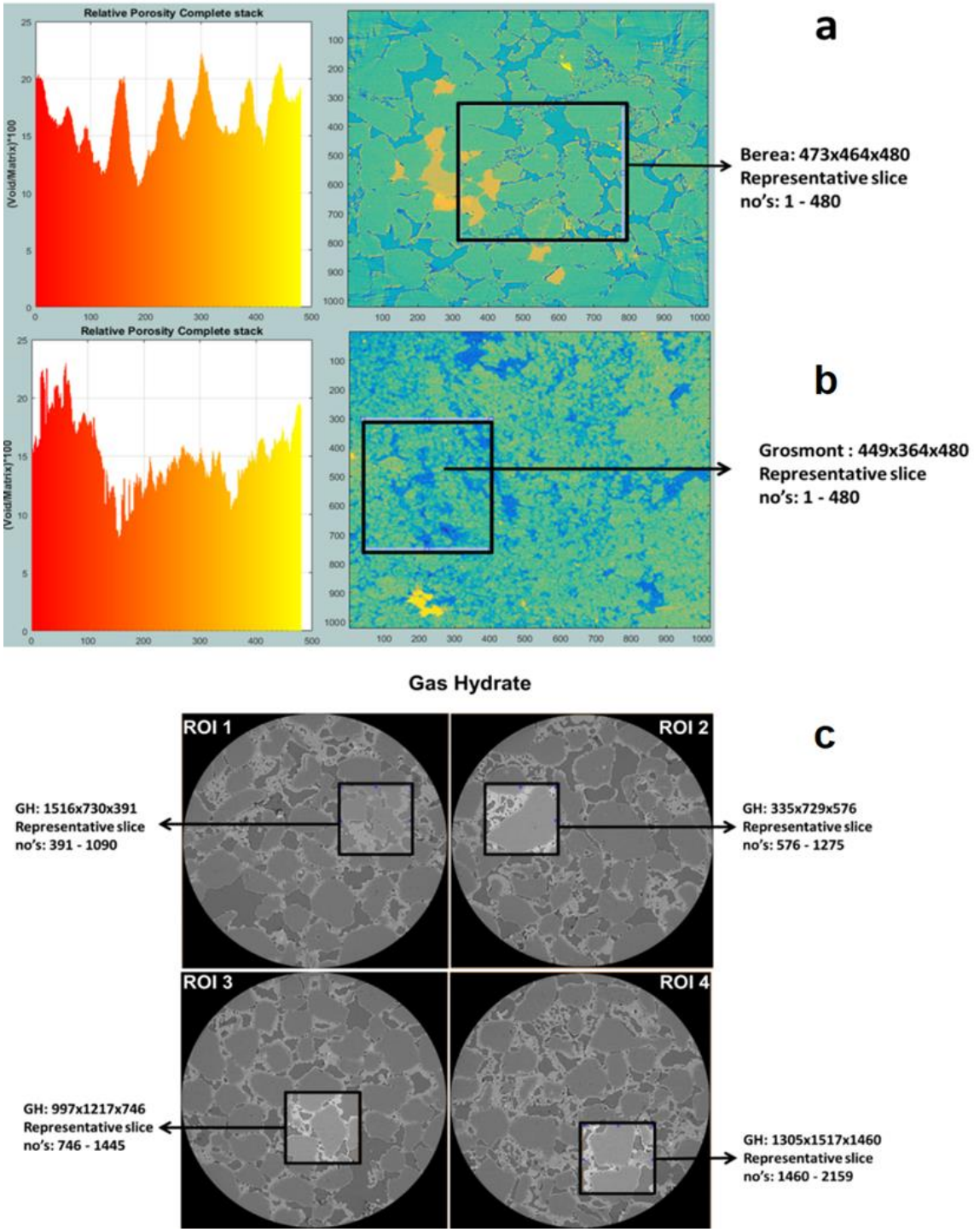

Figure 4. 4 The most suitable REV's of Berea Sandstone and Grosmont Carbonate rock shown in panel and Gas Hydrate-bearing sediment datasets shown in the panel b

4.5. Results and Discussions

4.5.1. Image Processing

XCT and synchrotron tomographic datasets were used to validate the functionality of CobWeb 1.0. A total of 12 region of interest's (ROI's) were thus investigated to determine suitable REVs. Figure 4. 4 shows the ROI's selected for the Berea, Grosmont and Gas hydrate samples. Image pre-processing is one of the essential and precautionary steps before imagesegmentation (Iassonov et al. 2009; Schlüter et al. 2014). Image filtering techniques such as blur, background intensity variation and contrast help in reducing artefacts. Image denoising filter such as median filter, non-local means filter, and anisotropic diffusion filter can assist in lowering the phase misclassification and improving the convergence rate of automatic segmentation schemes. In the case of XCT volume stack of Berea sandstone, the 3D reconstructed raw images (1024^3) had sufficiently high resolution and contrast, thus did not show any noticeable change on using the above mentioned filters. On the other hand, with XCT images (1024^3) of the Grosmont carbonate rock, non-local means filtering yielded in better visualization and performance results compared to anisotropic diffusion filter.

4.5.2. Dual Filtering of Gas Hydrate bearing Sediment

Due to ED artefacts affecting the quality of the hydrate-bearing sediment tomograms, the data had to undergo a data post-processing routine to enhance the image quality. Details of the image enhancement are published in (Sell et al. 2016). In brief, several image enhancement techniques were tested in preliminary studies including filters and filter combinations to gain best-fit results for further numerical simulations. To our knowledge, the combination of the non-local means and the anisotropic diffusion filter, both implemented in Avizo (ThermoFisher Scientific), works best for the given GH data.

The concept of the anisotropic diffusion filter (AD) filter is to smooth out noise in predefined areas of an image, but stopping at sharp edges representing boundaries between phases. This way, edges and sharp boundaries between phases are preserved, and image noise is significantly reduced (Kaestner et al. 2008; Porter and Wildenschild 2010).

A comparison of the current voxel with its six neighbors takes place, and diffusion is fulfilled when the threshold stop criterion is not exceeded. If the difference between one voxel and its six adjacent neighbors exceeds the given value no diffusion takes place. Another option to control the diffusion process of the filter is to reduce or increase the diffusion time. The parameter number of iterations defines how often the algorithm will be used on the data. The bigger this number is, the more blurred is the resulting image. Smoothing is performed by applying a Gaussian filter. For our investigations the threshold stop criterion was set to the value 22 968 as this is the approximated transition of the grain phase to hydrate. AD was run on CPU device with five iterations.

The non-local means filter (NLM) is a windowed version of the non-local means algorithm (Buades et al. 2005). The main aim is to de-noise data based on comparing voxels for similarities in a selected window in which a new weight for a voxel assigned. After a Gauss kernel was run on the weighted values, the new value will be assigned replacing the former grey values. The filter is most efficient if the image is affected by white noise. In Avizo the parameter window size, the local neighborhood and the similarity value can be customized. Furthermore, the NLM filter is also an appropriate tool for salt-and-pepper de-noising caused

by image sensor defects (Sarker et al. 2012). For this study, the NLM filter was run in 3D mode on CPU device. The *search window* was set to 21 and the *local neighborhood* to 6 at a similarity value of 0.71.

4.5.3. Phase Segmentation

4.5.4. Grosmont Carbonate and Berea Sandstone

The K-means algorithm was used for the segmentation of REV analysis of Berea and Grosmont rocks. K-means is one of the simplest unsupervised machine learning (ML) algorithms commonly used to address clustering (MacQueen 1967; Jain 2010; Chauhan et al. 2016b). The K-means algorithm iteratively calculates the Euclidean distance between the data points (pixel value) to its nearest centroid (cluster). The algorithm converges when the objective function, i.e. the mean square root error of Euclidean distance, reaches the minimum. This is, when no further pixel is left to be assigned to the nearest centroid (cluster). However, the K-means algorithm has the tendency to terminate without identifying the global minimum of the objective function. Therefore, it is recommended to run the algorithm several times to increase the likelihood that the global minimum of the objective function will be identified. The performance of the K-means algorithm is strongly governed by the initial choice of the cluster centres (Chauhan et al. 2016b).

The supervised ML techniques rely on features also termed as feature vectors (FVs). The FVs are sets of instances that represent descriptive information on which ML algorithm is used to train the classification model. They further identify these features in an unknown dataset and group them into respective classes. Least square support vector machine (LSSVM) is one such supervised ML technique, which in recent years has emerged as a reliable technique to segment digital rocks images (Chauhan et al. 2016b). (Khan et al. 2016) provides concise description and MATLAB® code snippet for the implementation of the LSSVM library on XCT images, whereas (Chauhan et al. 2016a) validated its best performance and accuracy in comparison to other common ML techniques. In practice, a FV is a group containing subsets of different pixel values. For example, the FV of class four is a group encapsulating pixel values corresponding to the pore, matrix rock, and noise. The pixel values were selected from a single 2D slice representative of the REV. This FV was used for training the classification model. The training performance was monitored using a 10 K-fold cross-validation technique (Larson 1931; Dietterich 2000).

4.5.5. Gas-Hydrate (GH) Bearing Sediment Dual-Clustering

The edge enhancement (ED) effect was significant in all the reconstructed slices of the GH dataset. The ED effect was seen around the quartz grains mostly, with high and low pixel intensities adjacent to each other. The high intensity pixel (EDH) values were very close to GH pixel values, while the low intensity pixel (EDL) values showed a variance between noise and brine phase pixel values. Therefore, immediate segmentation performed on the pre-filtered GH datasets using CobWeb 1.0 resulted in misclassification. Further parameterizing and tuning the unsupervised (K-means) and supervised (LSSVM) modules of CobWeb 1.0 specifically, distance function (i.e., functions euclidean distance *sqeuclidean*, sum of absolute differences *cityblock*, and *mandist*) and different permutation and combination between of kernel type, bandwidth and cross-validation parameters, showed significant improvement, but the

segmentation was still not optimal. The aim was to eliminate the ED features completely without altering the phase distribution between GH and the brine. This prompted to develop a GH-specific workflow as explained below. The appendix provides the MATLAB® script for this workflow comprised of 6 steps:

- **Step 1: Filtering and REV selection**

  Four REVs of size 4×700^3 were cropped from the raw (16 bit) data stack. These REVs were dual-filtered using NLM and ASD filters (see section 4.1.1). Figure 4. 5 show the pre-filtered raw dataset.

- **Step 2: K-means clustering**

  In this step, K-means segmentation is performed on the REV's to label the phases into different classes. The class sizes was varied between three to twenty, and it was thus established that class seven captured all the desired phases (noise, edge enhancement low intensities (EDL), brine, quartz, edge enhancement high intensities (EDH), GH).

- **Step 3: Indexing**

  The pixel indices corresponding to the respective classes (desired phases) were extracted from the segmented slice(s). Thereafter, using these pixel indices as reference, corresponding pixel values were extracted from the 16-bit raw images. The obtained pixel values represent noise, EDL, brine, quartz, EDH, and GH phases in the raw images. Then, histogram distribution of the pixel values in each phase was plotted. The skewness of the histogram plots was inspected visually and mean and standard deviation for each histogram was calculated. If there was an overlap of pixel intensities found in the different histograms (phases), step four is repeated.

- **Step 5: Rescaling raw REV**

  The pixel values corresponding to the phases, i.e brine, quartz, and GH, were replaced by their mean values, with an exception for EDH pixel values. The latter were replaced with the mean value of quartz. These assignments lead to optimal segregation of the phase boundaries in the raw dataset and finally to the elimination of the ED effect.

- **Step 6: K-means clustering**

  K-means segmentation with three classes was performed on the re-scaled dataset to obtain the final result.

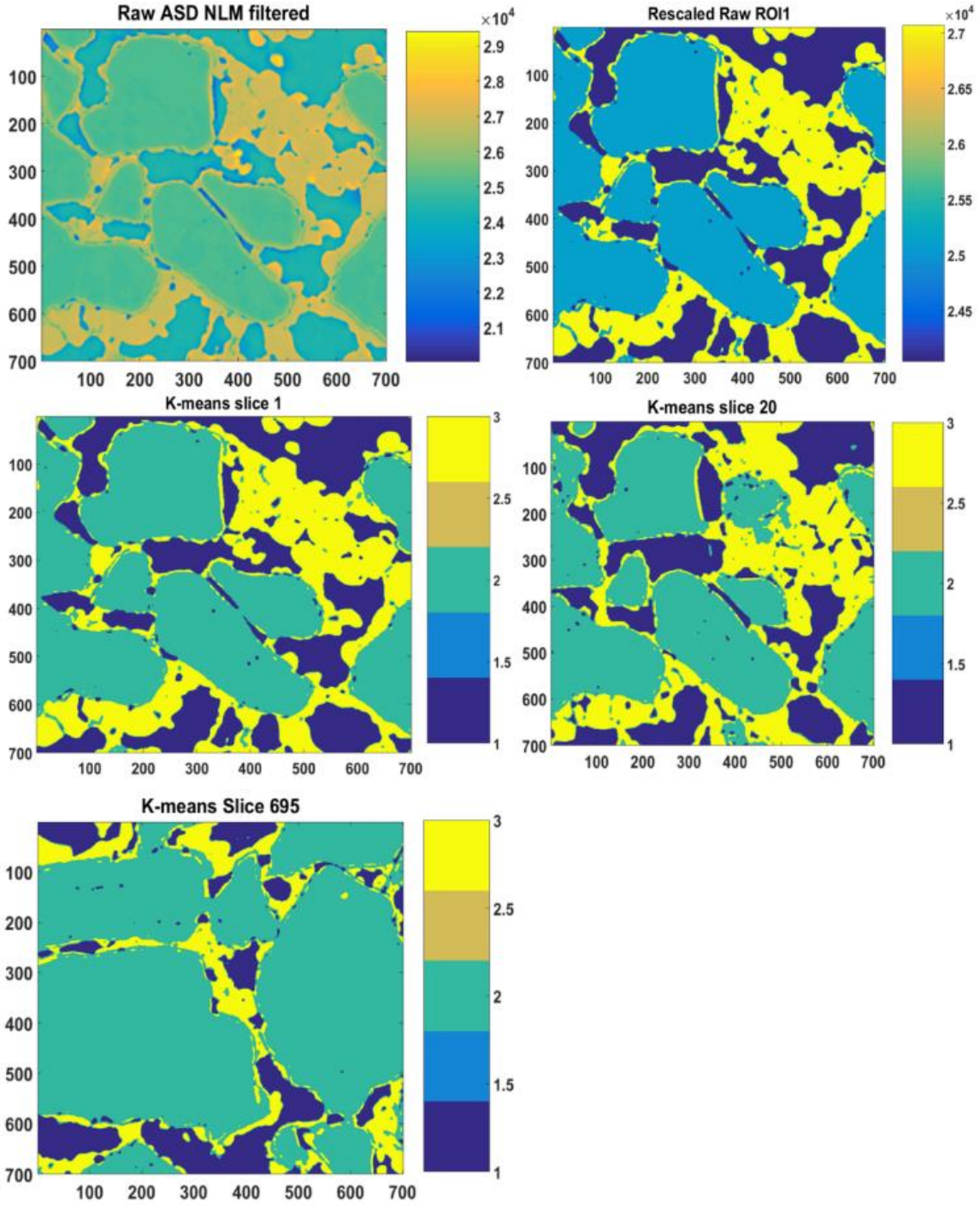

Figure 4. 5 2D filtered, rescaled, and segmented slices of gas hydrate REV1 dataset

4.5.6. Representative Elementary Volume

The representative elementary volume (REV) can be defined as the smallest volume, which should ideally represent the average effective macroscopic behavior of the geomaterial. As a result, the transport of the effective parameters (mass, momentum, energy) mathematically modelled within the REV become independent of the sample size (Wiącek and Molenda 2016).

Figure 4. 6 explains schematically the relationship between porosity and the volume of the porous media. In a small REV (region I), high fluctuation in porosity is contributed by the

heterogeneity at the pore scale. As the volume increases (region II), porosity starts tonormalize above some V_{min} value within a small standard deviation around a constant value of porosity. The porosity measured in this region is scale-independent, and an accurate representation of a large-scale system. The increase in REV value above a V_{max} may result in increase/decrease in porosity related to increases in heterogeneity, associated with `macroscopic' volume features (region III) (Wiącek and Molenda 2016). For heterogeneous porous media, porosity theoretically lies in between region I and region III depending on the effective parameter under investigation; however, determination of ideal region II for real heterogeneous system may be difficult and subjective (Zhang D et al. 2000; Gitman et al. 2006; Razavi et al. 2007; Al-Raoush and Papadopoulos 2010; Costanza-Robinson et al. 2011).

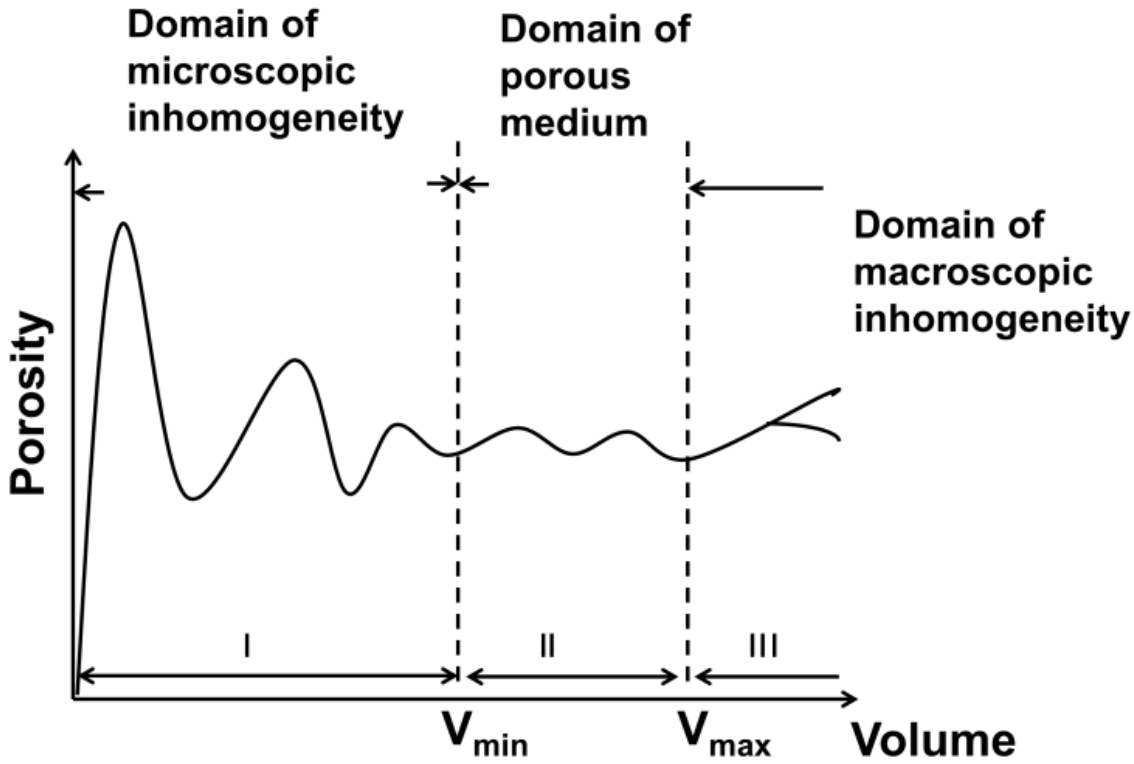

Figure 4. 6. Schematic representation of the relationship between porosity (φ) and volume (V) of porous media. Bachmat and Bear (1986).

In particular, while performing permeability tensor simulation using XCT data, the size of minimum REV should be assessed not only based on porosity but also on geometrical parameters such as pore size distribution, void ratio, and coordinate number (Al-Raoush and Papadopoulos 2010; Costanza-Robinson et al. 2011). For this study, we looked into different ROI's and REV sizes between 300^3 to 500^3 resolution, and established that REV of size 471 x 478 x 480 suited best. Figure 4. 7 shows the REV's of Berea sandstone and Grosmont carbonate rock and their respective geometrical parameters.

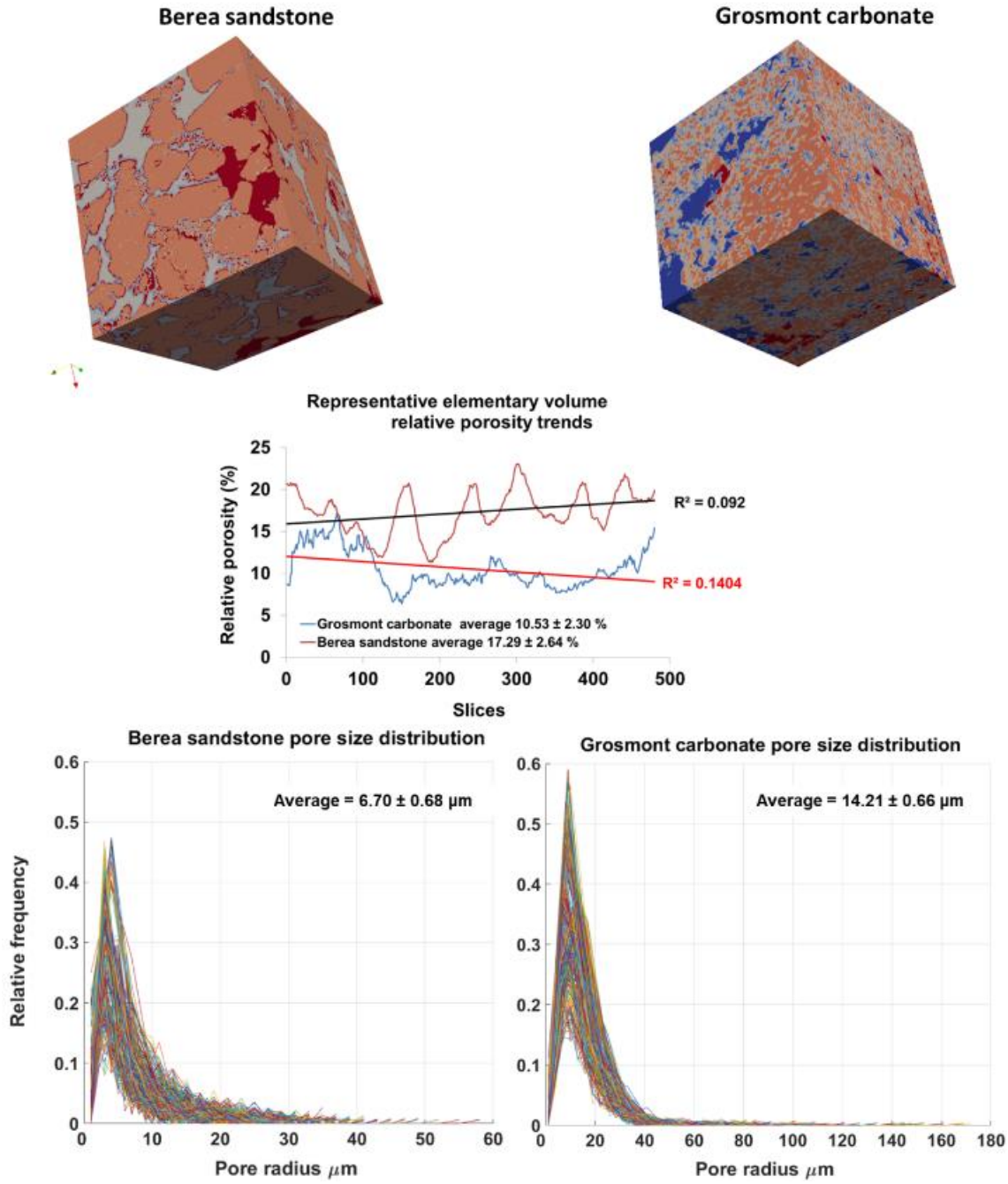

Figure 4. 7 Top panel shows surface plot of REVs Berea sandstone and Grosmont carbonate (size 471x478x480) using visualisation software ParaView. Middle plot shows the relative porosity (%) trend for Berea sandstone and Grosmont carbonate REVs samples. Bottom plot shows the pore size distribution of Berea sandstone and Grosmont carbonate. XCT images were segmented using K-means. In the case of Grosmont, a non-local means filter was used

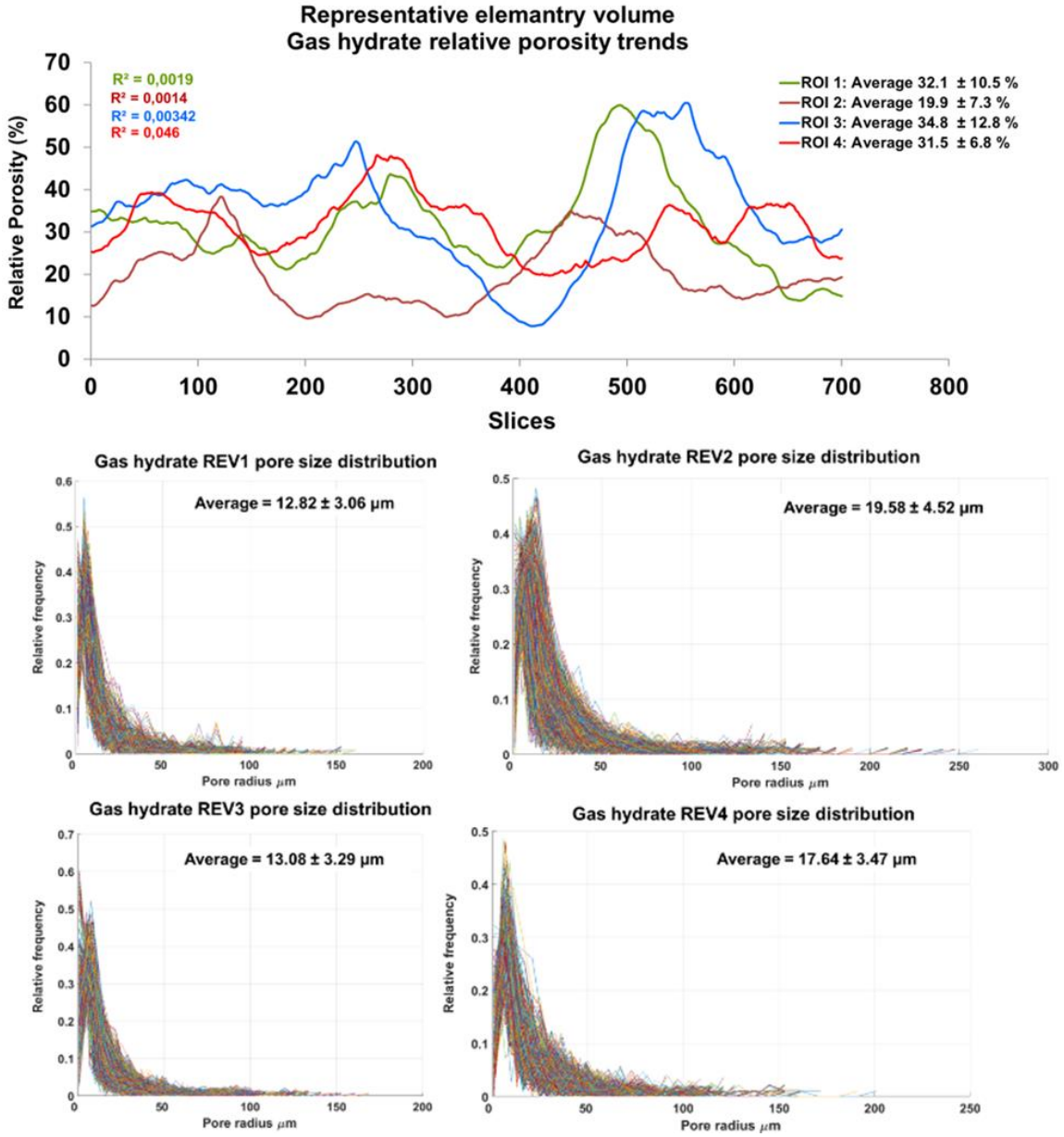

Figure 4. 8 The top panel shows relative porosity trend analysis of gas hydrates, the middle and bottom panel show the geometrical pore size distribution of the respective REVs. The analysis was performed using CobWeb 1.0

4.5.7. Estimation of Relative Porosity and Pore Size Distribution

In the case of the Grosmont Carbonate and Berea Sandstone, the respective REV's where segmented using K-means and LSSVM, as well as the PSD module based on the morphological scheme suggested in Rabbani et al. (2014) for the analysis. The mean relative porosity value of Berea sandstone is 17.3 ± 2.6 %, whereas for Grosmont carbonates mean porosity value is lower (10.5 ± 2.3 %) as shown Figure 4. 7. The regression coefficient value of R^2 = 0.092 for Berea sandstone porosity trend indicates that porosity remains constant throughout the REV sizes chosen, and therefore consolidated for scale-independent heterogeneities. In the case of Grosmont carbonate rock, the chosen REV size was the best found out of five others explored, which consolidate again for scale-independent heterogeneities. The average pore size distribution thus obtained was 6.70 μm ± 0.68 μm and 14.21 μm ± 0.66 μm for Berea and Grosmont plug samples, respectively.

Similarly, the porosity and PSD of the four GH REV's were analyzed using CobWeb 1.0 except for segmentation, which was performed using a different workflow as discussed above.

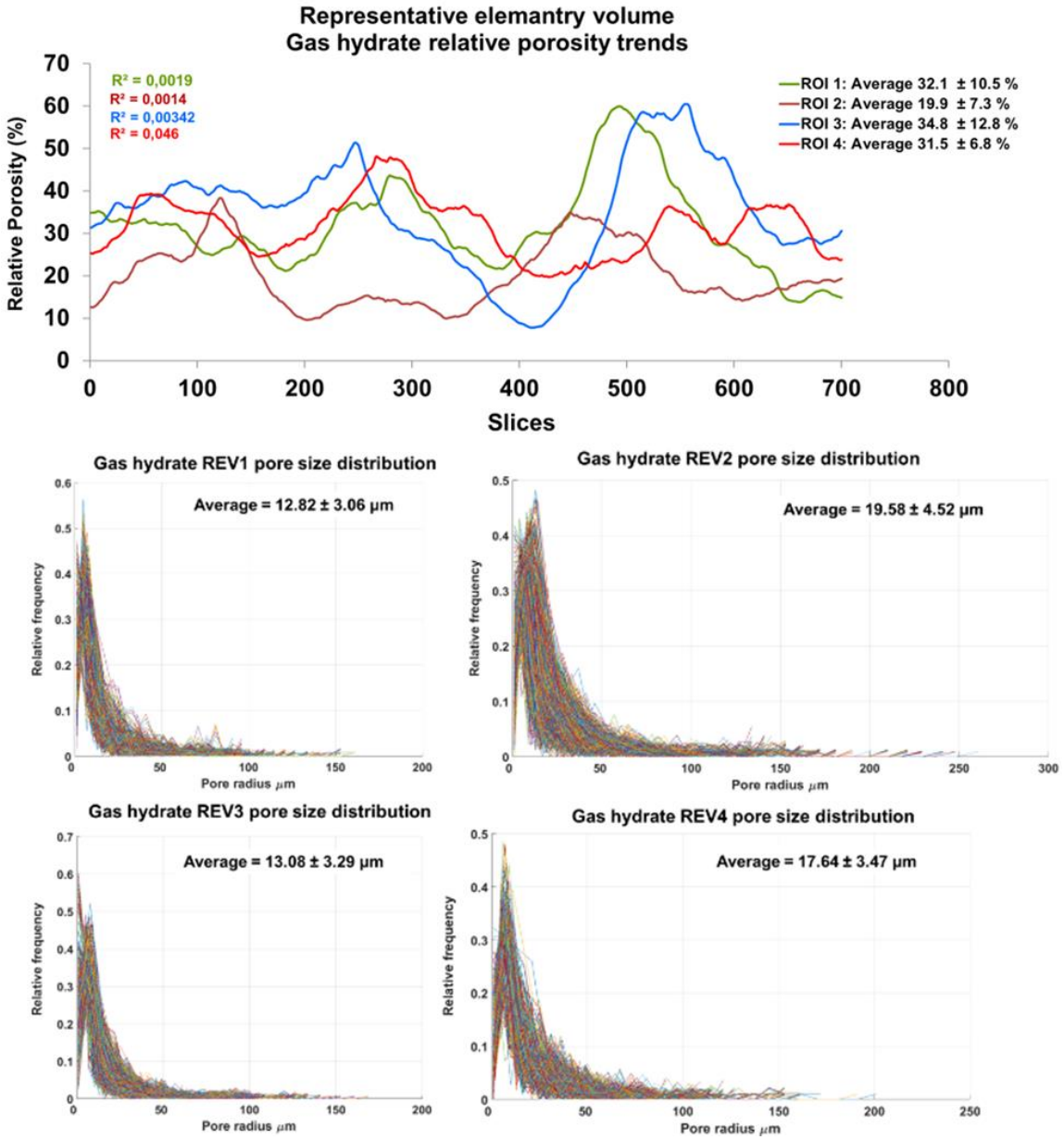

Figure 4. 8 shows the comparison of the porosity trends of different GH REV's. The selected REV's consolidate for the scale independent heterogeneities. However, there is high variance compared with the mean PSD values. The exact reason is unknown, but may be due to the drastic increase and decrease of the quartz grains as can be noticed in Figure 4. 5. The first and last 2D slices of ROI 1 in Figure 4. 5 show either non-isotropic or isotropic distribution of quartz grains, which might have contributed to the respective high and low standard deviation seen in the porosity distribution. Figure 4. 9 shows the surface and volume rendered plots of REV 1 and REV 2, due to the high accuracy of segmentation the quartz grain, brine and GH boundaries are clearly segregated and ED effect completely eliminated.

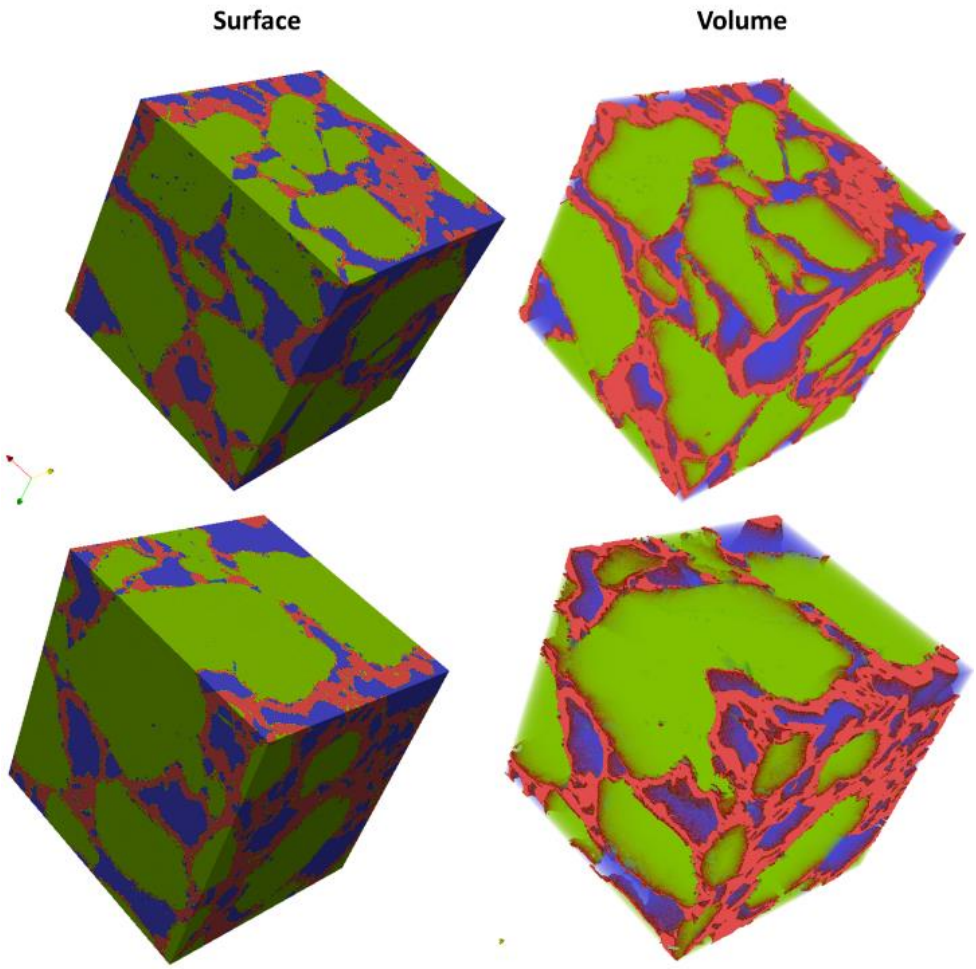

Figure 4. 9 Segmented REVs of gas hydrate sample displayed as surface and volume rendered plots. as analyzed using CobWeb 1.0 and exported to VTK format using CobWeb 1.0 ParaView plug-in. Quartz grain phase is represented in green color, gas hydrate in red, and in blue the liquid brine phase.

4.6. Conclusions and Outlook

This paper introduces with CobWeb 1.0 a visualization and image analysis toolkit dedicate to representative elementary volume analysis of digital rocks. It is developed on the MATLAB® framework and can be used as MATLAB® plugin or as a standalone executable. It relies on robust image segmentation schemes based on machine learning (ML) techniques, which can be tested and cross-validated, parallelly. Dedicated image preprocessing filters such as the non-local means, anisotropic diffusion, averaging and the contrast enhancement functions help to reduce artefacts and increase the signal to noise ratio. The petrophysical and geometrical properties such as porosity, pore size distribution and volume fractions can be computed fast on a single representative 2D slice of a complete REV 3D stack. This had been tested further using synchrotron datasets of the Berea Sandstone, a gas hydrate-bearing sediment and a tomography dataset of the Grosmont Carbonate rock. The gas hydrate dataset, despite it´s nanoscale resolution, was infested with strong edge enhancement (ED) artefacts, which causes discrepancies in diffenrentmodelling approaches. A combination of dual filtering and dual clustering approach is proposed to completely eliminate the ED effect in the gas hydrate sediments and the code is attached as an appendix. The REV studies performed on Berea Sandstone, Grosmont Carbonate rock and GH sediment using CobWeb1.0 shows relative porosity trends with very low linear regression values of 0.092, 0.1404, 0.0527 respectively.

CobWeb1.0 ability to acurately segment data with out any compramise on the data quality at a resonable speed makes it an favorable tool for REV analysis.

However, CobWeb1.0 is somewhat limited regarding its volume rendering capabilities, which will be one of the features to improve with the next version. The volume rendering algorithms yet implemented are not as sophisticated as in ParaView or DSI studio codes, which relies on the OpenGL marching cube scheme. At present, the densely nested loop structure appears to be the best choice for systematic processing. However, in future versions vectorization and indexing approaches (bsxfun, repmat) have to be tried and considered to check if there is a significant change in processing speed. MATLAB®—Java synchronization will be explored further to configure issues related to multi-threading and visualization (Java OpenGL).

In the science segments, the file readers and subroutines will be improved, to analyse and overlay scanning electron microscope data with XCT data to enhance mineral identification. A module CrackNet (crack network) is planned which will explicitly tackle segmentation of cracks, fissures in geomaterials using machine learning techniques and a mesh generation plugin (stl format) for 3D printing. Pore network extraction and skeletonization schemes such as modified maximum ball algorithm (Arand and Hesser 2017) and medial axis transformation (Katz and Pizer 2003) will be considered such that the data can be exported to open-source pore network modelling package (Gostick et al. 2016).

5. Results and Discussions

5.1. Results

This study presents an analysis and visualization software *CobWeb*, for image processing and image segmentation of X-ray tomographic rock images. These images, which are also known as digital rocks are obtained through high resolution X-ray tomography and synchrotron experiments. The implicit requirement of the research project was to develop an automated segmentation scheme and retrieve accurate petrophysical properties from the digital rock images. For this purpose, the potential of machine learning (ML) techniques where explored. The ML techniques offered diverse choice of algorithms which helps in clustering information in the spatial domain. A survey of such algorithms, namely, unsupervised, supervised and ensemble classifiers was conducted and a work flow was developed, for accurate (grayscale) image segmentation of Andesite digital rock images. The geometrical parameters such as porosity, pore size distribution (PSD) and volume fraction where calculated from the segmented images. An intra-comparison of the geometrical parameters obtained through these different ML algorithms showed district capabilities of the ML algorithm in term of accuracy and speed. In short, the winners where, K-means for computational speed and least square support vector machine (LSSVM) for accuracy. The study, also showed that the algorithm Fuzzy C-Means (FCM) was capable to quantify micro-pores when the tuning parameter (membership function) was set appropriately. Therefore the FCM approach can be useful in segmenting for low contrast and low porosity digital rocks samples such as Rotliegend sandstone.

A consecutive investigation, benchmarked the accuracy and performance of the ML techniques in a qualitative manner; which, time and again proved the ML capability to retrieve an optimal tradeoff in between (acquired) segmented information and processing speed. For this benchmark study three distinctive (reservoir analogous) digital rock types were used 1) inter-connected pores (Berea and Rotliegend sandstone), 2) micro pores (Synthetic sample), 3) non connected pores contain an assemblage of altered mineral (Andesite volcanic rock). The porosities obtained through image segmentation, were in good agreement (± 3 %) with the laboratory measurement and the porosity reported in the literature (Andrä et al. 2013a) (Andrä et al. 2013a). A new pore size distribution based on watershed analysis technique to calculate 2D pore network (Rabbani et al. 2014) from segmented images was implemented. This implementation increased the accuracy as it could, distinguishes, between different pore size and shapes based on it morphological features, unlike, geometrical PSD models, which is unable to characterize between closed pores, open pores and blind pores.

The use of validation metrics entropy, purity, mean square root error, receiver operational characteristic curve (ROC) and 10-fold cross validation helped in quantitative-accuracy-prediction of unsupervised, supervised and ensemble classifier techniques respectively. In terms of computational performance, K-means was superior to other ML techniques; this is, due to the use of a simple, (nearest-neighborhood) distance function for clustering, rather than, complex classification models (exception FCM) used by the other ML techniques. These, classification models in general are, optimization or surrogate- models, which require large amount of time and data for optimal classification. Despite this impedance (Rotliegend sandstone - low data quality) LSSVM was the most accurate. However, the efficiency of LSSVM in terms of accuracy and speed was largely governed by choice of the training dataset (feature vector selection). One of the important findings of this benchmark study was that,

FFANN is not suitable for phase segmentation analysis of digital rocks. As, ANN algorithms are tailored toward pattern recognition rather than, segmentation analysis.

A final effort was dedicated to software development, where the ML algorithms were integrated in a Graphical User Interface (GUI) name *"CobWeb 1.0"*. Detailed description of the software architecture is described in chapter four and the user manual of the software is appended in appendix B. In addition, for the first time, the removal of edge enhancement artefact (EDH) in the nano-tomographic images of gas-hydrate (GH) bearing sediments has been accomplished. A simple, clear and logical approach in combination with one of the ML technique is proposed in chapter four and the code is appended in appendix A.

5.2. Discussions

The main focus of this study was dedicated to image segmentation of digital rocks, which is only, the first step in the analysis of digital rock physics analysis. A holistic framework to test the accuracies of the segmented analysis would have been, for example, permeability flow fields or electric conductance using continuum based, lattice Boltzmann simulator (LBM) or topology based, pore-network modelling (PNM) approaches. This would give an insight in the uncertainties in upscaling from microscale-to-macroscale and to mesoscale processes. In the following, particular aspects that have caused uncertainties in segmentation and the improvements required in the analysis segment are discussed.

It was observed that the ML techniques tend to underestimate porosity values compared to manually segmented analysis at an REV scale (size > 500^3). This substantial degree of uncertainty is caused due to 2D slice-by-slice processing rather than the ML techniques. The 2D slice-by-slice approach, passes only, the spatial information (X, Y coordinate direction) to the ML algorithms, which ends up sorting the intensity variation in the spatial domain (local maxima). Therefore, the lack of temporal information (Z coordinate direction) restricts the degree of freedom to find at a global spatial-temporal optimum. In other words, as the temporal changes arise, due to bedding (sedimentary rock) or micro porosity (carbonate rocks) in the rock texture, they are represented as sudden spike or dip in porosity values; which to an inexperienced eye appear as artefact or anomalies– and often-then-not discarded. This correction has be introduced, in the current workflow, but has not been accounted for, in the work mentioned above. The 2D slice-by-slice processing scheme is much faster compared to the 3D approach. So, the choice of 2D processing for this research study was made to make it affordable to compute on desktop, laptop for near real-time and onsite evaluation.

Despite, the tedious tests with different setup for K-means, Fuzzy C-means (FCM), Feed Forward Artificial Neural Networks (FFANN), Least Square Support Vector Machines (LSSVM), Ensemble Classifiers (Bragging, Boosting) and benchmarked the best practices for segmentation. There is no universal solution; it is always related to the segmentation problem in hand. For example, FFANN which is more suited towards deep learning and it was inconsistent compared to other schemes in segmenting tomographic dataset. A subjective reasoning is that, the dataset where relatively simple or monotonous leading to the fast convergence to local minima and thereby misclassifications. In the category of ensemble classifiers; ensemble classification segregates itself from other ML schemes with regards to its training model(s) (Dietterich 2000). In a nutshell, the training framework is bootstrap of simple linear classification models; unlike other ML techniques which rely on single model; based on the feedback (misclassification rate) of these linear models a voting scheme is used to prioritise the mis-classified features and re-trained iteratively until a suitable training rate is achieved. For our study these linear classification model were treated as black-box. A potential

scientific problem could be to benchmark the best possible linear model(s) and customise plausible combination to segregate specific artefacts and enhanced segmentation.

In, the software segment, a conscious decision need to be taken if to dedicate CobWeb as a segmentation tool or expand it towards simulation software like MATH2MARKET, GeoDict or Volume Graphics. Realistically, it is a huge effort and need a collective effort. On the other side CobWeb provides an appropriate test platform, where new segmentation and filtration schemes can be tested and used as a complementary tool to the simulation software GeoDict and Volume Graphics. The simulation software have benchmarked solvers for performing flow, diffusion, dispersion, advection type simulation, but their accuracy relies heavily on the well segmented datasets. In the current CobWeb version image filtration algorithms are being improved and the porosity module, is expanded further to identify blind pores, open pores and closed pores.

Besides, the investigation and software development, further efforts are needed on communication. It is necessary that a common platform is created where, the scientific community, software development companies and engineering companies come together collaborate and benefit from each other's research. It is also necessary to jointly work with scientist in social sciences, on the communication and education of stakeholders and decision makers. As a first attempt, in Germany, the XCT workshop is periodically organized, which bring geoscientist, software and hardware companies together for discussion and possible collaborations.

6. Outlook

Since, reservoirs with fractures of high permeability are desired location for geothermal exploration for heat extraction and storage; concern for restricting radioactive contaminant dispersion; exploration of oil and gas inside petroleum reservoirs; mining and mineralization processes; deep earth system studies such as earthquakes and ocean floor hydrothermal venting and aquifer exploitation for fresh water supply (Berkowitz 2002; Sahimi 2011). Therefore, the fundamental understanding of the micromechanics of the fracture and thin fissures and it variation to change in temperature and pressure becomes even more crucial to calibrate numerical models for reliable prognosis (Joshi 1988; Mukherjee and Economides 1991; Mueller 2007; Cipolla et al. 2009; Brown et al. 2011; Ozkan et al. 2011). Moreover, the elastic, mechanical, fluid flow and electrical properties of these rocks are commonly related to pore morphology and their connectivity (Guéguen et al. 2009). Additionally, petrophysical and thermophysical information at macroscale through laboratory experiments before, during and after crack generation is essential both for parametrization and validation of the simulated results.

Similarly, at granular and grain contact level, by utilizing mineral composition and bulk chemical composition information obtained from SEM, EDX and XRD measurements; mineral identification and the associated crack fissures in the XCT images can be localized and quantitatively assessed. For this different colocation, indexing and reference approaches for accurate matching of different scales of datasets have to be considered.

The above mentioned discription summarises, broadly the work package „micro-tomographic quantification and reactive simulation analysis“, within the the BMWi sponsored bundprojekt ReSalt: (Reaktive Reservoirsysteme - Lösung und Fällung von Salzen und die Auswirkungen auf die hydraulischen und mechanischen Gebirgseigenschaften). Where, first, CobWeb’s ML segmentation techniques will be compared and calibrated with manual segmentation methods. Thereafter, CobWeb will be exploited and further improved to accurately characterize different kinds of cracks and perform micro-mechanics simulations using GeoDict. In future, subsequent research will focus on development of crack segmentation and analysis module CrackNet.

For modelling and flow simulations processes in the fractured medium, besides the commercial software GeoDict, topology based pore network modelling (PNM) using an open source pore network modelling package (OpenPNM) and Naiver-Stokes simulations directly on the porescale using Lattice Boltzmann Solver (LBM) will be tested. OpenPNM (Gostick et al. 2016) is an open source library written in Python language. Basically, it uses topology concept to generate network of pipes, these pipe networks can be further configured using predefined geometries such as stick and ball, Delaunay triangulation, voronio tessellation. The crack regions have to be extracted first from the segmented REV stacks and imported to into the above mentioned geometries. For this CobWeb has to be equipped with pore network extraction algorithms such as maximal ball method (Arand and Hesser 2017) or skeletalization/median axis transforms (Katz and Pizer 2003). Alternatively as CobWeb delivers accurate segmentation LBM simulation can be performed using Palabos (Latt 2009). LBM simulations are performed in a gridded or voxelized domain, which eliminates the need to construct meshes of the

pore-space from 3D images. The disadvantage is that the LBM simulation requiresexhaustive computational resources and is best suited for parallelized processing on clusters.

The software tool, CobWeb is somewhat limited regarding its volume rendering capabilities, which would be one of the features to improve with the next version. The volume rendering algorithms implemented is not as sophisticated as in ParaView or DSI studio codes, which relies on the OpenGL marching cube scheme. At present, the densely nested loop structure appears to be the best choice for systematic processing. However, in future versions vectorization and indexing approaches (*bsxfun, repmat*) have to be tried and considered to check if there is a significant change in processing speed. MATLAB®—Java synchronization should be explored further to configure issues related to multi-threading and visualization (Java OpenGL).

Summarising, the investigation in to ML techniques and its implementation has been a step forward in understanding the effect of accurate grayscale segmentation in digital rock analysis. Additionally, the computational software developed and the graphical user interfaces provides geologist and XCT analyst and easy and efficient analyses tool.

7. References

Al-Raoush, R., Papadopoulos, A., 2010. Representative elementary volume analysis of porous media using X-ray computed tomography. Powder Technology 200, 69–77. doi:10.1016/j.powtec.2010.02.011.

Altman, Y., 2014. Accelerating MATLAB Performance, CRC Press.

Ambrose, J., 1973. Computerized transverse axial scanning (tomography): Part 2. Clinical application. The British Journal of Radiology 46, 1023–1047. doi:10.1259/0007-1285-46-552-1023.

Amigó, E., Gonzalo, J., Artiles, J., Verdejo, F., 2009. A comparison of extrinsic clustering evaluation metrics based on formal constraints. Information Retrieval 12, 461–486. doi:10.1007/s10791-008-9066-8.

Andrä, H., Combaret, N., Dvorkin, J., Glatt, E., Han, J., Kabel, M., Keehm, Y., Krzikalla, F., Lee, M., Madonna, C., Marsh, M., Mukerji, T., Saenger, E.H., Sain, R., Saxena, N., Ricker, S., Wiegmann, A., Zhan, X., 2013a. Digital rock physics benchmarks—Part I: Imaging and segmentation. Benchmark problems, datasets and methodologies for the computational geosciences 50, 25–32. doi:10.1016/j.cageo.2012.09.005.

Andrä, H., Combaret, N., Dvorkin, J., Glatt, E., Han, J., Kabel, M., Keehm, Y., Krzikalla, F., Lee, M., Madonna, C., Marsh, M., Mukerji, T., Saenger, E.H., Sain, R., Saxena, N., Ricker, S., Wiegmann, A., Zhan, X., 2013b. Digital rock physics benchmarks—part II: Computing effective properties. Benchmark problems, datasets and methodologies for the computational geosciences 50, 33–43. doi:10.1016/j.cageo.2012.09.008.

Arand, F., Hesser, J., 2017. Accurate and efficient maximal ball algorithm for pore network extraction. Comput. Geosci. 101, 28–37. doi:10.1016/j.cageo.2017.01.004.

Aretz, A., Bär, K., Götz, A.E., Sass, I., 2016. Outcrop analogue study of Permocarboniferous geothermal sandstone reservoir formations (northern Upper Rhine Graben, Germany): impact of mineral content, depositional environment and diagenesis on petrophysical properties. International Journal of Earth Sciences 105, 1431–1452. doi:10.1007/s00531-015-1263-2.

Attix, F.H., 2007. Dosimetry Fundamentals: 11, In: Introduction to Radiological Physics and Radiation Dosimetry, Wiley-Blackwell, pp. 264–291.

Berg, S., Ott, H., Klapp, S.A., Schwing, A., Neiteler, R., Brussee, N., Makurat, A., Leu, L., Enzmann, F., Schwarz, J.-O., Kersten, M., Irvine, S., Stampanoni, M., 2013. Real-time 3D imaging of Haines jumps in porous media flow. Proc Natl Acad Sci USA 110, 3755. doi:10.1073/pnas.1221373110.

Berkowitz, B., 2002. Characterizing flow and transport in fractured geological media: A review. Quantitative links between porous media structures and flow behavior across scales 25, 861–884. doi:10.1016/S0309-1708(02)00042-8.

Berthod, M., Kato, Z., Yu, S., Zerubia, J., 1996. Bayesian image classification using Markov random fields. Image and Vision Computing 14, 285–295. doi:10.1016/0262-8856(95)01072-6.

Bezdek, J.C., Hathaway, R.J., Sabin, M.J., Tucker, W.T., 1987. CONVERGENCE THEORY FOR FUZZY C-MEANS: COUNTEREXAMPLES AND REPAIRS. IEEE Transactions on Systems, Man and Cybernetics 17, 873–877.

Bickle, M.J., 2009. Geological carbon storage. Nature Geoscience 2, 815 EP -. doi:10.1038/ngeo687.

Bleicher, A., Gross, M., 2015. User motivation, energy prosumers, and regional diversity: sociological notes on using shallow geothermal energy. Geothermal Energy 3, 12. doi:10.1186/s40517-015-0032-6.

Boever, E. de, Varloteaux, C., Nader, F.H., Foubert, A., Békri, S., Youssef, S., Rosenberg, E., 2012. Quantification and Prediction of the 3D Pore Network Evolution in Carbonate Reservoir Rocks. Oil Gas Sci. Technol. – Rev. IFP Energies nouvelles 67, 161–178. doi:10.2516/ogst/2011170.

Bradley, A.P., 1997. The use of the area under the ROC curve in the evaluation of machine learning algorithms. Pattern Recognition 30, 1145–1159. doi:10.1016/S0031-3203(96)00142-2.

Breede, K., Dzebisashvili, K., Liu, X., Falcone, G., 2013. A systematic review of enhanced (or engineered) geothermal systems: past, present and future. Geothermal Energy 1, 4. doi:10.1186/2195-9706-1-4.

Breiman, L., 1996. Bagging predictors. Machine Learning 24, 123–140. doi:10.1007/BF00058655.

Brooks, R.A., Chiro, G.D., 1976. Beam hardening in X-ray reconstructive tomography. Physics in Medicine & Biology 21, 390.

Brown, M., Ozkan, E., Raghavan, R., Kazemi, H., 2011. Practical Solutions for Pressure-Transient Responses of Fractured Horizontal Wells in Unconventional Shale Reservoirs. doi:10.2118/125043-PA.

Buades, A., Coll, B., Morel, J., 2005. A Review of Image Denoising Algorithms, with a New One. Multiscale Model. Simul. 4, 490–530. doi:10.1137/040616024.

Buschkuehle, B.E., Hein, F.J., Grobe, M., 2007. An Overview of the Geology of the Upper Devonian Grosmont Carbonate Bitumen Deposit, Northern Alberta, Canada. Natural Resources Research 16, 3–15. doi:10.1007/s11053-007-9032-y.

Cannon, R.L., Dave, J.V., Bezdek, J.C., 1986. Efficient Implementation of the Fuzzy c-Means Clustering Algorithms. IEEE Transactions on Pattern Analysis and Machine Intelligence 8, 248–255. doi:10.1109/TPAMI.1986.4767778.

Cebeiro, J., Morvidone, M., Nguyen, M.K., 2016. Back-projection inversion of a conical Radon transform. Inverse Problems in Science and Engineering 24, 328–352. doi:10.1080/17415977.2015.1034121.

Chan, J.C.-W., Paelinckx, D., 2008. Evaluation of Random Forest and Adaboost tree-based ensemble classification and spectral band selection for ecotope mapping using airborne hyperspectral imagery. Remote Sensing of Environment 112, 2999–3011. doi:10.1016/j.rse.2008.02.011.

Chaouachi, M., Falenty, A., Sell, K., Enzmann, F., Kersten, M., Haberthür, D., Kuhs, W.F., 2015. Microstructural evolution of gas hydrates in sedimentary matrices observed with

synchrotron X-ray computed tomographic microscopy. Geochemistry, Geophysics, Geosystems 16, 1711–1722. doi:10.1002/2015GC005811.

Chauhan, S., Rühaak, W., Anbergen, H., Kabdenov, A., Freise, M., Wille, T., Sass, I., 2016a. Phase segmentation of X-ray computer tomography rock images using machine learning techniques: an accuracy and performance study. Solid Earth 7, 1125–1139. doi:10.5194/se-7-1125-2016.

Chauhan, S., Rühaak, W., Khan, F., Enzmann, F., Mielke, P., Kersten, M., Sass, I., 2016b. Processing of rock core microtomography images: Using seven different machine learning algorithms. Computers & Geosciences 86, 120–128. doi:10.1016/j.cageo.2015.10.013.

Christ, G., 1984. Exact treatment of the dual-energy method in CT using polyenergetic x-ray spectra. Physics in Medicine & Biology 29, 1501.

Cipolla, C.L., Lolon, E., Mayerhofer, M.J., Warpinski, N.R., 2009. Fracture Design Considerations in Horizontal Wells Drilled in Unconventional Gas Reservoirs, Society of Petroleum Engineers.

Cnudde, V., Boone, M.N., 2013. High-resolution X-ray computed tomography in geosciences: A review of the current technology and applications. Earth-Science Reviews 123, 1–17. doi:10.1016/j.earscirev.2013.04.003.

Cortina-Januchs, M.G., Quintanilla-Dominguez, J., Vega-Corona, A., Tarquis, A.M., Andina, D., 2011. Detection of pore space in CT soil images using artificial neural networks. Biogeosciences 8, 279–288. doi:10.5194/bg-8-279-2011.

Costanza-Robinson, M.S., Estabrook, B.D., Fouhey, D.F., 2011. Representative elementary volume estimation for porosity, moisture saturation, and air-water interfacial areas in unsaturated porous media: Data quality implications. Water Resources Research 47. doi:10.1029/2010WR009655.

Culligan, K.A., Wildenschild, D., Christensen, S.B., William, G., Rivers, M.L., Tompson, A.F.B., 2004. Interfacial area measurements for unsaturated flow through a porous medium. Water Resources Research 40. doi:10.1029/2004WR003278.

Dierolf, M., Menzel, A., Thibault, P., Schneider, P., Kewish, C.M., Wepf, R., Bunk, O., Pfeiffer, F., 2010. Ptychographic X-ray computed tomography at the nanoscale. Nature 467, 436 EP -. doi:10.1038/nature09419.

Dietterich, T.G., 1998. Approximate Statistical Tests for Comparing Supervised Classification Learning Algorithms. Neural Computation 10, 1895–1923. doi:10.1162/089976698300017197.

Dietterich, T.G., 2000. Ensemble Methods in Machine Learning, In: Kittler, J., Roli, F. (Eds.) Multiple classifier systems. First international workshop, MCS 2000, Cagliari, Italy, June 21-23, 2000 : proceedings / Josef Kittler, Fabio Roli (eds.), Springer, Berlin, London, pp. 1–15.

Dunn, J.C., 1973. A Fuzzy Relative of the ISODATA Process and Its Use in Detecting Compact Well-Separated Clusters. Journal of Cybernetics 3, 32–57. doi:10.1080/01969727308546046.

Egmont-Petersen, M., Ridder, D. de, Handels, H., 2002. Image processing with neural networks- A review. Pattern Recognition 35, 2279–2301. doi:10.1016/S0031-3203(01)00178-9.

Elliott J. C., Dover S. D., 1982. X-ray microtomography. Journal of Microscopy 126, 211–213. doi:10.1111/j.1365-2818.1982.tb00376.x.

Esmaili, S., Mohaghegh, S.D., 2016. Full field reservoir modeling of shale assets using advanced data-driven analytics. Geoscience Frontiers 7, 11–20. doi:10.1016/j.gsf.2014.12.006.

Falenty, A., Chaouachi, M., Neher, S.H., Sell, K., Schwarz, J.-O., Wolf, M., Enzmann, F., Kersten, M., Haberthur, D., Kuhs, W.F., 2015. Stop-and-go in situ tomography of dynamic processes - gas hydrate formation in sedimentary matrices 71, s154. doi:10.1107/S2053273315097740.

Feldkamp, L.A., Davis, L.C., Kress, J.W., 1984. Practical cone-beam algorithm. Journal of the Optical Society of America A: Optics and Image Science, and Vision 1, 612–619. doi:10.1364/JOSAA.1.000612.

Fleiss, J.L., Cohen, J., Everitt, B.S., 1969. Large sample standard errors of kappa and weighted kappa. Psychological Bulletin, 72, 323–327.

Flukiger, F., Bernard, D., 2009. A new numerical model for pore scale dissolution of calcite due to CO2 saturated water flow in 3D realistic geometry: Principles and first results. Chemical Geology 265, 171–180. doi:10.1016/j.chemgeo.2009.05.004.

Freund, Y., Schapire, R.E., 1995. A decision-theoretic generalization of on-line learning and an application to boosting. A Decision-theoretic Generalization of On-line Learning and An Application to Boosting, 23–37.

Fusseis, F., Xiao, X., Schrank, C., Carlo, F. de, 2014. A brief guide to synchrotron radiation-based microtomography in (structural) geology and rock mechanics. Journal of Structural Geology 65, 1–16. doi:10.1016/j.jsg.2014.02.005.

Galar, M., Fernandez, A., Barrenechea, E., Bustince, H., Herrera, F., 2012. A review on ensembles for the class imbalance problem: Bagging-, boosting-, and hybrid-based approaches. IEEE Transactions on Systems, Man and Cybernetics Part C: Applications and Reviews 42, 463–484. doi:10.1109/TSMCC.2011.2161285.

Gerke, K.M., Karsanina, M.V., Mallants, D., 2015. Universal Stochastic Multiscale Image Fusion: An Example Application for Shale Rock. Scientific Reports 5, 15880 EP -. doi:10.1038/srep15880.

Giesche, H., 2006. Mercury Porosimetry: A General (Practical) Overview. Particle & Particle Systems Characterization 23, 9–19. doi:10.1002/ppsc.200601009.

Gitman, I.M., Gitman, M.B., Askes, H., 2006. Quantification of stochastically stable representative volumes for random heterogeneous materials. Archive of Applied Mechanics 75, 79–92. doi:10.1007/s00419-005-0411-8.

Gostick, J., Aghighi, M., Hinebaugh, J., Tranter, T., Hoeh, A, Michael, Day, H., Spellacy, B., Sharqawy, H, Mostafa, Bazylak, A., Burns Alan, Lehnert, W., Putz, A., 2016. OpenPNM: A Pore Network Modeling Package. Computing in Science & Engineering 18, 60–74. doi:10.1109/MCSE.2016.49.

Gouze, P., Luquot, L., 2011. X-ray microtomography characterization of porosity, permeability and reactive surface changes during dissolution. Journal of Contaminant Hydrology 120-121, 45–55. doi:10.1016/j.jconhyd.2010.07.004.

Guéguen, Y., Sarout, J., Fortin, J., Schubnel, A., 2009. Cracks in porous rocks: Tiny defects, strong effects. The Leading Edge 28, 40–47. doi:10.1190/1.3064145.

Gunstensen, A.K., Rothman, D.H., Zaleski, S., Zanetti, G., 1991. Lattice Boltzmann model of immiscible fluids. Physical Review A 43, 4320–4327. doi:10.1103/PhysRevA.43.4320.

Haykin, S.S., 1995. Neural networks: A comprehensive foundation, Macmillan, New York, NY, 696pp.

Hintze, M., Plasse, B., Bär, K., Sass, I., 2018. Preliminary studies for an integrated assessment of the hydrothermal potential of the Pechelbronn Group in the northern Upper Rhine Graben. Adv. Geosci. 45, 251–258. doi:10.5194/adgeo-45-251-2018.

Hopfield, J.J., 1982. Neural networks and physical systems with emergent collective computational abilities. Proc Natl Acad Sci USA 79, 2554. doi:10.1073/pnas.79.8.2554.

Hounsfield, G.N., 1973. Computerized transverse axial scanning (tomography): Part 1. Description of system. The British Journal of Radiology 46, 1016–1022. doi:10.1259/0007-1285-46-552-1016.

Iassonov, P., Gebrenegus, T., Tuller, M., 2009. Segmentation of X-ray computed tomography images of porous materials: A crucial step for characterization and quantitative analysis of pore structures. Water Resources Research 45. doi:10.1029/2009WR008087.

Ingo Sass and Dirk Brehm, 2016. Shallow Geothermal Systems - Recommendations on Design, Construction, Operation and Monitoring.

Jain, A.K., 2010. Data clustering: 50 years beyond K-means. Pattern Recognition Letters 31, 651–666. doi:10.1016/j.patrec.2009.09.011.

Jain, A.K., Murty, M.N., Flynn, P.J., 1999. Data Clustering: A Review. ACM Comput. Surv. 31, 264–323. doi:10.1145/331499.331504.

Joshi, S.D., 1988. Augmentation of Well Productivity With Slant and Horizontal Wells (includes associated papers 24547 and 25308). doi:10.2118/15375-PA.

Jovanović, Z., Khan, F., Enzmann, F., Kersten, M., 2013. Simultaneous segmentation and beam-hardening correction in computed microtomography of rock cores. Computers and Geosciences 56, 142–150. doi:10.1016/j.cageo.2013.03.015.

Kaestner, A., Lehmann, E., Stampanoni, M., 2008. Imaging and image processing in porous media research. Quantitative links between porous media structures and flow behavior across scales 31, 1174–1187. doi:10.1016/j.advwatres.2008.01.022.

Kalogirou, S.A., Florides, G.A., Pouloupatis, P.D., Panayides, I., Joseph-Stylianou, J., Zomeni, Z., 2012. Artificial neural networks for the generation of geothermal maps of ground temperature at various depths by considering land configuration. Energy 48, 233–240. doi:10.1016/j.energy.2012.06.045.

Katz, R.A., Pizer, S.M., 2003. Untangling the Blum Medial Axis Transform. International Journal of Computer Vision 55, 139–153. doi:10.1023/A:1026183017197.

Ketcham, R.A., Carlson, W.D., 2001. Acquisition, optimization and interpretation of X-ray computed tomographic imagery: applications to the geosciences. Benchmark problems, datasets and methodologies for the computational geosciences 27, 381–400. doi:10.1016/S0098-3004(00)00116-3.

Khan, F., Enzmann, F., Kersten, M., 2016. Multi-phase classification by a least-squares support vector machine approach in tomography images of geological samples. Solid Earth 7, 481–492. doi:10.5194/se-7-481-2016.

Khan, F., Enzmann, F., Kersten, M., Wiegmann, A., Steiner, K., 2012. 3D simulation of the permeability tensor in a soil aggregate on basis of nanotomographic imaging and LBE solver. Journal of Soils and Sediments 12, 86–96. doi:10.1007/s11368-011-0435-3.

Kohavi, R., 1995. A Study of Cross-Validation and Bootstrap for Accuracy Estimation and Model Selection Proceedings of the 14th International Joint Conference on Artificial Intelligence, San Francisco, CA, pp. 1137–1143.

Kohavi, R., Quinlan, J.R., 2002. Data Mining Tasks and Methods: Classification: Decision-tree Discovery: Handbook of Data Mining and Knowledge Discovery, In: Klösgen, W., Zytkow, J.M. (Eds.), Oxford University Press, Inc, New York, NY, USA, pp. 267–276, URL: http://dl.acm.org/citation.cfm?id=778212.778254.

Kohonen, T., 1990. The self-organizing map. Proceedings of the IEEE 78, 1464–1480. doi:10.1109/5.58325.

Larson, S.C., 1931. The shrinkage of the coefficient of multiple correlation. Journal of Educational Psychology, Vol 22(1), Jan 1931, 45-55 22, 45–55.

Latt, J., 2009. Palabos, parallel lattice Boltzman Solver, http://www.lbmethod.org/palabos/, [accessed 23 April 2018].

Lee, J., Sidle, R., 2010. Texas A&M “Gas-Reserves Estimation in Resource Plays”. SPE Economics & Management Journal 2.

Leu, L., Berg, S., Enzmann, F., Armstrong, R.T., Kersten, M., 2014. Fast X-ray Micro-Tomography of Multiphase Flow in Berea Sandstone: A Sensitivity Study on Image Processing. Transport in Porous Media 105, 451–469. doi:10.1007/s11242-014-0378-4.

Levenberg, K., 1944. A method for the solution of certain non-linear problems in least squares. Quart. Appl. Math. 2 (1944), 164-168 2, 164–168.

Luquot, L., Gouze, P., 2009. Experimental determination of porosity and permeability changes induced by injection of CO2 into carbonate rocks. Chemical Geology 265, 148–159. doi:10.1016/j.chemgeo.2009.03.028.

Machel, H.G., Hunter, I.G., 1994. Facies models for middle to late devonian Shallow-Marine carbonates, with comparisons to modern reefs: a guide for facies analysis. Facies 30, 155–176. doi:10.1007/BF02536895.

MacQueen, J. (Ed.), 1967. Some methods for classification and analysis of multivariate observations, University of California Press, 281-297.

Madonna, C., Almqvist, B.S.G., Saenger, E.H., 2012. Digital rock physics: numerical prediction of pressure-dependent ultrasonic velocities using micro-CT imaging. Geophysical Journal International 189, 1475–1482. doi:10.1111/j.1365-246X.2012.05437.x.

Marone, F., Hintermüller, C., McDonald, S., Abela, R., Mikuljan, G., Isenegger, A., Stampanoni, M., 2009. X-ray Tomographic Microscopy at TOMCAT. Journal of Physics: Conference Series 186, 12042.

Marone, F., Stampanoni, M., 2012. Regridding reconstruction algorithm for real-time tomographic imaging. Journal of Synchrotron Radiation 19, 1029–1037. doi:10.1107/S0909049512032864.

Marquardt, D., 1963. An Algorithm for Least-Squares Estimation of Nonlinear Parameters. Journal of the Society for Industrial and Applied Mathematics 11, 431–441. doi:10.1137/0111030.

Meilă, M., 2003. Comparing Clusterings by the Variation of Information, In: Schölkopf, B., Warmuth, M.K. (Eds.) Learning Theory and Kernel Machines, Springer Berlin Heidelberg, Berlin, Heidelberg, pp. 173–187.

Metz, C.E., 1978. Basic principles of ROC analysis. Seminars in Nuclear Medicine 8, 283–298. doi:10.1016/S0001-2998(78)80014-2.

Mohaghegh, S., 2000a. Virtual-intelligence applications in petroleum engineering: Part 1—Artificial neural networks. Journal of Petroleum Technology 52, 64–73.

Mohaghegh, S., 2000b. Virtual-intelligence applications in petroleum engineering: Part 2—evolutionary computing. Journal of Petroleum Technology 52, 40–46.

Mohaghegh, S., 2000c. Virtual-intelligence applications in petroleum engineering: Part 3—fuzzy logic. Journal of Petroleum Technology 52, 82–87.

Mohaghegh, S.D., 2011. Reservoir simulation and modeling based on artificial intelligence and data mining (AI&DM). Journal of Natural Gas Science and Engineering 3, 697–705.

Mohaghegh, S.D., 2013. Reservoir modeling of shale formations. Journal of Natural Gas Science and Engineering 12, 22–33.

Mueller, M.C., 2007. Prediction of lateral variability in fracture intensity using multicomponent shear-wave surface seismic as a precursor to horizontal drilling in the Austin Chalk. Geophysical Journal International 107, 409–415. doi:10.1111/j.1365-246X.1991.tb01402.x.

Mukherjee, H., Economides, M.J., 1991. A parametric comparison of horizontal and vertical well performance. SPE Formation Evaluation (Society of Petroleum Engineers); (United States) 6:2. doi:10.2118/18303-PA.

Noiriel, C., Luquot, L., Madé, B., Raimbault, L., Gouze, P., van der Lee, J., 2009. Changes in reactive surface area during limestone dissolution: An experimental and modelling study. Chemical Geology 265, 160–170. doi:10.1016/j.chemgeo.2009.01.032.

Ochs, R.A., Goldin, J.G., Abtin, F., Kim, H.J., Brown, K., Batra, P., Roback, D., McNitt-Gray, M.F., Brown, M.S., 2007. Automated classification of lung bronchovascular anatomy in CT using AdaBoost. Medical Image Analysis 11, 315–324. doi:10.1016/j.media.2007.03.004.

Oh, W., Lindquist, W.B., 1999. Image Thresholding by Indicator Kriging. IEEE Transactions on Pattern Analysis and Machine Intelligence 21, 590–602. doi:10.1109/34.777370.

Ommaya, A.K., Murray, G., Ambrose, J., Richardson, A., Hounsfield, G., 1976. Computerized Axial Tomography: Estimation of Spatial and Density Resolution Capability. The British Journal of Radiology 49, 604–611. doi:10.1259/0007-1285-49-583-604.

Ozkan, E., Brown, M.L., Raghavan, R., Kazemi, H., 2011. Comparison of Fractured-Horizontal-Well Performance in Tight Sand and Shale Reservoirs. doi:10.2118/121290-PA.

Pal, N.R., 1996. On minimum cross-entropy thresholding. Pattern Recognition 29, 575–580. doi:10.1016/0031-3203(95)00111-5.

Pal, N.R., Pal, S.K., 1989. Entropic thresholding. Signal Processing 16, 97–108. doi:10.1016/0165-1684(89)90090-X.

Pham, T.D. Image segmentation using probabilistic fuzzy c-means clustering, International Conference on Image Processing (Cat. Proceedings 2001), 722-725 vol.1.

Piller, M., Schena, G., Nolich, M., Favretto, S., Radaelli, F., Rossi, E., 2009. Analysis of Hydraulic Permeability in Porous Media: From High Resolution X-ray Tomography to Direct Numerical Simulation. Transport in Porous Media 80, 57. doi:10.1007/s11242-009-9338-9.

Porter, M.L., Wildenschild, D., 2010. Image analysis algorithms for estimating porous media multiphase flow variables from computed microtomography data: a validation study. Computational Geosciences 14, 15–30. doi:10.1007/s10596-009-9130-5.

Quinlan, J.R., 1996. Bagging, Boosting, and C4.5 In Proceedings of the Thirteenth National Conference on Artificial Intelligence, AAAI Press, pp. 725–730.

Rabbani, A., Jamshidi, S., Salehi, S., 2014. An automated simple algorithm for realistic pore network extraction from micro-tomography images. Neural network applications to reservoirs: Physics-based models and data models 123, 164–171. doi:10.1016/j.petrol.2014.08.020.

Razavi, M., Muhunthan, B., Al Hattamleh, O., 2007. Representative Elementary Volume Analysis of Sands Using X-Ray Computed Tomography. Geotechnical Testing Journal 30, 212–219. doi:10.1520/GTJ100164.

Renard, F., Bernard, D., Desrues, J., Ougier-Simonin, A., 2009. 3D imaging of fracture propagation using synchrotron X-ray microtomography. Earth and Planetary Science Letters 286, 285–291. doi:10.1016/j.epsl.2009.06.040.

Rosin, P.L., 2001. Unimodal thresholding. Pattern Recognition 34, 2083–2096. doi:10.1016/S0031-3203(00)00136-9.

Sahimi, M., 2011. Flow and Transport in Porous Media and Fractured Rock, Wiley-VCH Verlag GmbH & Co. KGaA, Weinheim, Germany.

Sarker, S., Chowdhury, S., Laha, S., Dey, D., 2012. Use of non-local means filter to denoise image corrupted by salt and pepper noise. Signal & Image Processing: An International Journal (SIPIJ) 27, 223–235.

Sato, T., Ikeda, O., Yamakoshi, Y., Tsubouchi, M., 1981. X-ray tomography for microstructural objects. Applied Optics 20, 3880–3883. doi:10.1364/AO.20.003880.

Schapire, R.E., Freund, Y., Bartlett, P., Lee, W.S., 1998. Boosting the margin: A new explanation for the effectiveness of voting methods. Annals of Statistics 26, 1651–1686.

Schintgen, T., 2015. Exploration for deep geothermal reservoirs in Luxembourg and the surroundings - perspectives of geothermal energy use. Geothermal Energy 3, 9. doi:10.1186/s40517-015-0028-2.

Schlüter, S., Sheppard, A., Brown, K., Wildenschild, D., 2014. Image processing of multiphase images obtained via X-ray microtomography: A review. Water Resources Research 50, 3615–3639. doi:10.1002/2014WR015256.

Seiffert, C., Khoshgoftaar, T.M., van Hulse, J., Napolitano, A., 2008. RUSBoost: Improving classification performance when training data is skewed 19th International Conference on Pattern Recognition, 2008. ICPR 2008 ; 8-11 Dec. 2008, Tampa, Florida, USA, IEEE, Piscataway, NJ, pp. 1–4.

Sell, K., Saenger, E.H., Falenty, A., Chaouachi, M., Haberthür, D., Enzmann, F., Kuhs, W.F., Kersten, M., 2016. On the path to the digital rock physics of gas hydrate-bearing sediments – processing of in situ synchrotron-tomography data. Solid Earth 7, 1243–1258. doi:10.5194/se-7-1243-2016.

Shan, X., Chen, H., 1993. Lattice Boltzmann model for simulating flows with multiple phases and components. Physical Review E 47, 1815–1819. doi:10.1103/PhysRevE.47.1815.

Sheppard, A.P., Sok R.M, Averdunk H., 2005. Improved Pore Network Extraction Methods Improved Pore Network Extraction Methods.

Sijbers, J., Postnov, A., 2004. Reduction of ring artefacts in high resolution micro-CT reconstructions. Physics in Medicine & Biology 49, N247.

Sok, R.M., Knackstedt, M.A., Varslot, T., Ghous, A., Latham, S., Sheppard, A.P., 2010. Pore Scale Characterization of Carbonates At Multiple Scales: Integration of Micro-CT, BSEM, And FIBSEM.

Stampanoni, M., Groso, A., Isenegger, A., Mikuljan. G, Chen, Q., Bertrand, A., Henein. S, Betemps, R., Frommherz, U., Böhler, P., Meister, D., Lange, M., Abela, R., 2006. Trends in synchrotron-based tomographic imaging: the SLS experience, In: Proc. of SPIE, 63180M-6318-14, URL: https://doi.org/10.1117/12.679497.

Stehman, S.V., Czaplewski, R.L., 2003. Introduction to special issue on map accuracy. Environmental and Ecological Statistics. 10:301-308. 10, 301–308.

Stern, P.C., Janda, K.B., Brown, M.A., Steg, L., Vine, E.L., Lutzenhiser, L., 2016. Opportunities and insights for reducing fossil fuel consumption by households and organizations. Nature Energy 1, 16043 EP -. doi:10.1038/nenergy.2016.43.

Strehl, A., 2002. Relationship-based Clustering and Cluster Ensembles for High-dimensional Data Mining.

Sund, T., Eilertsen, K., 2003. An algorithm for fast adaptive image binarization with applications in radiotherapy imaging. IEEE Transactions on Medical Imaging 22, 22–28. doi:10.1109/TMI.2002.806431.

Suykens, J.A.K., Vandewalle, J., 1999. Least Squares Support Vector Machine Classifiers. Neural Processing Letters 9, 293–300. doi:10.1023/A:1018628609742.

Tissen, C., Menberg, K., Bayer, P., Blum, P., 2019. Meeting the demand: geothermal heat supply rates for an urban quarter in Germany. Geothermal Energy 7, 9. doi:10.1186/s40517-019-0125-8.

Tölke, J., Krafczyk, M., Schulz, M., Rank, E., 2002. Lattice Boltzmann simulations of binary fluid flow through porous media. Philosophical Transactions of the Royal Society of London A: Mathematical, Physical and Engineering Sciences 360, 535–545. doi:10.1098/rsta.2001.0944.

van de Casteele, E., van Dyck, D., Sijbers, J., Raman, E., 2002. An energy-based beam hardening model in tomography. Physics in Medicine & Biology 47, 4181–4190. doi:10.1088/0031-9155/47/23/305.

Vapnik, V.N., Chervonenkis, A.Y., 1974. Theory of Pattern Recognition [in Russian], Nauka, USSR.

Vogel, H.-J., Tölke, J., Schulz, V.P., Krafczyk, M., Roth, K., 2005. Comparison of a Lattice-Boltzmann Model, a Full-Morphology Model, and a Pore Network Model for Determining Capillary Pressure–Saturation Relationships. Vadose Zone Journal 4, 380–388. doi:10.2136/vzj2004.0114.

Wiącek, J., Molenda, M., 2016. Representative elementary volume analysis of polydisperse granular packings using discrete element method. Particuology 27, 88–94. doi:10.1016/j.partic.2015.08.004.

Wildenschild, D., Sheppard, A.P., 2013. X-ray imaging and analysis techniques for quantifying pore-scale structure and processes in subsurface porous medium systems. Quantitative links between porous media structures and flow behavior across scales 51, 217–246. doi:10.1016/j.advwatres.2012.07.018.

Yanowitz, S.D., Bruckstein, A.M., 1989. A new method for image segmentation. Computer Vision, Graphics, and Image Processing 46, 82–95. doi:10.1016/S0734-189X(89)80017-9.

Zack, G.W., Rogers, W.E., Latt, S.A., 1977. Automatic measurement of sister chromatid exchange frequency. J Histochem Cytochem 25, 741–753. doi:10.1177/25.7.70454.

Zhang D, Zhang R, Chen S, Soll, W.E., 2000. Pore scale study of flow in porous media: Scale dependency, REV, and statistical REV. Geophysical Research Letters 27, 1195–1198. doi:10.1029/1999GL011101.

Appendix

Appendix A: MATLAB snippet for removal for Edge Enhancement Effect in gas hydrate datasets

1.1 Gas Hydrate Segmentation

1.2 Step 1

The Dual Clustering approach, by which first the 16-bit raw tomographic images of gas hydrate was filtered using Anisotropic Diffusion Filter (ASD), and then with Non-Local Means filter (NLM), to minimize the edge enhancement (ED) artefacts.

1.3 Step 2

- read slice by slice 3D prefiltered raw data
- for this example the reading is restricted
- to only four slices (700x700x4); it can be changed using nZ variable

```
mfname= ''GasHydrat_ROI4_AD_NLM ';
ifname=[mfname,'.raw'];
nX=700;
nY=700;
nZ=4;
ldim = 1;
xDi=[nX nY]';
grenzwert=0; clusterS =7;

ifid=fopen(ifname,'r');
M=zeros(nX,nY,nZ,'uint16');
SeData = nZ-ldim;
SeData  = 1:1:SeData;
dim = size(M);


for k=ldim:nZ
    disp(sprintf('Reading slice no. %d....',k));
    s=sprintf('Slice: % d', k');
    S=fread(ifid, [xDi(1) xDi(2)], 'uint16');
    M(:,:,k)=S;
    %figure; imagesc(M(:,:,k)); colorbar;
end
```

```
Reading slice no. 1....
Reading slice no. 2....
Reading slice no. 3....
Reading slice no. 4....
```

1.4 Display image

```
figure; imagesc(M(:,:,1)); colorbar;
title('Raw Prefiltered ASD NLM')
```

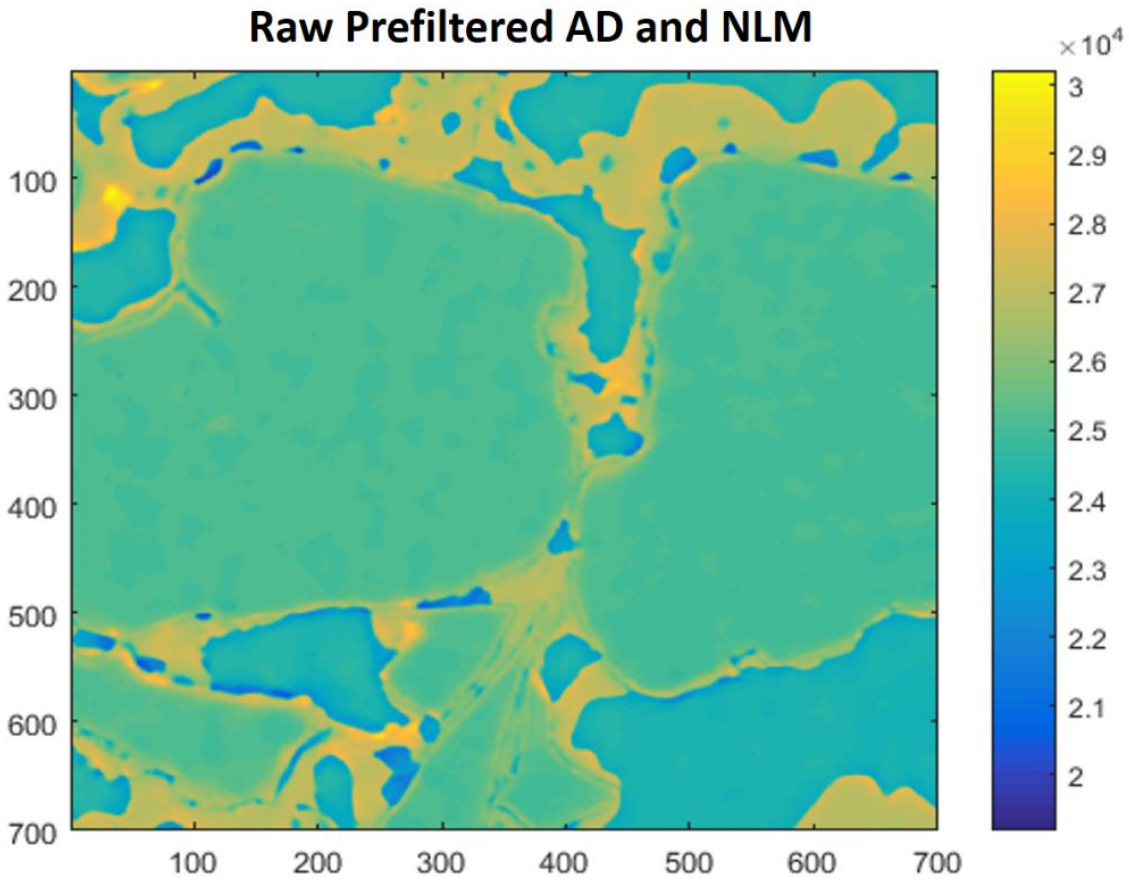

1.5 Concatenate raw data into single array

```
% concatenate array will be used in step three

M = M(:,:,ldim:nZ);
rawM = double(M(:));
```

1.6 Perform k-means clustering

Here, clustering is restricted to class 7 optimal to enable clustering of all the available features:

```
for ii = 1:2
    R=double(M(:,:,ii));
    [r,c,v]=find(R>grenzwert);
    cyl=R>grenzwert;
    R1=cyl.*R;
    [m, n, w]=find(R1);
    G = kmeansK(w,clusterS);
    S=sparse(r,c,G,size(R,1),size(R,2));
    M_seg=full(S);
    SegImg(:,:,ii)=M_seg;
    %figure; imagesc(SegImg(:,:,ii)); colormap(parula(5)); colorbar;
    %title('K-means prefiltered');
end
```

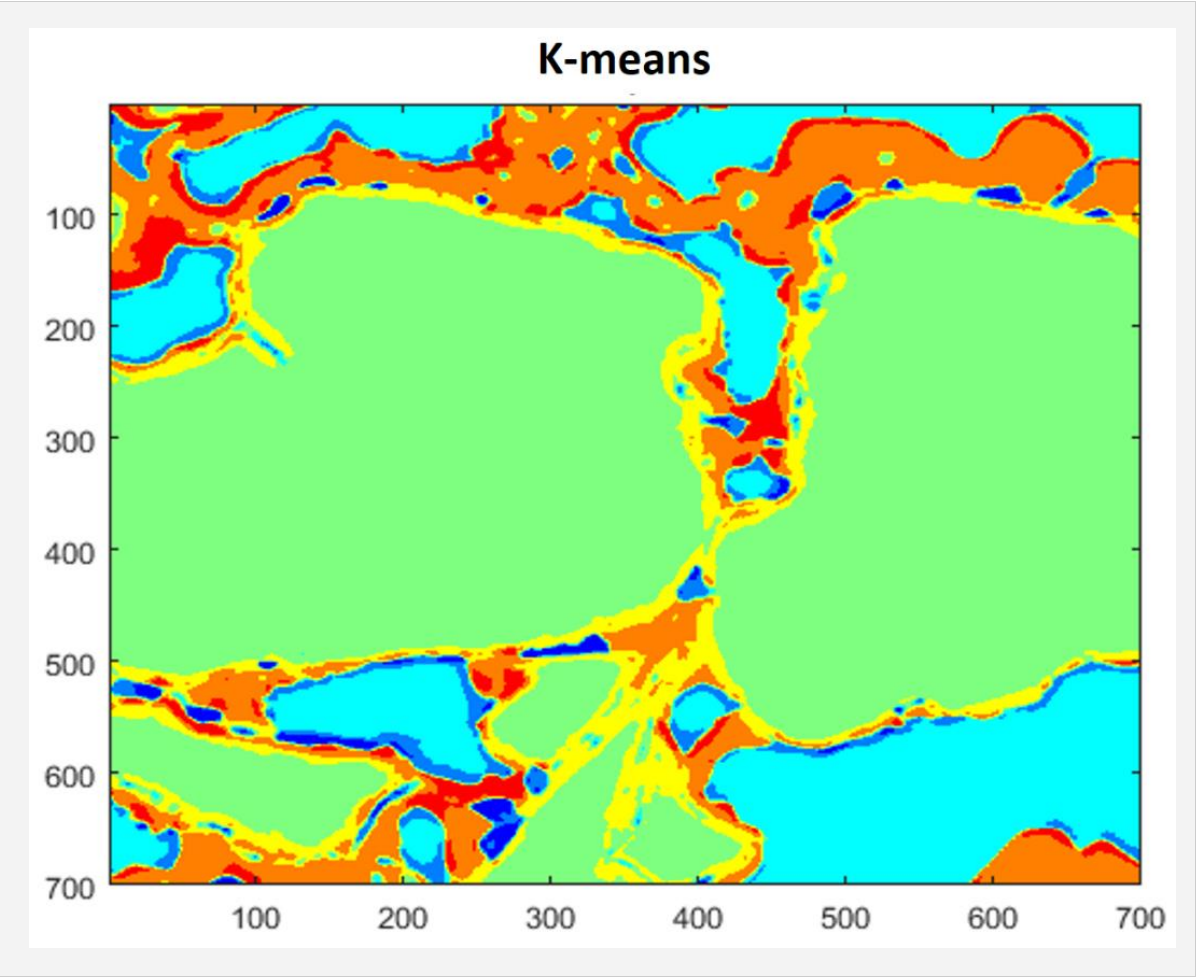

1.7 Display image

```
figure; h = imagesc(SegImg(:,:,1)); colormap(jet(max(h.CData(:))));
title('K-means prefiltred');
```

1.8 Step three

The purpose is to |index out| pixel values of different phases:

```
% noise
% edge enhanced low (EDL)
% liquid
% quartz
% edge enhanced high (EDL)
% gas hydrate
% from the concatenated raw images matrix using segmented class values
% thereafter compare their histogram % _as sanity check_
% to identify if any overlapping boundaries
```

1.9 Index noise pixels

```
rangeNl = 0;
indN = find(h.CData(:)==rangeNl);
rawO = rawM(indN);
```

1.10 Plot histogram noise

```
[cN, countN] = hist(rawO, 10);
%figure; bar(countN, cN);
%title('noise')
```

1.11 Index EDL pixels

```
rangeNu = 2;
indD = find(h.CData(:)>rangeNl & h.CData(:)<=rangeNu);
rawD = rawM(indD);
```

1.12 Plot histogram noise

```
[cD, countD] = hist(rawD, 100);
%figure; bar(countD, cD);
%title('Edge Enhanced low noise')
```

1.13 Index liquid pixels

```
rangeLl = 1;
rangeLu = 3;

indL = find(h.CData(:)>=rangeLl & h.CData(:)<=rangeLu);
if min(SegImg(indL))==rangeLl & max(SegImg(indL))==rangeLu
    rawL = rawM(indL);
    min_rawL = min(rawL);
    max_rawL = max(rawL);
    Avg_rawL = mean(rawL);
else
    fprintf('min and max for liquid dont match.....\n')
    return
end
```

1.14 Plot histogram liquid

```
[cL, countL] = hist(rawL, 100);
figure; bar(countL, cL);
title('Liquid')
```

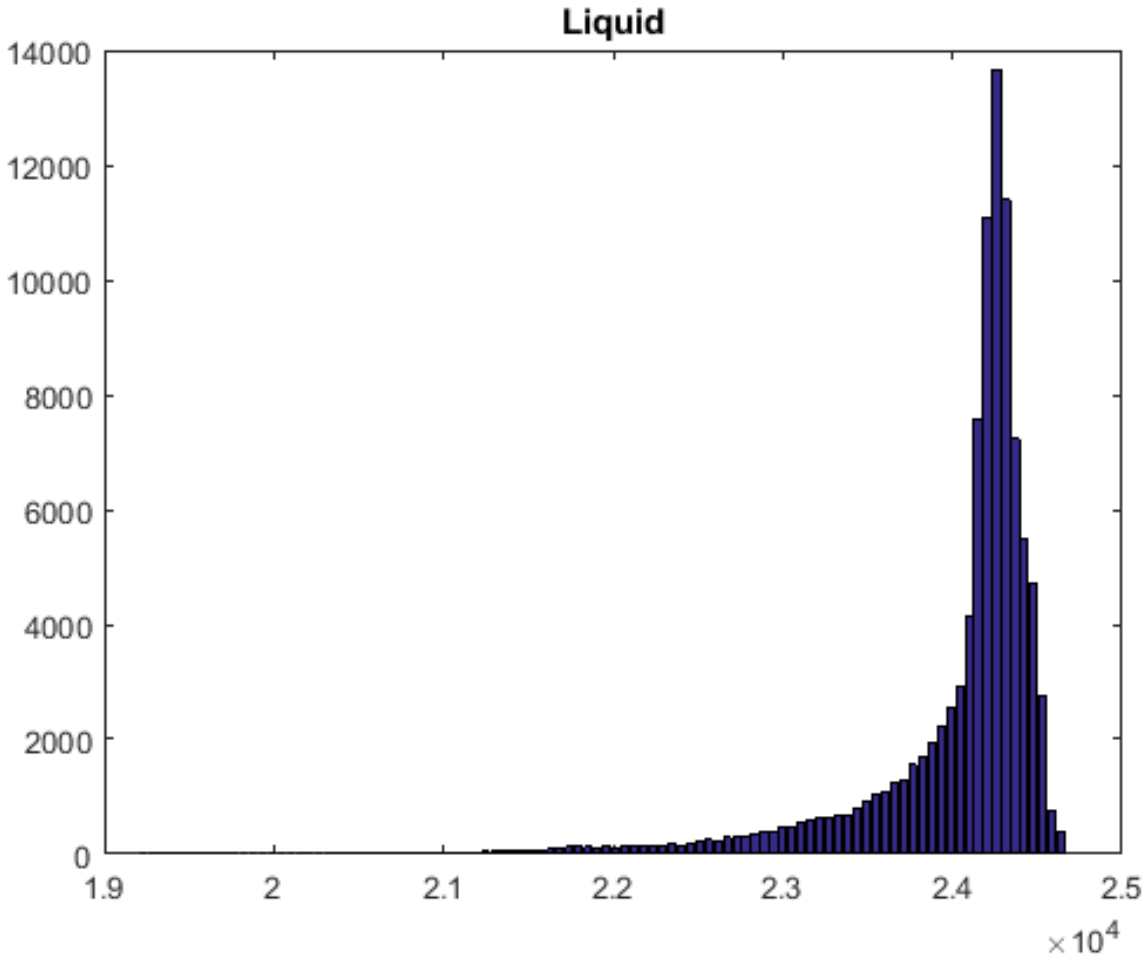

1.15 Index EDH pixels

```
rangeE = 5;
indE = find(h.CData(:)==rangeE);
if min(SegImg(indE))==rangeE
    rawE = rawM(indE);
    min_rawE = min(rawE);
    max_rawE = max(rawE);
    Avg_rawE = mean(rawE);
else
    fprintf('min and max for EDH dont match.....\n')
    return
end
```

1.16 Plot histogram EDH

```
[cE, countE] = hist(rawE, 10);
figure; bar(countE, cE);
title('Edge Enhanced high noise')
```

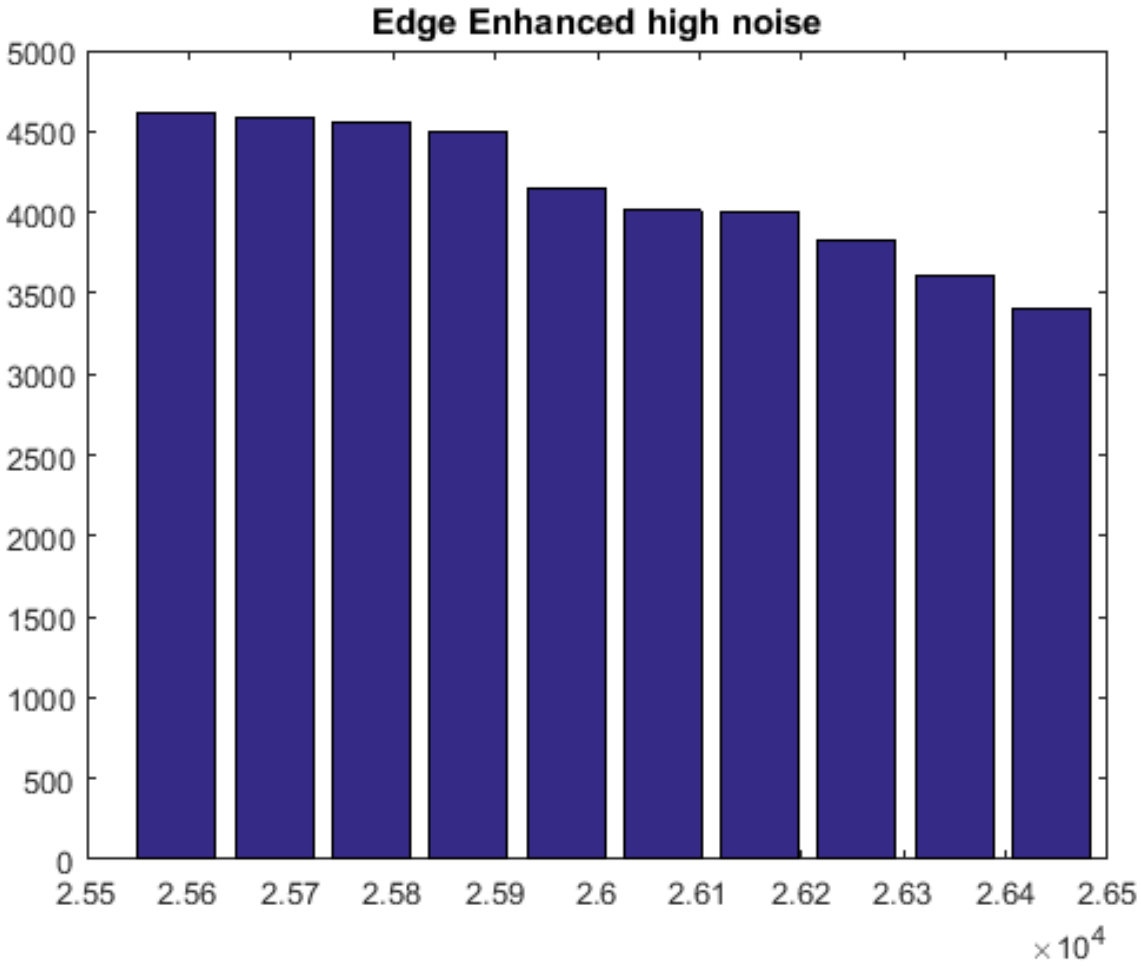

1.17 Quartz index phases

```
rangeQu = 4;
```

1.18 Quartz

```
indQ = find(h.CData(:)==rangeQu);
if min(SegImg(indQ)) == rangeQu
    rawQ = rawM(indQ);
    min_rawQ = min(rawQ);
    max_rawQ = max(rawQ);
    Avg_rawQ = mean(rawQ);
else
    fprintf('min and max for quartz dont match.....\n')
    return
end
%indQ = find(h.CData(:)>=rangeQl & h.CData(:)<=rangeQu);
```

1.19 Plot histogram quartz

```
[cQ, countQ] = hist(rawQ, 100);
figure; bar(countQ, cQ);
title('Quartz')
```

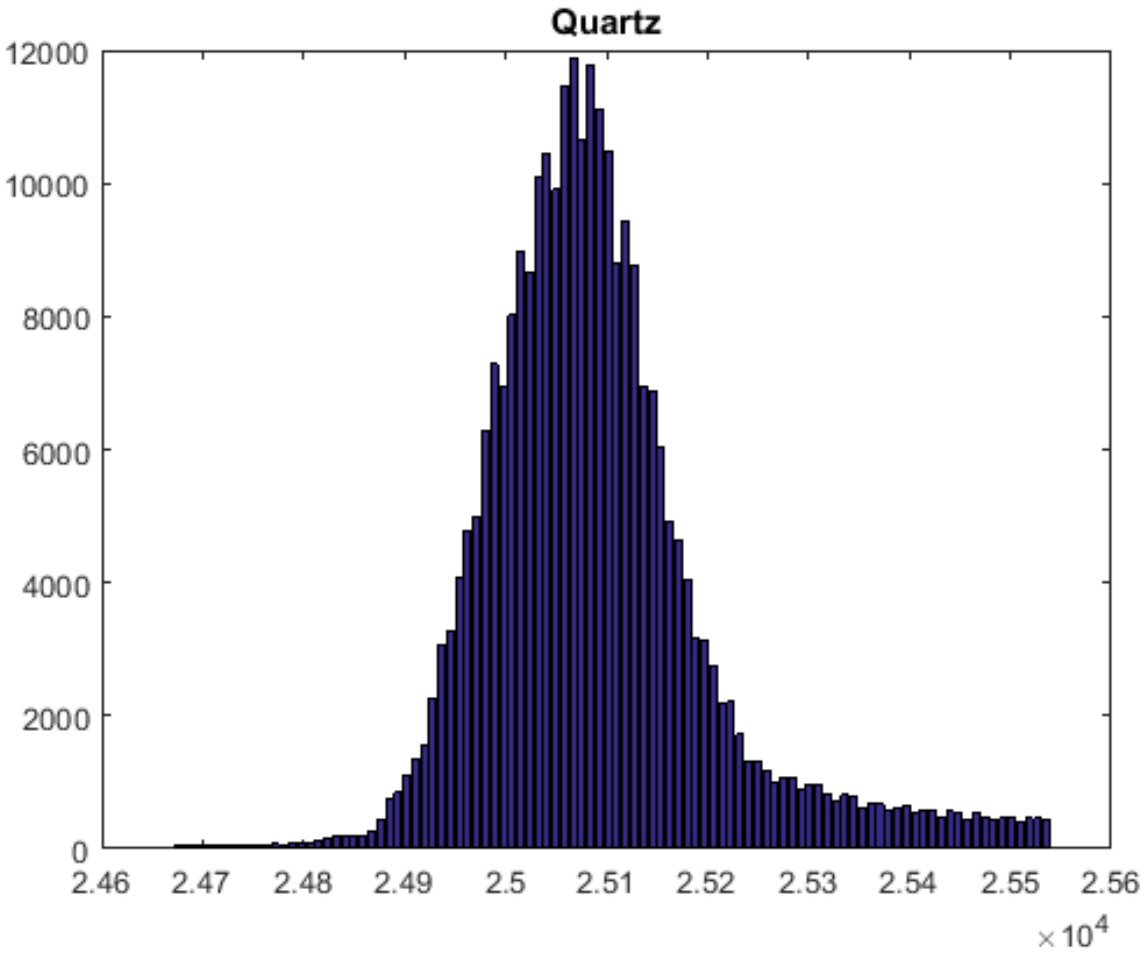

1.20 Gas Hydrate

```
rangeMl =6;
rangeMu =7;
%indM =find(h.CData(:)>=rangeMu);
indM = find(h.CData(:)>=rangeMl & h.CData(:)<=rangeMu);
if min(SegImg(indM))==rangeMl & max(SegImg(indM))==rangeMu
    rawMu = rawM(indM);
    min_rawMu = min(rawMu);
    max_rawMu = max(rawMu);
    Avg_rawMu = mean(rawMu);
elseif min(SegImg(indM))==rangeMu & max(SegImg(indM))==rangeMu
    rawMu = rawM(indM);
    min_rawMu = min(rawMu);
    max_rawMu = max(rawMu);
    Avg_rawMu = mean(rawMu);
else
    fprintf('min and max for gas hydrate dont match.....\n')
    return
end
```

1.21 Plot Histogram Gas Hydrate

```
[cM, countM] = hist(rawMu, 100);
figure; bar(countM, cM);
title('Methane')
```

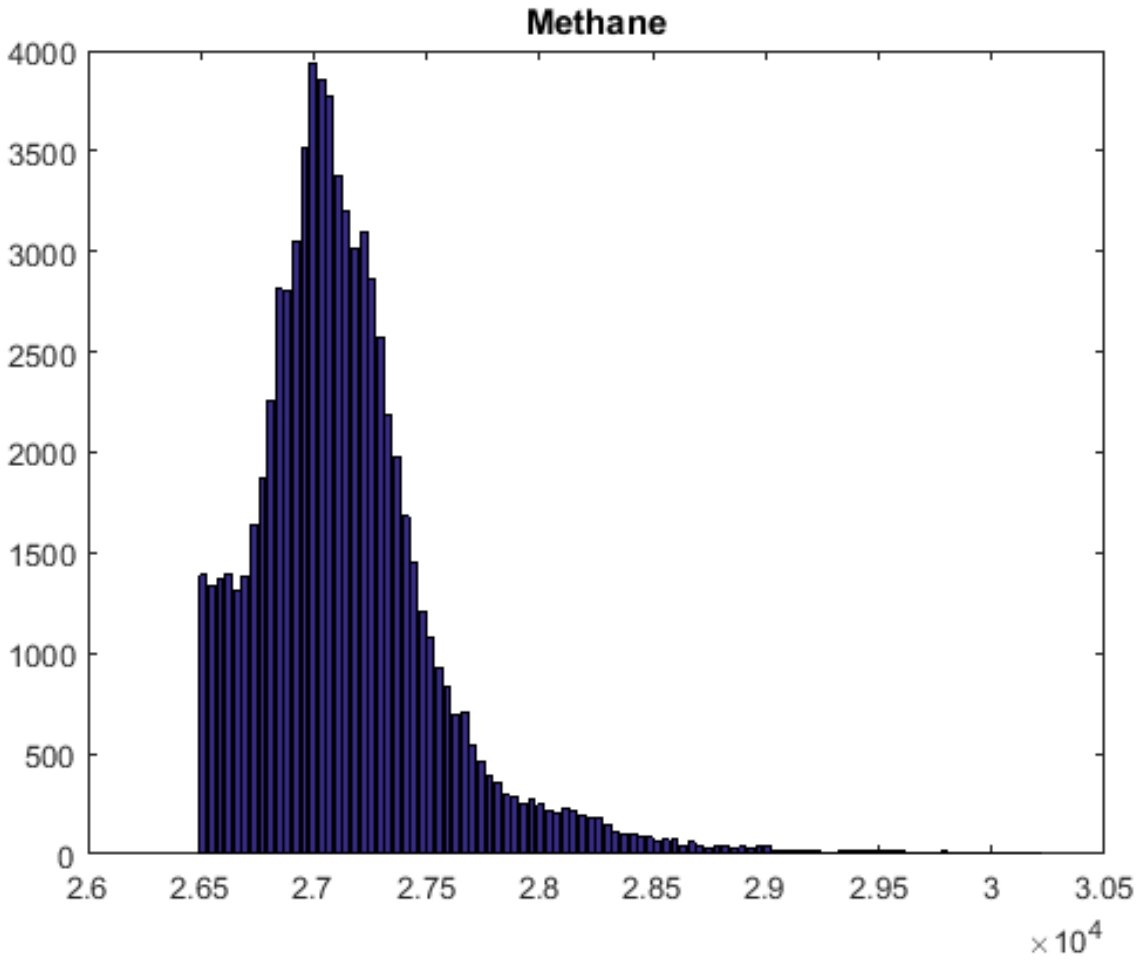

1.22 Step 4 - rescaling the raw images

First min-max and mean of respective phases are calculated for the respective (raw) phases (obtained above), which thereafter are replaced by their respective mean values.

```
%average values
```

1.23 With an exception to GH dataset

Where EDH (raw pixels) are replaced with average quartz values:

```
%as they are in close vicinity to quartz pixel values

M_replace = M(:);
min_li = min_rawL;
max_li =max_rawL;
avg_li =Avg_rawL;
min_Qz = min_rawQ;
max_Qz = max_rawQ;
avg_Qz = Avg_rawQ;
min_EDH = min_rawE;
max_EDH = max_rawE;
avg_EDH = Avg_rawE;
min_GH = min_rawMu;
max_GH = max_rawMu;
avg_GH = Avg_rawMu;

%------------------------------------------------------------------------
% indxes of liquid pixels
%------------------------------------------------------------------------
Ind_rep_L = find(M_replace>=min_li & M_replace <= max_li);
```

```
% replacement by average liquid value
if min(M_replace(Ind_rep_L))==min_li & max(M_replace(Ind_rep_L)==max_li)
    M_replace(Ind_rep_L)=avg_li;
else
    fprintf('min and max for liquid dont match.....\n')
    return
end

%-------------------------------------------------------------------------
% indxes of quartz pixels
%-------------------------------------------------------------------------
Ind_rep_Q = find(M_replace>= min_Qz & M_replace<= max_Qz);
% replacement by average quartz value
if min(M_replace(Ind_rep_Q))==min_Qz & max(M_replace(Ind_rep_Q))==max_Qz
    M_replace(Ind_rep_Q)= avg_Qz;
else
    fprintf('min and max for quartz dont match.....\n')
    return
end
%-------------------------------------------------------------------------
% indxes of EDH pxels
%-------------------------------------------------------------------------
Ind_rep_E = find(M_replace>= min_EDH & M_replace<=max_EDH);
%
```

1.24 Replace by average quartz values

```
if min(M_replace(Ind_rep_E))==min_EDH & max(M_replace(Ind_rep_E))==max_EDH
    M_replace(Ind_rep_E)= avg_Qz;
else
    fprintf('min and max for EDH dont match.....\n')
    return
end

%-------------------------------------------------------------------------
%indexes of gas hydrate pixels
%-------------------------------------------------------------------------
Ind_rep_M = find(M_replace>=min_GH & M_replace<=max_GH);
% replacement by average gas hydrate value
if min(M_replace(Ind_rep_M))== min_GH & max(M_replace(Ind_rep_M))==max_GH
    M_replace(Ind_rep_M)= avg_GH;
else
    fprintf('min and max for methane dont match.....\n')
    return
end

%-------------------------------------------------------------------------
```

1.25 Reshape rescaled array

```
%-------------------------------------------------------------------------
M_replaced = reshape(M_replace,[dim(1), dim(2), dim(3)]);
clear M_replace;
figure; imagesc(M_replaced(:,:,1));
title('Rescaled Raw');
```

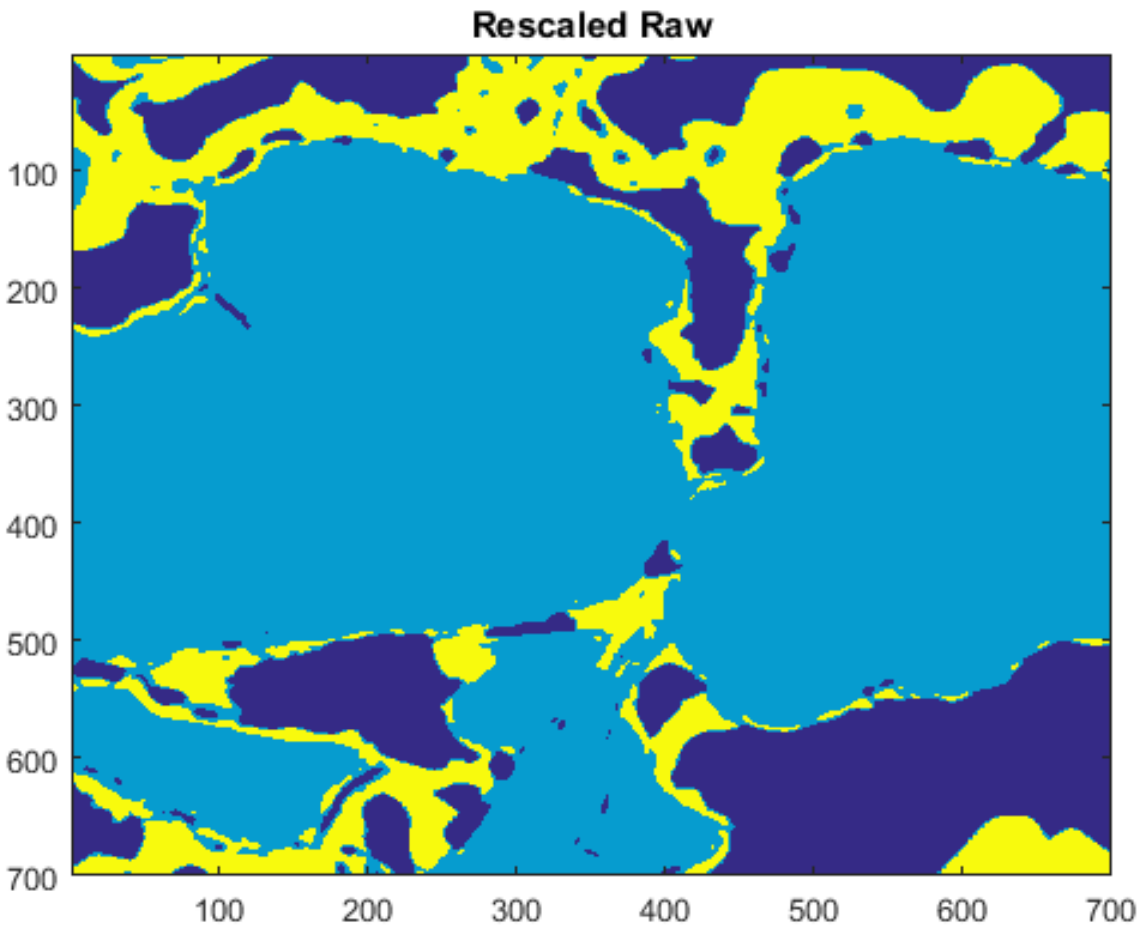

1.26 Step 5

K-means clustering is performed on the rescaled images to obtain segmetation in three classes:

```
clusterS =3;
initialcenters = [avg_li,avg_Qz,avg_GH];
for ii = 1:dim(3)
    R=double(M_replaced(:,:,ii));
    [r,c,v]=find(R>grenzwert);
    cyl=R>grenzwert;
    R1=cyl.*R;
    [m, n, w]=find(R1);
    G = kmeans(w,clusterS,'Distance','sqeuclidean','start',initialcenters');
    S=sparse(r,c,G,size(R,1),size(R,2));
    M_seg=full(S);
    SegImg(:,:,ii)=M_seg;
    %figure; imagesc(SegImg(:,:,ii)); colormap(parula(5)); colorbar;
end

figure; imagesc(SegImg(:,:,1)); colormap(parula(5)); colorbar;
title('Gas Hydrate ROI');

fclose('all');
```

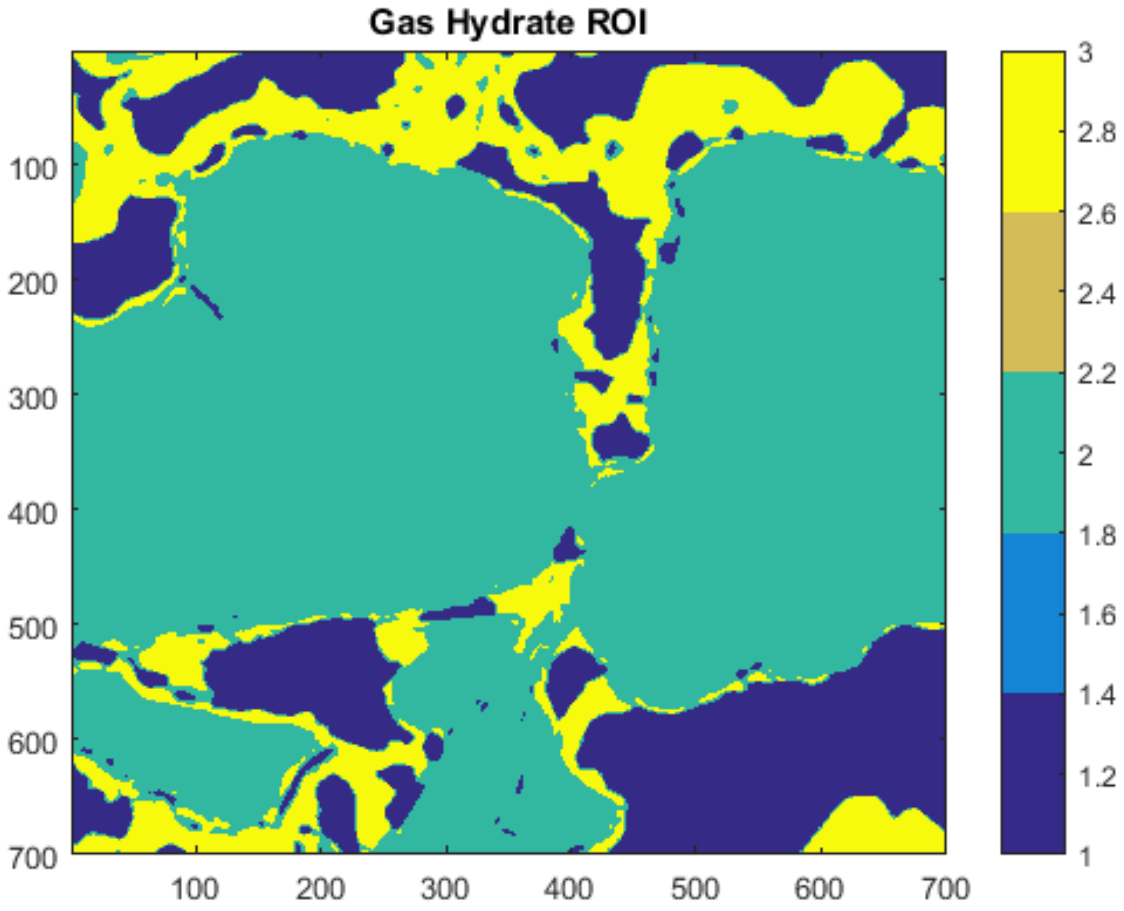

Published with MATLAB® R2015b

Appendix B: CobWeb User Manual

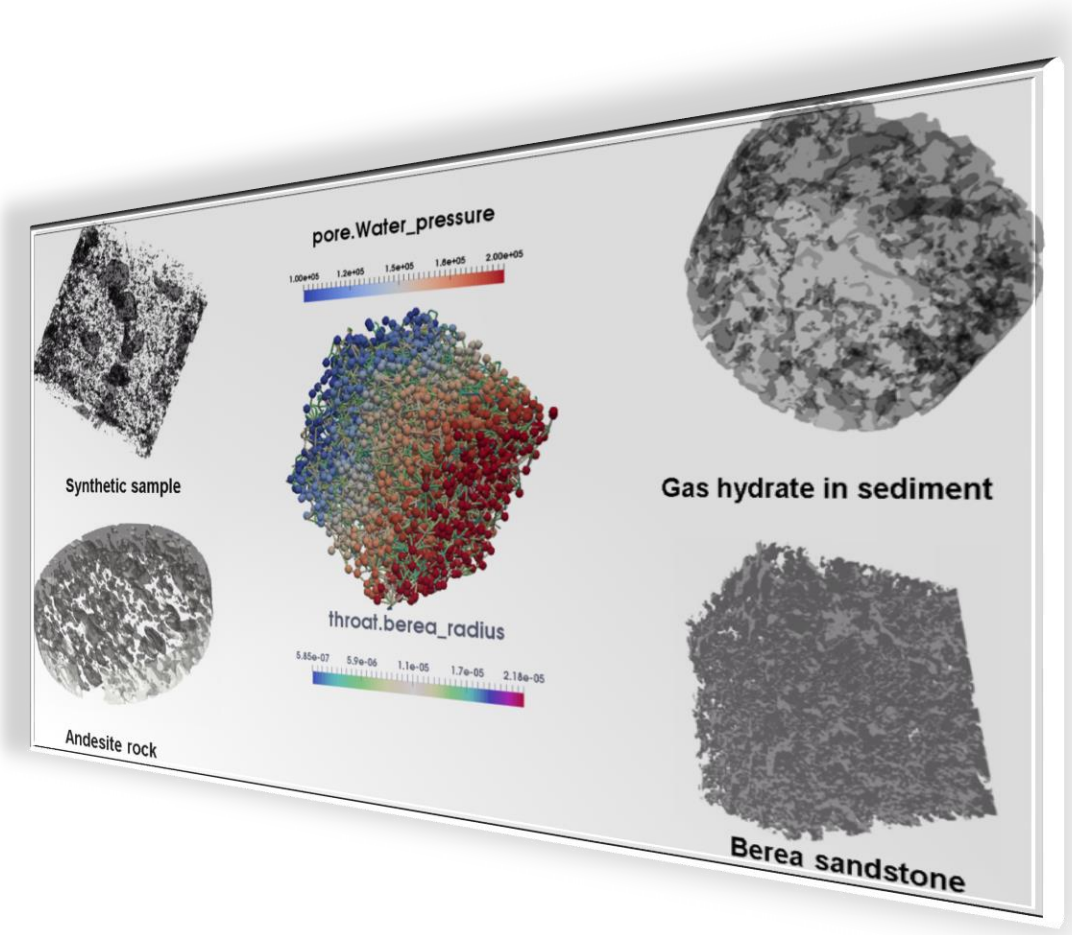

User Manual

ADAPTIVE SOLUTIONS

TECHNISCHE UNIVERSITÄT DARMSTADT

Table of Contents

1. Introduction to CobWeb 1.0

1.1 Overview

1.2 About this Manual

1.3 Service

1.4 Feedback

2. System Requirements

2.1 Operating System

2.2 Hardware

2.2.1 Display

2.2.2 User Rights

2.2.3 Recommended setup

2.2.4 Third Party Software

2.2.5 Remote access

3. Installation Instructions

3.1 Matlab Runtime License

3.2 ParaView

3.3 Microsoft® Excel

3.4 CobWeb 1.0

4. Getting Started

4.1 CobWeb 1.0 Interface & Tools

4.1.1 Toolbar

4.1.2 Inspector

4.1.3 Preprocessing Panel

4.1.4 Display Window

4.1.5 History Window

4.1.6 Control panel

5. Demonstration

5.1 Loading TIFF Data

5.2 Loading RAW Data

5.3 Image Processing

5.3.1 Representative Elementary Volume

5.3.2 Image Inspection

5.3.3 Image Segmentation — Unsupervised Machine Learning Technique

5.3.4 Image Segmentation — Supervised Machine Learning Technique

6. Visualization

6.1 Geometrical Parameters

6.1.1 Relative Porosity

6.1.2 Pore Size Distribution

6.1.3 Volume Fraction

6.2 Validation
6.3 Exporting Data
6.4 Volume Rendering
6.4.1 Volume Rendering with CobWeb 1.0
6.4.2 Volume Rendering with ParaView
7. Limitation
8. Trouble Shooting

List of Tables

Table 1: Product information 107

Table 2: Supported operating systems 107

Table 3: Recommended hardware settings 108

Table 4: Third party applications and plugin 109

Table 5: MCR Installation 110

Table 6: ParaView Installation 110

Table 7: CobWeb executable installation 111

Table 8: Data types 124

Table 9: Metrics for validation 145

Table 10: Plugins and their respective file formats 148

Table 11: Limitation of CobWeb 1.0 157

List of Figures

Figure 1: CobWeb executable and associated files. 111

Figure 2: The CobWeb 1.0 interface after startup 112

Figure 3: Tools available in the toolbar 113

Figure 4: Zoom toolbar and right click menu options 114

Figure 5: Rotate tool and right click menu options 115

Figure 6: Data cursor tool and right click menu options. The left and right plots show the dataview option either as the datapin (left) or window (right) option. 115

Figure 7: Colorbar tool and right click menu options 116

Figure 8: Legend tool and right click menu options 117

Figure 9: Scale tool and right click menu options 118

Figure 10: Inspector panel and its subpanels 119

Figure 11: Left side, option -> sub options for different types of segmentation. Right side option -> sub options for different types of image filters 120

Figure 12: Left side, option -> sub options for different types of distance functions. Right side, option -> sub options of geometrical characteristics 121

Figure 13: Evoking geometrical parameters with a right click 121

Figure 14: Control panel of the CobWeb 1.0 123

Figure 15: The figure schematically denotes the steps to load TIFF files in to CobWeb 1.0 124

Figure 16: Loading process 125

Figure 17: Files loaded 125

Figure 18: Loading a RAW file 126

Figure 19: Dimensions of RAW data are to be given by the user 126

Figure 20: Processing XCT data 127

Figure 21: ROI selection pop-up menu 128

Figure 22: ROI cropping 128

Figure 23: Noise pixel selection 129

Figure 24: Image inspection 130

Figure 25: Image processing 131

Figure 26: K-means segmentation 132

Figure 27: Image segmentation with supervised ML techniques 133

Figure 28: Input of pixel information 133
Figure 29: Training and testing supervised ML technique 134
Figure 30: Plotting porosity 136
Figure 31: Porosity processing menu and input 136
Figure 32: Porosity of single slice 137
Figure 33: Porosity of complete stack 138
Figure 34: Pore size distribution processing menu and input 139
Figure 35: Pore size distribution of single slice 140
Figure 36: Pore size distribution of complete stack 141
Figure 37: Volume fraction processing menu and input 142
Figure 38: User input and volume fraction of single slice 143
Figure 39: Volume fraction of complete stack 144
Figure 40: Plotting entropy 145
Figure 41: Plotting receiver operational characteristics (ROC) 146
Figure 42: Plotting k-fold cross-validation 147
Figure 43: Export stack to ParaView 148
Figure 44: Export geometrical parameters 149
Figure 45: Export validation metrics 149
Figure 46: Volume rendering options in CobWeb 1.0 150
Figure 47: Volume rendering using CobWeb 1.0 151
Figure 48: Export segmented REVs in .vkt format 151
Figure 49: Loading VKT file in ParaView 152
Figure 50: VKT file loaded in ParaView 152
Figure 51: Slice mode in ParaView 153
Figure 52: Surface mode in ParaView 153
Figure 53: Volume rendered mode in ParaView 154
Figure 54: Pore volume in ParaView 154
Figure 55: Hydrate volume in ParaView 155
Figure 56: Gas volume in ParaView 156

1. Introduction to CobWeb 1.0

CobWeb 1.0 is a sophisticated and practical image analysis and visualisation software based on Machine Learning (ML) techniques. It is tailored for accurate image segmentation and representative elementary volume analysis (REV) of digital rock images and geomaterials obtained from X-ray tomography imaging. The graphical user interface (GUI) is simple and intuitive, and the analysis and subsequently generated figures can be used for presentations and publication.

We hope you enjoy working with CobWeb 1.0!

Disclaimer: CobWeb 1.0 IS NOT FOR CLINICAL USE

This manual assumes that you are familiar with Microsoft Windows® operating systems. If you need help with features specific to Windows systems, please refer to the documentation supplied by your computer.

1.1. Overview

The software was developed to assist the geoscientific community. Through years of research, we came to the conclusion that software available to the community working at pore-scale analysis and modelling pore-scale community lacks accurate image segmentation approaches and is manually driven. Image segmentation is essential for generating representative pore network models or for performing pore scale simulations, which help to monitor transport processes and thermal properties within desired REVs. Discrepancies due to inaccurate segmentation of artefacts can cause anomalies and thereby lead to inaccuracies in upscaling studies. Therefore, at the core of this software, a robust workflow has been implemented to perform accurate image segmentation based on the state-of-the art machine learning libraries with minimum manual intervention.

The current version is capable of processing (reconstructed) XCT files in .tiff and .raw format. Tools to zoom in, zoom out, crop and for color scale assist in the interpretation of XCT data. Noise filters such as non-local means, anisotropic diffusion, median and contrast adjustments are implemented to increase signal to noise ratio. The user can choose from five segementation algorithms, namely kmeans, fuzzy c-means (unsupervised), support vector machine (supervised), bragging and boosting (enable classifiers) for accurate segmentation and cross-validation. Material properties like relative porosities, pore size distribution, volume fraction (pore, matrix, mineral phases) can be quantified and vizualised.

1.2. About the Manual

CobWeb is designed to be as intuitive as possible, but you might occasionally need help. To locate information on particular functions, refer to this manual which includes a comprehensive table of contents and an index to help you find the information you need.

The manual contains information about

- System requirements
- Getting started
- Importing and exporting data
- Limitations
- Index

2. System Requirements

CobWeb 1.0 is a software package designed for analysis and visualisation of voxel data obtained from industrial CT instruments. It can be used for application in geosciences, animations and many other related fields. It is not suitable for CT reconstruction.

Table 1: Product information

Product name	**CobWeb**
Release	**1.0**

CT instruments[a]	• **CT reconstruction**
	  ○ **Cone beam**
	  ○ **Fan beam**
	  ○ **Parallel beam**

Document ID	**CobWebUserManual-v001-en**

[a]contact APS Antriebs-, Prüf und Steuertechnik GmbH for details on CT instruments

2.1. Operating System

The software has been tested and approved for following operating systems:

Table 2: Supported operating systems

Platform	Operating System
Windows:	**Windows 7 Professional 64 bit** **Windows 8.1 Professional 64 bit** **Windows 10 Professional 64 bit**

2.2. Hardware

The volume rendering, image processing, data loading and processing capability rely on a suitable graphic card, CPU and hard drive. Therefore, we recommend a dedicated workstation with the following configuration:

Table 3: Recommended hardware settings

Description	Features
Processor	• **Minimum:** **Intel® Core™ i5, or AMD Bulldozer.** • **Recommended:** **Latest Intel or AMD multi-core processors, e.g., Intel® Core™ i7 or Xeon® E5 processors with 2.4 GHz or higher**
RAM	• **Minimum:** **CobWeb 1.0 requires a minimum of 8 GB memory** • **Recommended:** **Data sets with 1024^3 pixels minimum 16 GB or higher** **Data sets with 2048^3 pixels minimum of 32 GB or higher**

Graphics Card	**Dedicated NVIDIA or AMD graphics cards with at least 1 GB VRAM and OpenGL 3.3 support**
	• **CobWeb 1.0 has been tested on NVIDIA® GeForce GTX 430**
	• **Recommended:**
	  ○ **NVIDIA® GeForce GTX 770 or higher**
	  ○ **AMD FirePro™ 3D V5900 or higher**
	  ○ **AMD Radeon™ HD 7950 or higher**

2.2.1. Display

Minimum display resolution: 1920 x 1080.

2.2.2. User Rights

Please make sure every user has user or administration rights.

2.2.3. Recommended Setup

For industrial purpose with work station or PC

- 64-bit CobWeb 1.0
- Intel® Xeon® i7 processors and 32 GB RAM
- 64-bit hardware
- 64-bit operating system

NOTE: CobWeb 1.0 should be executed on your local machine.
It is not recommended to use different types of graphic cards on the same computer.

2.2.4. Third Party Software

CobWeb 1.0 is developed using MATLAB R2015b. Therefore, an appropriate MATLAB compiler license is required to run the software. This has been included with the installation package or otherwise can be downloaded from the link given in the following table.
A plugin for additional reporting, analysis and animation has been configured in CobWeb 1.0.

Table 4: Third party applications and plugin

Product Name	Application and Version
MATLAB®	**R2015b (9.0) 64-bit windows runtime license** https://de.mathworks.com/products/compiler/matlab-runtime.html
Microsoft® Excel	**Reporting and Analysis** • Microsoft® Excel 15 (part of Microsoft® Office 2013) • Microsoft® Excel 16 (part of Microsoft® Office 2016) • **Microsoft® Office 365 versions are not supported.**
ParaView	**Animation and Volume Rendering** • ParaView 5.0.1 or higher should be installed https://www.paraview.org/download/
DSI Studio	**Animation and Volume Rendering** • DSI studio http://dsi-studio.labsolver.org/

2.2.5. Remote Access

Remote access to CobWeb 1.0 is not recommended. You should run the software locally on your own
computer. If you use remote access to run CobWeb 1.0, you may encounter problems such as low performance, a corrupt user interface display, application crashes, etc.

3. Installation Instruction

3.1. MATLAB Runtime License

Step 1

- The CobWeb 1.0 application is compiled using the MATLAB 2015b compiler.
- The MATLAB Compiler Runtime (MCR) enables you to run applications compiled within MATLAB using the MATLAB Compiler.
- The MCR does not require a MATLAB license and can be used to run the MATLAB compiled program on computers which do not have MATLAB installed.

Therefore, the first step is to install MCR:

Table 5: MCR Installation

Product Name	Application and Version
Windows®	Double click the self-extracting MATLAB Runtime installer that you downloaded from the web or supplied by APS GmbH R2015b runtime will have the name MCR_R2015b_win64_installer.exe. Double clicking the installer extracts the necessary files and automatically starts the installer.

3.2. ParaView

Step 2

ParaView

- ParaView used for volume rendering.

Table 6: ParaView Installation

Product Name	Application and Version
Windows®	https://www.paraview.org/download/ Version v5.0 or higher Download ParaView-5.0.1-Qt4-OpenGL2-Windows-64bit.exe. Double clicking the installer extracts the necessary files and automatically starts the installer.

3.3. Microsoft® Excel

Step 3

The optional reporting functions using an Excel Add-In support the following Microsoft® Excel versions:

- Microsoft® Excel 13 (part of Microsoft® Office 2010) and higher

3.4. CobWeb

Step 4

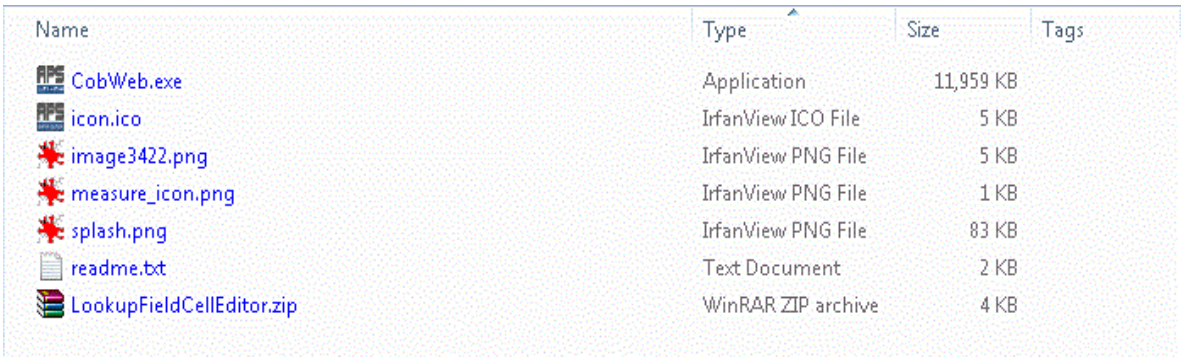

Figure 1: CobWeb executable and associated files.

Table 7: CobWeb executable installation

Product Name	Application and Version
Windows®	The CD or zip file supplied by APS GmbH should contain the files shown in Figure 1. Double click the CobWeb.exe executable. If the MCR shown in Step 1 has been installed properly, the APS splash screen will be displayed during the installation purpose. The splash screen will disappear after a few seconds and the CobWeb application will be docked on the toolbar. The following icon will appear: 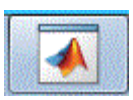

Maximise the application by right clicking and selecting maximise. The CobWeb 1.0 interface consists of seven main elements:

- Toolbar
- Preprocessing options
- Display window
- History window
- Control panel (buttons)
- Visualisation window
- Status bar

Figure 2 displays the main elements' respective locations.

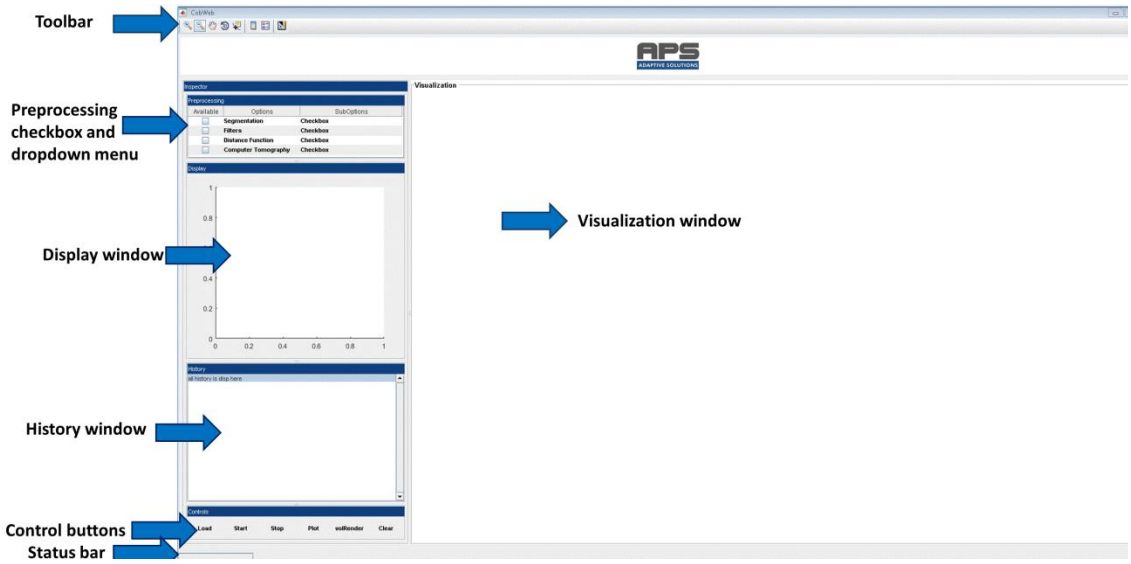

Figure 2: The CobWeb 1.0 interface after startup

4.Getting Started

4.1. CobWeb 1.0 Interface & Tools

It is essential to become familiar with various parts of the CobWeb 1.0 interface and tools before starting work with it.
The seven main parts of CobWeb 1.0 interface are:

- Toolbar
- Preprocessing options
- Display window
- History window
- Control panel (buttons)
- Visualisation window
- Status bar

4.1.1. Toolbar

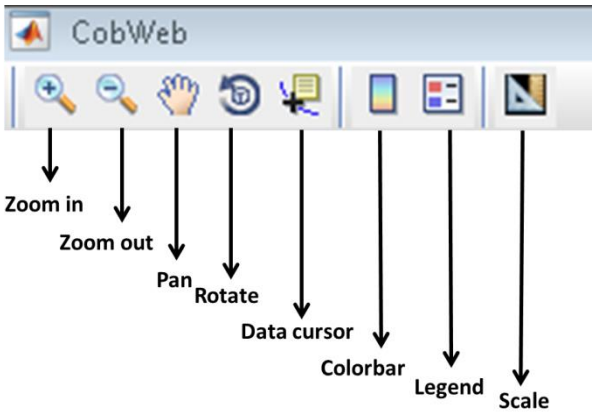

Figure 3: Tools available in the toolbar

Zoom: *The zoom in and zoom out tools are used to magnify and reduce within the 2D slice window.*

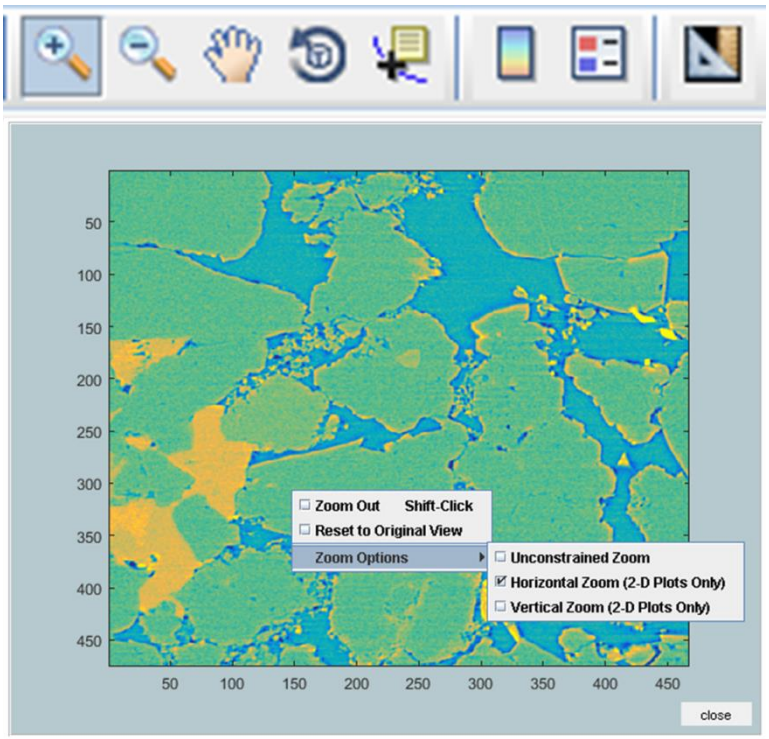

Figure 4: Zoom toolbar and right click menu options

Figure 4 displays how right clicking on the displayed image opens uimenu with other options such as vertical zoom and horizontal zoom.

- Select the **Zoom in** or **Zoom out** option from the **toolbar** by left clicking.
- Then, placing the mouse cursor on the 2D image, **left click** to zoom in and out.
- You can also zoom in and out by **left clicking,** then **holding** and **dragging left to right** on an ROI.

Pan: *The pan tool can be used to navigate within the 2D slice in a horizontal or vertical direction*.

- The pan function is **activated** by selecting it from **the toolbar** and placing it on the border of the 2D window frame and thereafter using left click to move the frame.

Rotate: *The rotate tool can be used to rotate the 3D rendered plot or 2D slice plot.*

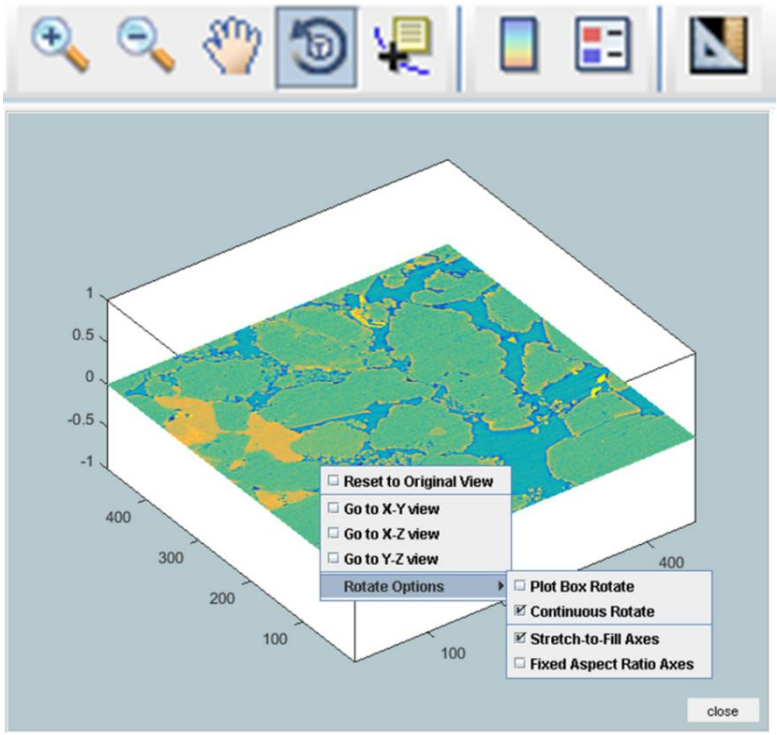

Figure 5: Rotate tool and right click menu options

- As demonstrated in Figure 5, after selecting the pan option from the toolbar, left click and hold on the displayed image and move the cursor left and right to rotate the image. The image can be rotated in a clock-wise or anti-clockwise direction.
- Right clicking opens a uimenu with further sub options (see Figure 5).

Data cursor: *The data cursor gives the position and the value of the point selected depending on the datatype 16-bit or 8-bit, as shown in Figure 6. Several options and sub options are available for the user.*

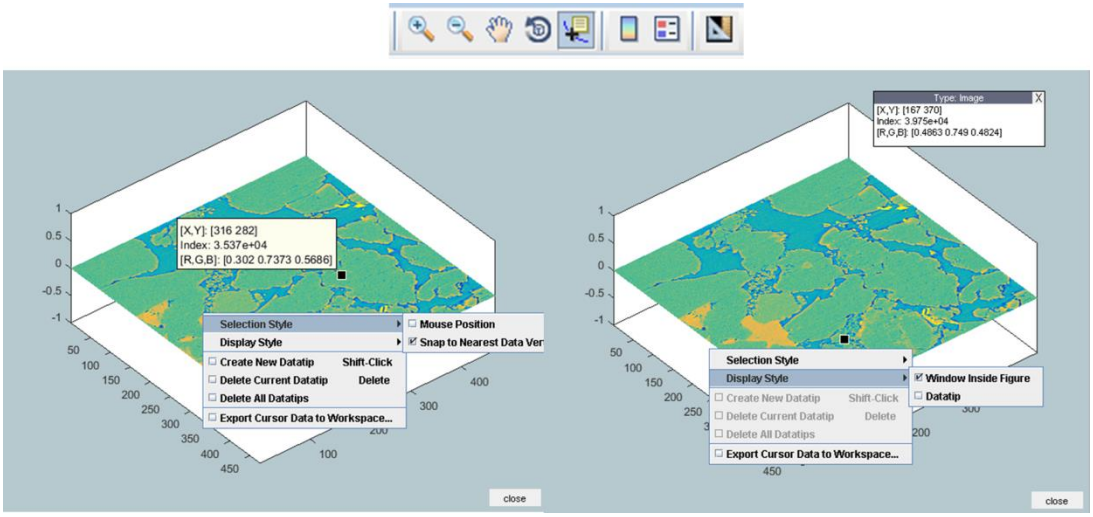

Figure 6: Data cursor tool and right click menu options. The left and right plots show the dataview option either as the datapin (left) or window (right) option.

- Figure 6 (left) shows the mouse position datapin option.
- Figure 6 (right) shows the window option.

Colorbar: *The colorbar option displays a vertical colorbar to the right of the current axes or chart. Colorbars display the current colormap and indicate the mapping of data values in the colormap.*

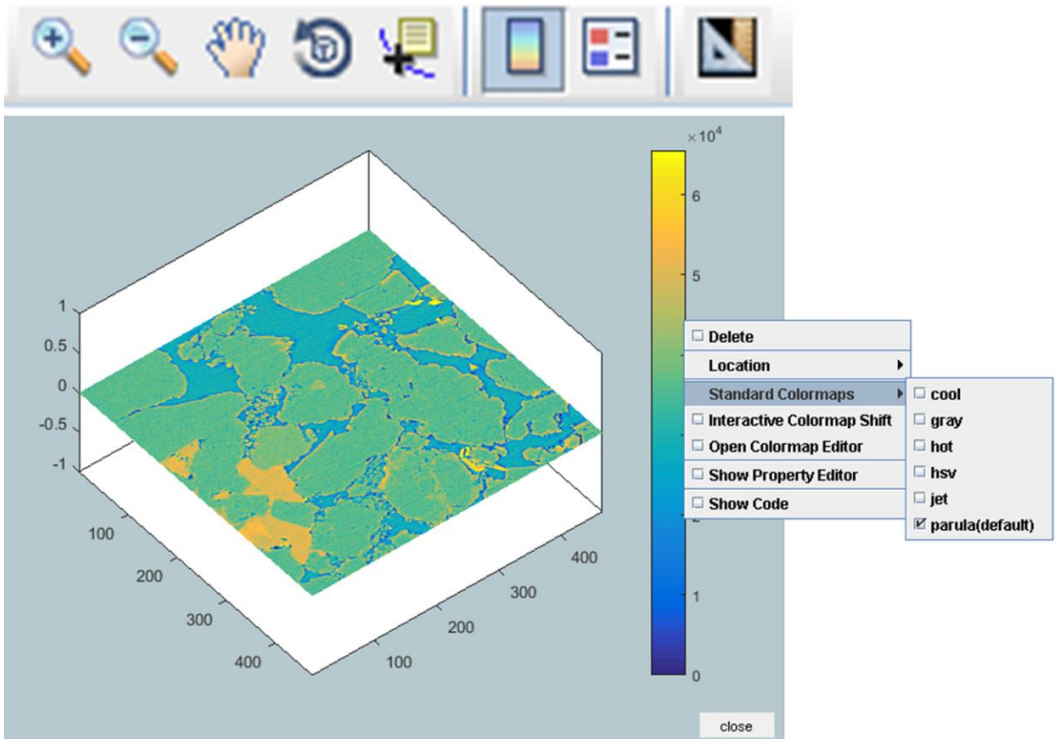

Figure 7: Colorbar tool and right click menu options

Figure 7 shows the available colormaps for visualisation.

Legend: *This option inserts a legend representing the data points.*

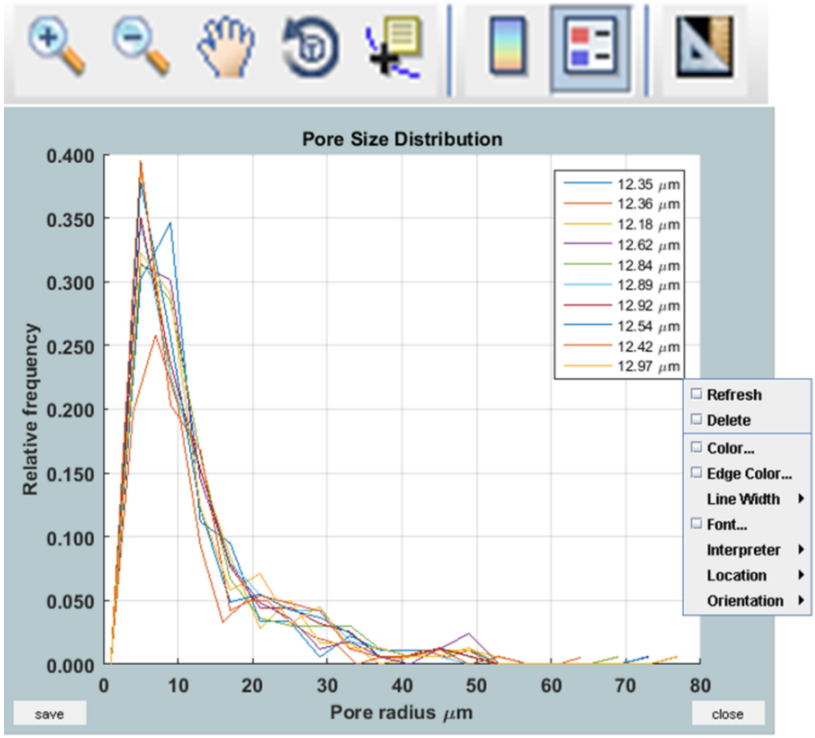

Figure 8: Legend tool and right click menu options

NOTE: Legend option activated on analysis plots, such as geometrical properties (pore size distribution, porosity, volume fraction), validation properties (entropy, roc curves and 10-fold cross validation).

Scale: *The scale tool is used to measure the distance of the XCT material. Based on the given resolution of the image, the distance is converted to millimetre scale.*

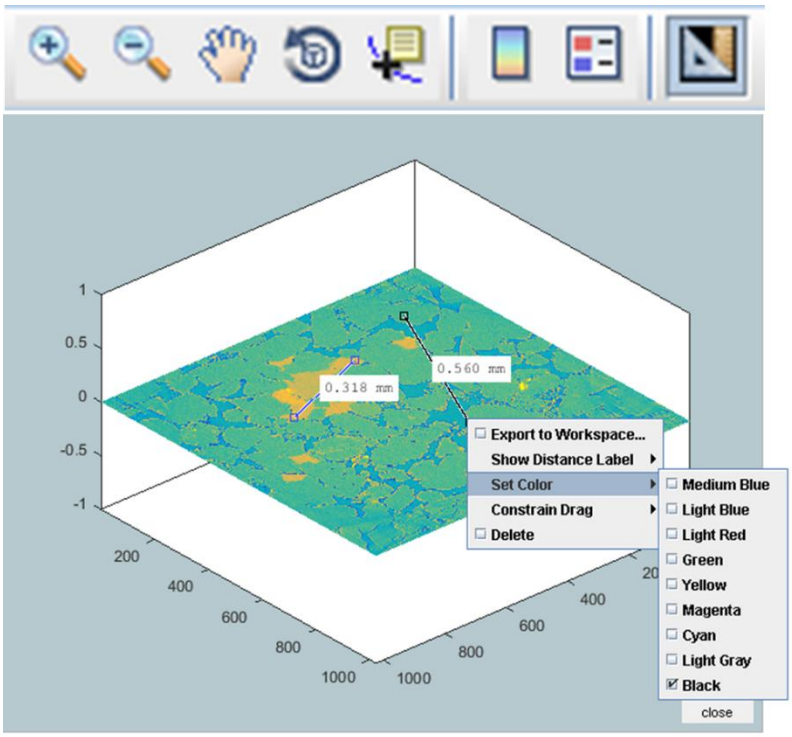

Figure 9: Scale tool and right click menu options

As shown in Figure 9, a right click on scale displays different colour shades and several sub options.

4.1.2. Inspector

The Inspector panel, which lies on the right side of the CobWeb layout (shown in Figure 10), is where the initialisation (Preprocessing panel), visualisation (Display window), information (History window) and control (Controls buttons) can be accessed.

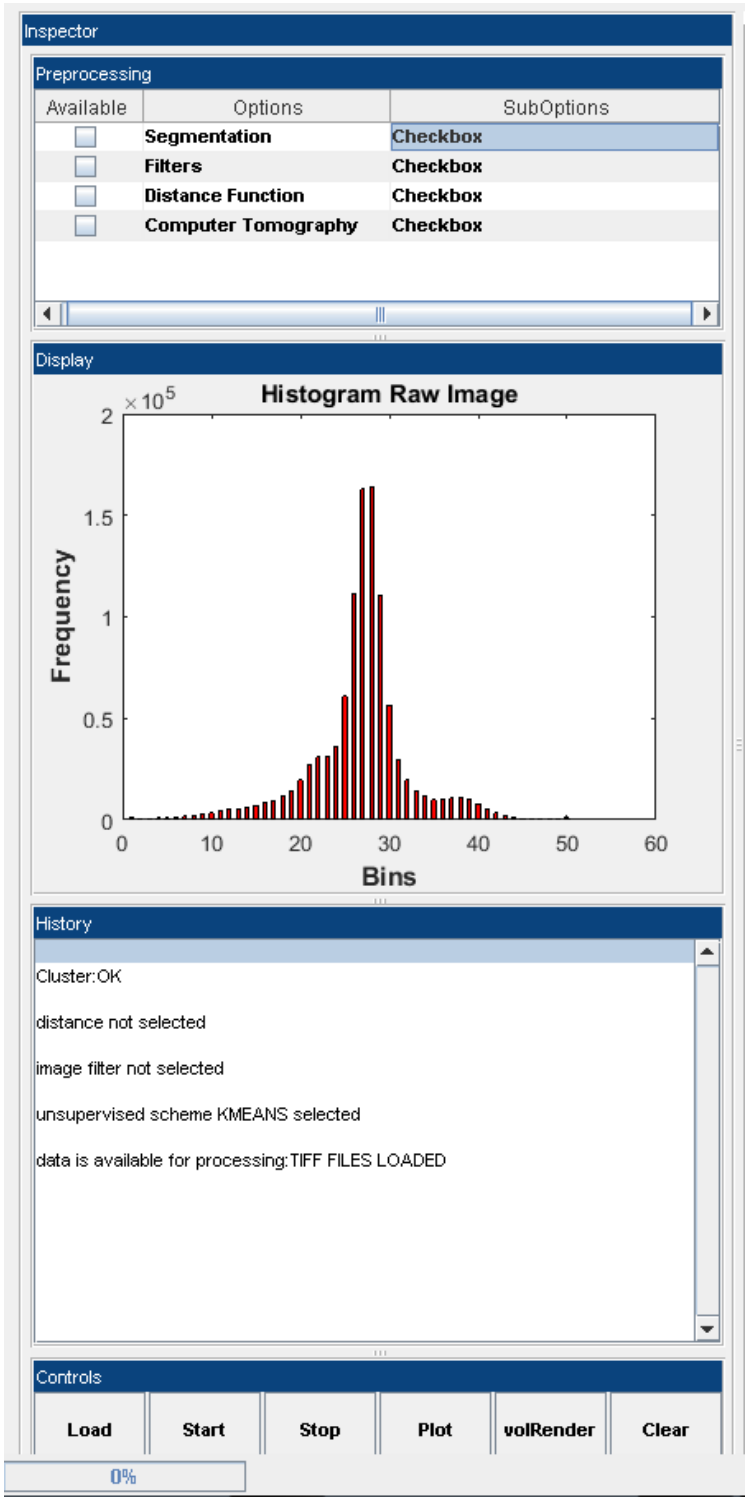

Figure 10: Inspector panel and its subpanels

4.1.3. Preprocessing Panel

The preprocessing panel is a uitable which gives a list of different options and sub options. By selecting relevant checkboxes, the options can be initialised. Then, by choosing appropriate sub options, specific actions can be performed.

Segmentation: *Segmentation is an image analysis step where a grayscale image is divided into clear partitions (clusters) based on its grayscale intensity. Geometrical analysis or analysis of information such as pore size distribution, porosity, and volume fraction can be performed or extracted only from segmented images.*

To **start** the **XCT analysis** using CobWeb 1.0, it is **mandatory** to **select** the **option segmentation** and one of one of **its sub options**. **Failing** to do so will display an **error** in the history panel: "**segmentation not initialised"**.

To enable segmentation: **first, left click** to select the **checkbox** in the first column; **second,** click on the **drop-down menu** in the first row and select one of the segmentation schemes, as shown in Figure 11.

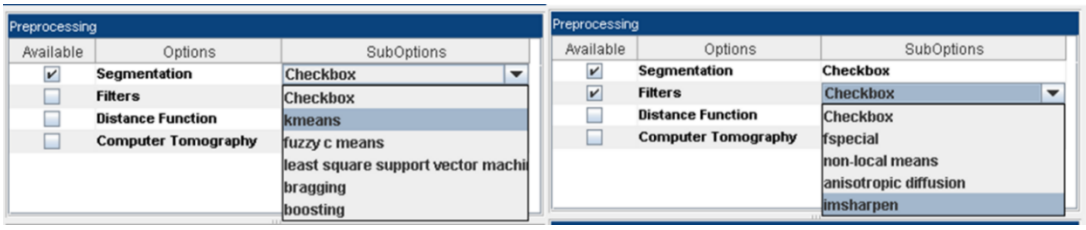

Figure 11: Left side, option -> sub options for different types of segmentation. Right side option -> sub options for different types of image filters

Filters: *Image filtration is a preprocessing step performed before segmentation. Image filtration helps reduce different kinds of artefact in XCT images and increases the accuracy and convergence rate of the segmentation algorithms.*

To enable the filers: **first, left click** to select the **checkbox** in the first column; **second** click on the **drop-down menu** in the second row and select one of the filter schemes as shown in Figure 11.

Distance function: *The distance function is used in combination with segmentation schemes. In general, it helps in finding distance between observations in close vicinity. In other words, it helps in segregating clusters.*

They are several options of distance function available, as shown in **Figure 12**. **By default, K-means** calculates cluster **centroids** with the **squared Euclidean distance** function.

To enable the distance functions: **first,** left click **to** select the **checkbox** in the first column; **second,** click on the **drop-down menu** in the third row and select one of the distance schemes as shown in Figure 12.

NOTE: The **distance function** option is **not applicable** to segmentation schemes **Least Square Support Vector Machine, Bragging, Boosting**.

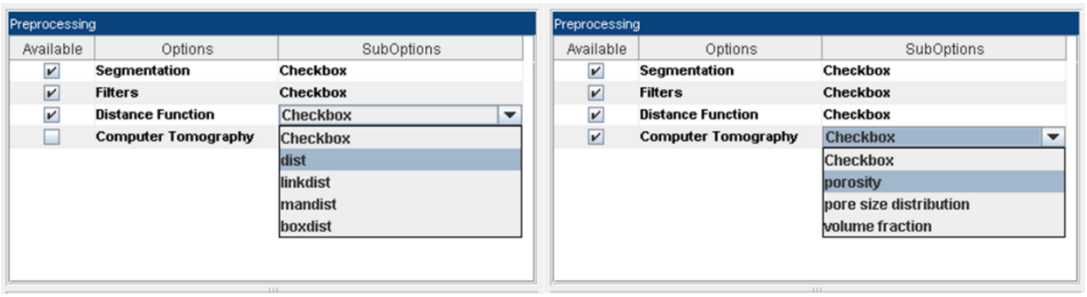

Figure 12: Left side, option -> sub options for different types of distance functions. Right side, option -> sub options of geometrical characteristics

Computer Tomography: *Geometrical analysis such as porosity, pore size distribution and volume fractions (pore, mineral and matrix) can be obtained for a chosen 2D or complete 3D segmented stack.*

The geometrical parameters can be calculated only after segmentation has been completed. To view the respective geometrical parameter, select the **checkbox** beside the option *computer tomography* with **left click,**. **then** click on the **drop-down menu** to select the relelvant sub option as shown in Figure 12. Thereafter, **click** the **plot** button in the **controls** panel.

NOTE: Geometrical parameters can also be plotted by placing the **cursor** on the **segmented slice**, **right click** and navigate to the respective option as shown in Figure 13.

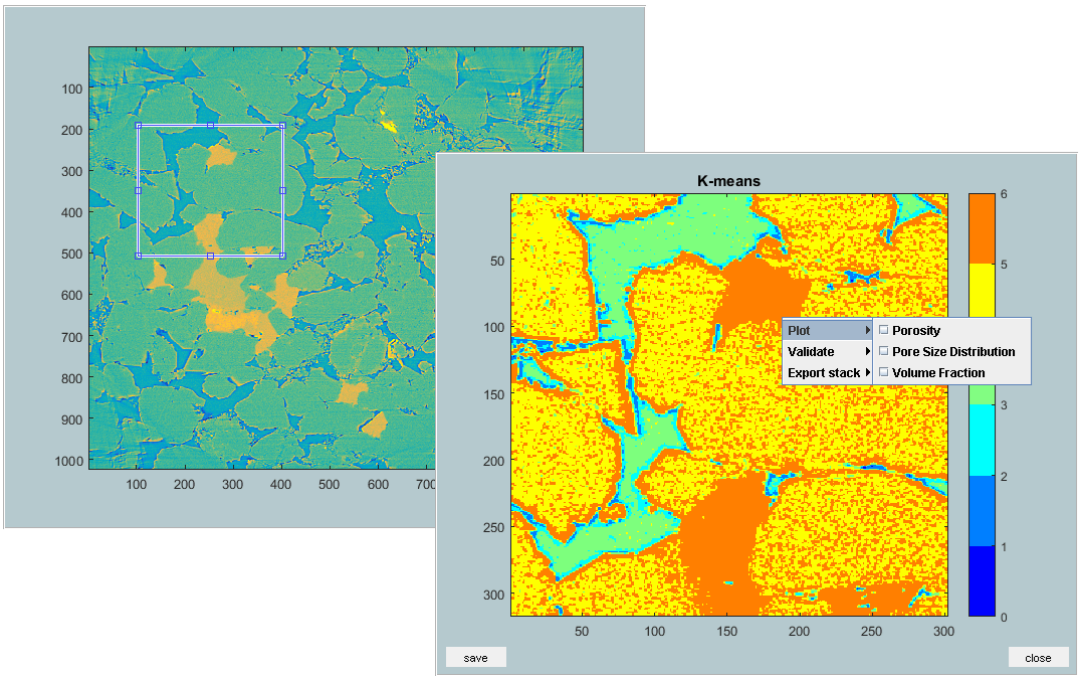

Figure 13: Evoking geometrical parameters with a right click

4.1.4. Display Window

The display window can be used to get an overview of the XCT raw images and histogram characteristics. Once the XCT stack has been loaded, at the first instance a film of 2D slices is displayed shown in the left plot in Figure 14. The film is stored by default in the base folder, which is marked with a red box in Figure 14. Once the film is completed a histogram plot of the last raw image is displayed, as shown in Figure 14.

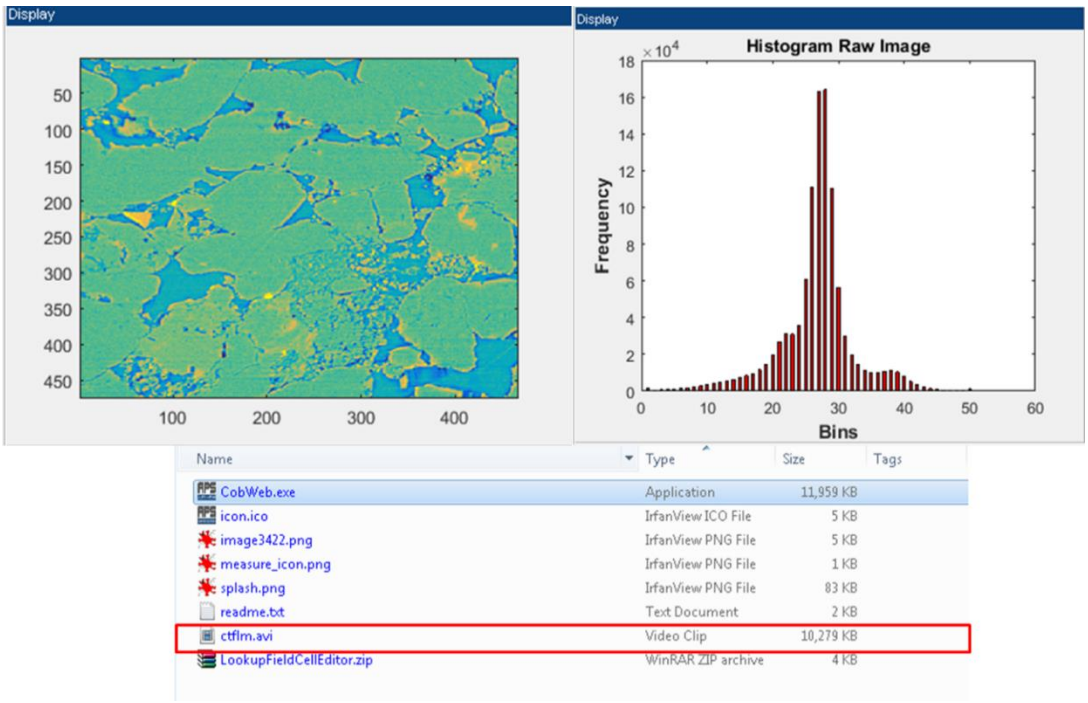

Figure 14: CobWeb 1.0 Display window displays XCT film of the 2D slices and histogram characteristics of the XCT images. The XCT film is saved in the base folder in .avi format.

4.1.5. History Panel

The history panel displays information about the parameters selected, possible errors and possible suggestions.

Figure 15: CobWeb 1.0 history window

4.1.6. Control Panel

The control panel contains six buttons and a status bar. The buttons turn red during processing and turn transparent once processing has been finished. The progress can also be monitored in the status bar.

Load: Clicking on the load button allows the XCT stack or images in RAW and TIFF format to be loaded.
Start: The Start button initiates processing.
Stop: The Stop button stops the execution of the process. The user needs to start again from step **Load**.
Plot: The Plot button plots the respective analysis in the visualisation
VolRender: Plots the 3D volume rendered plot of the XCT slices.
Clear: Clear all information.

Figure 14: Control panel of the CobWeb 1.0

NOTE: The stop function does not always stop execution for files that run a long time or files that call built-ins or MEX-files that run a long time.

5. Demonstration

This section will discuss step-by-step how to read, processes and analyse XCT data using CobWeb 1.0. All operations are performed using the **Control Buttons** in the **Control Panel**.

5.1. Loading TIFF Data

CobWeb 1.0 can only read the data types specified in Table 9.

Table 8: Data types

Data Type	
Image Slices	
TIFF	grayscale (8 bit, 16 bit)
Volume	
TIFF	grayscale (8 bit, 16 bit)
RAW	signed/unsigned 8 bit integer
RAW	signed/unsigned 16 bit integer
RAW	signed/unsigned 32 bit integer (20 bit effective range)

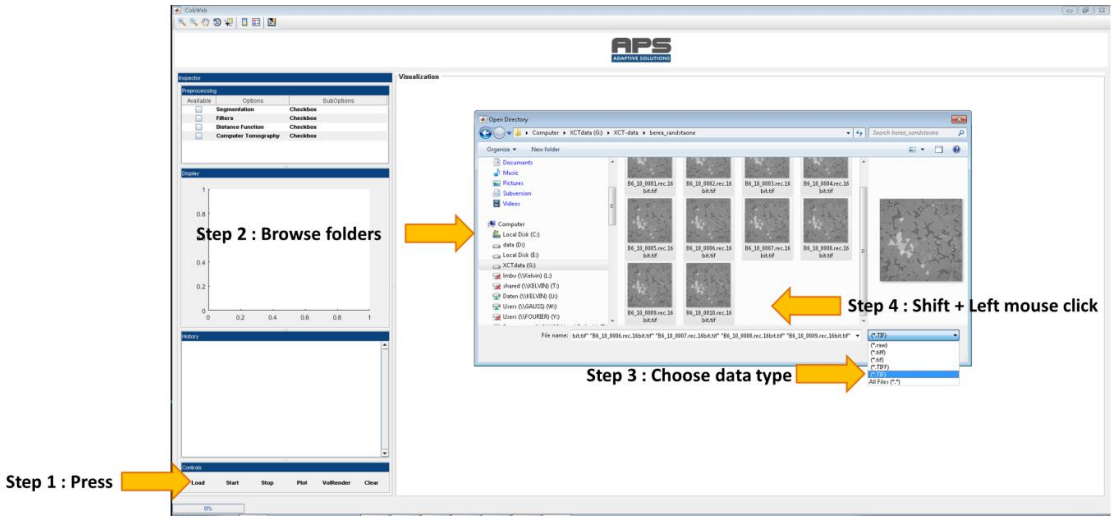

Figure 15: The figure schematically denotes the steps to load TIFF files in to CobWeb 1.0

TIFF image files and TIFF stacks (volume) can be loaded in CobWeb 1.0. CobWeb 1.0 can only handle grayscale XCT files.

- Step 1 (Figure 15): **Left click** the **Load** button. This will open a file explorer panel.
- Step 2 (Figure 15): Browse to the location of the TIFF files.
- Step 3 (Figure 15): From the drop-down menu, choose either TIFF file type or the All files option to display tiff files or all files, respectively.
- Step 4 (Figure 15): By clicking the Shift key on your keyboard + left click, the desired number of slices can be selected. Then click on the OK button on the explorer panel.
- The loading process can be **abandoned** by clicking on the **cancel** button.

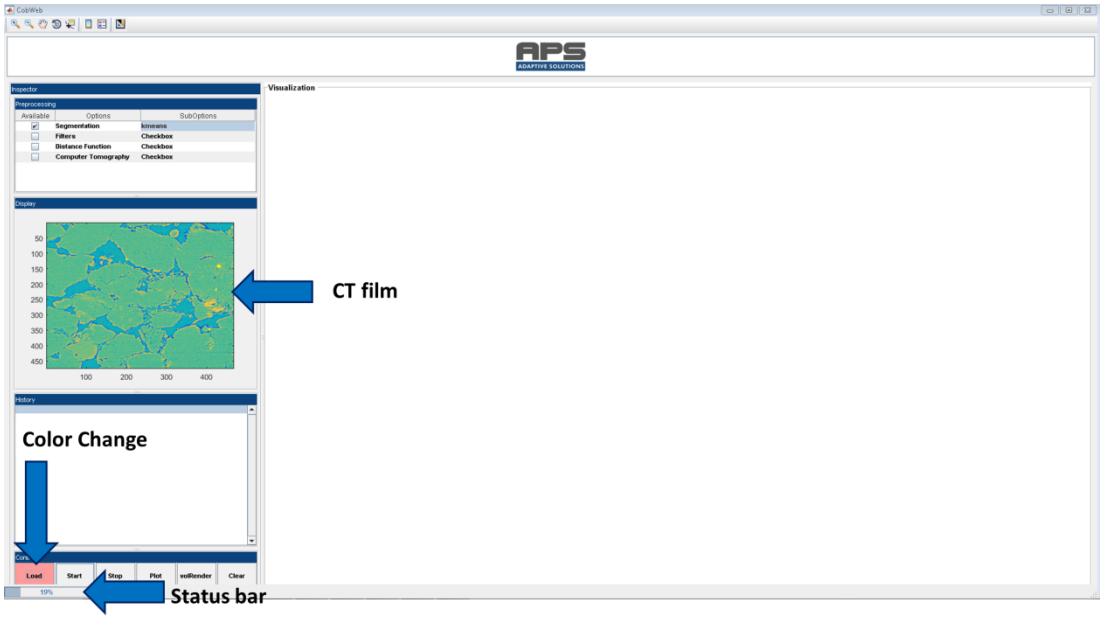

Figure 16: Loading process

- Figure 16: During the loading process, the **Load** button turns **red.**
- Figure 16: The loading process can be **monitored** using the **status bar.**
- Figure 16: The display window displays slices (2D film) during the loading process.

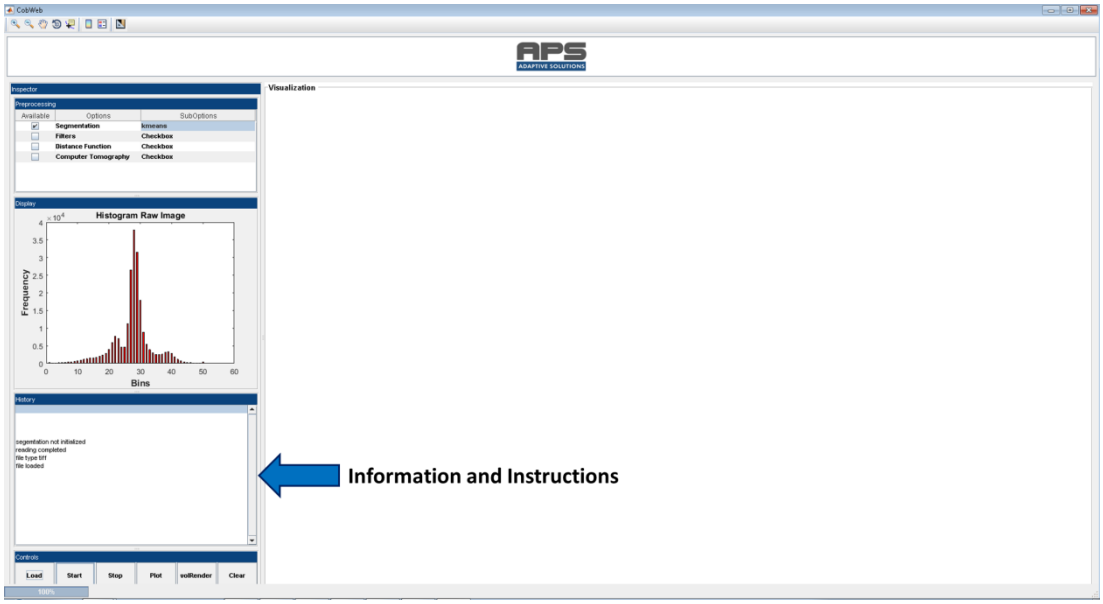

Figure 17: Files loaded

- Figure 17: The colour of the **Load** button turns transparent when the loading/reading is finished.
- Figure 17: Information, such as the data type and the next steps, is displayed in the history panel.

5.1.1. Loading RAW Data

NOTE: The dimension and the data type of the 3D stack should be known beforehand.

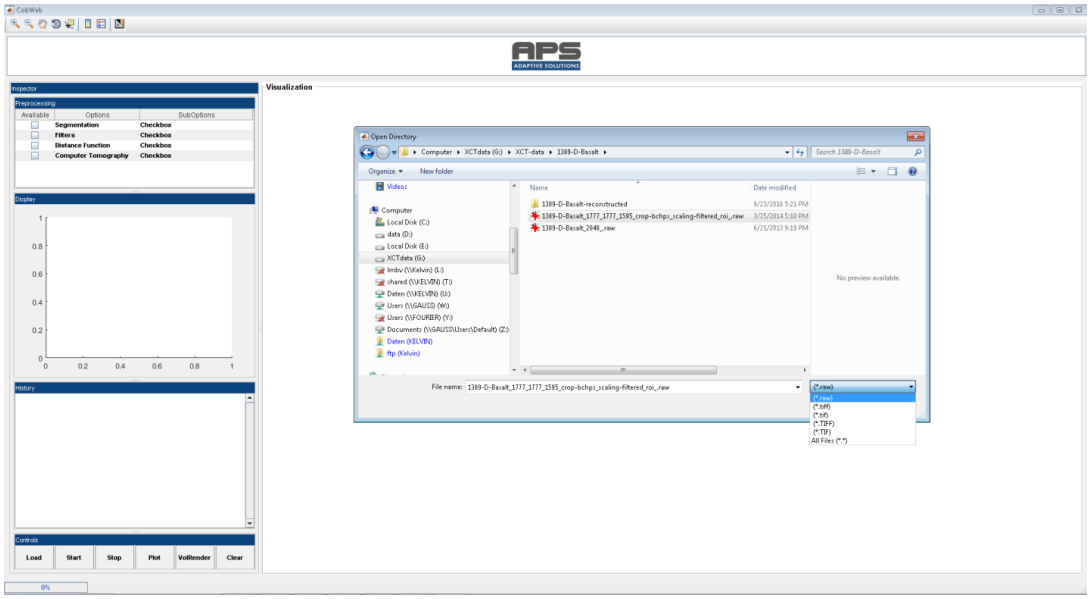

Figure 18: Loading a RAW file

- RAW files can be loaded in a similar manner to that shown in Figure 15.
- Figure 18: Instead of TIFF, the **RAW option** has to be selected from the **drop-down menu**.
- The loading process can be **abandoned** by clicking the **cancel button** or **closing the pop-up menu**.

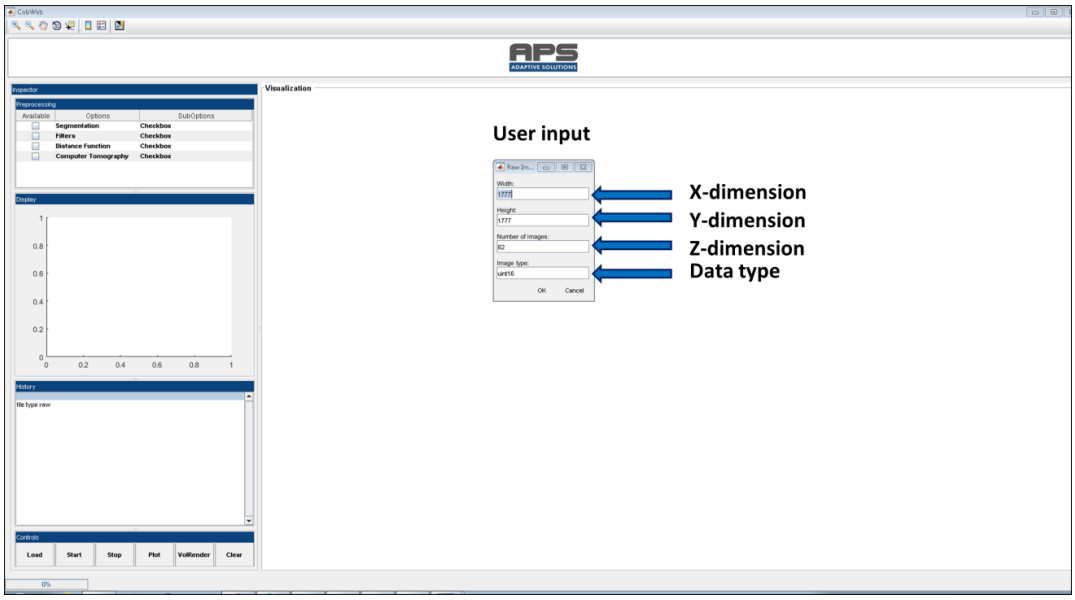

Figure 19: Dimensions of RAW data are to be given by the user

- Once the correct file has been selected, a **pop-up menu appears** where the dimensions of the **Width (X-dimension), Height (Y-dimension), Number of images ((Z-dimension)** and **data type** have to be **entered by the user,** as shown in Figure 19.

5.2. Image Processing

After loading the relevant file, the next step is to start processing.

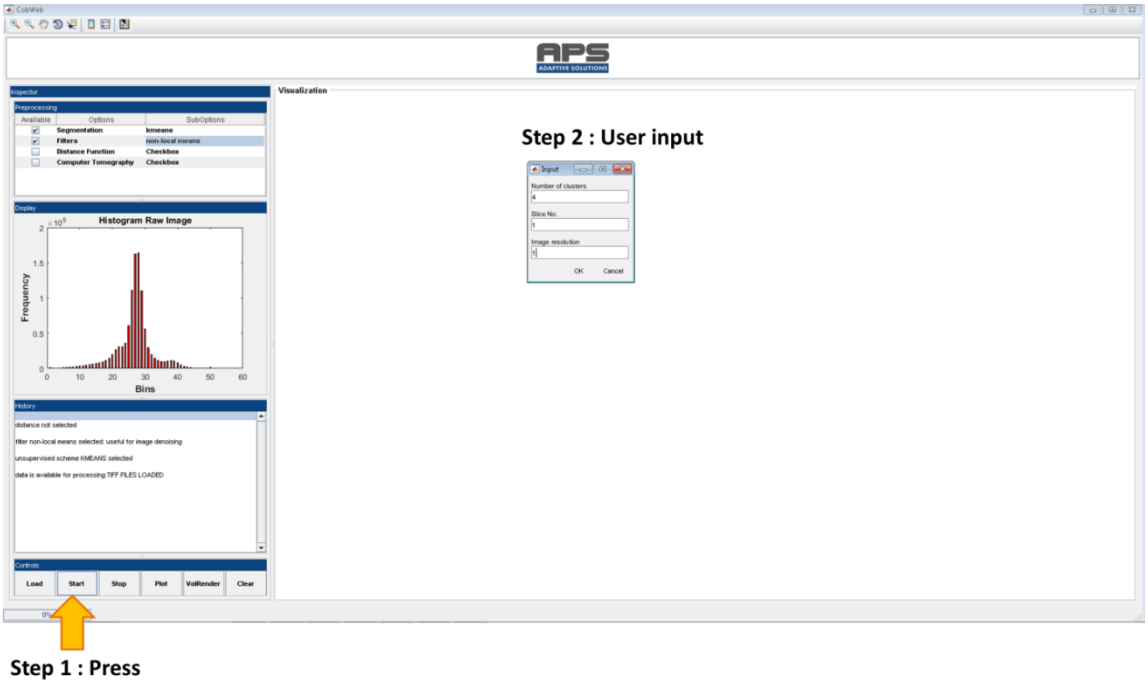

Figure 20: Processing XCT data

- Step 1 (Figure 20): C**lick on the Start button** to initialise image processing
- Step 2 (Figure 20): Enter the initializing parameters in the pop-up menu.
    - Cluster – Integer value
    - Slice number – Integer value
    - Image resolution – Integer value (in micrometre)

5.2.1. Representative Elementary Volume Selection

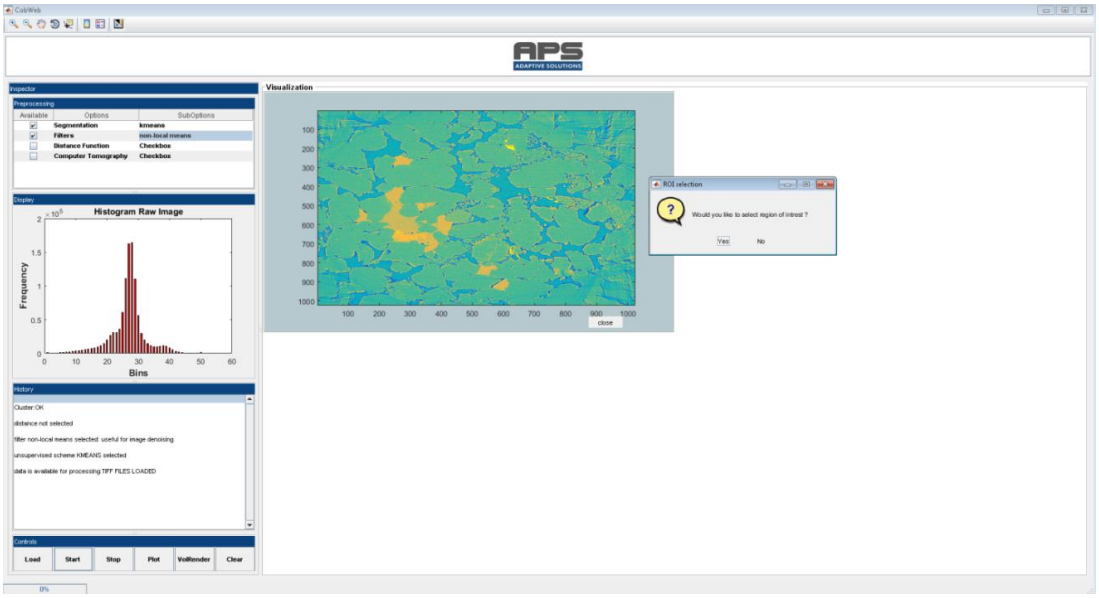

Figure 21: ROI selection pop-up menu

Once the initiating parameters are correctly entered:

- Figure 21: ROI selection option pop-up
    - The **Yes** option **activates** the **crop settings**
    - Selecting the **No** option means the **complete image** will be **processed**

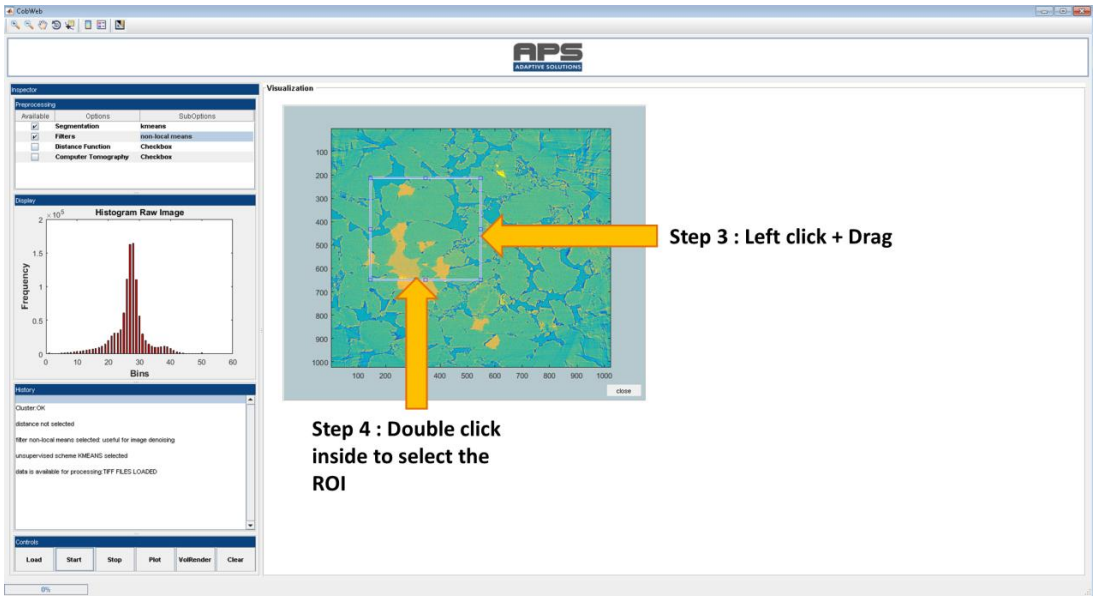

Figure 22: ROI cropping

- Step 3 (Figure 22): ROI can be fixed (selected) by **dragging the bounding box** to the desired size using **left click**.
- Step 4 (Figure 22): Double click inside the bounding box to crop the ROI region.

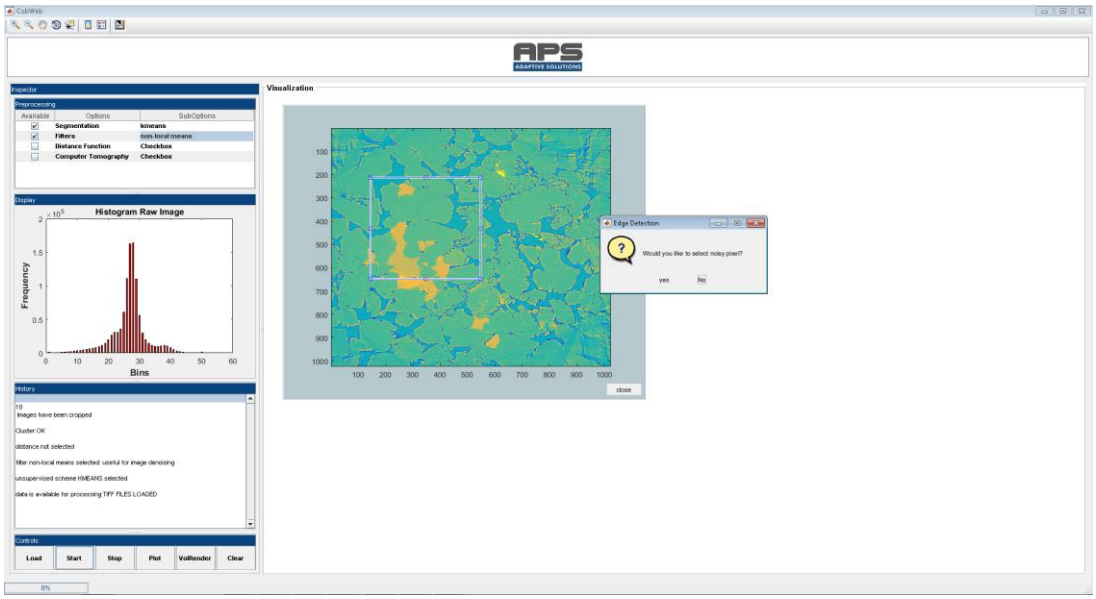

Figure 23: Noise pixel selection

- As shown in Figure 23, there is a possibility to assist the segmentation algorithm by giving a priori information about the noisy pixel. This option is **not useful for REV/ROI analysis**.
- Figure 23: This step can be **ignored** by clicking the default option **No**.

5.2.2. Image Inspection

Limitation: To view the image characteristics, the Start process must be interrupted.

- This is done by **closing the pop-up window** in Figure 21
- Doing so breaks the processing chain and thus the image characteristics can be inspected using toolbar options as shown in Figure 24.
- A **disadvantage** is that **processing** must be **initialised again** by clicking the start button (see section 6.3 for more information).

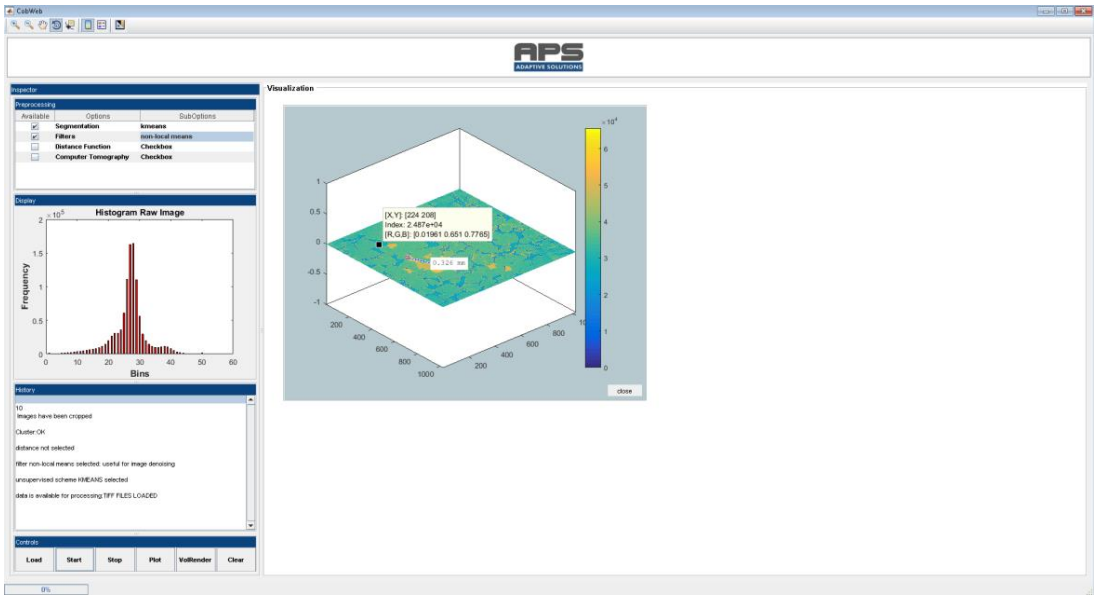

Figure 24: Image inspection

5.2.3. Image Segmentation — Unsupervised Machine Learning Techniques

The bullet points mentioned below are **relevant** if the **algorithms K-means and Fuzzy C-means** are **chosen** in the **preprocessing uimenu**.

Brief description: *The user must input the number of clusters. Based on the input (numerical value), the REV or the complete stack is segmented.*

- Once the steps specified from 6.3 to 6.3.1 are performed, the image filtration and image segmentation starts.

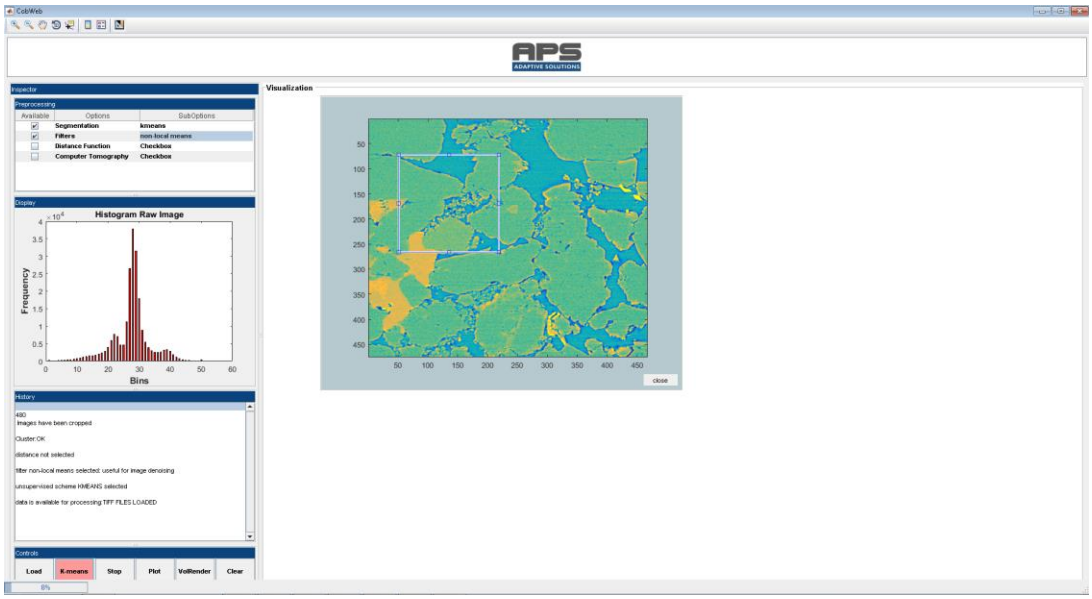

Figure 25: Image processing

- Figure 25 shows a snapshot of the CobWeb interface during segmentation. The **text** of the Start button **changes** to the segmentation algorithm (**Start -> K-means**) and the **colour** of the button changes to **red**.
- Once the processing is finished, **updated information,** such as processing time and setting, is displayed in the **history window**.

NOTE: Not just one slice but all slices or the volume data has been processed.

NOTE: If the segmentation **stops** for some **unknown reason** (Ping sound), either **re-click** the **start button** (with red background colour and text) or **clear** the setting by clicking the **Clear button** and start again by loading the file.

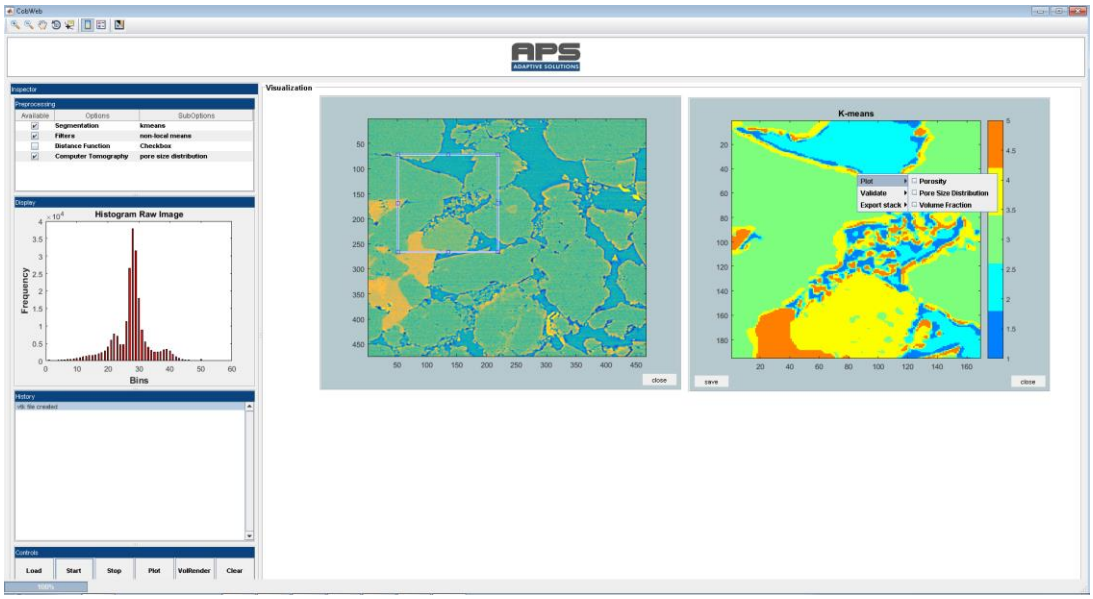

Figure 26: K-means segmentation

- Figure 26 shows how, by clicking the **Plot** button (left click), the segmented slice is **displayed** in a **separate pan window**.

5.2.4. Image Segmentation — Supervised Machine Learning Technique

The bullet points mentioned below are **relevant** if the algorithm **Least Square Support Vector Machine, Bragging and Boosting** are selected from the preprocessing uitable.

Brief description: *In the case of supervised ML techniques, the user selects different cluster centres (phases). These user inputs are used by the ML algorithm to train the model. After the training is completed, the REV is segmented into respective user defined phases.*

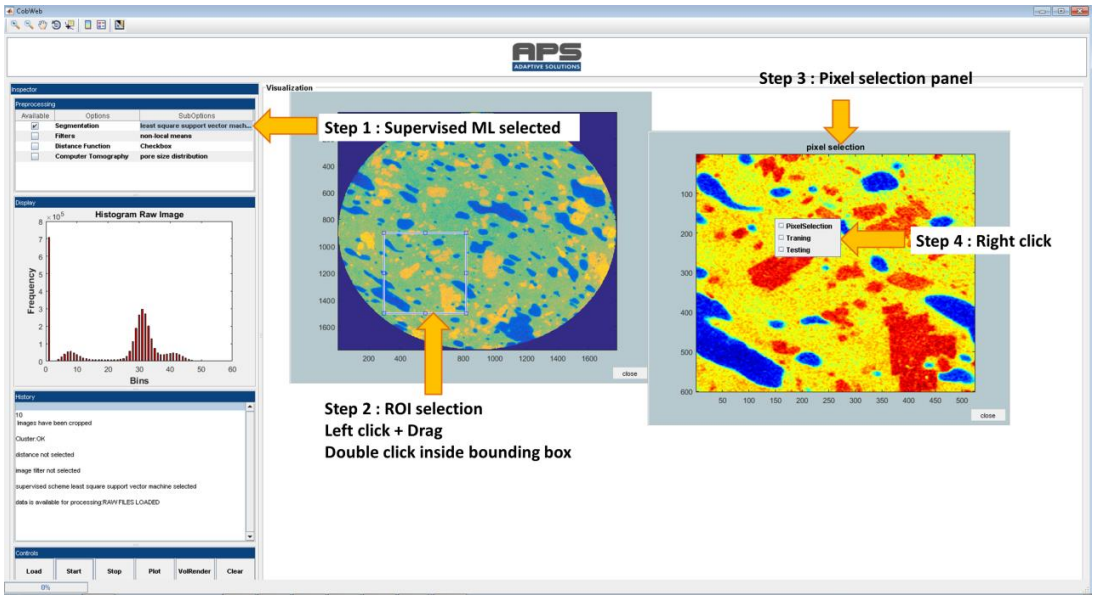

Figure 27: Image segmentation with supervised ML techniques

- Step 1 (Figure 27): Select one of the **supervised algorithms**.
- Step 2 (Figure 27): The action in Step 1 shows the ROI selection. For further details about image preprocessing and REV selection, please see section 6.3 to 6.3.1
- Step 3 (Figure 27): Once the ROI is selected, the ROI is displayed in a separate window panel: “Pixel selection”.
- Step 4 (Figure 27): **Right click** on the **ROI image** and select the first option **Pixel Selection**, this will pop up a pixel table panel.

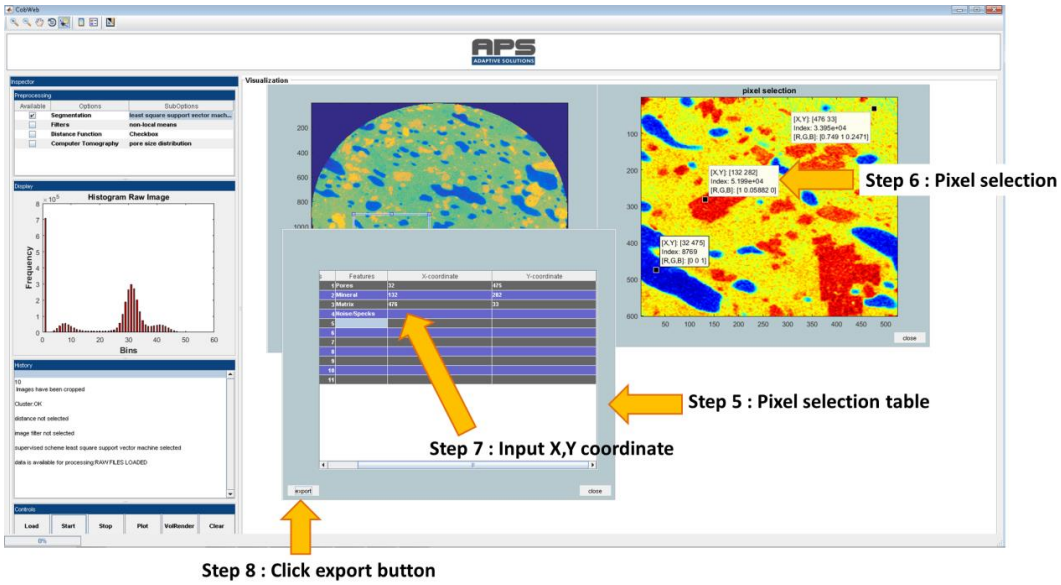

Figure 28: Input of pixel information

- Step 5: Figure 28 shows the pixel selection panel.
- Step 6 (Figure 28): Using the data cursor tool from the toolbar, different cluster centres (phases) can be investigated.
- Step 7 (Figure 28): Features (pore, mineral, matrix, noise etc.) and their respective X, Y coordinates obtained in Step 6 must be typed into the pixel table.

- There is the possibility to define up to eleven features in a serial order without any gaps.
- Step 8 (Figure 27): Click the export button. The export function transfers this information (internally) to the training model.

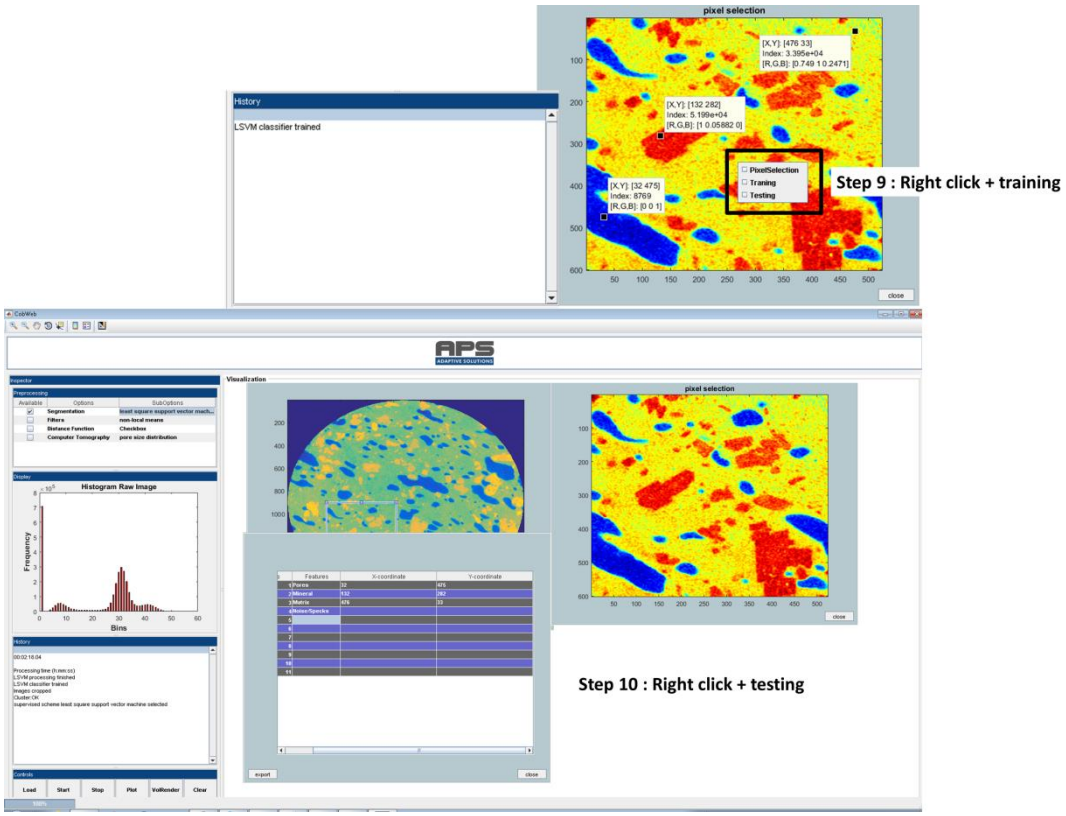

Figure 29: Training and testing supervised ML technique

- The next step is to train the model
- Step 9 (Figure 29): **Right click** on the **ROI image** and select the second option, **"Training"**. Once the model is suitably trained the information is displayed in the history panel.
- The last step is initializing segmentation
- Step 10 (Figure 29): **Right click** on the **ROI image** and select the third option, **"Testing"**.
- Once processing has finished, the information is displayed in the history panel. Thereafter, the segmented image can be viewed by clicking the plot button.

6. Visualisation

This chapter covers visualisation of different parameters such as:

- Geometrical properties
  - Relative porosity
  - Pore size distribution
  - Volume fraction
- Validation matrices
  - Entropy
  - Receiver operation characteristics
  - 10-fold cross validation
- Export
  - ParaView format
  - Excel format
  - MATLAB format
  - ASCII format
- Volume rendering with ParaView
  - Pore phase
  - Matrix phase
  - Mineral phase

6.1. Geometrical Properties

To derive geometrical properties, it is necessary that segmentation has already completed.

6.1.1. Relative Porosity

- Figure 30 shows plotting porosity. **Right click** on the segmented slice select **Plot -> Porosity**.
- A processing menu pop-up appears with three options: **Complete stack, Slice-by-Slice** and **Cancel**.
  - **Complete stack**: The porosity of the complete stack is plotted.
  - **Slice-by-Slice**: The porosity of the selected slice is plotted.
  - **Cancel**: The process is abandoned.

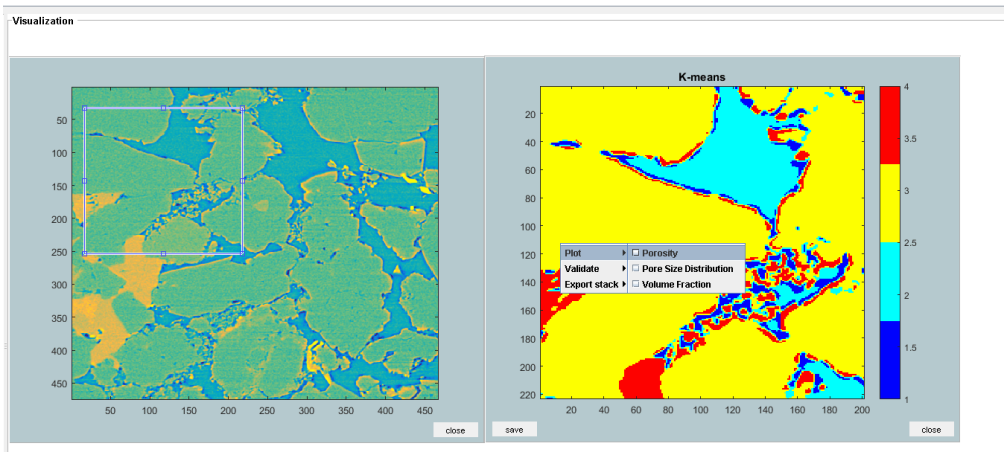

Figure 30: Plotting porosity

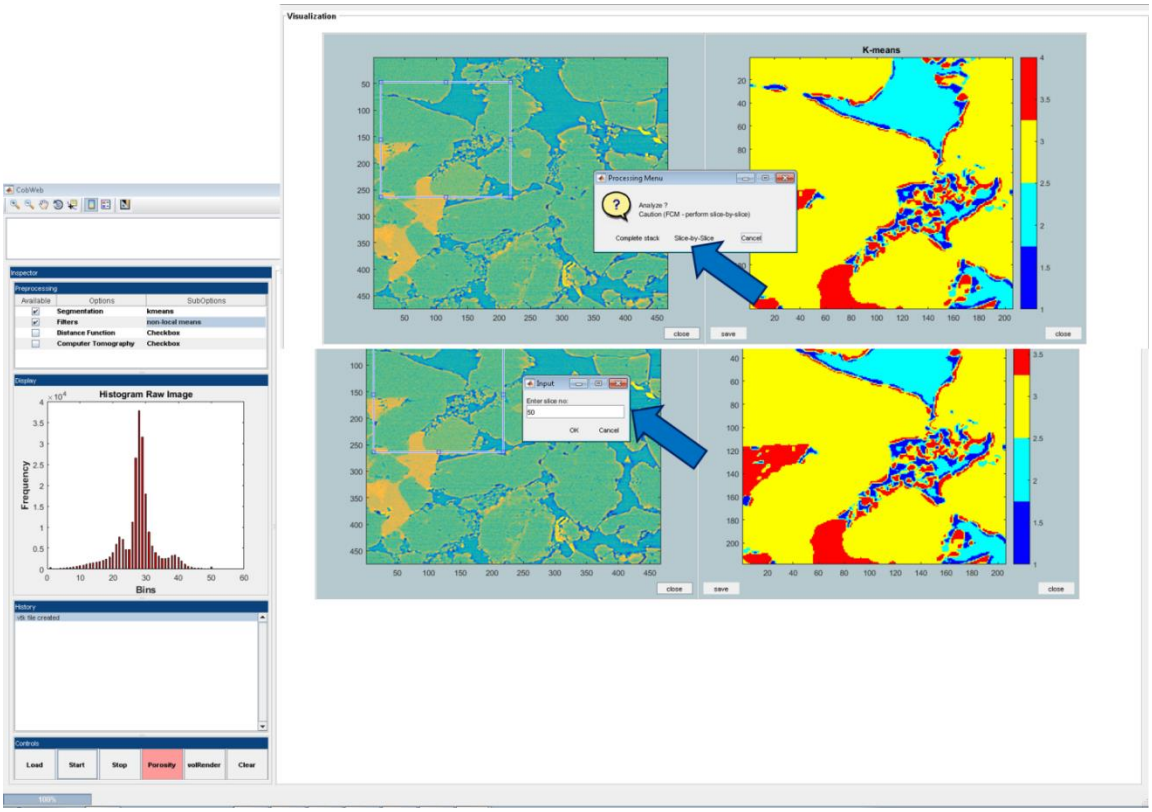

Figure 31: Porosity processing menu and input

- Figure 31 displays the **Slice-by-Slice** option **selected** and the **slice numbe**r to be **typed** by the user **as input**.
- By clicking the save option on the window panel the current plot can be saved at a desired location.

NOTE: The status bar might show a 100% status, but the plot is not shown. **Please be patient, the display of the plot window depends on your system configuration.** The plot appears as soon as the message **plotting finished** is display in the **history window**.

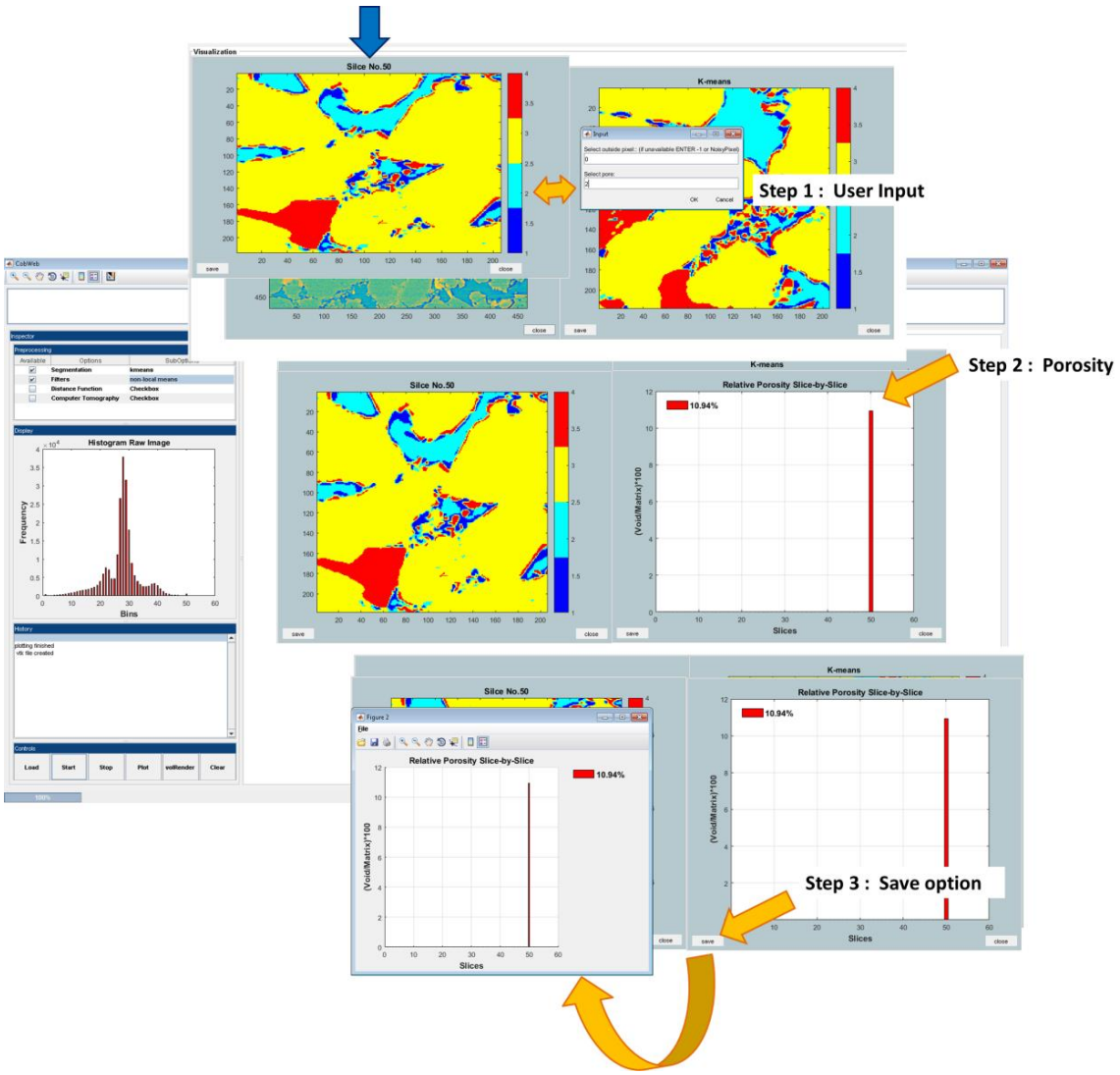

Figure 32: Porosity of single slice

- Figure 32 displays the slice (no. 50) in a new window.
- Step 1 (Figure 32): **Enter** the **cluster number** assigned to the **pore phase** and noise phase. If the noise phase is not displayed or has not been assigned a cluster value, enter zero.
- Figure 32 displays **the slice** (no. 50) plotted in a **new window. Input** in this case no. 2.
- Step 2 (Figure 32): **Relative porosity** of the **single slice** is plotted in a **new window**.
- Step 3 (Figure 32): By clicking the save option, the image can be exported into the desired image format.

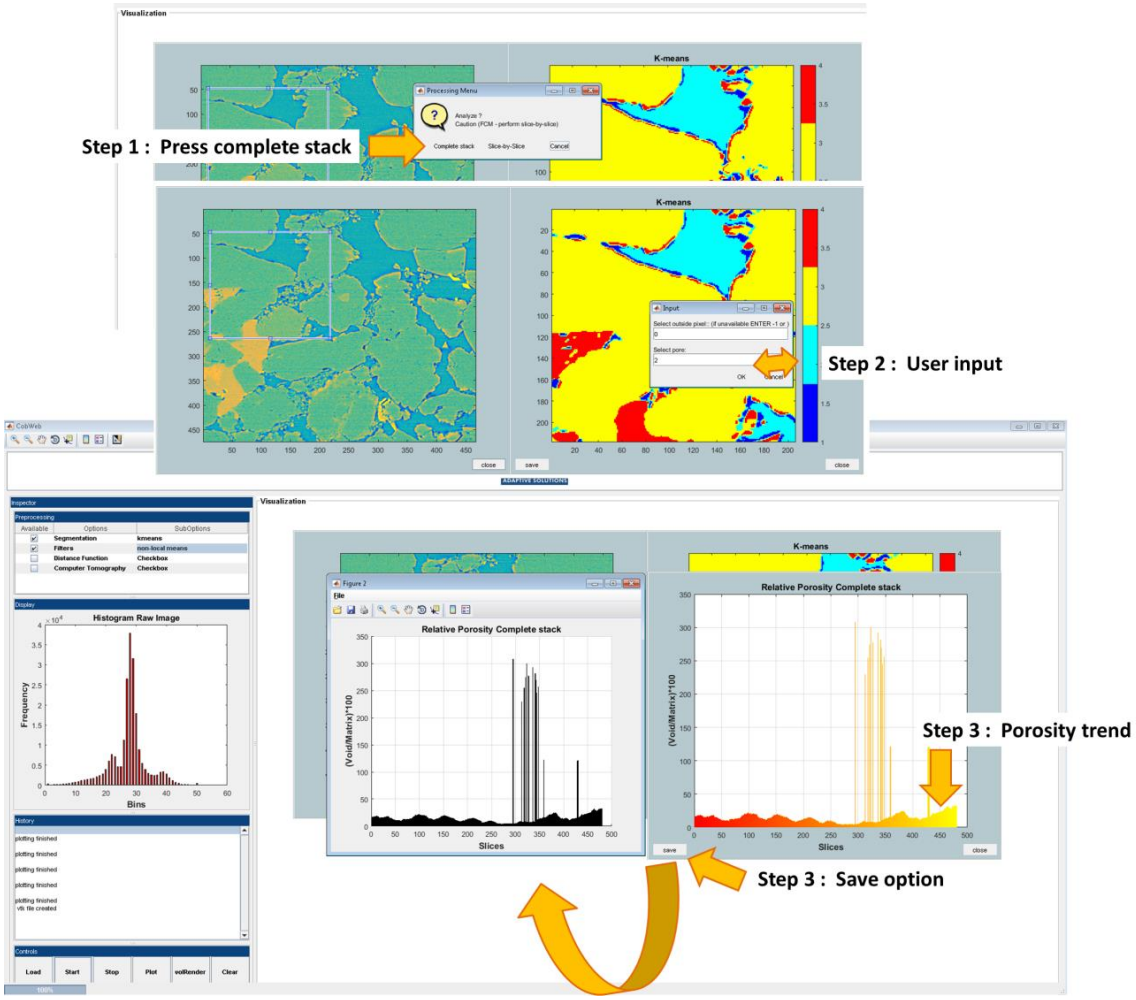

Figure 33: Porosity of complete stack

- Step 1 (Figure 33): The porosity of the REV can be plotted by clicking complete stack option.
- Step 2 (Figure 33): **Enter** the **cluster number** assigned to the **pore phase** and the noise phase. If the noise phase is not displayed or has not been assigned a cluster value, enter zero.
- Step 3 (Figure 33): By clicking the save option, the image can be exported into a desired image format.
- ---

6.1.2. Pore Size Distribution

- To plot pore size distribution: **right click** on the segmented slice and select **Plot -> Pore Size Distribution** (PSD), as shown in Figure 34.
- A processing menu pop-up appears with three options: Complete stack, Slice-by-Slice and Cancel.
    - **Complete stack**: The PSD of the complete stack is plotted.
    - **Slice-by-Slice**: The PSD of the selected slice is plotted.
    - **Cancel**: The process is abandoned.

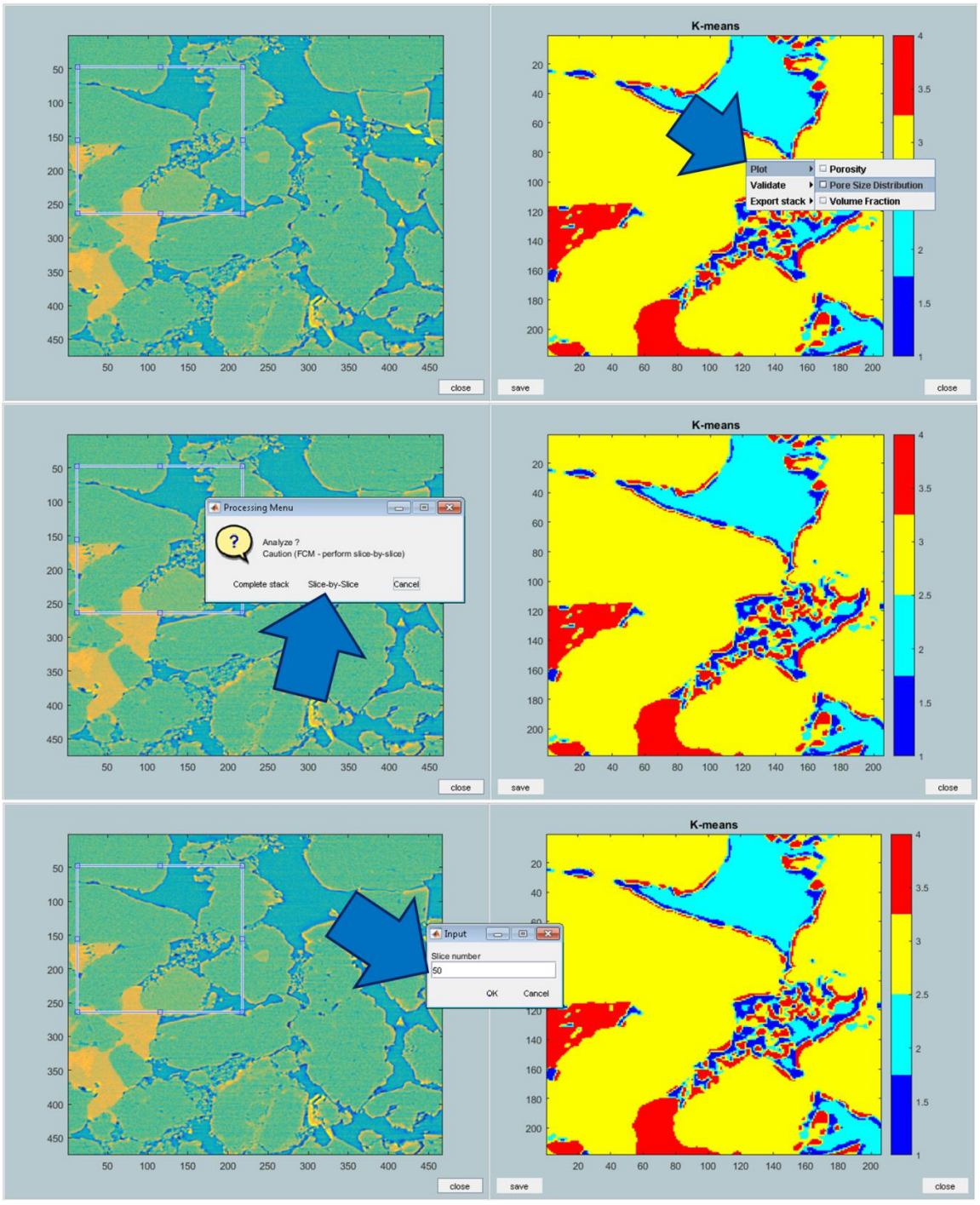

Figure 34: Pore size distribution processing menu and input

- Figure 34 displays the **Slice-by-Slice** option where the **slice number** has to be **entered by the user.**
- The **slice** (no. 50) is then displayed in a **new window**, as shown in Figure 34.

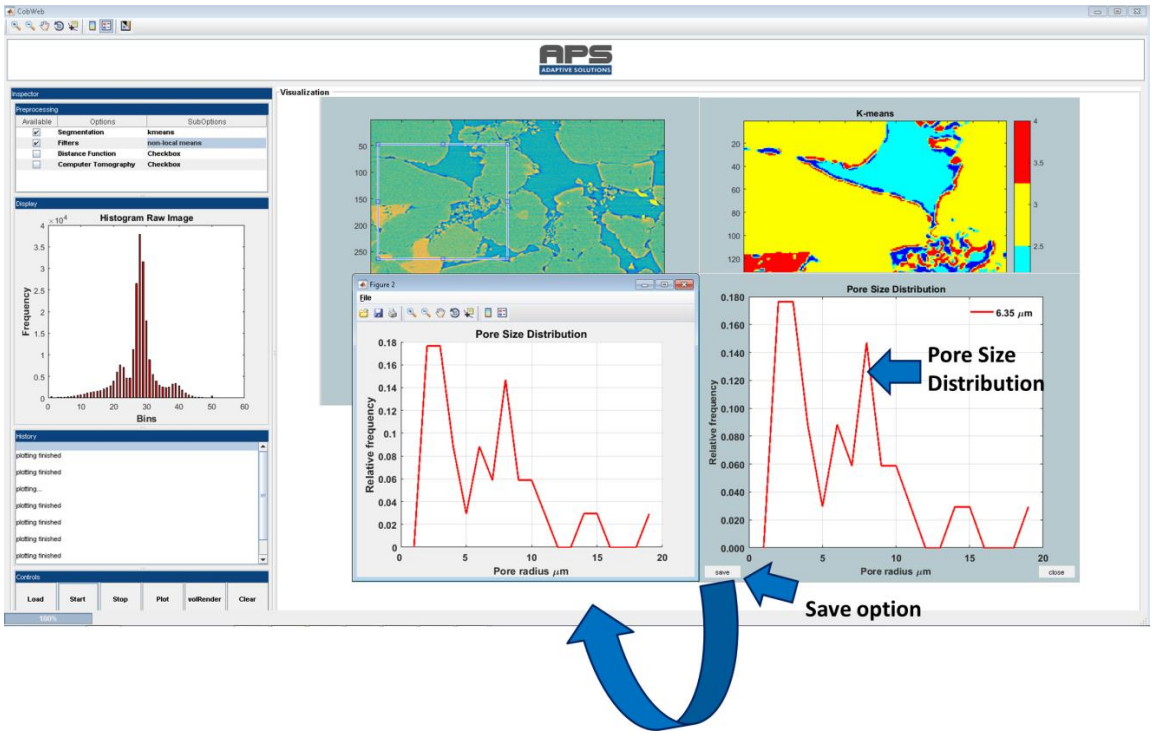

Figure 35: Pore size distribution of single slice

- The PSD of the respective slice is plotted in a new window, as shown in Figure 35.
- By clicking the save option, the plotted PSD can be saved in a desired image format.

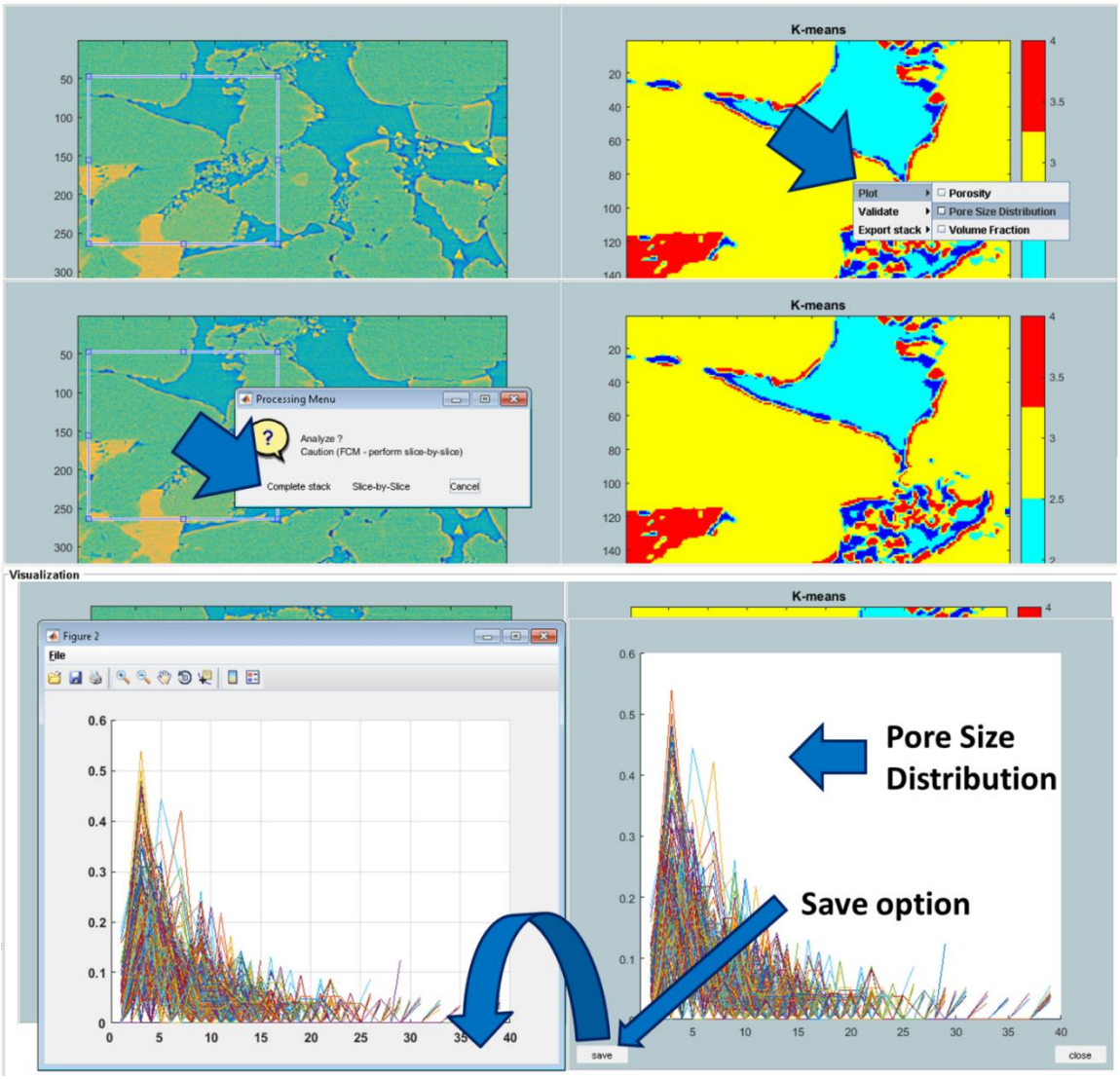

Figure 36: Pore size distribution of complete stack

- Figure 36 displays the steps to retrieve the PSD of the REV and the option to save the plot.

NOTE: The status bar might show a 100% status, but the plot is not shown. **Please be patient, the display of the plot window depends on your system configuration.** The plot appears as soon as the message **plotting finished** is display in the **history window**.

6.1.3. Volume Fraction

- To plot volume fraction, **right click** on the segmented slice and select **Plot -> Volume Fraction**, as shown in Figure 37.
- A processing menu pop-up appears with three options: Complete stack, Slice-by-Slice and Cancel.
    - **Complete stack**: The volume fraction of the complete stack is plotted.

- **Slice-by-Slice**: The volume fraction of the selected slice is plotted.
- **Cancel**: The process is abandoned.

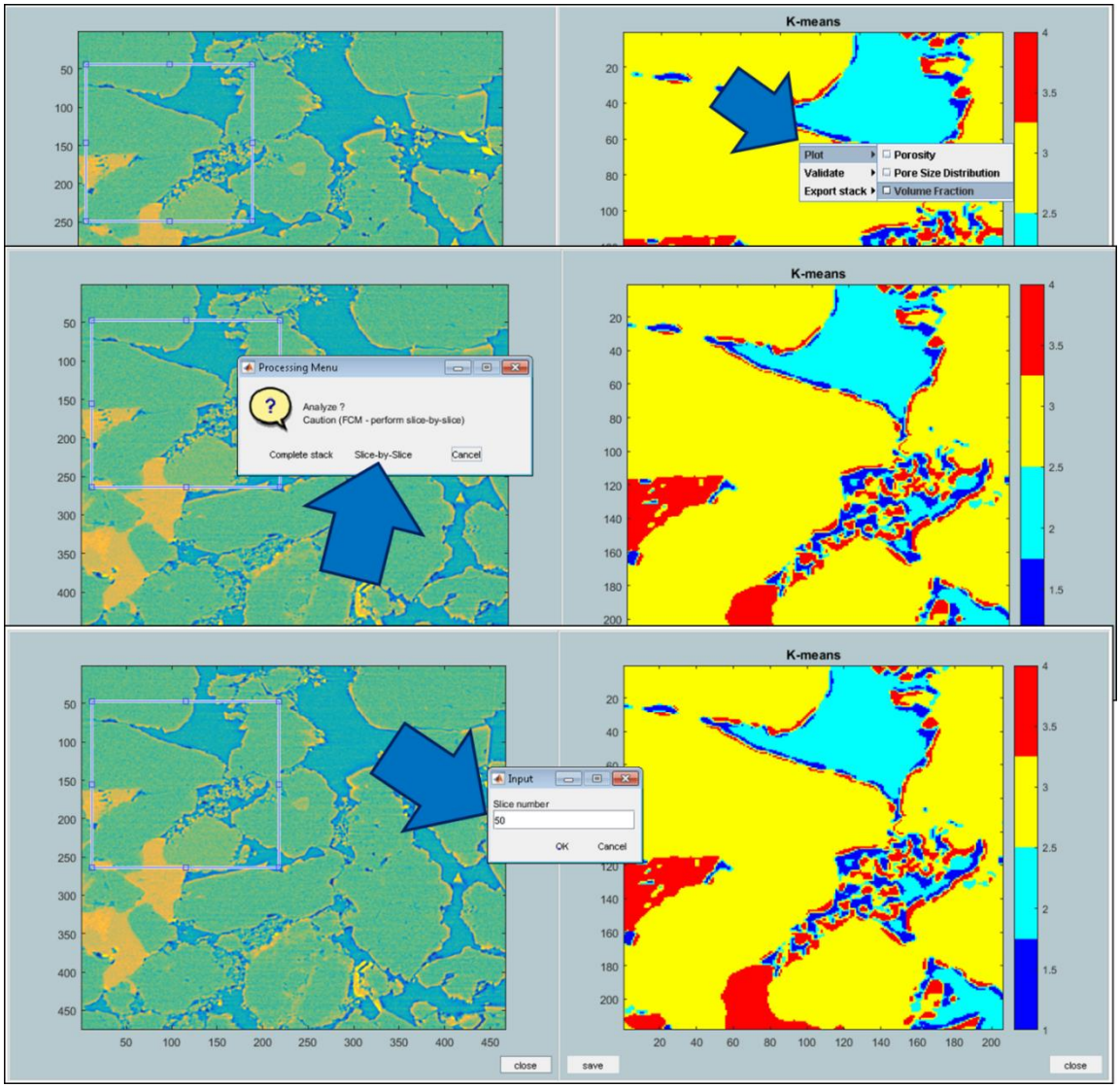

Figure 37: Volume fraction processing menu and input

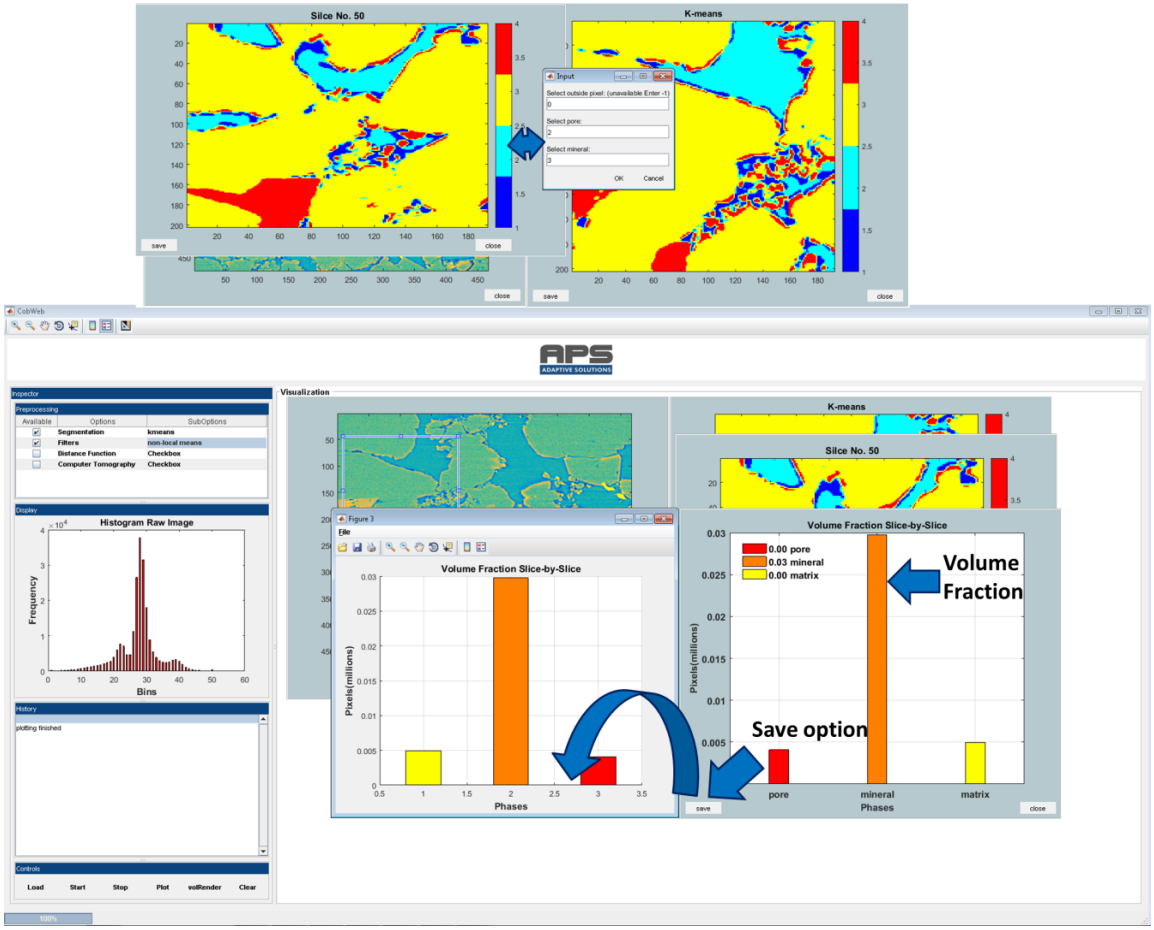

Figure 38: User input and volume fraction of single slice

- Figure 38 (top panel) shows the **slice** (no. 50) plotted in a **new window**.
- Figure 38 (top panel): The **user** assigns the cluster number to the **pore phase** and the **mineral phase** (in this case, pore = 2 and mineral = 3).
- Figure 38 (bottom panel) shows the **save option**. By clicking the save button, the plotted image can be saved in the desired image format.

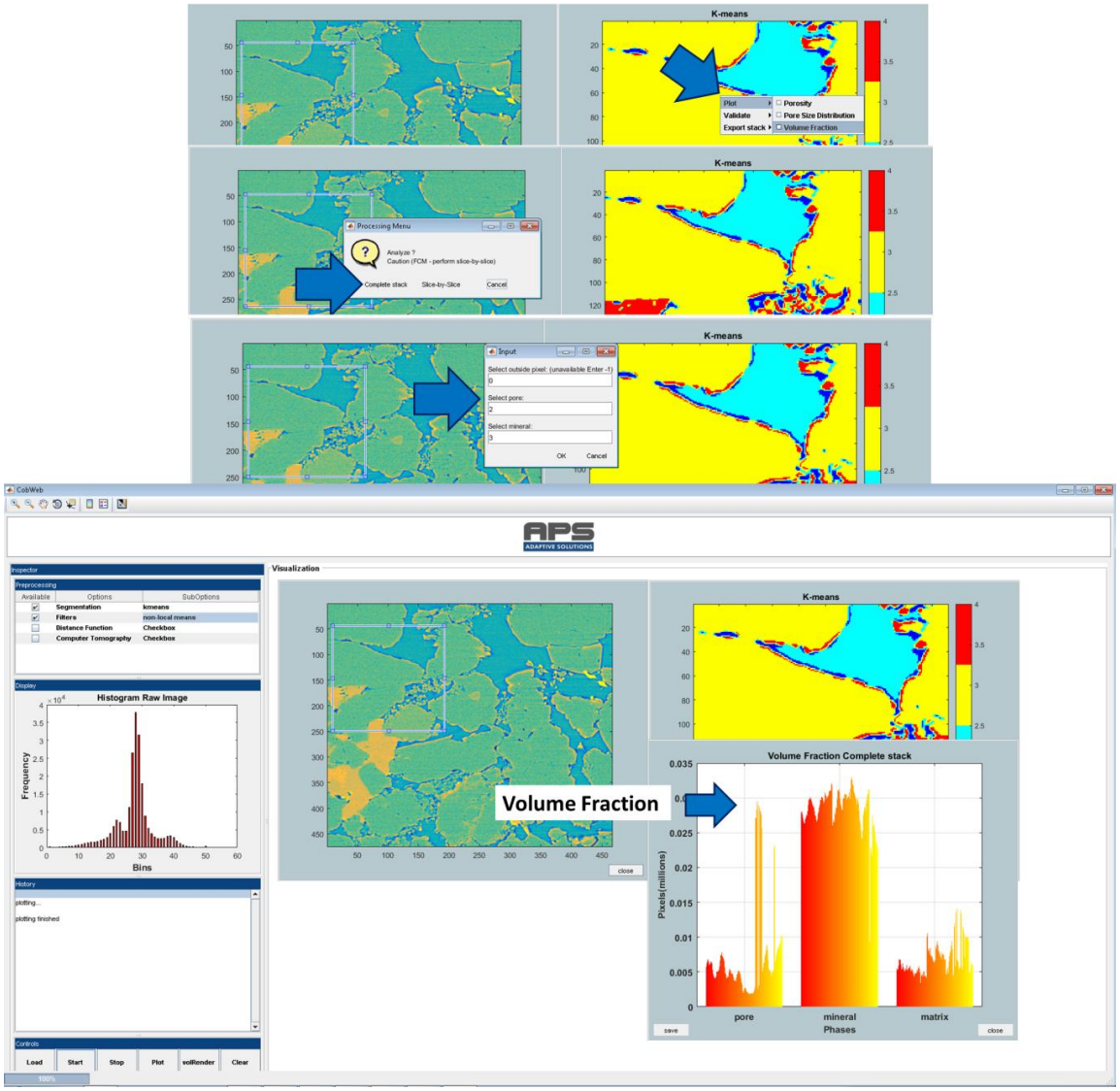

Figure 39: Volume fraction of complete stack

- Figure 39 (top, middle and bottom panels) shows the steps to retrieve the volume fraction of the REV. In this case, the plotted image cannot be saved in the desired file format due to technical limitations.

NOTE: The status bar might show a 100% status, but the plot is not shown. **Please be patient, the display of the plot window depends on your system configuration.** The plot appears as soon as the message **plotting finished** is display in the **history window**.

6.2. Validation

The validation analysis is performed to check the accuracy of the segmentation algorithms. Table 10 gives an overview of the algorithms and their respective metrics.

Table 9: Metrics for validation

Algorithms	Validation Metrics
K-means	**Entropy**
Fuzzy C-means	**Entropy**
Least Square Support Vector Machine	**Receiver Operation Characteristics**
Bragging	**K-fold Cross Validation**
Boosting	**k-fold Cross Validation**

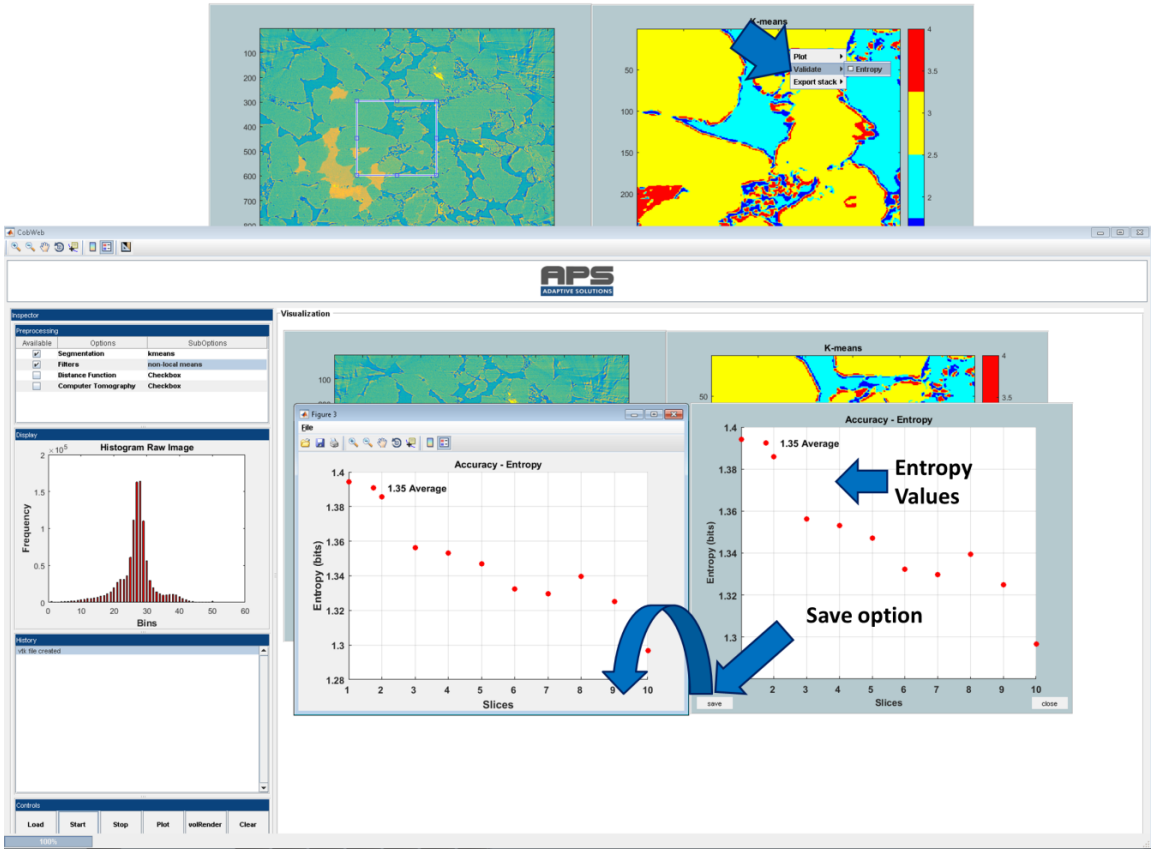

Figure 40: Plotting entropy

- Figure 40 (top panel) shows plotting Entropy. Right click on the segmented image and select validation → Entropy
- Figure 40 (bottom panel) shows how the plotted Entropy can be saved in the desired image format by clicking the save option.

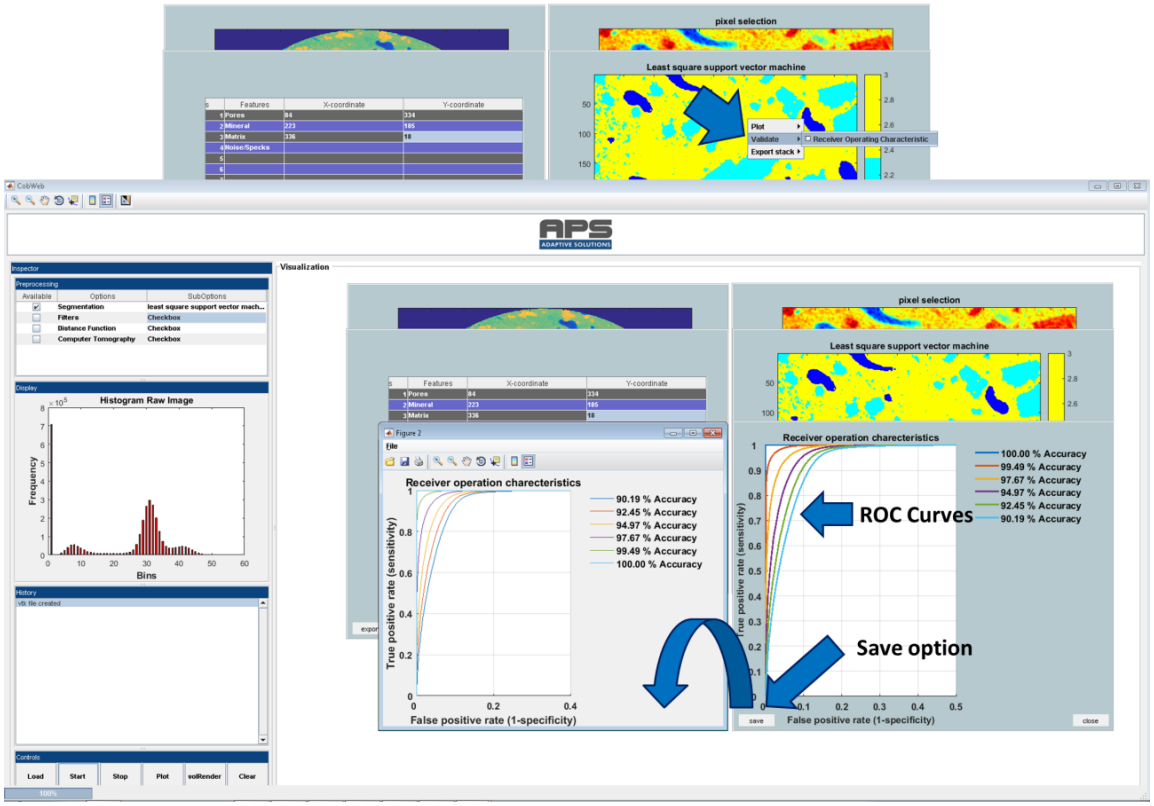

Figure 41: Plotting receiver operational characteristics (ROC)

- Figure 41 (top panel:, To plot receiver operation charecteristics (ROC), right click on the segmented image and **select validation → Receiver Operation Charecteristics**.
- Figure 41 (bottom panel): The plotted ROC can be saved in the desired image format by clicking the save option (see Figure 41).

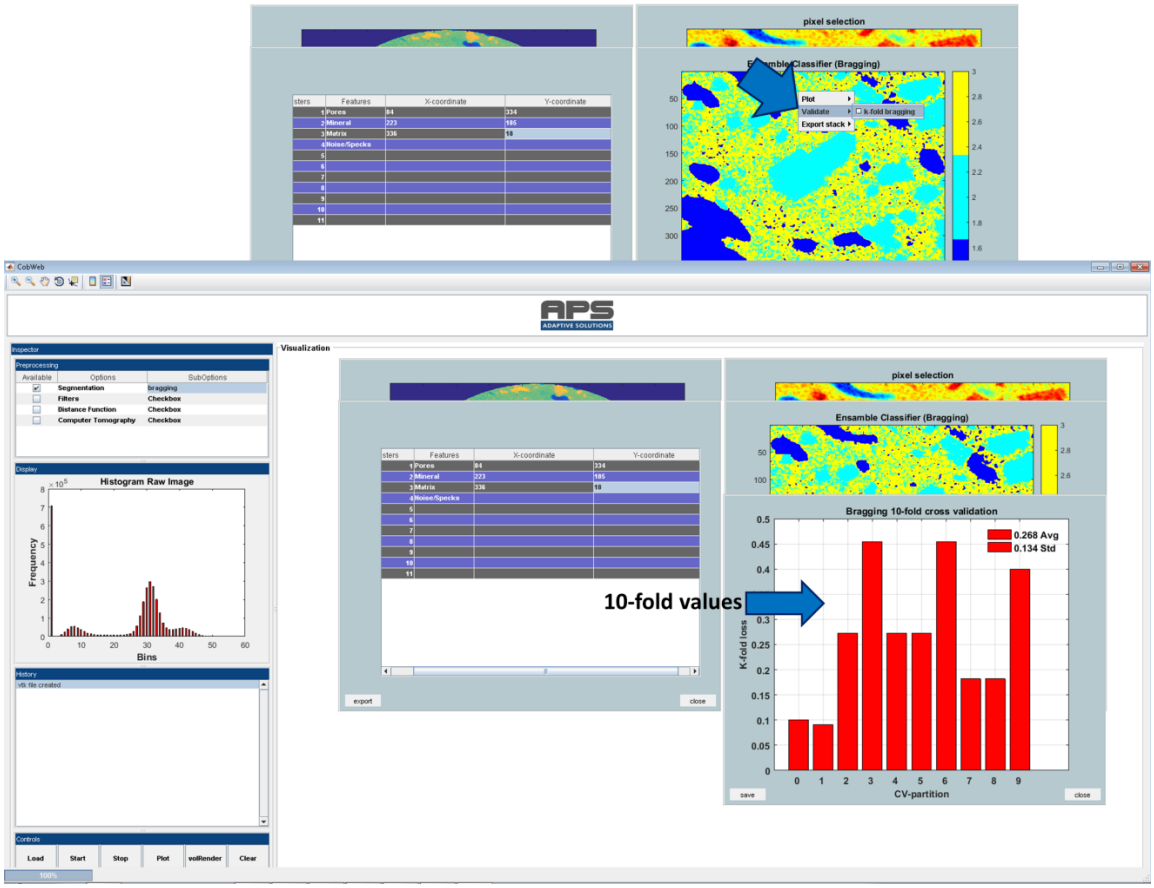

Figure 42: Plotting k-fold cross-validation

- Figure 42 (top panel) shows the plotting of K-fold cross validation. **Right click** on the segmented image and **select validation → k-fold bragging**.
- Figure 42 (bottom panel) show the plotted k-fold plot can be saved in the desired image format by clicking the save option.
- In the case of K-fold cross validation for Boosting, follow the same procedure as shown in the above bullet points.

6.3. Export

The processed XCT data can be exported into different formats. Table 10 gives an overview of the different file formats and associated CobWeb products

Table 10: Plugins and their respective file formats

Export Plugins	File Format	CobWeb Products
ParaView	**.vkt**	Segmented stack, as shown in Figure 43
Excel	**.xlsx**	• Relative porosity • Pore size distribution • Volume fraction • Entropy • ROC • K-fold Shown in Figure 44 and Figure 45
MATLAB	**.mat**	• Pore size distribution • Volume fraction • Entropy • ROC • K-fold Shown in Figure 44 and Figure 45
ASCII	**.txt**	• Pore size distribution • Volume fraction • Entropy • ROC • K-fold Shown in Figure 44 and Figure 45

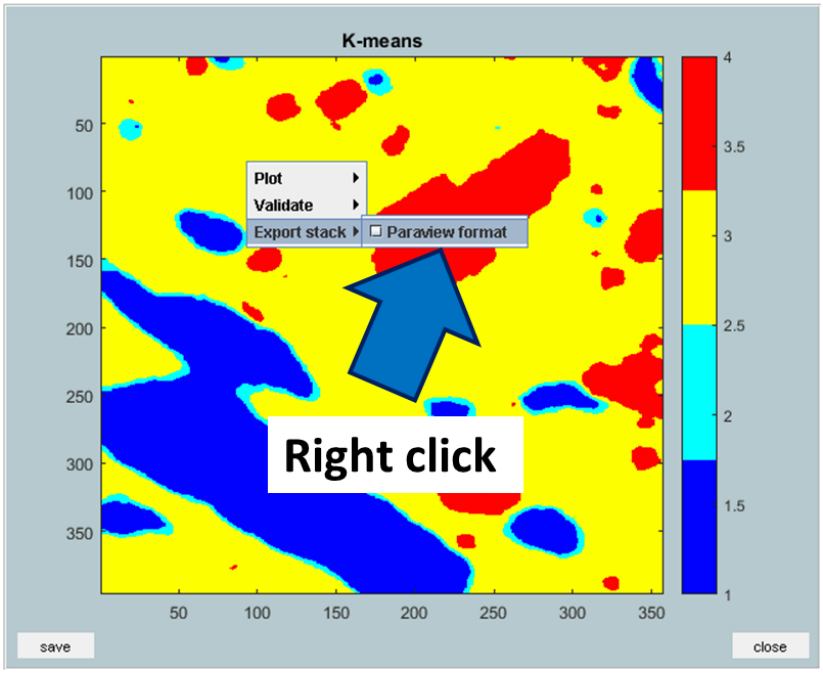

Figure 43: Export stack to ParaView

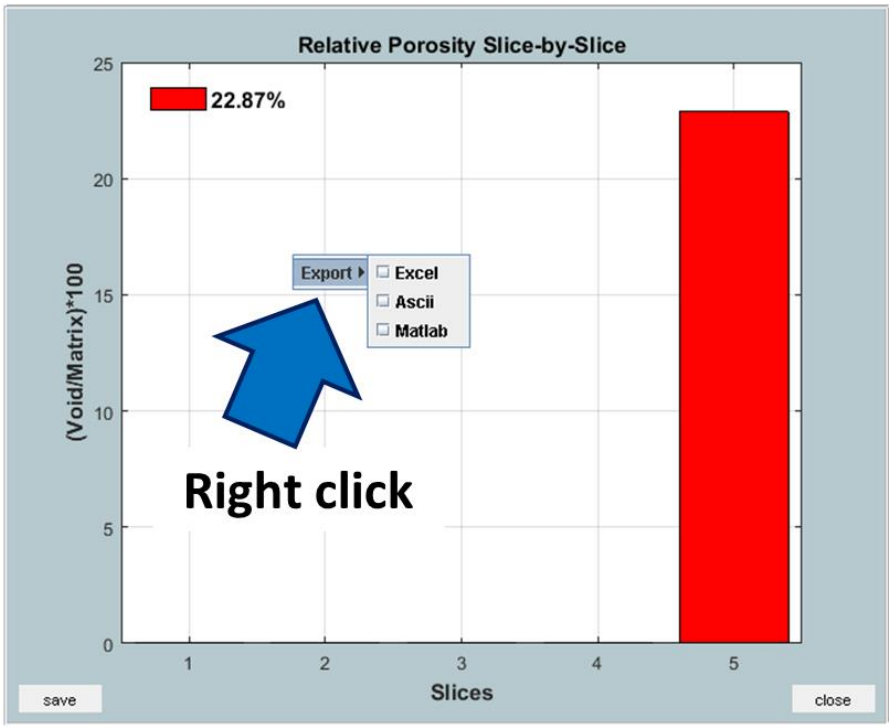

Figure 44: Export geometrical parameters

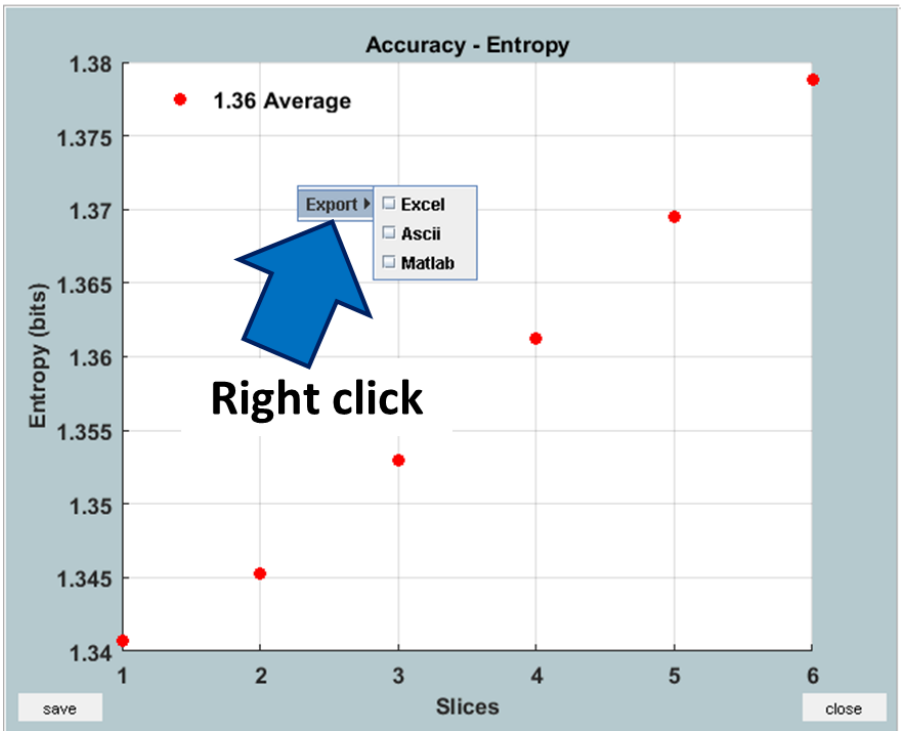

Figure 45: Export validation metrics

6.4. Volume Rendering

The volume rendering function is demonstrated here using a gas hydrate dataset, which was obtained from synchrotron measurements. CobWeb 1.0 is limited with respect to its volume

rendering capabilities compared to other XCT analysis software. This may be improved in future.

As an alternative, the data can be exported into .vkt format and can be visualised using the open source visualisation software ParaView.

6.4.1. Volume Rendering with CobWeb 1.0

- The complete REV can be rendered in CobWeb 1.0 by clicking the volume rendering button in the control panel.

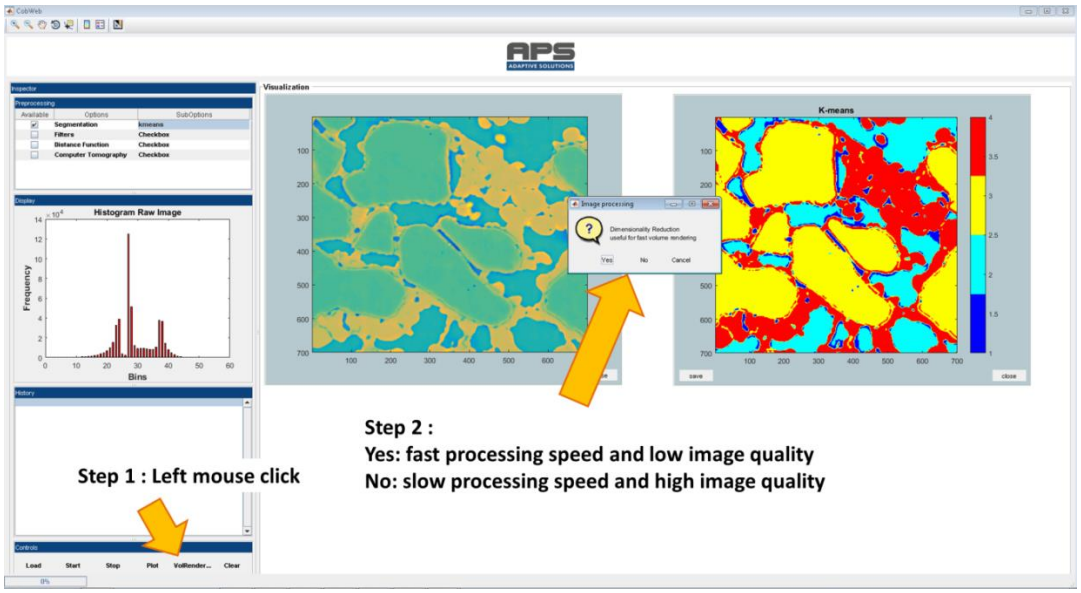

Figure 46: Volume rendering options in CobWeb 1.0

- Step 1 (Figure 46): **Click on** the **VolRendering** button on the **control panel.**
- Based on the system configuration, the REV stack can either be plotted in reduced resolution or in the original resolution.
- Step 2 (Figure 46): By choosing (clicking) the **Yes option**, the resolution of the REV stack will be reduced by a factor of 10, thereby **optimizing processing speed** and **degrading image quality**.
- Step 2 (Figure 46): By choosing (clicking) the **No option,** the REV is **rendered** in its **original resolution**. RAM capacity above 40 GB is best suited for this option.

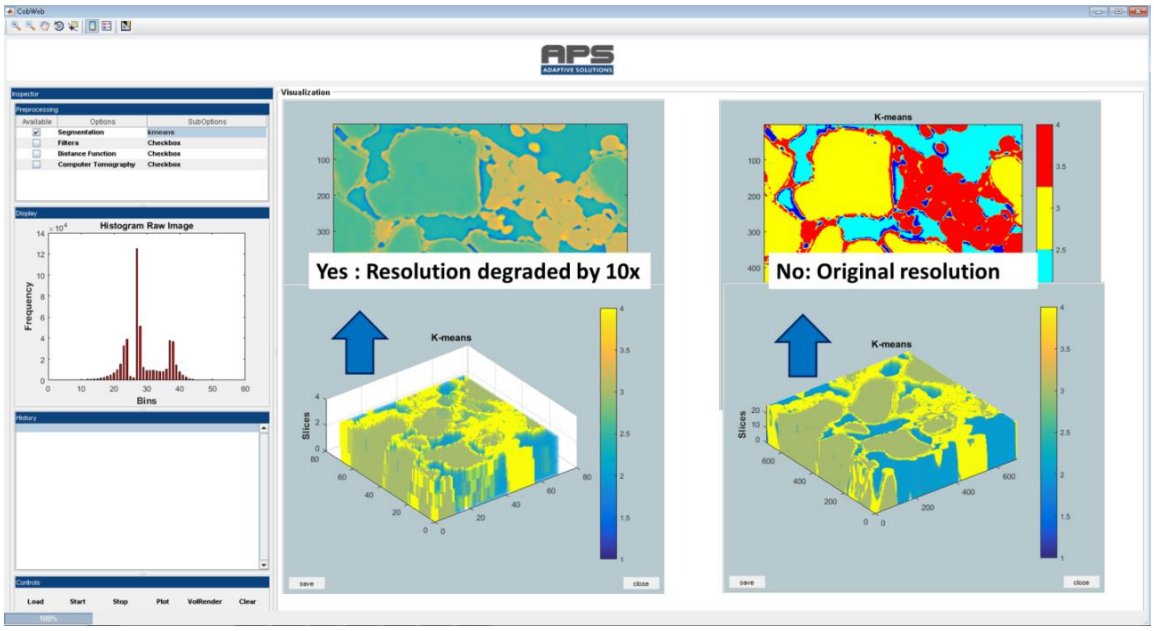

Figure 47: Volume rendering using CobWeb 1.0

- Figure 47 displays the rendered REV of gas hydrate in reduced (Yes option selected) and high resolutions (No option selected).

6.4.2. Volume Rendering with ParaView

To visualise the data in ParaView:

- Export the segmented stack into the ParaView format, as shown in Figure 48.
- The file can be saved at a desired location. Once the file has been created, the information is updated in the History window.

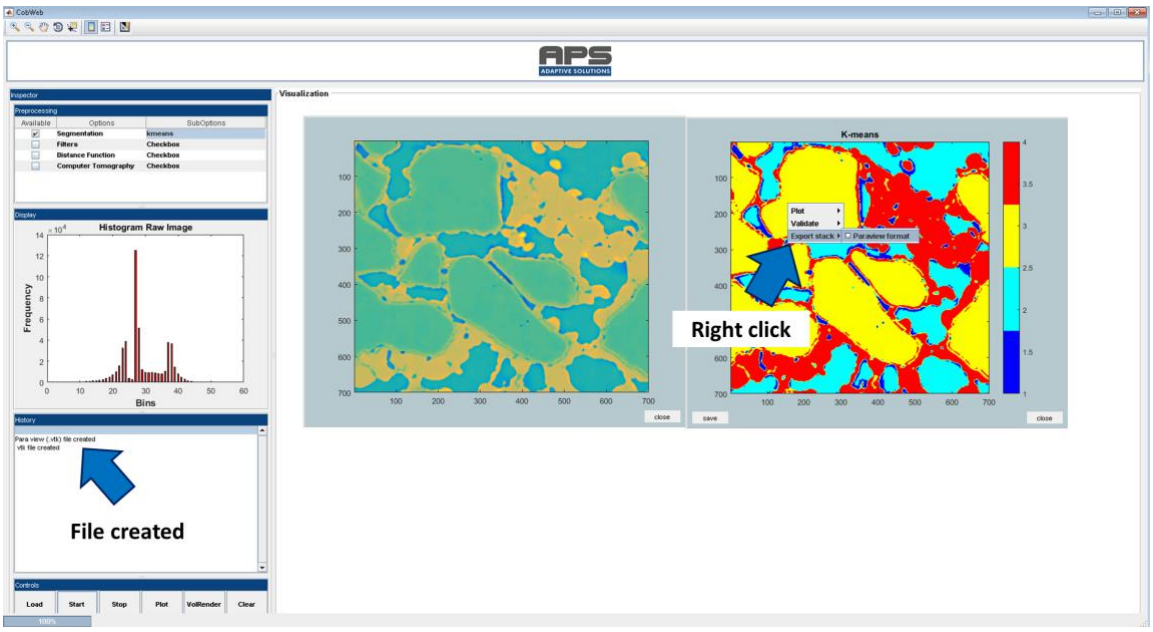

Figure 48: Export segmented REVs in .vkt format

- Figure 49 displays steps to load the .vkt file into ParaView. This is done by clicking on the folder button or using the file menu to import the file.

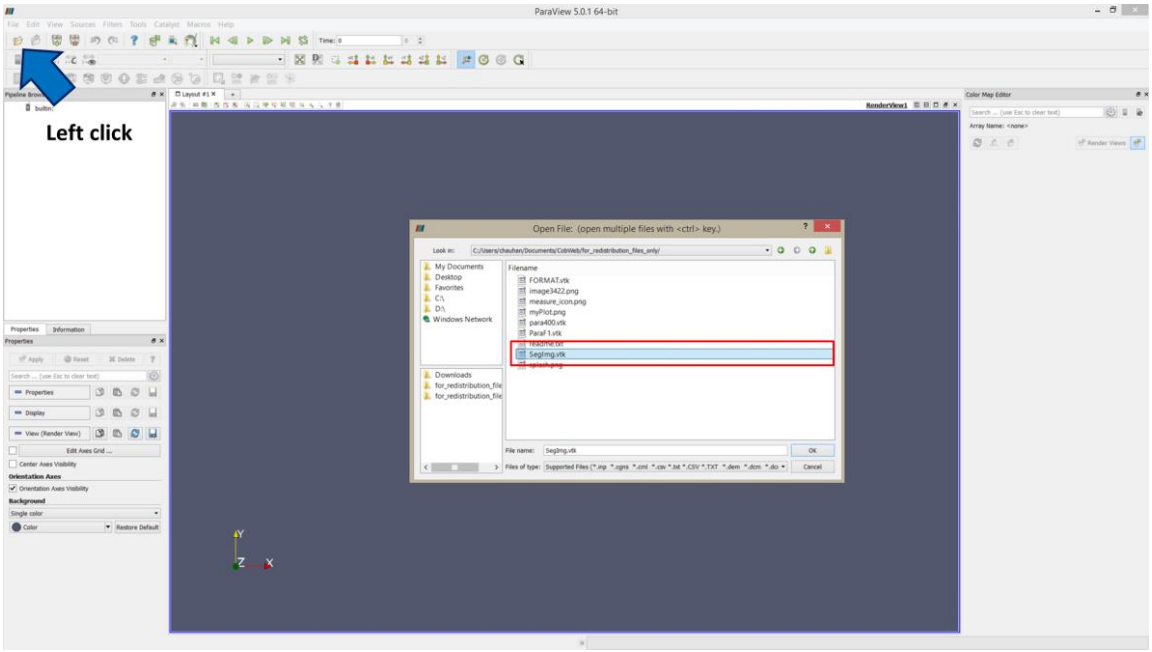

Figure 49: Loading VKT file in ParaView

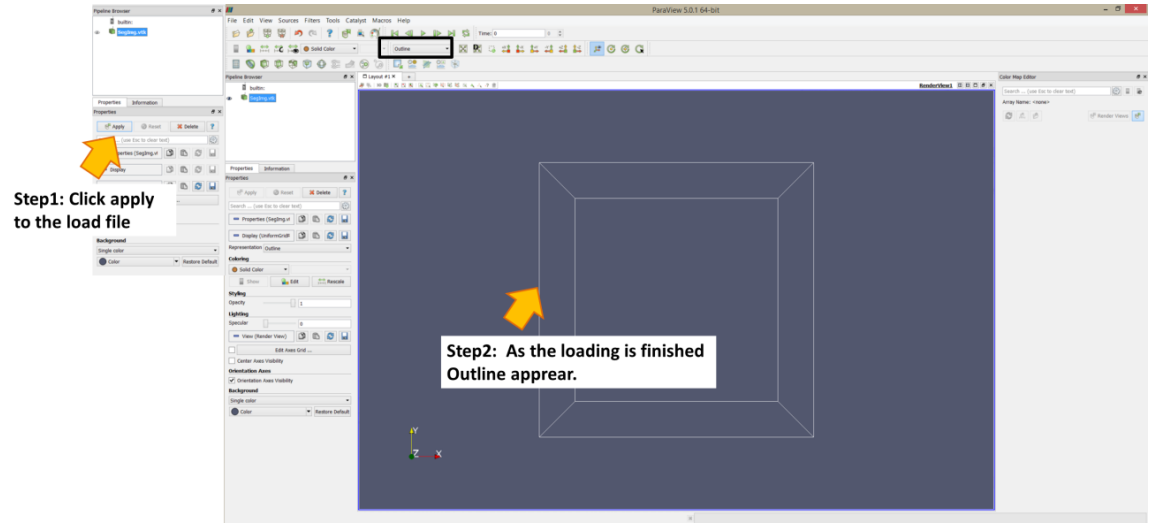

Figure 50: VKT file loaded in ParaView

- Step 1 (Figure 50): Once the file has been loaded, click the apply button to send the data to be read into ParaView. The reading may take time, depending on the system configuration.
- Step 2 (Figure 50): If the reading has been successfully completed, an outline or bounding box appears.

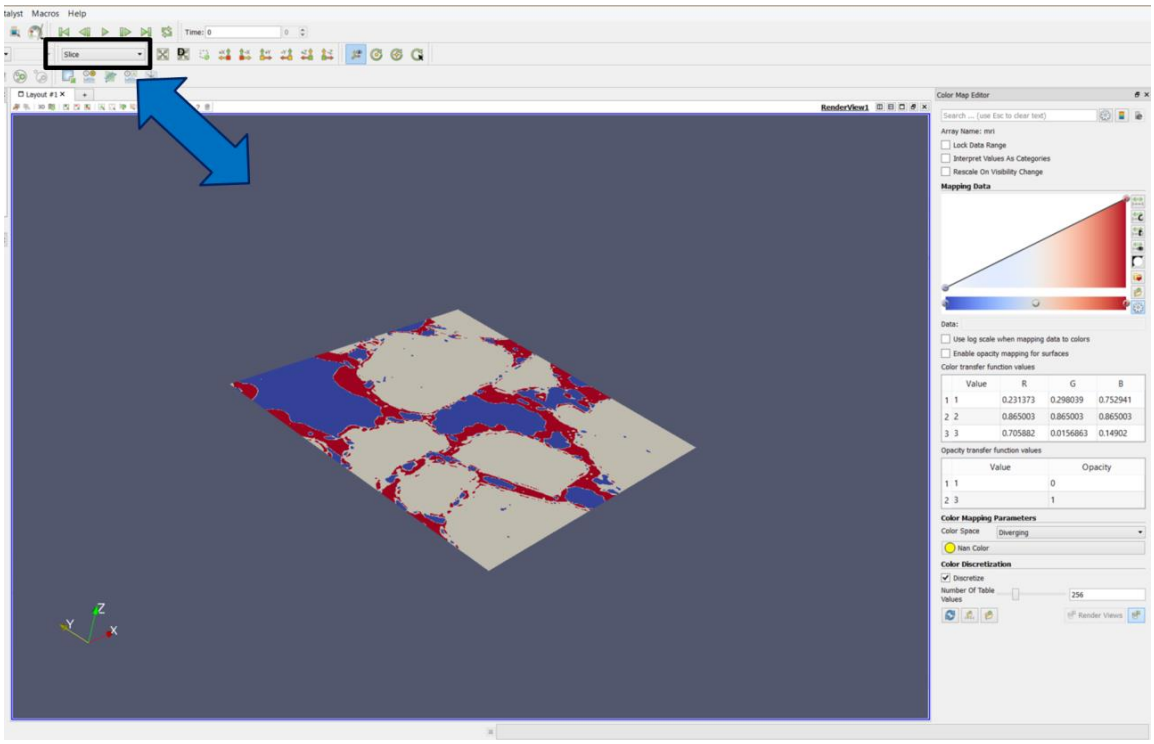

Figure 51: Slice mode in ParaView

- Figure 51: It is **advised** to view the **stack first in slice mode**. This can be done through the drop-down menu, marked in Figure 51 with a black box.

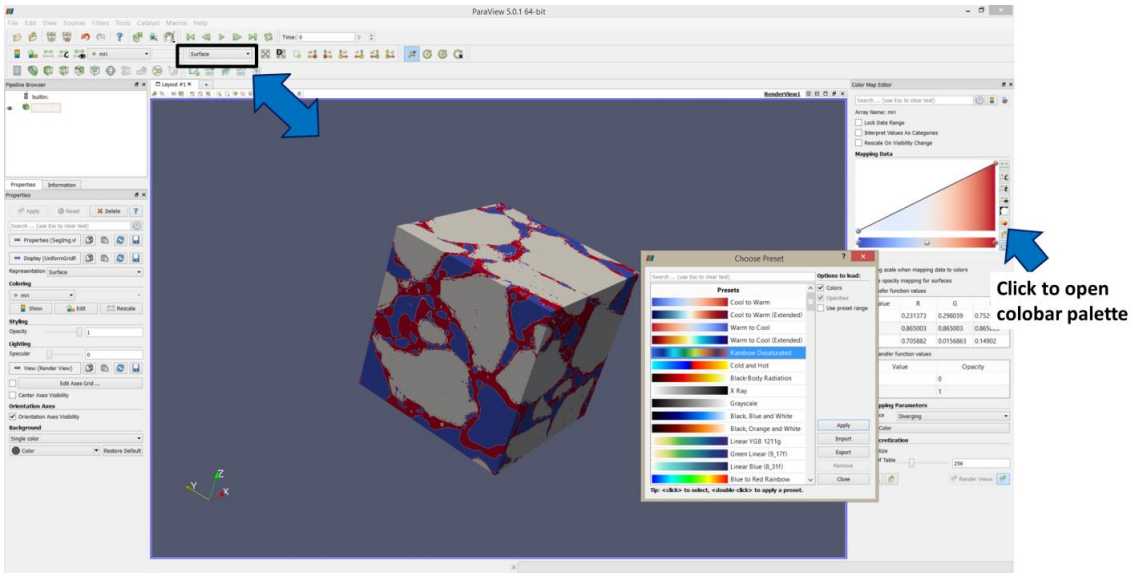

Figure 52: Surface mode in ParaView

- Figure 52: By changing the option from Slice -> Surface, using the drop-down menu highlighted in the black box, the complete stack can be further visualised in surface mode.
- Figure 52: To choose a different colour palette, left click on the icon.

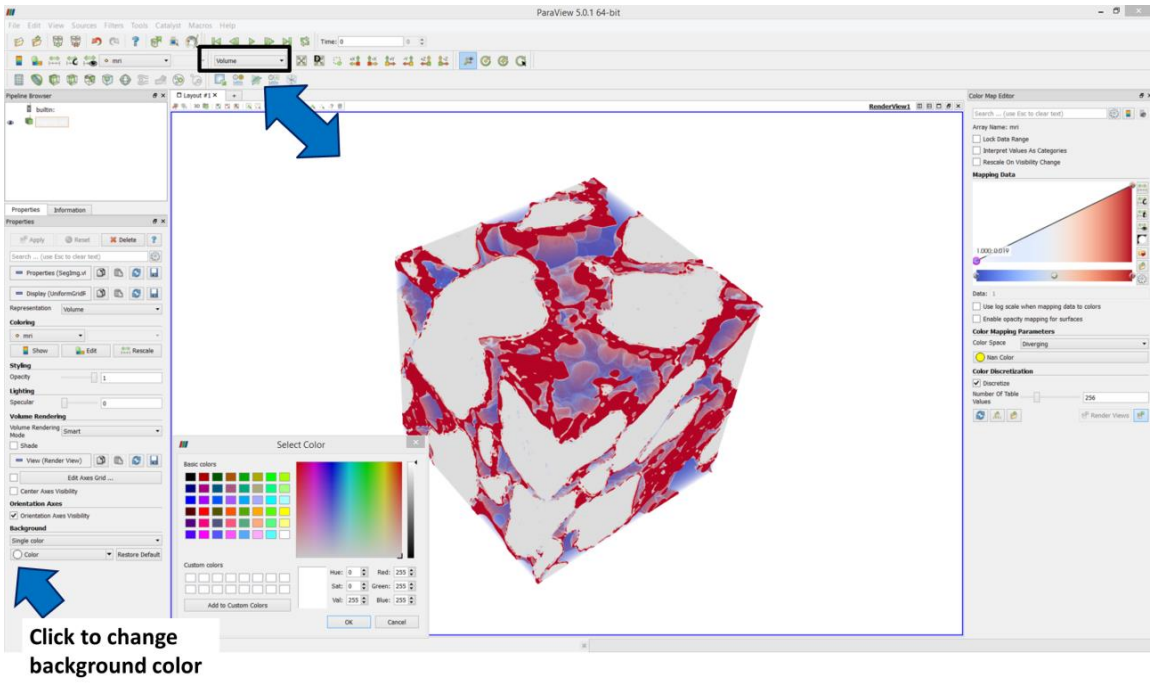

Figure 53: Volume rendered mode in ParaView

- Figure 53 shows the volume rendered plot. This is achieved by selecting the volume option highlighted by the black box in Figure 53. The stack can be further modified with different textures and opacity.
- Figure 53 also points out the option to change the background colour.

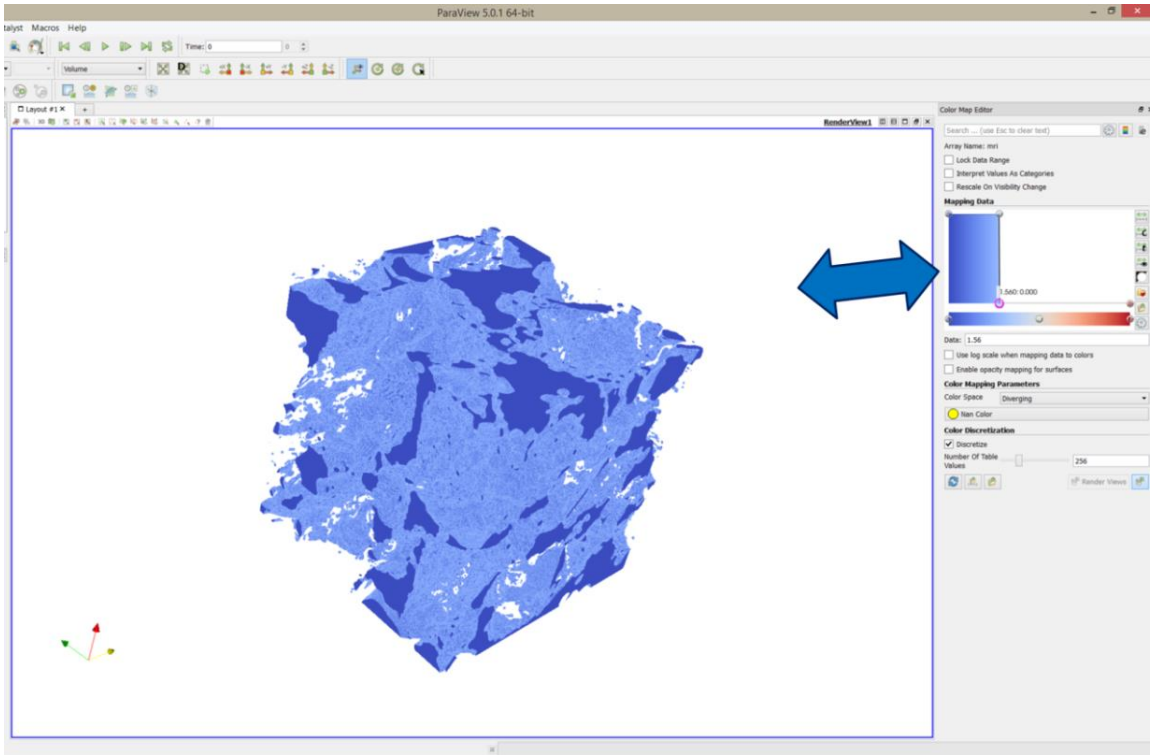

Figure 54: Pore volume in ParaView

- By altering the colorbar, different phases can be highlighted or suppressed.

- Figure 54: The pore phase is extracted by maximizing the blue phase and flattening the other phases.
- Figure 54: Different phases, in this case pore, hydrate and gas, can be extracted by altering the colour scale as shown in Figure 54, 55 and 56.

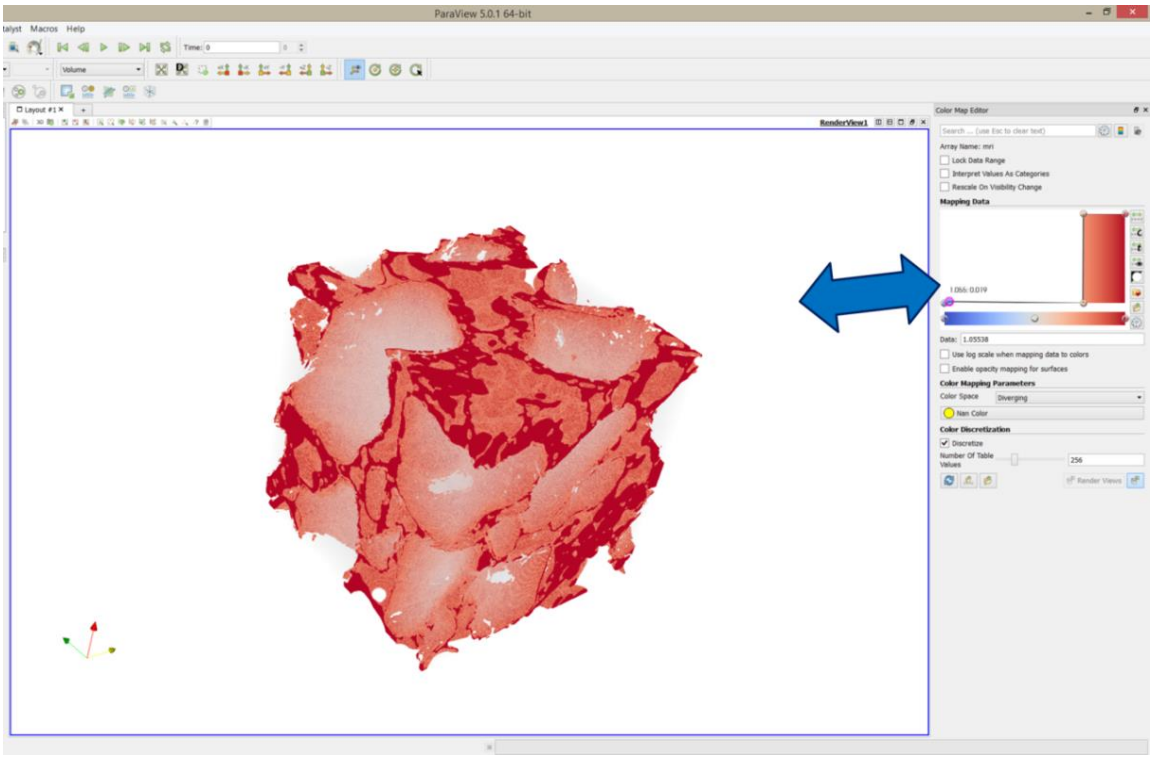

Figure 55: Hydrate volume in ParaView

- Figure 55: The **gas-hydrate phase** is extracted by **maximizing** the **red phase** and **flattening** the **other phases**.

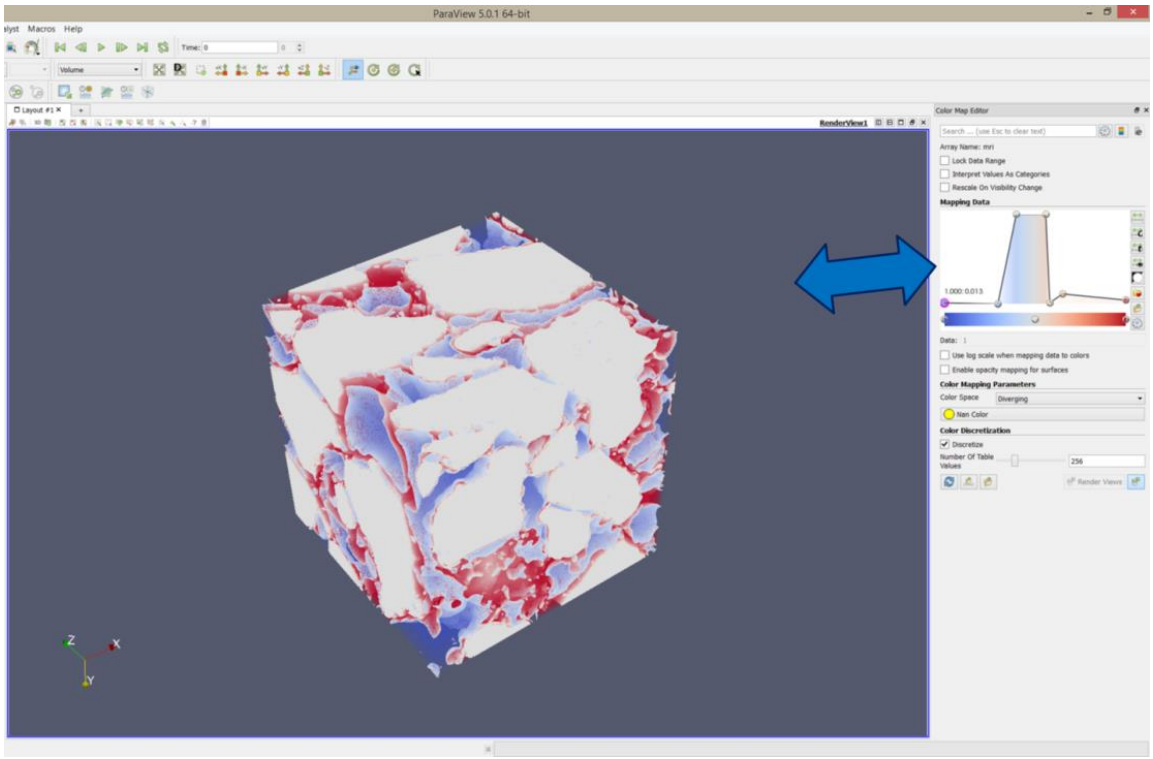

Figure 56: Gas volume in ParaView

- Figure 56: The **matrix phase** is extracted by **maximizing** the **gray phase** and **reducing** the **other phases**.

ParaView is a state-of-the-art open source visualisation software and can perform many other functions which cannot be covered in this manual. For more information, please refer to online tutorials and the documentation guide on ParaView website.

https://www.paraview.org/documentation/

7. Limitations

Table 11: Limitation of CobWeb 1.0

CobWeb 1.0
The number of interations in the case of FCM is hard coded up to 80 • **80 iterations give a fair balance between accuracy and speed**
In the case of FCM segmentation the colour scheme differs from slice-to-slice • **For example, cluster 4 might get the colour red for slice no. 1 and the colour blue for slice no. 50** **This is caused by the MATLAB FCM library as it chooses random starting points to initialise clusters.**
Some of the distance functions may not work for K-means or FCM • **The distance functions were configured for self-organised maps (SOM)** • **The SOM segmentation scheme was removed as it was not compatible with the standalone mode.**
Filters • **Non-local means is only implemented as a 2D filter because filtration is done slice-by-slice** • **Filtration works in tandem with segmentation, thus, viewing slices after filtration is not possible.**
The stop button does not instantaneously stop or kill the process.
In LSSVM segmentation, based on the user-supplied X, Y coordinate, an area around the coordinate axis is scanned and pixel values are extracted. The grid size of this area is fixed to 36 x 36 pixels. This implementation gave the best balance between accuracy and speed. **But in some cases, this might cause discrepancies in segmentation based on different feature ratios.**
The generated 2D XCT film has a low visualisation quality. • **We recommend using ParaView to generate XCT film.**
CobWeb's volume rendering capabilities are limited. Therefore for superior volume rendering results, we recommend using ParaView, as explained in section 7.4.1.
CobWeb 1.0 can read only RAW and TIFF files.

8. Trouble Shooting

Table 12: Troubleshooting

Problems	Possible Causes	Possible Solutions
3D Rendering problems, **such as** the **graphical window not upload**ing**, texture not appear**ing**.**	Outdated graphic card.	Upgrade graphic card.
	If onboard graphic card is installed.	The onboard graphic card may be inefficient for the CobWeb 1.0. Update.
Performance is low.	There is not enough RAM available due to other running applications.	Close other applications and if possible restart CobWeb 1.0.
Performance is extremely low when working with large data sets.	The size of the data sets exceeds the installed RAM capacity.	If possible install more RAM or select less number of data slices. Or use different sizes or ROI (region of interest).
The application hangs or crashes when working with large data sets.	The size of the data sets exceeds the installed RAM, the swap space is not activated or too small.	• Activate the swap space. • Enlarge the size of the swap space to about the order of magnitude of the RAM. • Install more RAM. • Reduce the size of the data set, select fewer slices.
On a **PC or notebook with two graphic cards: The application crashes.**	Automatic switching between the graphics cards does not work properly.	Deactivate the onboard graphic card in the BIOS in order to use the dedicated graphic card of the notebook or PC.
The application crashes when trying to open an animation saved to an .avi file using a	• The codec is not compatible with the selected settings of the .avi. • Most codecs are continuously being developed and are	• Install the 64-bit version of this codec. • Select a different codec.

third-party codec package.	not always free of bugs. • A 32-bit version instead of a 64-bit version of the codec is installed.	
CobWeb 1.0 does not start for a user with administrator rights.		Go to the CobWeb 1.0 folder and start the executable .exe directly.
When double clicking a file in Windows Explorer, it is not opened by CobWeb.	The files are not linked to the executablefile of CobWeb 1.0.	Go to the CobWeb 1.0 folder and start the executable .exe directly.

Curriculum Vitae

Mr. Swaroop Chauhan

23.03.1982, Hyderabad, India

Experience

Since 2018
Johannas Gutenberg University Mainz, Germany
Project Scientist

2012 - 2017
Technical University Darmstadt, Germany
Project Scientist

2010 - 2011
Hamtec Consultancy – EUMETSAT, Darmstadt, Germany
Satellite Product Engineer

2006 - 2009
Institute for Meteorology and Climate Research, Forschungszentrum Karlsruhe, Germany
Project Scientist

2004-2006
Department of Civil Engneering, Remote Sensing Lab, Indian Institute of Technology, Kanpur, India

Education

08.2002 - 06.2004
Masters in Atmospheric Sciences
Department of Atmospheric and Space Sciences
Univeristy of Pune, India

Grade Point Average, A, Note 1,4

Master Thesis, title, "Aerosol Size Distribution Using PREDE Skyradiometer Data over the region of Pune" Note 1,3

Summer Internship, title, "Morphology of Cosmic Dust Sperules, collected using MACDUC (Magnetic Cosmic Dust Collector) from Indian Ocean expedition"

08.2000 - 2002
Bachlor in Mathematics, Physics and Chemistry
Osmania Univeristy Hyderabad
Hyderabad, India
First division, Note: 2,0

1985-1997
Secondary School Certificate (Allgem. Hochschulreife)
Secondary Education Andhra Pradesh, Indien
Hyderabad, India
First division, Note: 2,0

Languages

Hindi (native), English (fluent), German (fluent)